Model Complexes for Reactive Intermediates in Cytochrome P450 Nitric Oxide Reductase (P450nor)

by

Ashley B. McQuarters

A dissertation submitted in partial fulfillment
of the requirements for the degree of
Doctor of Philosophy
(Chemistry)
in the University of Michigan
2017

Doctoral Committee:

Professor Nicolai Lehnert, Chair
Professor Vincent Pecoraro
Professor Lucy Waskell
Assistant Professor Paul Zimmerman

To my parents:

William and Cathy McQuarters

Acknowledgements

Nicolai, thank you for your mentorship over the past several years! I appreciate that you always challenged me to solve complex problems. Your unwavering support has made me into a best version of a scientist that I can be. The leadership and mentoring experiences I gained in your laboratory are invaluable.

The Lehnert laboratory has been a great place to work, thanks for all the laughs everyone! Lauren Goodrich, thank you for your mentorship – you taught me how to problem solve and that it is crucial to never give up. I learned you must be relentless to solve problems! To Shawn Eady and Amy Speelman, we kept each other sane through the difficult times and celebrated our successes together. I am grateful for our friendship and I look forward to a lifetime of friendship.

Mom and Dad, thank you for your love, support, and enthusiasm of my education. Your drive to be successful has taught me the value of hard work. You always pushed me to go beyond what I thought I was capable of. I would not be the person I am without you!

Alex, we made it! Your love, friendship, and constant support are irreplaceable. This is just the beginning of our lifetime of happiness together.

Table of Contents

Acknowledgements ..... **ii**

List of Tables ..... **v**

List of Figures ..... **vii**

List of Schemes ..... **xxviii**

Abstract ..... **xxx**

Chapter 1. Introduction **1**

1.1 The Nitrogen Cycle 1

1.2 Fungal NO Reductase 3

1.3 Scope of Thesis 16

1.4 References 19

Chapter 2: Modeling the Key Intermediate in P450nor: Electronic Structure and Reactivity **21**

2.1 Reduction of a Ferric Bis-Picket Fence Porphyrin with O-Benzylhydroxylamine 24

2.2 Synthesis and Spectroscopic Characterization of [Fe(3,5-Me-BAFP)(NHOMe)] 34

2.3 One-electron Oxidation of the Ferric Hydroxylamide Porphyrin Complex 39

2.4 Electronic Structure of the Intermediate *I* Model Complex 50

2.5 Reactivity of $[Fe(3,5\text{-}Me\text{-}BAFP)(NHOMe)]^{+}$ with NO 54

2.6 Experimental Section 58

2.7 References 75

Chapter 3: Stable Analogues for Ferrous HNO Complexes: Characterization and Reactivity of Ferrous Heme-Nitrosoalkane Complexes **79**
3.1 Characterization of Ferrous Porphyrin RNO Complexes 81
3.2 Vibrational Analysis of [Fe(TPP)(iPrNO)] 98
3.3 Reactivity of Ferrous Heme-Nitrosoalkane Complexes 104
3.4 Experimental Section 115
3.5 References 132

Chapter 4: Ferric Heme-Nitrosyl Complexes: Synthesis, Spectroscopic Properties, and Stabilities **133**
4.1 Synthesis and Characterization of Ferric Heme-Nitrosyl Complexes 138
4.2 Stability of $\{FeNO\}^6$ Complexes 148
4.3 Crystallographic Studies 152
4.4 The Role of Halides for Stability 155
4.5 Nuclear Resonance Vibrational Spectroscopy (NRVS) 161
4.6 Experimental Section 172
4.7 References 196

Chapter 5: Conclusions **200**
Conclusions 200

List of Tables

Table 2.1 Selected bond lengths for [Fe(3,5-Me-BAFP)(NH_3)$_2$], Fe[TDCP(NO_2)$_8$P(H_2O)$_2$], [Fe(TPP)(1-BuNH_2)$_2$], [Fe(TPP)(BzNH_2)$_2$], and [Fe(TPP)(Ph$CH_2CH_2NH_2$)$_2$] 30

Table 2.2 Comparison of geometric parameters of selected iron porphyrin complexes to [Fe(3,5-Me-BAFP)(NHOMe)] and the calculated structure of this complex with BP86/TZVP (P^{2-} = porphine) 38

Table 2.3 NH_3 concentrations (mM) determined from the assay of the bulk material of [Fe(3,5-Me-BAFP)(NH_3)$_2$]. The theoretical [NH_3] is based on the amount of [Fe(3,5-Me-BAFP)(NH_3)$_2$] used in the assay 71

Table 3.1 Comparison of geometric and vibrational parameters and BP86/TZVP calculated structures of ferrous porphyrin PhNO complexes (P = porphine^{2-}). 84

Table 3.2 Comparison of geometric parameters and vibrational frequencies for selected ferrous porphyrin complexes 97

Table 3.3 Comparison of geometric and vibrational parameters and BP86/TZVP calculated structures of ferrous iPrNO/NHO heme complexes (P = porphine^{2-}) 102

Table 4.1 Comparison of geometric parameters for selected $\{FeNO\}^6$ complexes 154

Table 4.2 Comparison of vibrational frequencies for selected $\{FeNO\}^6$ complexes 160

List of Figures

Figure 1.1 Processes that occur in the nitrogen cycle. ANAMMOX stands for Anerobic Ammonium Oxidation. Reproduced from: Lehnert, Coruzzi, Hegg, Seefeldt & Stein, “NSF Workshop Report: Feeding the World in the 21st Century: Grand Challenges in the Nitrogen Cycle”, 2016. 2

Figure 1.2 NO-bound ferric heme in the active site of P450nor from *Fusarium oxysporum* 3

Figure 1.3 Top: optimized structures, geometric parameters and calculated N-O stretching frequencies of [Fe(P)(X)(NO)] complexes obtained with BP86/TZVP (P = porphine^{2-}, X = axial ligand). Bottom: important Fe-NO orbital interactions, calculated for [Fe(P)(OC(=O)CF_3)(NO)] with BP86/TZVP. A) and B) the two strong π backbonding interactions, C) the weak σ interaction, and D) the antibonding σ*_d_z^2 interaction responsible for the bending of the Fe-NO unit 7

Figure 1.4 Left: The crystal structure of [Fe(3,5-Me-BAFP)(NO)]. The hydrogen atoms are omitted for clarity and thermal ellipsoids are shown at 30% probability. Adapted from reference 27. Right: Top down view of a space filling model of [Fe(3,5-Me-BAFP)(NO)]. 13

Figure 2.1 Left: UV-vis spectra of [Fe(3,5-Me-BAFP)(ClO_4)] (black) and of the product of the reaction of this complex with excess NH_2OBn (blue) in toluene at room temperature. Right: UV-vis spectra of [Fe(3,5-Me-BAFP)(PF_6)] (black) and of the product of the reaction of this complex with excess NH_2OBn (red) in toluene at room temperature 26

Figure 2.2 EPR spectra of [Fe(3,5-Me-BAFP)(ClO_4)] (black) and of the product of the reaction of this complex with excess NH_2OBn (blue) in toluene. Spectra were measured at 10 K. EPR spectra of [Fe(3,5-Me-BAFP)(PF_6)] (black) and of the product of the reaction of this complex with excess NH_2OBn (red) in 2-Me-THF. Spectra were measured at 6 K. 27

Figure 2.3 Crystal structure of [Fe(3,5-Me-BAFP)(NH_3)$_2$]. Hydrogen atoms and a solvent molecule (toluene) are omitted for clarity. Thermal ellipsoids are shown at 30% probability..... 28

Figure 2.4 Left: UV-vis spectra of [Fe(3,5-Me-BAFP)(PF_6)] and of the isolated reaction product, [Fe(3,5-Me-BAFP)(NHOMe)] (blue), in 2-Me-THF at room temperature. Right: EPR spectrum of [Fe(3,5-Me-BAFP)(NHOMe)] in toluene at 6 K..... 35

Figure 2.5 NRVS-derived vibrational density of states (VDOS) for the precursor, [^{57}Fe(TPP)(SbF_6)] (black), and the isolated reaction product, [^{57}Fe(3,5-Me-BAFP)(NHOMe)] (blue). Bottom: Calculated (BP86/TZVP) NRVS VDOS spectrum of [Fe(P)(NHOMe)] 36

Figure 2.6 Left: Crystal structure of [Fe(3,5-Me-BAFP)(NHOMe)]. Hydrogen atoms and the disorder of the NHOMe ligand are omitted for clarity. The thermal ellipsoids are shown at 30% probability. Right: Schematic drawing of [Fe(3,5-Me-BAFP)(NHOMe)]. 37

Figure 2.7 CV of a 3 mM solution of [Fe(3,5-Me-BAFP)(NHOMe)] in 1,2-DCE, where the working electrode is glassy carbon and the counter electrode is platinum with a Ag wire pseudo-reference at room temperature. Right: Schematic representation of the one-electron oxidation of [Fe(3,5-Me-BAFP)(NHOMe)], which could result in the oxidation of the iron-NHOMe unit, or the porphyrin co-ligand... 40

Figure 2.8 Top: UV-vis spectra for the SEC oxidation of [Fe(3,5-Me-BAFP)(Cl)] (green to blue) in an OTTLE UV-vis cell, taken in 0.10 M tetrabutylammonium hexaflourophosphate solution in 1,2-dichloroethane at room temperature. The working and counter electrodes are Pt mesh. Bottom: Re-reduction of the oxidation product (blue to green), showing that the oxidation is fully reversible 42

Figure 2.9 Left: UV-vis spectra of the titration of a ~11 μM solution of [Fe(3,5-Me-BAFP)(Cl)] (green) with the chemical oxidant $[N(C_6H_4Br\text{-}4)_3][SbCl_6]$, in dichloromethane, to form the ferric porphyin radical complex, $[Fe(3,5\text{-}Me\text{-}BAFP)(Cl)]^+$ (green). Right: UV-vis spectra obtained upon addition of the excess oxidant, showing that the reaction is complete after the addition of one equivalent of oxidant 43

Figure 2.10 Top Left: UV-vis spectra of [Fe(3,5-Me-BAFP)(Cl)] (black) and after addition of ~1 equiv. $[N(C_6H_4Br\text{-}4)_3][SbCl_6]$, in dichloromethane, lead to the formation of the ferric porphyrin radical complex, $[Fe(3,5\text{-}Me\text{-}BAFP)(Cl)]^+$ (blue). The reaction product after stirring for 5.5 hours under an inert atmosphere at room temperature is shown in green. Top right: Subsequent reaction of the oxidized species with excess ferrocene reforms the [Fe(3,5-Me-BAFP)(Cl)] precursor (green). Bottom: EPR spectra of a 1.2 mM solution of the ferric chloride complex, [Fe(3,5-Me-BAFP)(Cl)], and of the reaction product upon addition of ~1 equiv. $[N(C_6H_4Br\text{-}4)_3][SbCl_6]$, measured at 5 K in dichloromethane..... 45

Figure 2.11 Left: UV-vis spectra of the reaction of a ~6 μM solution of [Fe(3,5-Me-BAFP)(NHOMe)] (black) with 1.1 equiv. $[DAcFc][SbF_6]$ in toluene (blue). Right: UV-vis spectra of the reaction of a ~38 μM solution of [Fe(3,5-Me-BAFP)(NHOMe)] (black) with 1.1 equiv. $[DAcFc][SbF_6]$ in toluene (blue). All reactions were carried out under an inert atmosphere at -80°C..... 48

Figure 2.12 EPR spectra of a 0.1 mM solution of the ferric complex, [Fe(3,5-Me-BAFP)(NHOMe)], and of the reaction product upon addition of ~1 equiv. $[DAcFc][SbCl_6]$, measured at 5 K in dichloromethane..... 49

Figure 2.13 rRaman spectra of frozen solutions of [Fe(3,5-Me-BAFP)(NHOMe)] (black), the reaction product upon addition ~1 equiv. $[DAcFc][SbF_6]$ (blue), the reaction product(s) after the solution is warmed to room temperature (green),

and a low-spin ferric complex, [Fe(3,5-Me-BAFP)(1-MI)$_2$]SbF_6 (black) in toluene/DME (power = 28 mW)..... 51

Figure 2.14 4.2 K low-field (53 mT) Mössbauer spectrum of a ~2 mM solution of [Fe(3,5-Me-BAFP)(NHOMe)] frozen in a 5:1 ratio of toluene/DME 53

Figure 2.15 4.2 K Mössbauer spectrum of a ~0.3 mM solution of [Fe(3,5-Me-BAFP)(NHOMe)]$^+$ frozen in a 5:1 ratio of toluene/DME..... 53

Figure 2.16 Left: *In situ* UV-vis monitoring of the reaction of [Fe(3,5-Me-BAFP)(NHOMe)]$^+$ (blue) with excess NO gas in green, which is indicative of [Fe(3,5-Me-BAFP)(SbF_6)]. Right: Further reaction with NO gas to form a six-coordinate ferric heme-nitrosyl complex, [Fe(3,5-Me-BAFP)(NO)(L)]$^+$, where L is a neutral ligand..... 55

Figure 2.17 CVs of a ~3 mM solution of [Fe(3,5-Me-BAFP)(Cl)] in 1,2-dichloroethane where the working electrode is glassy carbon and the counter electrode is platinum with a Ag wire pseudo-reference at room temperature 58

Figure 2.18 ^{1}H-NMR spectra of the ferric chloride complex, [Fe(3,5-Me-BAFP)(Cl)], measured in CD_2Cl_2 with the line width set to 0.3 Hz. Bottom: The reaction product upon addition of ~1.0 equiv. [N(C_6H_4Br-4)$_3$][$SbCl_6$] in dichloromethane to form [Fe(3,5-Me-BAFP)(Cl)]$^+$ 59

Figure 2.19 Left: UV-vis spectra of a solution of [Fe(3,5-Me-BAFP)(NHOMe)] (black) and the reaction product upon addition of ~1 equiv. [DAcFc][SbF_6] in toluene (blue). Note that the oxidant is dissolved in DME. Right: Comparison

of the reaction product (blue) and [Fe(3,5-Me-BAFP)(SbF_6)] in toluene (green). 60

Figure 2.20 Top: EPR spectrum of the reaction of [Fe(3,5-Me-BAFP)(NHOMe)] with ~1 equiv. [DAcFc][SbF_6] in a 5:1 toluene/DME mixture at room temperature. Bottom: EPR spectrum of [Fe(3,5-Me-BAFP)(SbF_6)] in a 5:1 toluene/DME mixture. Both EPR spectra were taken at 5 K 60

Figure 2.21 Top left: *In situ* UV-vis monitoring of the decomposition of [Fe(3,5-Me-BAFP)(NHOMe)]$^+$ (blue) over a one hour time period (green). Top right: Fit of the UV-vis band at 570 nm over time. The data are fit to a single exponential function with k_{obs} = 1.7*10^{-4} s^{-1} ($t_{1/2}$ = 68 minutes). Bottom: *In situ* UV-vis monitoring of the warming of the oxidized species (shown in top left graph; blue) over a 10 minute time period to the final product [Fe(3,5-Me-BAFP)(SbF_6)] (green) 61

Figure 2.22 rRaman spectrum of a frozen solution of 0.94 mM of [Fe(3,5-Me-BAFP)(SbF_6)] in 5:1 toluene/DME mixture measured at 77 K (power = 30 mW). The * denotes bands from toluene 62

Figure 2.23 ^{1}H-NMR spectra of [Fe(3,5-Me-BAFP)(SbF_6)] recorded in CD_2Cl_2 with the line width set to 1 Hz. The inset graph shows the β-pyrrole hydrogens of the porphyrin co-ligand. 65

Figure 2.24 Left: Gas IR spectra of the reaction of a solution of 0.28 mM [Fe(3,5-Me-BAFP)(NHOMe)]$^+$ with excess NO gas in a 5:1 toluene/DME mixture (blue) and control reactions under same conditions with 150 µL N_2O (black) and NO

gas (purple) added in a 5:1 toluene/DME mixture. The headspace of the flask was transferred to a gas IR cell at room temperature. Right: Comparison of the gas IR spectra of 0.28 mM [Fe(3,5-Me-BAFP)(NHOMe)] with excess NO gas in a 5:1 toluene/DME mixture (black) and with the addition of 3 equiv. trifluoroacetic acid. 150 μL of N_2O is a 100% N_2O yield 69

Figure 2.25 Calibration curve of absorbance versus NH_4Cl concentration (μM) in water (blue) and water-toluene mixtures (red). 71

Figure 3.1 UV-vis spectra of the precursor, [Fe(TPP)(BF_4)] (black), and of the isolated reaction product, [Fe(TPP)(PhNO)] (green), in dichloromethane at room temperature..... 82

Figure 3.2 Top: Overlay of the IR spectra of [Fe(TPP)(PhNO)] (black), and the ^{15}N-labeled complex, [Fe(TPP)(Ph^{15}NO)] (green), measured in KBr pellets. Bottom: Zoom into of the N-O stretching frequency region of the IR spectra 87

Figure 3.3 Top: Comparison of the IR spectra of the isolated product, [Fe(TPP)(Ph^{15}NO)], prepared by reacting [Fe(TPP)] with different equivalents of Ph^{15}NO. The N-O stretching frequency region is identical when excess Ph^{15}NO (black) versus ~1 equiv. Ph^{15}NO (blue) is used. Bottom: Overlay of the IR spectra of [Fe(TPP)($PhNO)_2$] (black) and the ^{15}N-labeled complex, [Fe(TPP)($PhNO)_2$] (blue), measured in KBr pellets. 88

Figure 3.4 UV-vis spectra of the precursor, [Fe(3,5-Me-BAFP)] (black), and of the isolated reaction product, [Fe(3,5-Me-BAFP)(PhNO)] (blue), in THF at room temperature..... 89

Figure 3.5 UV-vis spectra of the precursor, [Fe(TPP)] (black), and of the isolated reaction product, [Fe(TPP)(iPrNO)] (red), in THF at room temperature. Note that complex likely has THF bound to the iron center 90

Figure 3.6 Left: Overlay of the IR spectra of [Fe(TPP)(iPrNO)] (black), and of the ^{15}N-labled complex, [Fe(TPP)(iPr^{15}NO)] (blue), measured in KBr pellets. Right: Zoom into the N-O stretching frequency region of the IR spectra 91

Figure 3.7 Top: Crystal structures of the two unique ferrous PhNO complexes in the unit cell of the co-crystallized compounds [Fe(TPP)(PhNO)(PhNH$_2$)] (left) and [Fe(TPP)(PhNO)(THF)] (right). Bottom: Crystal structures of [Fe(3,5-Me-BAFP)(PhNO)(2-Me-THF)] (left) and [Fe(TPP)(iPrNO)(THF)] (right) 93

Figure 3.8 View looking down the *meso* carbon group of the heme plane in [Fe(TPP)(PhNO)(THF)]. All of the hydrogen atoms and phenyl groups of the porphyrin ligand are omitted for clarity 95

Figure 3.9 Top: NRVS-derived vibrational density of states (VDOS) for [^{57}Fe(TPP)(iPrNO))] (black) and the ^{15}N-labeled iPrNO complex (blue). Bottom: BP86/TZVP calculated NRVS VDOS for [Fe(P)(iPrNO)] (black) and [Fe(P)(iPrNO)(THF)] (blue) 101

Figure 3.10 BP86/TZVP calculated NRVS VDOS for [Fe(P)(NHO)] (black), [Fe(P)(NHO)(THF)] (blue), and [Fe(P)(NHO)(MI)] (green) 103

Figure 3.11 UV-vis spectra of the titration of ~14 μM [Fe(TPP)(PhNO)] (black) in THF with a NO saturated solution of dichloromethane, forming the ferrous NO complex [Fe(TPP)(NO)] (blue). Right: Changes in the absorption at 476 nm upon addition of the NO solution, showing that the reaction is complete after the addition of ~0.90 equivalent of the NO saturated dichloromethane solution 105

Figure 3.12 UV-vis spectra of the titration of ~13 μM [Fe(TPP)(PhNO)] (black) with a solution of MI in dichloromethane, forming the six-coordinate complex [Fe(TPP)(PhNO)(MI)] (purple). Right: UV-vis spectra of the titration of ~51 μM [Fe(TPP)(PhNO)] (black) with a solution of MI in dichloromethane, forming the six-coordinate complex [Fe(TPP)(PhNO)(MI)] (purple). In both cases, the reaction is complete after the addition of ~1.0 equivalent MI to the solution 106

Figure 3.13 UV-vis spectra of [Fe(TPP)(PhNO)(MI)] (purple) and of the reaction product upon addition of 50 μL of NO gas (~6 equiv.) in dichloromethane, which is the ferrous NO complex, [Fe(TPP)(NO)] (blue) 108

Figure 3.14 UV-vis spectra of a solution of [Fe(TPP)(PhNO)] (black), with ~1 equiv. MI added to the solution (purple), and 50 equiv. MI added to the same solution (blue) 108

Figure 3.15 UV-vis spectra of [Fe(TPP)(iPrNO)] (black) and of the reaction of this complex with 18 equiv. of acetic acid after stirring for ~24 hours (green) in CH_2Cl_2. Right: EPR spectra of EPR-silent [Fe(TPP)(iPrNO)] (black) and of the

product after reaction with 18 equiv. of acetic acid and stirring for ~24 hours (green; 18 equiv.) in CH_2Cl_2 110

Figure 3.16 Top: UV-vis spectra of the titration of ~16 μM [Fe(TPP)(iPrNO)] (black) in CH_2Cl_2 with a NO saturated solution of dichloromethane, forming the ferrous NO complex [Fe(TPP)(NO)] (blue). Inset: Changes in the absporption at 476 nm upon addition of the NO solution, showing that the reaction is complete after the addition of ~0.60 equivalent of the NO saturated dichloromethane solution. Bottom left: UV-vis spectra of the titration of ~16 μM [Fe(TPP)(iPrNO)] (black) with a solution of MI in dichloromethane, forming the six-coordinate complex [Fe(TPP)(iPrNO)(MI)] (purple). Bottom right: UV-vis spectra of the titration of ~74 μM [Fe(TPP)(iPrNO)] (black) with a solution of MI in dichloromethane, forming the six-coordinate complex [Fe(TPP)(PhNO)(MI)] (purple)..... 115

Figure 3.17 UV-vis spectra of the titration of ~16 μM [Fe(TPP)(iPrNO)(MI)] (purple) in CH_2Cl_2 with a NO saturated solution of dichloromethane, forming the ferrous NO complex [Fe(TPP)(NO)] (blue). Inset: Changes in the absorption at 476 nm upon addition of NO solution, showing that the reaction is complete after the addition of ~0.60 equivalent of the NO saturated dichloromethane solution 116

Figure 3.18 Left: Overlay of the IR spectra of the precursor, [Fe(3,5-Me-BAFP)] (black), and of the reaction product, [Fe(3,5-Me-BAFP)(PhNO)] (red),

measured in KBr pellets. Right: Zoomed of the N-O stretching frequency region of the IR spectra..... 116

Figure 3.19 UV-vis spectra of [Fe(TPP)(iPrNO)] (black) and of the reaction product of this complex with excess trifluoroacetic acid (red; 4 equiv.) in CH_2Cl_2... 117

Figure 3.20 ^{1}H-NMR spectrum of [Fe(TPP)(PhNO)] in CD_2Cl_2 with the line width set to 0.3 Hz at room temperature..... 123

Figure 3.21 ^{1}H-NMR spectrum of [Fe(3,5-Me-BAFP)(PhNO)] in CD_2Cl_2 (with TMS) with the line width set to 0.3 Hz at room temperature 126

Figure 4.1 Top: Comparison of the UV-vis spectra of the precursor, [Fe(TPP)(SbF_6)] (black), the {FeNO}^{7} complex [Fe(TPP)(NO)] (blue), and the {FeNO}^{6} complex [Fe(TPP)(NO)]SbF_6 (purple, redissolved under non-NO saturated conditions), isolated from the reaction of the iron(III)-SbF_6 complex with excess NO gas in dichloromethane. All spectra recorded at room temperature. Bottom: Overlay of the IR spectra of the precursor, [Fe(TPP)(SbF_6)] (black), [Fe(TPP)(NO)] (blue), and [Fe(TPP)(NO)]SbF_6 (purple) measured in KBr pellets..... 140

Figure 4.2 CV of ~6.6 mM [Fe(TPP)(NO)] in CH_2Cl_2 at room temperature. The working electrode was a glassy carbon and the counter electrode was a platinum electrode with a Ag wire pseudo-reference with tetrabutylammonium hexafluorophosphate was used as the electrolyte..... 142

Figure 4.3 Left: UV-vis spectra of the titration of ~10 μM [Fe(TPP)(NO)] (black) with the chemical oxidant [DAcFc][SbF_6] (dissolved in dimethoxyethane) in

dichloromethane, forming the ferric NO complex $[Fe(TPP)(NO)]^+$ (purple). Right: Changes of the absorption at 550 nm upon addition of the oxidant, showing that the reaction is complete after the addition of one equivalent of oxidant 144

Figure 4.4 Left: UV-vis SEC used for the formation of $[Fe(TPP)(NO)]^+$ (black), compared to $[Fe(TPP)(NO)]^+$ (purple) generated by chemical oxidation, both recorded in dichloromethane. These data show that identical species are formed by both methods. Right: UV-vis spectra of [Fe(TPP)(NO)] before (black) and after addition of the chemical oxidant $[DAcFc][SbF_6]$ (dissolved in dimethoxyethane) in dichloromethane, leading to the formation of the ferric NO complex, $[Fe(TPP)(NO)]^+$ (purple). Subsequent reaction of the oxidized species with ferrocene reforms the $\{FeNO\}^7$ precursor (blue) 145

Figure 4.5 Left: Solution IR spectra of 1.8 mM [Fe(TPP)(NO)] (black) in CH_2Cl_2 and of the reaction product (purple) after the addition of ~1.30 equiv. $[DAcFc][SbF_6]$ to the solution. The N-O stretch at 1676 cm^{-1} shifts to 1850 cm^{-1} upon oxidation. The bands at 1702 and 1672 cm^{-1} are the C-O stretching frequencies (ester groups) of the respective $DAcFc^{0/+}$ reagents. Right: EPR spectra of the same solution used for the solution IR experiments (on the left) at 4K. The black spectrum represents the $\{FeNO\}^7$ complex with a broad, isotropic S = 1/2 signal at g = 2.0, and the purple spectrum represents the solution of the corresponding oxidized species, $[Fe(TPP)(NO)]^+$, which is EPR silent and contains a minor g = 6 signal that spin integrates to <5% of a ferric impurity 146

Figure 4.6 Comparison of the UV-vis spectra of the five-coordinate {FeNO}^{6} complex [Fe(TPP)(NO)]$^+$ (green), to the six-coordinate complex [Fe(TPP)(NO)(MI)]$^+$ (purple), and the [Fe(TPP)(SbF_6)] precursor in dichloromethane..... 147

Figure 4.7 Left: Solution IR spectra of a 2.4 mM solution of [Fe(TPP)(NO)] (black) in CH_2Cl_2 and of the reaction product after the addition of ~1.25 equiv. [DAcFc][SbF_6] to the solution (shown in blue). The N-O stretching frequency of the {FeNO}^{6} complex at 1850 cm^{-1} remains unchanged after one hour of stirring in solution (green). The bands at 1672/1702 cm^{-1} belong to the DAcFc$^{0/+}$ oxidant. Right: Continued monitoring of the {FeNO}^{6} complex over a 27 hour time period shows minimal NO loss. For these experiments, aliquots were taken from a stirring solution and transferred into a solution IR cell .. 149

Figure 4.8 EPR spectra of the same sample measured in the solution IR experiments shown in Figure S19, obtained at 4K. The black spectrum represents the {FeNO}^{7} precursor with a broad, isotropic *S* = 1/2 signal at g = 2.0, and the blue spectrum represents the corresponding oxidized species, [Fe(TPP)(NO)]$^+$, which is EPR silent and contains a minor g = 6 signal that spin integrates to <5% of a ferric species..... 150

Figure 4.9 Top: Crystal structures of the two different 5C {FeNO}^{6} complexes in the unit cell for [Fe(TPP)(NO)]BF_4. Bottom: Crystal structure of [Fe(TPP)(NO)(MI)]PO_2F_2. 153

Figure 4.10 Top: Overlay of the UV-vis spectra of [Fe(TPP)(NO)] (black) and of the reaction product after the addition of ~1.30 equiv. [DAcFc][SbF_6] to the solution (blue), and of the product of the subsequent reaction with ~1.3 equivalent [TBA][Cl] (green). The later spectrum is identical to that of [Fe(TPP)(Cl)]. Bottom: Overlay of the UV-vis spectra of [Fe(TPP)(NO)] (black) and of the reaction product after the addition of ~1.30 equiv. [DAcFc][SbF_6] to the solution (blue), and of the product of the subsequent reaction with ~1.3 equivalent [TBA][Br] (green). The later species is likely [Fe(TPP)(Br)]..... 155

Figure 4.11 Left: UV-vis spectra of the ferric precursor, [Fe(TPP)(Cl)] (black), and of the corresponding reaction product after bubbling the solution with NOg to form [Fe(TPP)(NO)(Cl)] (red), in CH_2Cl_2. Right: The reaction product after flushing the solution with argon gas (green), which results in reformation of the starting material [Fe(TPP)(Cl] (black)..... 158

Figure 4.12 Crystal structure of [Fe(TPP)(NO)(Cl)]. The hydrogen atoms are omitted for clarity and thermal ellipsoids are shown at 40% probability 159

Figure 4.13 Overlay of the UV-vis spectra of [Fe(TPP)(NO)] (black) and of the reaction product after the addition of ~1.30 equiv. [DAcFc][SbF_6] to the solution (blue), and of the product of the subsequent reaction with ~1.3 equivalent [TBA][I] (green). The product from the later reaction is identical to the precursor [Fe(TPP)(NO)]..... 159

Figure 4.14 Top: NRVS-derived vibrational density of states (VDOS) for [^{57}Fe(TPP)(NO)(Cl)] (black) and the $^{15}N^{18}O$ labeled complex (green). Middle:

NRVS VDOS for [^{57}Fe(TPP)(NO)(MI)]SbF_6 (black) and the $^{15}N^{18}O$ labeled complex (purple). Bottom: NRVS VDOS for [^{57}Fe(TPP)(NO)]SbF_6 (black) and the $^{15}N^{18}O$ labeled complex (green) 163

Figure 4.15 rRaman spectrum of a 2 mM solution of [Fe(TPP)(NO)(MI)]SbF_6 in dichloromethane (power = 31 mW). Note: The $\{FeNO\}^6$ complex was formed by the reaction of [Fe(TPP)(SbF_6)] with excess NO gas in the presence of ~1 equiv. MI 164

Figure 4.16 Top: rRaman spectrum of a ~2 mM solution of [Fe(TPP)(NO)(MI)]SbF_6 (power = 31 mW). Bottom: rRaman spectrum of a ~2 mM solution of the corresponding $^{15}N^{18}O$-labeled complex, [Fe(TPP)($^{15}N^{18}O$)(MI)]SbF_6 (bottom; power = 28 mW). There is one isotope sensitive feature at 598 cm^{-1} that shifts to 586 cm^{-1} upon $^{15}N^{18}O$ labeling. 165

Figure 4.17 Experimental vibrational stretching frequency correlation of the Fe-NO stretching frequency versus the N-O stretching frequency based on this work and published data. 5C $\{FeNO\}^6$ complexes [Fe(TPP)(NO)]BF_4 and [Fe(OEP)(NO)]ClO_4 are depicted in blue. 6C $\{FeNO\}^6$ complexes with an axial thiolate ligand *trans* to the NO are shown in purple: Cyt. P450cam (+camphor, norcamphor, and adamantanone), Cyt. P450nor, CPO, and [Fe(OEP)(NO)(SR-H_2)]ClO_4 171

Figure 4.18 Left: UV-vis spectra monitoring the stability of [Fe(TPP)(NO)]SbF_6 for 3 hours in dichloromethane at room temperature. Right: IR spectra monitoring

the stability of [Fe(TPP)(NO)]SbF_6 for 2 hours in dichloromethane at room temperature..... 172

Figure 4.19 Left: UV-vis spectra for the SEC oxidation of [Fe(TPP)(NO)] (green to blue) in an OTTLE UV-vis cell, measured in a 0.10 M tetrabutylammonium hexafluorophosphate solution in dry CH_2Cl_2 at room temperature. The working and counter electrodes were both a Pt mesh. Right: Re-reduction of the oxidation product (blue to green), showing that the oxidation is fully reversible 172

Figure 4.20 Top: IR spectra for the SEC oxidation of [Fe(TPP)(NO)] (blue to green), measured in a 0.30 M tetrabutylammonium hexafluorophosphate solution in dry CH_2Cl_2 at room temperature. Bottom: Re-reduction of the oxidation product (green to blue), which shows that the oxidation is fully reversible. 173

Figure 4.21 Top left: UV-vis spectra for the SEC oxidation of [Fe(TPP)(NO)] in the presence of ~1 equiv. MI (blue to purple) in an OTTLE UV-vis cell, measured in a 0.10 M tetrabutylammonium hexafluorophosphate solution in dry CH_2Cl_2 at room temperature. The working and counter electrodes were both a Pt mesh. Top right: Re-reduction of the oxidation product (blue to green) shows that the oxidation is not reversible, resulting in the generation of the starting [Fe(TPP)(NO)] complex and a ferric bis imidazole (MI) complex. Bottom: UV-vis spectra for the SEC oxidation of [Fe(TPP)(NO)] in the presence of excess MI (blue to green) in an OTTLE UV-vis cell, measured in a 0.10 M n-Bu_4PF_6

solution in dry CH_2Cl_2 at room temperature. The working and counter electrodes were both a Pt mesh..... 174

Figure 4.22 Top: IR spectra for the SEC oxidation of [Fe(TPP)(NO)] in the presence of ~1 equiv. MI (blue to purple), measured in a 0.10 M tetrabutylammonium hexafluorophosphate solution in dry CH_2Cl_2 at room temperature. Bottom: Re-reduction of the oxidation product (green to blue) shows that the oxidation is reversible..... 175

Figure 4.23 Comparison of the UV-vis spectra of $[Fe(TPP)(NO)(MI)]^+$ generated via different methods in dichloromethane: UV-vis SEC (green), chemical oxidation (black), and addition of NO gas to [Fe(TPP)(SbF6)] with ~1 equiv. MI (blue)..... 176

Figure 4.24 Left: Solution IR spectra of a 1.5 mM solution of [DAcFc][SbF_6] (blue) in dimethoxyethane and of aliquots taken from a stirring solution of [DAcFc][SbF_6] over time at room temperature. The C-O stretching frequency at 1702 cm^{-1} slowly decreases in intensity as a large new band at 1678 cm^{-1} appears (orange). Right: Solution IR spectra of the decomposed solution of [DAcFc][SbF_6] (orange) and of a 1.5 mM solution of DAcFc in dimethoxyethane (black), showing that the band at 1672 cm^{-1} is the C-O stretching frequency of DAcFc 176

Figure 4.25 Left: *In situ* UV-vis monitoring of the decomposition of $[Fe(TPP)(NO)]^+$ (blue to black). $[Fe(TPP)(NO)]^+$ was generated via chemical oxidation of a solution of ~10 μM [Fe(TPP)(NO)] with 1.14 equiv. of [DAcFc][SbF_6] (the

oxidant was dissolved in DME). Right: Fit of the UV-vis band at 370 nm over time 177

Figure 4.26 Solution IR spectra of a 1.8 mM solution of [Fe(TPP)(NO)] (black) in the presence of ~1 equiv. MI in CH_2Cl_2 and of the reaction product (in purple) after the addition of ~1.40 equiv. [DAcFc][SbF_6] to the solution. The N-O stretch at 1676 cm^{-1} shifts to 1920 cm^{-1} upon oxidation. The band at 1850 cm^{-1}(*) corresponds to a small amount of five-coordinate $[Fe(TPP)(NO)]^+$. The bands at 1702 and 1672 cm^{-1} are the C-O stretching frequencies of the respective $DAcFc^{0/+}$ reagents. Right: Continued monitoring of the $\{FeNO\}^6$ complex over a 6 hour time period shows slow NO loss and at the same time an increase in the 1850 cm^{-1} band of the 5C $\{FeNO\}^6$ complex 177

Figure 4.27 Left: *In situ* UV-vis monitoring of the decomposition of $[Fe(TPP)(NO)(MI)]^+$ (purple to black). $[Fe(TPP)(NO)(MI)]^+$ was generated via chemical oxidation of a solution of ~5 μM [Fe(TPP)(NO)] with ~1.3 equiv. of [DAcFc][SbF_6] (the oxidant was dissolved in DME) in the presence of ~1 equiv. of MI. Right: Fit of the UV-vis band at 430 nm over time. 178

Figure 4.28 Top: IR spectrum of [Fe(TPP)(NO)] (black). Bottom: IR spectrum of the reaction product of [Fe(TPP)(NO)]SbF_6 with [TBA][I] under an NO atmosphere, which results in the iron NO complex, [Fe(TPP)(NO)], I_2, and [TBA][SbF_6] (green)..... 178

Figure 4.29 Top: Overlay of the IR spectra (measured in KBr pellets) of [^{57}Fe(TPP)(NO)(Cl)] (black) and the $^{15}N^{18}O$ labeled complex (green). Bottom:

Zoomed in comparison of [^{57}Fe(TPP)(NO)(Cl)] (black) and the ^{15}N^{18}O labeled complex (green). 179

Figure 4.30 Left: Overlay of the IR spectra of the precursor, [Fe(TPP)(SbF_6)] (black), and of the iron NO complex, [Fe(TPP)(NO)] (red), measured in KBr pellets. Right: ^{1}H-NMR spectrum of [Fe(TPP)(NO)] recorded in CD_2Cl_2, with the line width set to 1 Hz 182

Figure 4.31 ^{1}H-NMR spectrum of [Fe(TPP)(NO)]SbF_6 recorded in CD_2Cl_2, with the line width set to 1 Hz 183

Figure 4.32 Overlay of the IR spectra of the precursor, [Fe(TPP)(SbF_6)] (black), and of the isolated ferric NO product, [Fe(TPP)(NO)(MI)]SbF_6 (purple), measured in KBr pellets 184

Figure 4.33 Top Left: UV-vis spectra of the ferric precursor, [Fe(TPP)(SbF_6)] (black), and the isolated ferric NO product, [Fe(TPP)(MI)(NO)]SbF_6 (purple), dissolved in CH_2Cl_2. Note: the {FeNO}^{6} complex was prepared from the reaction of [Fe(TPP)(SbF_6)] with ~1 equiv. MI and excess NO gas. Top Right: UV-vis spectra of the ferric precursor, [Fe(TPP)(PF_6)], in the presence of ~1 equiv. MI (black), and after reaction of the solution with excess NO gas, resulting in the formation of [Fe(TPP)(MI)(NO)]PF_6 (purple) in CH_2Cl_2. Bottom: UV-vis monitoring of the dissolution of the bulk material, [Fe(TPP)(NO)(MI)]SbF_6 (purple), prepared via the method described above in dichloromethane in the absence of NO gas 185

Figure 4.34 Left: Overlay of the IR spectra of the precursor, [Fe(TPP)(Cl)] (black), and of the iron NO complex, [Fe(TPP)(NO)(Cl)] (red), measured in KBr pellets. Right: Overlay of the IR spectra of the ferric NO complex, [Fe(TPP)(NO)(Cl)] (black), and of the same solid after ~3 months in the glovebox freezer (blue), indicating very small NO loss over time 186

Figure 4.35 Left: Overlay of the IR spectra (taken in KBr pellets) of the precursor, [Fe(TPP)(SbF_6)] (black), which, upon reaction with NO gas and [TBA][Br], yields the iron NO complex, [Fe(TPP)(NO)(Br)], and [TBA][SbF_6] (purple). Right: Overlay of the IR spectra of the two iron NO complexes with halide coordination, [Fe(TPP)(NO)(Cl)] (blue) and [Fe(TPP)(NO)(Br)] (purple), measured in KBr pellets 187

Figure 4.36 Left: UV-vis spectra of [Fe(TPP)(NO)] (black) with the chemical oxidant (dissolved in dimethoxyethane) [DAcFc][SbF_6], in dichloromethane, to form the ferric NO complex, $[Fe(TPP)(NO)]^+$ (blue). Then, ~1 equiv. MI was added to the solution of $[Fe(TPP)(NO)]^+$ to form the corresponding $[Fe(TPP)(NO)(MI)]^+$ complex (purple). Right: UV-vis spectra of [Fe(TPP)(NO)] (black) with ~1 equiv. MI added to the solution in dichloromethane 189

Figure 4.37 Left: Solution IR spectra of a 3.2 mM solution of [Fe(TPP)(NO)] (black) in the presence of ~1 equiv. MI in CH_2Cl_2 and of the reaction product (in purple) after the addition of ~1.20 equiv. [DAcFc][SbF_6] to the solution. The N-O stretch at 1676 cm^{-1} shifts to 1920 cm^{-1} upon oxidation. The band at 1850 cm^{-1}(*) corresponds to a small amount of five-coordinate $[Fe(TPP)(NO)]^+$. The bands at 1702 and 1672 cm^{-1} are the C-O stretching frequencies of the

respective DAcFc$^{0/+}$ reagents. Right: EPR spectra of the same solution used in the solution IR experiments (on the left) at 4K 189

List of Schemes

Scheme 1.1 Proposed mechanism for N_2O production in P450nor. 5

Scheme 2.1 Proposed mechanism for N_2O production in P450nor. The oval represents the porphyrin ligand..... 21

Scheme 2.2 Synthetic route to form a model for Intermediate *I* in P450nor..... 22

Scheme 2.3 Target complex, [Fe(3,5-Me-BAFP)(NHOMe)],for modeling the proposed Fe(IV)-$NHOH^-$ intermediate in the catalytic cycle of P450nor 23

Scheme 2.4 Proposed disproportionation mechanism of NH_2OH by ferric porphyrin complexes, derived from the reaction of $[Fe(TPPS)]^{3-}$ with excess NH_2OH. This mechanism is adapted from reference 3. 31

Scheme 2.5 Proposed disproportionation mechanism of NH_2OH by ferric porphyrin complexes, derived from the reaction of $[Fe(TEPyP)]^{5+}$ with excess NH_2OH. This mechanism is adapted from reference 3. 32

Scheme 2.6 Chemical oxidation of [Fe(3,5-Me-BAFP)(NHOMe)] and the decomposition of the oxidized complex to [Fe(3,5-Me-BAFP)(SbF_6)] 46

Scheme 2.7 Bond vectors showing the C-N stretching frequency mode of the porphyrin core, which is known as the oxidation state marker band (ν_4). Adapted from reference 41..... 50

Scheme 2.8 Proposed reaction mechanism of the reaction of [Fe(3,5-Me-BAFP)(NHOMe)]$^{+}$ with low equivalents of NO gas at -80°C 56

Scheme 3.1 Proposed reactions of iron(II)-RNO complexes with (1) NO to make a ferric hyponitrite type species and (2) acid to form an analogue of Intermediate *I* 80

Scheme 3.2 Schematic drawing of [Fe(3,5-Me-BAFP)(PhNO)] 86

Scheme 3.3 Summary of the reactivity observed with five- and six-coordinate ferrous heme RNO (R = IPr, PhNO) complexes and NO. 106

Scheme 3.4 Proposed reactivity of [Fe(TPP)(iPrNO)] with acid resulting in an Intermediate *I* type model, which then decomposes into a ferric species, N_2O, and iPrOH 112

Scheme 4.1 Proposed reaction mechanism of the reaction of [Fe(3,5-Me-BAFP)(NHOMe)]$^{+}$ with low equivalents of NO gas at -80°C 137

Scheme 4.2 The reductive nitrosylation mechanism (or known as autoreduction) 156

Abstract

Nitric oxide (NO) is involved in many important biological processes in humans, but the overproduction of NO has detrimental consequences for human health. In contrast, denitrifying organisms efficiently detoxify NO. Fungi produce NO during anaerobic respiration, and detoxify NO by reduction to nitrous oxide (N_2O) using a Cytochrome P450-type nitric oxide reductase (P450nor). The active site of this enzyme contains a ferric heme coordinated to a proximal cysteinate ligand. In the proposed mechanism, the ferric heme binds NO and is reduced to a ferrous HNO complex. It is speculated that this intermediate is protonated to a formally iron(IV)-$NHOH^-$ species as the critical intermediate for NO reduction.To elucidate whether an iron(IV)-$NHOH^-$ type intermediate is catalytically competent for N-N bond formation, I prepared the first model complex for such a species using a bis-picket fence porphyrin as supporting ligand. Using resonance Raman and Mossbauer spectroscopy I was able to show that the electronic structure of out model is best described as an iron(III)-NHOMe(radical) species, and not an iron(IV) complex or a porphyrin radical species. This complex has a half live of 68 minutes at –80^{o}C. This species reacts with NO gas to form a ferric species, however N_2O is not formed. Future studies will determine if an N-N bond was formed by analysis

of the N-containing products. Next, we investigated whether ferrous HNO complexes are catalytically competent intermediates in P450nor. We synthesized iron(II)-RNO complexes, where the N-atom is substituted with an alkyl group (R = iPr, Ph) rather than a H-atom. The reaction of these complexes with NO results in an iron(II)-NO complex, rather than N-N bond formation. The addition of a neutral thiol ligand *trans* to the RNO ligand could activate these complexes toward N-N bond formation. Finally, a new method to synthesize ferric heme-nitrosyl complexes was developed, which allowed us to determine key factors that result in denitrosylation of ferric heme-nitrosyl complexes. This opens up the door to study the P450nor reaction of an iron(III)-NO complex with a hydride to form a ferrous HNO complex.

Chapter 1

Introduction

1.1 The Nitrogen Cycle

The nitrogen cycle is an important biogeochemical process on Earth, as nitrogen is an essential building block for all forms of life.[1-3] The main sources of nitrogen for plants are from gaseous dinitrogen (N_2) from the atmosphere and nitrate (NO_3^-) from inorganic fertilizers and minerals. However, plants cannot directly use N_2 instead it is reduced into ammonia (NH_3/NH_4^+) by nitrogen fixation (see Figure 1.1). Ammonia is then oxidized by nitrifying microbes in the soil into nitrate (NO_3^-), followed by denitrification, where NO_3^- is stepwise reduced to nitrous oxide (N_2O) by bacteria and fungi:

$$NO_3^- \xrightarrow{nar} NO_2^- \xrightarrow{nir} {}^{\bullet}NO \xrightarrow{nor} N_2O$$

In the last step, N_2O is further reduced into N_2 (by bacteria) to begin the cycle over again. These natural processes (along with lightning) result in ~120 megatons of bioavailable nitrogen per year. An equal amount is generated by humans, primarily from the Haber-Bosch process (reduction of N_2 to ammonia) and the planting of leguminous crops.[4,5] Agricultural practices in developed countries tend to overfertilize the soil to ensure that nitrogen is not a limited nutrient. On average only ~30-50% of the nitrogen is being used by the crop plants.[6] The

overabundance of bioavailable nitrogen is a major environment problem. For example, nitrifying microbes produce more NO_3^- resulting in bacteria and fungi releasing NO and N_2O into the atmosphere. This is a problem because NO depletes the ozone and N_2O is potent greenhouse gas (and the UV irradiation of this molecule in the stratosphere produces NO).[4] Another detrimental consequence is nitrate runoff into ground water, rivers, and ponds creating "dead zones" by eutrophication[6] as shown in Figure 1.1. Based on this, it is important to understand the large number of enzymes involved in denitrification. One class of enzymes that carries out the two-electron reduction of NO to N_2O are called Nitric Oxide Reductases (NOR). One of these enzymes, fungal NOR (P450nor) is discussed in detail in Section 1.2. This thesis is focused on modeling intermediates in the mechanism of NO reduction by this enzyme.

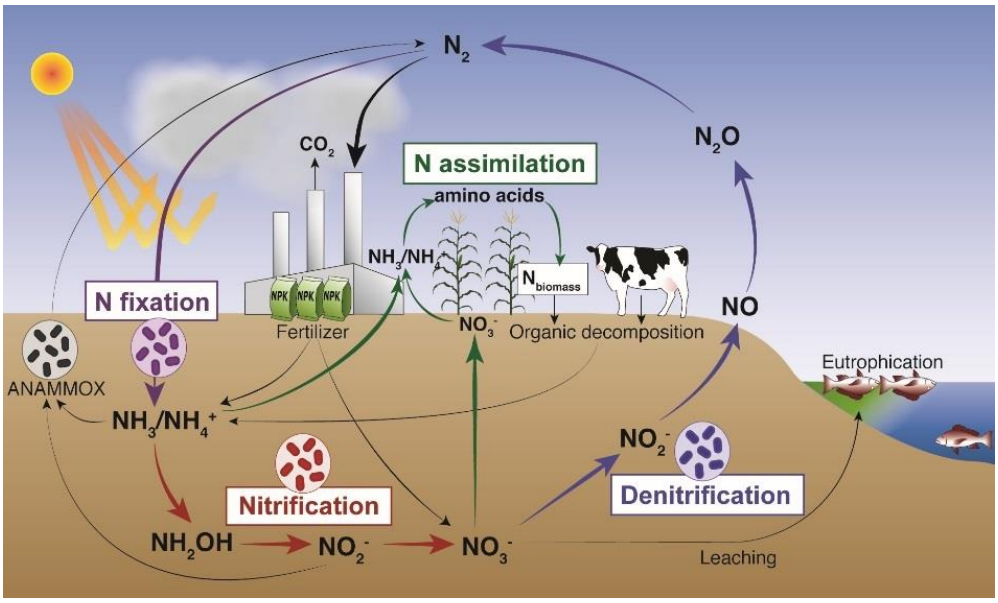

Figure 1.1. Processes that occur in the nitrogen cycle. ANAMMOX stands for Anerobic Ammonium Oxidation. Reproduced from: Lehnert, Coruzzi, Hegg, Seefeldt & Stein, "NSF Workshop Report: Feeding the World in the 21st Century: Grand Challenges in the Nitrogen Cycle", 2016.

1.2 Fungal NO Reductase (P450nor)

Denitrifying fungi reduce nitrate stepwise to nitrous oxide (N_2O) for anerobic respiration. As part of this process, NO is reduced to N_2O to prevent the accumulation of this toxic metabolite.[7,8] Cytochrome P450 nitric oxide reductases (P450nor) are used for NO reduction in soil dwelling fungi (ie. *Fusarium oxysporum*) and yeast (ie. *Trichosporon cutaneum*). These enzymes belong to the Cytochrome P450 super family most of which perform oxidative (monooxygenase) chemistry. Unlike typical Cytochrome P450s, P450nor is unique for its function as a reductase, even though the active site of P450nor is structurally similar to its monooxygenase counterparts. Also, despite this structural similarity, P450nor cannot catalyze monooxygenase reactions. The active site of P450nor contains a single heme *b* with a proximal cysteinate ligand.[9,10] Figure 1.2 shows the crystal structure of the NO-bound ferric heme active site of P450nor, determined for the enzyme from *Fusarium oxysporum*.[11] This enzyme performs NO reduction

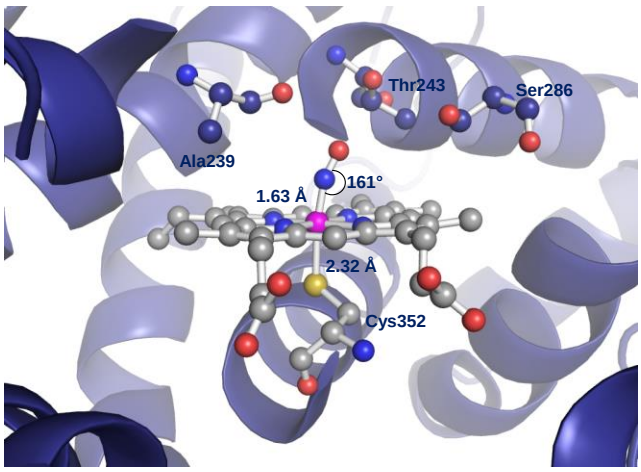

Figure 1.2. NO-bound ferric heme in the active site of P450nor from *Fusarium oxysporum*. This image was generated using PyMOL from PDB code 1CL6 (adapted from reference 11).

following (1) with a turnover rate estimated to about 500 s^{-1}. Interestingly, NAD(P)H is directly utilized in this process without the aid of an electron transfer protein.[12]

$$2NO + NAD(P)H + H^+ \longrightarrow N_2O + H_2O + NAD(P)^+ \quad (1)$$

Proposed Mechanism of P450nor

In the first step of catalysis, the ferric heme complex of P450nor binds NO to form a ferric heme-nitrosyl, a $\{FeNO\}^6$ complex in the Enemark-Feltham notation (where the superscript "6" represents the number of iron d-electrons plus the NO $\pi*$ electrons),[13] as the first intermediate of the reaction.[14,15] NO binding goes along with a shift of the Soret band from 413 to 431 nm.[15] The NO complex is further characterized by N-O and Fe-NO stretching frequencies of 1851 and 530 cm^{-1}, respectively.[16] The crystal structure in Figure 1.2 shows that the Fe-N-O unit is bent in this complex with a bond angle of 161°.[11] In the next step of catalysis, a hydride (from NAD(P)H; $NaBH_4$ can also be used in the laboratory) is transferred directly to the ferric NO complex.[17] This reaction causes a characteristic change in the Soret band, which shifts from 431 to 444 nm.[15] The lifetime of this "Intermediate I" is 100 ms, making it difficult to study this species spectroscopically. From resonance Raman spectroscopy, the Fe-NO stretching frequency of this intermediate is 596 cm^{-1}.[18] Based on the above reaction sequence, Intermediate I corresponds to a reduced $\{FeN(H)_nO\}^8$ complex (n = 0 – 2) of unknown protonation state. Since the complete mechanism of P450nor is not currently known, Density Functional Theory (DFT) and QM/MM calculations have helped shed light on the details of the reaction.[19,20] From DFT, the ground state of the ferric heme-nitrosyl

complex is best described as an iron(II)-NO^+ complex, which is in agreement with the spectroscopic properties of this species. Then, direct hydride transfer from NAD(P)H to the ferric nitrosyl complex generates a ferrous HNO species as shown

Scheme 1.1. Proposed mechanism for N_2O production in P450nor.

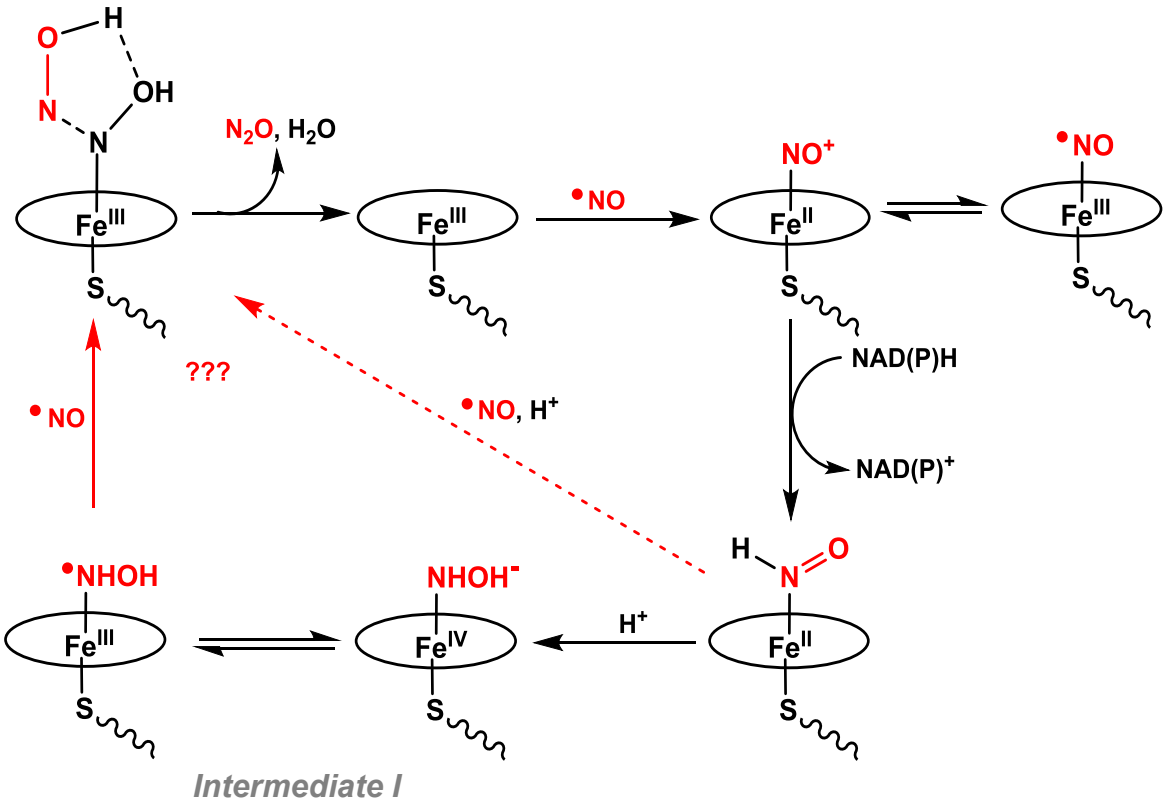

in Scheme 1.1. Here, protonation of the N-atom is more likely, because (a) it is strongly energetically favored by DFT total energy calculations,[19] and (b) experimentally, the Mb(II)-NHO adduct has been shown to be N-protonated.[21] At this point, the ferrous HNO species could react directly with a second equivalent of NO to form the N-N bond and generate a ferric hyponitrite intermediate. Alternatively, due to the strong donicity of the cysteinate ligand, the ferrous HNO complex could be further protonated, resulting in a formally Fe(IV)-$NHOH^-$ species.

Based on recent QM/MM calculations, the electronic structure of this intermediate could also be described as an Fe(III)-NHOH(radical) complex were a NHOH radical is bound to a low-spin Fe(III) and the spins are antiferromagnetically coupled (total spin $S = 0$). Then, the subsequent addition of NO generates again a ferric hyponitrite complex, which readily decomposes into N_2O and H_2O, closing the catalytic cycle (see Scheme 1.1). Based on these results, the critical Intermediate *I* is either identified with the ferrous HNO complex or the corresponding, doubly protonated species, iron(IV)-$NHOH^-$. Due to the lack of experimental insight into the nature of Intermediate *I*, model complexes can be helpful to elucidate the proposed mechanism of P450nor, and to characterize the detailed electronic structures of the key intermediates.

Six-Coordinate Ferric Heme-Nitrosyl Complexes

The ground state of ferric heme-nitrosyls is best described as Fe(II)-NO^+ ($S = 0$, diamagnetic), which is dominated by two strong π backbonding interactions between the occupied d_{xz}/d_{yz} orbitals of the iron center and the empty π^* orbitals of the NO^+ ligand (where the Fe-NO vector corresponds to the z-axis).[22,23] The corresponding antibonding molecular orbitals are shown in Figure 1.3 (A, B). In addition, a Fe-NO σ bond is present, which, however, is weak, due to the very low energy of the corresponding donor orbital of the NO^+ ligand (see Figure 1.3.C).[24] Based on this bonding description, the Fe-NO bond in the ground state of ferric heme-nitrosyls is very strong. Surprisingly, however, as evident from the equilibrium NO binding constants, ferric heme-nitrosyls contain thermodynamically

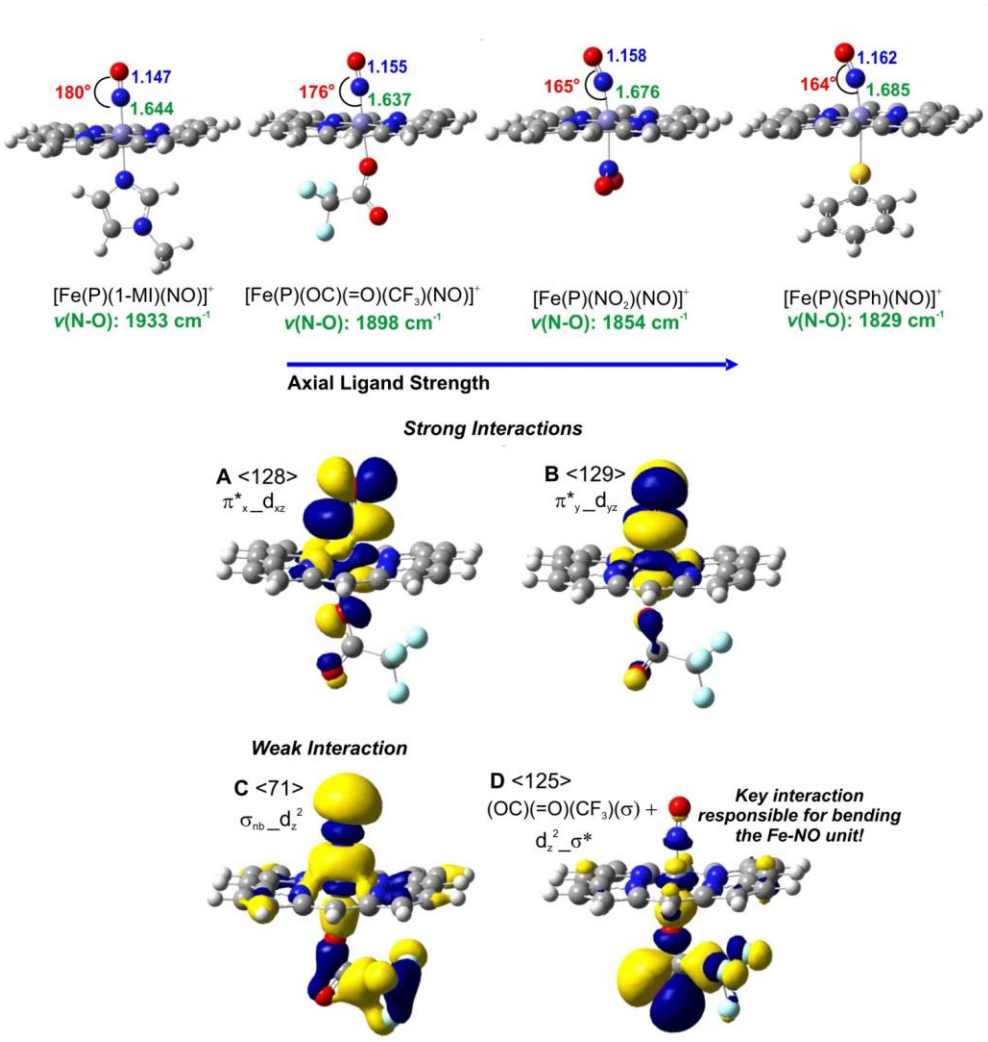

Figure 1.3. Top: optimized structures, geometric parameters and calculated N-O stretching frequencies of [Fe(P)(X)(NO)] complexes obtained with BP86/TZVP (P = porphine^{2-}, X = axial ligand). Bottom: important Fe-NO orbital interactions, calculated for [Fe(P)(OC(=O)CF_3)(NO)] with BP86/TZVP. A) and B) the two strong π backbonding interactions, C) the weak σ interaction, and D) the antibonding σ*_d_z^2 interaction responsible for the bending of the Fe-NO unit. Adapted from reference 24.

weak Fe-NO bonds (K_{eq} = 10^3 - 10^5 M^{-1}) relative to the analogous ferrous {FeNO}^{7} complexes (K_{eq} = 10^{10} - 10^{12} M^{-1}).[8,25,26] This apparent contradiction is caused by the presence of a low-lying high-spin Fe(III)-NO(radical) state that is dissociative with respect to the Fe-NO bond, and that plays a key role for NO dissociation.[22]

This is a general property of ferric heme-nitrosyls and is independent of the axial ligand.

Nevertheless, the nature of the axial ligand has a profound effect on the properties of the Fe-NO unit in $\{FeNO\}^6$ complexes. Ferric heme-nitrosyls with axial neutral N-donors (such as imidazole, pyridine, or pyrazole) have completely linear Fe-N-O units and N-O and Fe-NO stretching frequencies in the 1900 cm^{-1} and 595 cm^{-1} range, respectively.[22,27] On the other hand, thiolate-coordination to ferric heme-nitrosyls results in a bent Fe-N-O unit (<Fe-N-O = 161 – 165°) and a decrease in the Fe-NO (510 – 530 cm^{-1}) and N-O stretching frequencies (1800 - 1850 cm^{-1}),[11,28-30] which implies a weakening of the Fe-NO and N-O bonds. The bent Fe-N-O unit was first observed in the crystal structure of ferric NO-bound P450nor (see Figure 1.2), but it was initially suspected that the bending in this case could be due to partial reduction of the iron-NO group in the X-ray beam. Alternatively, the bending of the Fe-N-O unit could also be due to steric crowding in the protein active site of P450nor. Richter-Addo and co-workers crystallized the first thiolate-coordinated model complex, [Fe(OEP)(SR-H_2)(NO)] (SR-H_2 = S-2,6-$(CF_3CONH)_2C_6H_3$, OEP^{2-} = dianion of octaethylporphyrin) with an Fe-N-O bond angle of 160°,[28] which confirmed that the observed bent Fe-N-O unit in the P450nor crystal structure is in fact due to an electronic effect. Further computational studies indicated that this bending is caused by the thiolate ligand, which induces a σ-trans effect on the bound NO via population of an Fe-N-O σ* fully antibonding orbital (see Figure 1.3).[23] This causes the bending of the Fe-N-O unit and weakens both the Fe-NO and N-O bonds, causing a downshift in the Fe-

NO and N-O stretching frequencies (see Figure 1.3D). For comparison, this type of antibonding Fe-N-O interaction is not observed in $[Fe(Porph)(NO)(MI)]^{+}$ complexes (IM = imidazole derivative, Porph = dianion of generic porphyrin) and as a result, the Fe-N-O unit remains linear in these cases.[31]

Recently, Richter-Addo and co-workers crystallized the first ferric heme-nitrosyl complex with an axial anionic O-donor ligand, $[Fe(TPP)(OC(=O)CF_3)(NO)]$ (where TPP^{2-} = dianion of tetraphenylporphyin), by a heterogeneous crystal-gas method.[24] This complex is synthesized by diffusion of NO gas into crystals of the five-coordinate precursor $[Fe(TPP)(OC(=O)CF_3)]$ for 12 hours, resulting in the addition of NO to the iron center. This is evidenced by the appearance of a N-O stretching band at 1901 cm^{-1}. Interestingly, in this case, the Fe-N-O unit is almost linear with a bond angle of 176°, which is in between the Fe-N-O bond angles observed in ferric heme-nitrosyls with neutral N-donor and anionic thiolate ligation. Furthermore, the DFT-optimized structure of the non-fluorinated acetate complex, $[Fe(P)(OC(=O)CH_3)(NO)]$ (where P^{2-} = porphine), has an Fe-N-O angle that bends by 5° more, compared to both the experimental and DFT-optimized structures of the trifluoroacetate-bound analog. The comparison of these acetate-ligated complexes to other ferric nitrosyls such as $[Fe(P)(NO)(MI)]^{+}$, $[Fe(P)(NO)(NO_2)]$, and [Fe(P)(NO)(SPh)] indicated that the donor strength of the axial ligand actually directly modulates the degree of Fe-N-O bending and the Fe-NO and N-O bond strengths. Figure 1.3 shows that this is in fact the case: here, stronger donation from the axial ligand to the iron center leads to weaker Fe-NO and N-O bonds and causes the Fe-N-O unit to bend more. This is a result of increased backbonding

into the σ* orbital of the Fe-N-O unit, depicted as the d_z^2_ σ* molecular orbital in Figure 1.3D. In the imidazole complex $[Fe(P)(NO)(MI)]^+$, this Fe-N-O antibonding orbital is unoccupied; however in complexes with the anionic ligands, this orbital becomes partially occupied.[23,24] As one would expect, the largest admixture is observed with thiolate ligands, which are the strongest donors that show the most bent Fe-N-O units.

These results have a number of important implications for the role of $\{FeNO\}^6$ species in biology. First, due to their Fe(II)-NO^+ type electronic structures, the bound NO^+ ligand in ferric heme-nitrosyls is electrophilic and reactive toward nucleophiles like amines and thiols. In P450nor, the electrophilic NO^+ ligand enables reaction with NAD(P)H to generate the key Intermediate *I*. Second, the fact that the bound NO is intrinsically labile in $\{FeNO\}^6$ complexes enables facile dissociation of NO from ferric hemes, which is of functional significance for NO transporter proteins, such as nitrophorins, and NO producing enzymes such as nitric oxide synthase (NOS) and nitrite reducing globins.[8] All of these NO generating enzymes produce ferric heme-nitrosyl adducts as the enzyme-product complexes. Without the lability of the Fe-NO bond, these enzymes could not release the bound NO ligands from their active sites and would become inactivated. These biological functions are further modulated by the trans ligand. In particular, a trans thiolate ligand leads to a further weakening of the Fe-NO bond and further promotes NO dissociation, for example in NOS.

Based on these results, the general properties of ferric heme-nitrosyl complexes are well understood. However, the generation of stable *thiolate-bound*

ferric heme-nitrosyl model systems still remains highly elusive due to their inherent instability.

Ferrous Heme HNO Model Complexes

Based on QM/MM calculations, it has been proposed that the {FeNHO}^{8} complex could react with NO directly to form an N-N bond, yielding a ferric hyponitrite species, as the central step of P450nor catalysis (see Figure 1.2).[19,20] Alternatively, the N-N bond formation reaction could be mediated by the corresponding, doubly protonated intermediate. Model complexes are ideally suited to further investigate the reactivity of these proposed intermediates, as they allow for the preparation of synthetic analogs of both of these species via a precise control of the proton state of the complex. However, until recently, there were no heme model complexes available that could generate a stable {FeNHO}^{8} species in order to investigate its reactivity. This is due to disproportionation of the bound HNO ligand in simple [Fe(Porph)(NHO)] complexes as observed by Ryan and co-workers.[32] This yields H_2 and the corresponding {FeNO}^{7} complex:

$$2[Fe(Porph)(NHO)] \longrightarrow [Fe(Porph)(NO)] + H_2$$

Recently, however, our group was able to prepare a long-lived five-coordinate {FeNHO}^{8} heme complex by sterically shielding the Fe-NHO unit using a bis-picket fence porphyrin, 3,5-Me-BAFP^{2-} (3,5-Me-BAFP^{2-} = dianion of tetra(2,6-bis(3,5-dimethylphenoxy)phenyl)porphyrin) as illustrated in Figure 1.4.[33] Here, the picket fence greatly slows down the disproportionation of the bound HNO ligand. {FeNHO}^{8} complexes have generally been synthesized in the literature by the one-

electron reduction of {FeNO}^{7} complexes to the corresponding {FeNO}^{8} species as shown in equation (2), followed by protonation with a weak acid, equation (3):

$$[Fe(Porph)(NO)] + 1e^- \longrightarrow [Fe(Porph)(NO)]^- \quad (2)$$

$$[Fe(Porph)(NO)]^- + H^+ \longrightarrow [Fe(Porph)(NHO)] \quad (3)$$

However, in our hands the bulk electrolysis according to equation (2) often generates bulk material of {FeNO}^{8} complexes that is quite impure. Instead, bulk {FeNO}^{8} complexes were prepared by us in a novel synthesis via the initial one-electron reduction of an iron(II)-porphyrin precursor to generate an iron(II)-porphyrin$^-$ monoanion (radical) complex, as shown in equation (4). Subsequent addition of NO gas then yields the {FeNO}^{8} complex in pure form, equation (5):

$$[Fe(Porph)] + 1e^- \longrightarrow [Fe(Porph)]^- \quad (4)$$

$$[Fe(Porph)]^- + NO \longrightarrow [Fe(Porph)(NO)]^- \quad (5)$$

In order to generate the {FeNHO}^{8} species, the {FeNO}^{8} complex is then reacted with acetic acid to protonate the bound NO$^-$ ligand. The UV-vis spectrum of the {FeNHO}^{8} complex shows typical ferrous porphyrin absorption features with a Soret band at 426 nm, which also closely resembles that of the Mb(II)-HNO adduct prepared by Farmer and co-workers (Soret band at 423 nm).[21,33] In addition, the HNO ligand stays bound to the iron center in solution, as N_2O is not detected. This protonation is completely reversible, as the {FeNHO}^{8} complex can be deprotonated with a phosphazene base, P_1-*t*Bu-tris(tetramethylene), and reprotonated with acetic acid. Surprisingly, when the {FeNHO}^{8} complex is reacted with low equivalents of NO, no ferric product is generated but instead, the {FeNO}^{7} complex is formed (evidenced by *in situ* UV-vis spectroscopy).[33] This is likely due

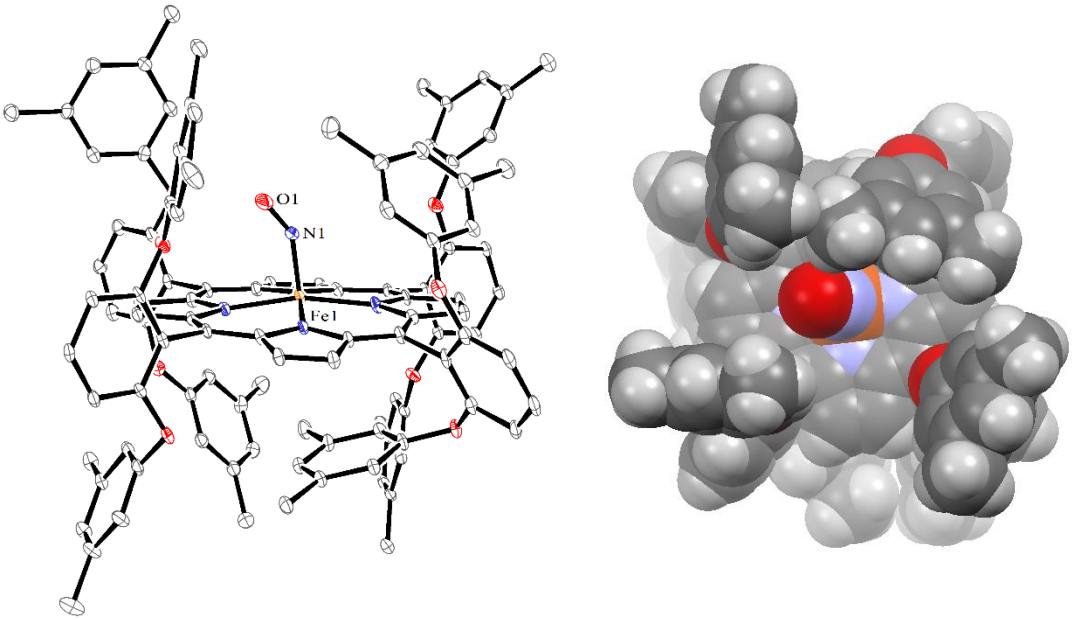

Figure 1.4. Left: The crystal structure of [Fe(3,5-Me-BAFP)(NO)]. The hydrogen atoms are omitted for clarity and thermal ellipsoids are shown at 30% probability. Adapted from reference 33. Right: Top down view of a space filling model of [Fe(3,5-Me-BAFP)(NO)].

to the fact that NO is a stronger ligand and displaces the bound HNO ligand. Because no N-N bond formation is observed at all, this suggests that {FeNHO}^{8} complexes are not catalytically competent intermediates in the mechanism of P450nor (and other NO reductases). However, in order to further solidify these conclusions, corresponding six-coordinate {FeNHO}^{8} complexes need to be synthesized and reacted with NO. Since the HNO ligand has a small *trans* effect,[34] it should be possible to generate these species and explore their reactivity in the future.

Nevertheless, these results suggest that the doubly protonated {FeNHOH}^{8} species is the actual Intermediate *I*, catalytically competent for N-N bond formation. Here, the cysteine ligand has a key role for the formation of this species. In the presence of an axial histidine ligand, like in the Mb(II)-NHO adduct, the ferrous HNO complex is stable and not further protonated. In contrast, the ferrous HNO

complex in P450nor could be basic enough to pick up an additional proton from aqueous solution.[17] DFT calculations indicate that the basicity of this species is due to the strong donation of electron density from the proximal cysteinate ligand to the iron center.[19] This donation from the cysteine ligand would cause formation of the doubly protonated Fe(IV)-$NHOH^-$/Fe(III)-NHOH(radical) intermediate, which is then perfectly set up to react with another equivalent of NO. Further work on $\{FeN(H)O\}^8$ model complexes is necessary to solidify this conclusion.

Spectroscopic Characterization of Intermediate I

As previously mentioned, the $\{FeNO\}^6$ complex in P450nor is reduced by two-electrons (from NAD(P)H) to form Intermediate *I*, which has a lifetime of ~100 ms. This lifetime has made it challenging to study the protonation state of this intermediate with spectroscopy. Intermediate *I* is either the singly protonated ferrous NHO complex, or the doubly protonated iron(IV)-$NHOH^-$/iron(III)-NHOH(radical) species. There is some experimental evidence that suggests Intermediate *I* is the doubly protonated, iron(III)-NHOH(radical) type species. Pulsed radiolysis of hydroxylamine (NH_2OH) was shown to generate NHOH(radical) and water.[35] The irradiation of NH_2OH in the presence of the ferric complex of P450nor forms a species with a UV-vis spectrum identical to that Intermediate *I* (Soret band at 444 nm).[17] This result implies that Intermediate *I* is the doubly protonated species. More recently, Intermediate *I* was generated in ~20% yield and characterized by Magnetic Circular Dichroism (MCD) and Mössbauer spectroscopy by Neese and co-workers.[36] First, the MCD spectrum at

5 K of the ferric resting state of the enzyme has a very intense signal around ~25,000 cm^{-1} (~400 nm) with a $+\Delta\varepsilon/-\Delta\varepsilon$ intensity pattern, which is indicative of a low-spin (ls) ferric heme.[37] The ls ground state of this complex using the MCD preparation conditions was confirmed by EPR spectroscopy at helium temperatures. It should be noted that this is in contrast with EPR studies that report the ferric resting state of P450nor contains a mixture of high- and low-spin complexes (where the low-spin fraction results from water coordination).[38] Nevertheless, the $\{FeNO\}^6$ complex was formed by the addition of NO gas to this complex resulting in the disappearance of the main MCD signal at ~25,000 cm^{-1} (~400 nm). Next, NADH was added to the $\{FeNO\}^6$ species (under NO limited conditions) to generate Intermediate *I* in 20% yield. The MCD spectrum exhibits a large ls ferric signal in the MCD spectrum that looks identical to that of the ferric resting enzyme. Though the sample is not entirely pure, there are no new features at the Soret band position characteristic for Intermediate *I* at 445 nm (~22,500 cm^{-1}). Based on this, the signal observed in the MCD spectrum is only from the decomposed ferric product, and it is proposed that Intermediate *I* is diamagnetic. To gain further insight about the magnetic properties, ^{57}Fe Mössbauer spectroscopy was employed. The Mössbauer spectrum of the ferric resting state is magnetically split and is fit with an δ = 0.32 mm/s and ΔE_Q = 2.96 mm/s. The $\{FeNO\}^6$ complex is a quadrupole doublet with an δ = 0.15 mm/s and ΔE_Q = 1.31 mm/s. The addition of NADH to a solution of the $\{FeNO\}^6$ complex results in a Mössbauer spectrum with a quadrupole doublet with an δ = 0.24 mm/s and ΔE_Q = 1.95 mm/s. The application of a magnetic field results in behavior characteristic of

a diamagnetic complex, which is in agreement with the MCD data. Interestingly, the isomer shift value observed for Intermediate *I* is within the range for low-spin ferric hemes of 0.15 – 0.25 mm/s. Unfortunately, there is not Mossbauer data available for ferrous heme NHO complexes. Because of this, DFT calculations were used to calculate the Mössbauer parameters using B3LYP*/B3 for the singly protonated ferrous NHO complex, and the doubly protonated, iron(IV)-$NHOH^-$/iron(III)-NHOH(radical) complexes. The predicted isomer shits are not that different for the ferrous NHO complex (0.26 mm/s) and the iron(III)-NHOH(radical) complex (0.23 mm/s), However, the DFT calculations indicate a much lower isomer shift value of 0.09 mm/s for the iron(IV)-$NHOH^-$ complex, which implies that Intermediate *I* is not this species. Furthermore, it is difficult to envision a S = 0 ground state for an iron(IV)-$NHOH^-$ species, since all other reported model complexes and enzymes that are six-coordinate have an S = 1, or 2 ground state.[39-41] In summary, the protonation state of Intermediate *I* is still not resolved in P450nor.

1.3 Scope of Thesis

This thesis is focused on model complexes for intermediates in the reaction cycle of P450nor. Chapter 2 focuses on generating a chemical model for the formally iron(IV)-$NHOH^-$ (Intermediate *I*) using a bis-picket fence porphyrin (3,5-Me-$BAFP^{2-}$). In Section 2.1, the reactivity of ferric porphyrins, [Fe(3,5-Me-BAFP)(X)] (where X = ClO_4^- and PF_6^-) with NH_2OBn is reported. In Section 2.2, a new synthetic route to yield ferric complex, [Fe(3,5-Me-BAFP)(NHOMe)], and in-

depth characterization of this complex is presented. Section 2.3 is focused on the one-electron oxidation of [Fe(3,5-Me-BAFP)(NHOMe)] to form the corresponding oxidized complex as a model for Intermediate *I*. Spectroscopic characterization of the oxidized species, $[Fe(3,5\text{-}Me\text{-}BAFP)(NHOMe)]^{+}$, examines whether the oxidation is iron, or ligand (NHOMe) centered in Section 2.4. Lastly, the reactivity of the oxidized species with NO to determine if this species is catalytically competent in P450nor is described in Section 2.5. In Section 2.1, the initial reactivity studies of $[Fe(3,5\text{-}Me\text{-}BAFP)(ClO_4)]$ with NH_2OBn were carried out by former graduate student, Dr. Lauren Goodrich, and her undergraduate Claire Goodrich. Section 2.1 is reported in *Z. Anorg. Allg. Chemie*: **McQuarters, A.B.**; Goodrich, L. E.; Goodrich, C. M.; Lehnert, N. *Z. Anorg. Allg. Chemie* "Disproportionation of O-Benzylhydroxylamine Catalyzed by a Ferric Bis-Picket Fence Porphyrin Complex" **2013**, *639*, 1520 – 1526.[42] The Mössbauer data collection and analysis for $[Fe(3,5\text{-}Me\text{-}BAFP)(NHOMe)]^{0/+}$ complexes was carried out by postdoc Elizabeth Blaesi in Prof. Carsten Krebs' group at Pennsylvania State University in Section 2.3. A second manuscript is currently in preparation that will include additional spectroscopic studies of MI (MI = 1-methylimidazole) bound complex, $[Fe(3,5\text{-}Me\text{-}BAFP)(NHOMe)(MI)]^{+}$. Also, it will have further analysis of the N-containing products from the reaction of $[Fe(3,5\text{-}Me\text{-}BAFP)(NHOMe)]^{+}$ with NO.

In Chapter 3, a set of ferrous heme RNO complexes are reported. Ferrous RNO complexes are stable analogues for $\{FeNHO\}^8$ species. The synthesis of ferrous porphyrin RNO (R = Ph, iPr) complexes using the tetraphenylporphyrin

(TPP^{2-}) and bis-picket fence porphyrin (3,5-Me-$BAFP^{2-}$) co-ligands is described in Section 3.1. Nuclear Resonance Vibrational Spectroscopy (NRVS) with DFT analysis of [Fe(TPP)(iPrNO)] is reported in Section 3.2. Section 3.3 describes the reactivity of these complexes with NO and strong acids. The synthesis and characterization of [Fe(TPP)(iPrNO)] was completed by undergraduate student Diamond Thomas. We did the reactivity studies of her complex with NO and acid together. Chapter 3 is adapted from a manuscript in preparation: **McQuarters, A.B.**; Thomas, D. J.; Alp, E. E.; Hu, M. Y.; Zhao, J.; Lehnert, N. "Stable Analogues for Ferrous Heme-HNO Complexes: Synthesis and Characterization of Heme-Nitrosoalkane Complexes".

In Chapter 4, five- and six-coordinate ferric heme-nitrosyl ($\{FeNO\}^6$) complexes are studied. In P450nor, direct hydride (from NAD(P)H) transfer to an $\{FeNO\}^6$ complex results in a ferrous NHO complex. To model this reaction, formation of stable ferric heme-nitrosyl model complexes is crucial. Section 4.1 reports the preparation of $\{FeNO\}^6$ complexes using the established literature method. Along with this, a new synthetic route to prepare these complexes via chemical oxidation of the respective $\{FeNO\}^7$ precursor is described. For these studies, the tetraphenylporphyrin (TPP^{2-}) ligand is used. With a new method of preparation in hand, the stability of $[Fe(TPP)(NO)]^+$ and $[Fe(TPP)(NO)(MI)]^+$ is investigated in Section 4.2. The crystal structures of three new $\{FeNO\}^6$ complexes are described in Section 4.3. Section 4.4 explores the effect of halide salts on the stability of the $\{FeNO\}^6$ complexes. Then, Nuclear Resonance Vibrational Spectroscopy (NRVS) is utilized to determine the electronic properties of these $\{FeNO\}^6$ complexes, as

described in Section 4.4. Chapter 4 is adapted from a manuscript in preparation: **McQuarters, A.B.**; Kampf, J. W.; Alp, E. E.; Hu, M. Y.; Zhao, J.; Lehnert, N. "To be Stable or Not to be Stable: the Tale of Ferric Heme-Nitrosyl Complexes".

1.4 References

1. Averill, B. A. *Chem. Rev.* **1996**, *96*, 2951-2964.
2. Zumft, W. G. *Microbiol. Mol. Biol. Rev.* **1997**, *61*, 533-616.
3. Suzuki, S.; Kataoka, K.; Yamaguchi, K. *Acc. Chem. Res.* **2000**, *33*, 728-735.
4. Fields, S. *Environ. Health Perspect.* **2004**, *112*, A556-A563.
5. Erisman, J. W.; Sutton, M. A.; Galloway, J.; Klimont, Z.; Winiwarter, W. *Nature Geosci* **2008**, *1*, 636-639.
6. Galloway, J. N.; Leach, A. M.; Bleeker, A.; Erisman, J. W. *Philosophical Transactions of the Royal Society B: Biological Sciences* **2013**, *368*.
7. Ferguson, S. J. *Curr. Opin. Chem. Biol.* **1998**, *2*, 182-193.
8. Lehnert, N.; Berto, T. C.; Galinato, M. G. I.; Goodrich, L. E. In *The Handbook of Porphyrin Science*; Kadish, K. M., Smith, K. M., Guilard, R., Eds.; World Scientific: New Jersey, 2011; Vol. 14, p 1-247.
9. Daiber, A.; Shoun, H.; Ullrich, V. *J. Inorg. Biochem.* **2005**, *99*, 185-193.
10. Zhang, L.; Kudo, T.; Takaya, N.; Shoun, H. *International Congress Series* **2002**, *1233*, 197-202.
11. Shimizu, H.; Obayashi, E.; Gomi, Y.; Arakawa, H.; Park, S. Y.; Nakahara, K.; Adachi, S.; Shoun, H.; Shiro, Y. *J. Biol. Chem.* **2000**, *275*, 4816-4826.
12. Nakahara, K.; Tanimoto, T.; Hatano, K.; Usuda, K.; Shoun, H. *J. Biol. Chem.* **1993**, *268*, 8350-8355.
13. Enemark, J. H.; Feltham, R. D. *Coord. Chem. Rev.* **1974**, *13*, 339-406.
14. Franke, A.; Stochel, G.; Noriyuki, S.; Higuchi, T.; Okuzono, K.; Eldik, R. V. *J. Am. Chem. Soc.* **2005**, *127*, 5360-5375.
15. Shiro, Y.; Fuji, M.; Iizuka, T.; Adachi, S.; Tsukamoto, K.; Nakahara, K.; Shoun, H. *J. Biol. Chem.* **1995**, *270*, 1617-1623.
16. Obayashi, E.; Tsukamoto, K.; Adachi, S.-i.; Takahashi, S.; Nomura, M.; Iizuka, T.; Shoun, H.; Shiro, Y. *J. Am. Chem. Soc.* **1997**, *119*, 7807-7816.
17. Daiber, A.; Nauser, T.; Takaya, N.; Kudo, T.; Weber, P.; Hultschig, C.; Shoun, H.; Ullrich, V. *J. Inorg. Biochem.* **2002**, *88*, 343-352.
18. Obayashi, E.; Takahashi, S.; Shiro, Y. *J. Am. Chem. Soc.* **1998**, *120*, 12964-12965.
19. Lehnert, N.; Praneeth, V. K. K.; Paulat, F. *J. Comput. Chem.* **2006**, *27*, 1338-1351.
20. Riplinger, C.; Neese, F. *ChemPhysChem* **2011**, *12*, 3192-3203.
21. Lin, R.; Farmer, P. J. *J. Am. Chem. Soc.* **2000**, *122*, 2393-2394.
22. Praneeth, V. K. K.; Paulat, F.; Berto, T. C.; Debeer George, S.; Nather, C.; Sulok, C. D.; Lehnert, N. *J. Am. Chem. Soc.* **2008**, *130*, 15288-15303.

23. Paulat, F.; Lehnert, N. *Inorg. Chem.* **2007**, *46*, 1547-1549.
24. Xu, N.; Goodrich, L. E.; Lehnert, N.; Powell, D. R.; Richter-Addo, G. B. *Angew. Chem. Int. Ed.* **2013**, *52*, 3896-3900.
25. Cooper, C. E. *Biochim. Biophys. Acta* **1999**, *1411*, 290-309.
26. Hoshino, M.; Ozawa, K.; Seki, H.; Ford, P. C. *J. Am. Chem. Soc.* **1993**, *115*, 9568-9575.
27. Soldatova, A. V.; Ibrahim, M.; Olson, J. S.; Czernuszewicz, R. S.; Spiro, T. G. *J. Am. Chem. Soc.* **2010**, *132*, 4614-4625.
28. Xu, N.; Powell, D. R.; Cheng, L.; Richter-Addo, G. B. *Chem. Commun.* **2006**, 2030-2032.
29. Pant, K.; Crane, B. R. *Biochemistry* **2006**, *45*, 2537-2544.
30. Goodrich, L. E.; Paulat, F.; Praneeth, V. K. K.; Lehnert, N. *Inorg. Chem.* **2010**, *49*, 6293-6316.
31. Ellison, M. K.; Scheidt, W. R. *J. Am. Chem. Soc.* **1999**, *121*, 5210-5219.
32. Choi, I.-K.; Liu, Y.; Feng, D.; Paeng, K.-J.; Ryan, M. D. *Inorg. Chem.* **1991**, *30*, 1832-1839.
33. Goodrich, L. E.; Roy, S.; Alp, E. E.; Zhao, J.; Hu, M. Y.; Lehnert, N. *Inorg. Chem.* **2013**, *52*, 7766-7780.
34. Goodrich, L. E.; Lehnert, N. *J. Inorg. Biochem.* **2013**, *118*, 179-186.
35. Buxton, G. V.; Greenstock, C. L.; Helman, W. P.; Ross, A. B. *J. Phys. Chem. Ref. Data* **1988**, *17*, 513-886.
36. Riplinger, C.; Bill, E.; Daiber, A.; Ullrich, V.; Shoun, H.; Neese, F. *Chemistry – A European Journal* **2014**, *20*, 1602-1614.
37. Galinato, M. G. I.; Spolitak, T.; Ballou, D. P.; Lehnert, N. *Biochemistry* **2011**, *50*, 1053-1069.
38. Shiro, Y.; Fuji, M.; Isogai, Y.; Adachi, S.; Iizuka, T. *Biochemistry* **1995**, *34*, 9052-9058.
39. Anastasi, A. E.; Comba, P.; McGrady, J.; Lienke, A.; Rohwer, H. *Inorg. Chem.* **2007**, *46*, 6420-6426.
40. de Visser, S. P.; Oh, K.; Han, A.-R.; Nam, W. *Inorg. Chem.* **2007**, *46*, 4632-4641.
41. Neese, F. *J. Inorg. Biochem.* **2006**, *100*, 716-726.
42. McQuarters, A. B.; Goodrich, L. E.; Goodrich, C. M.; Lehnert, N. *Z. Anorg. Allg. Chem.* **2013**, *639*, 1520-1526.

Chapter 2

Modeling the Key Intermediate in P450nor: Electronic Structure & Reactivity

In the proposed mechanism of P450nor, the ferric heme binds NO and is subsequently reduced by NAD(P)H to generate a Fe(II)-NHO complex , as shown in Scheme 2.1. It is further speculated that this intermediate is then protonated to yield a formally Fe(IV)-$NHOH^-$ species as the critical intermediate for NO reduction. This intermediate then reacts with a second equivalent of NO to produce N_2O, H_2O, and the Fe(III) heme resting state to complete the catalytic cycle. Since the exact mechanism of NO reduction by P450nor is not known, it is insightful to use synthetic models to further elucidate the mechanism of this enzyme, in

Scheme 2.1. Proposed mechanism for N_2O production in P450nor. The oval represents a generic porphyrin ligand.

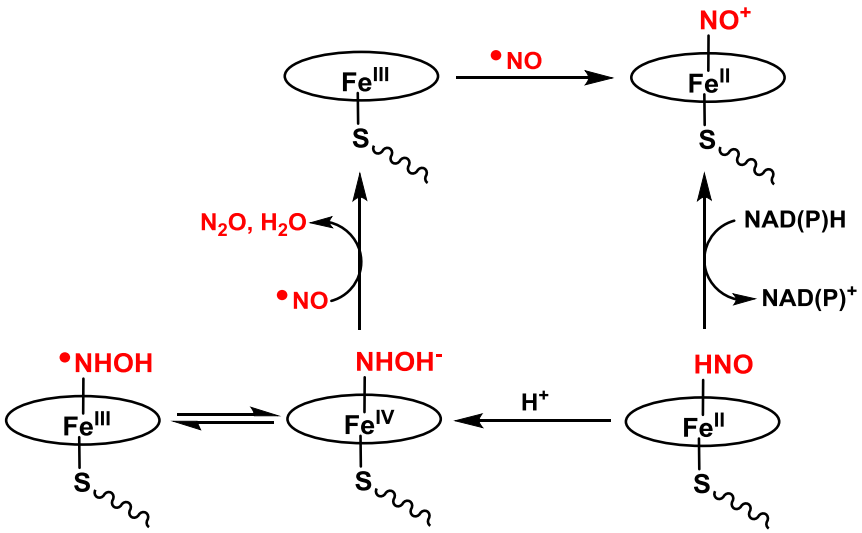

particular the nature, electronic structure, and reactivity of the central intermediate for catalysis.

We propose the synthesis of the desired iron(IV)-$NHOH^-$ intermediate through one-electron oxidation of the corresponding ferric precursor iron(III)-NHOH complex as shown in Scheme 2.2. In this work, the hydroxylamine ligand (NH_2OH) is deprotonated to a hydroxylamide ligand ($NHOH^-$), and then reacted with a ferric heme complex prior to one-electron oxidation to the target ferryl species. Since iron(IV) porphyrins are highly reactive, a bis-picket-fence porphyrin is used to protect the bound hydroxylamide ligand from degradation by providing steric shielding for the iron-bound intermediate. Surprisingly, there are no reports of stable iron(III)-NHOH-type complexes, which is likely due to the thermal instability of NH_2OH[1,2] and its propensity to disproportionate when reacted with metal centers.[3-5] To increase the stability of NH_2OH, we functionalized the oxygen atom of the hydroxylamine ligand (NH_2OR) with a methyl group to form a room temperature stable hydroxylamide ligand and direct the nitrogen atom to the iron center of the target complex, [Fe(3,5-Me-BAFP)(NHOMe)], illustrated in Scheme 2.3.

Scheme 2.2. Synthetic route to form a model for Intermediate *I* in P450nor.

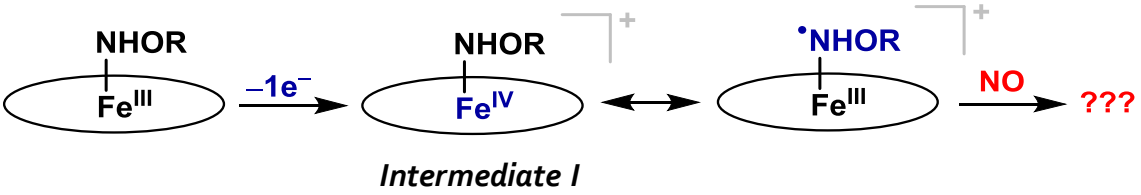

This chapter focuses on the synthesis and spectroscopic characterization of a formally iron(IV)-hydroxylamide ($NHOR^-$, where R = Me) intermediate using synthetic heme models. Section 2.1 explores the reactivity of NH_2OBn with a ferric bis-picket fence porphyrin complex in attempts to synthesize $[Fe(3,5\text{-Me-BAFP})(NH_2OBn)_2]^+$. Section 2.2 addresses the synthesis and characterization of ferric porphyrin hydroxylamide complexes. Section 2.3 discusses the one-electron oxidation of these complexes to form the ferryl intermediate. Section 2.4 investigated the reactivity of our iron(IV)-NHOMe model complex towards NO to determine whether the proposed iron(IV)-$NHOH^-$ intermediate of P450nor is catalytically competent for NO reduction.

Scheme 2.3. Target complex, [Fe(3,5-Me-BAFP)(NHOMe)],for modeling the proposed Fe(IV)-$NHOH^-$ intermediate in the catalytic cycle of P450nor.

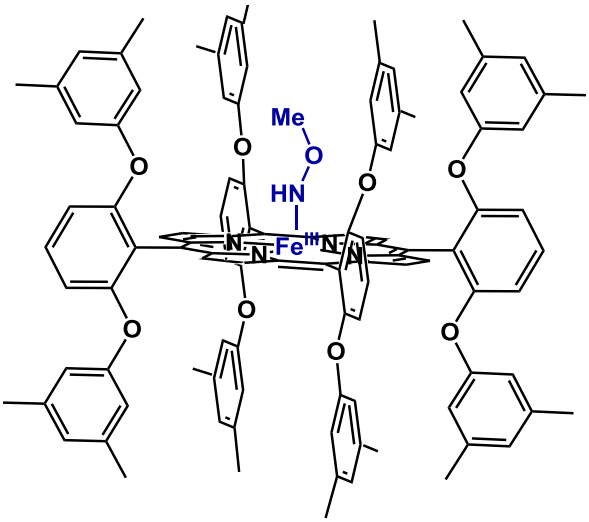

The studies described in this chapter are in part adapted from with permission from: McQuarters, A.B.; Goodrich, L. E.; Goodrich, C. M.; Lehnert, N. *Z. Anorg. Allg. Chemie* **2013**, *639*, 1520 – 1526.[6] The initial studies on the disproportionation

reaction of O-Benzylhydroxylamine with the [Fe(3,5-Me-BAFP)(ClO_4)] complex were performed by former graduate student, Dr. Lauren Goodrich, and her undergraduate student Claire Goodrich. The data collection and analysis for the Mössbauer studies described in section 2.3 were performed by postdoc Elizabeth Blaesi in Prof. Carsten Krebs' group at Pennsylvania State University.

2.1 Reduction of a Ferric Bis-Picket Fence Porphyrin with O-Benzylhydoxylamine

The bis-picket fence porphyrin, H_2[3,5-Me-BAFP] (3,5-Me-BAFP = dianion of tetra(2,6-bis(3,5-dimethylpheoxy)phenyl)porphyrin), was synthesized in 3 steps in an overall yield of 10% by literature protocols.[7] Next, the complex [Fe(3,5-Me-BAFP)(Cl)] was prepared by metallation of 3,5-Me-$BAFP^{2-}$ with $FeCl_2$ in refluxing DMF in 67% yield. This was followed by reaction with $AgClO_4$ in refluxing 2-Me-THF to afford [Fe(3,5-Me-BAFP)(ClO_4)] (**1)** in 62% yield. The ferric complex [Fe(3,5-Me-BAFP)(PF_6)] (**2)** was synthesized in the same way using $AgPF_6$ in 78% yield. The purity of these complexes was assessed by UV-vis, IR, and EPR spectroscopy. The UV-vis spectrum of the precursor complex **1** exhibits the Soret band at 416 nm and a prominent Q band at 525 nm in toluene as shown in Figure 2.1. Upon addition of excess NH_2OBn, the Soret band shifts immediately (after ~5 minutes) to 433 nm and the main Q band is now observed at 537 nm. These changes are accompanied by a dramatic sharpening of the Soret band. These spectral changes are characteristic for the formation of a ferrous porphyrin

complex. Similar spectral changes occur when **2** is reacted with excess NH_2OBn (see Figure 2.1, right).

In order to detect intermediates in the reaction of [Fe(3,5-Me-BAFP)(PF_6)] with NH_2OBn a number of experiments were completed. The reaction of stoichiometric amounts of NH_2OBn (ie. 1 or 2 equivalents) with **2** was explored via UV-vis spectroscopy (at room temperature). The obtained UV-vis spectra correspond to a mixture of the starting ferric porphyrin complex and the ferrous product (see below for further characterization). Based on this, it is not possible to observe any potential ferric porphyrin intermediates at room temperature. In addition, kinetic experiments monitored by UV-vis spectroscopy were attempted to obtain a rate constant for the reaction of [Fe(3,5-Me-BAFP)(PF_6)] with excess NH_2OBn (approx. 27 equivalents). However, this reaction is complete within mixing time of the solutions, so stopped-flow spectroscopy will have to be employed to determine the rate constant (the focus of additional, future studies). Lastly, we tested whether N_2O is a product of the reaction of [Fe(3,5-Me-BAFP)(PF_6)] with excess NH_2OBn as shown earlier for the reaction of ferric porphyrins with NH_2OH. Indeed, gas headspace analysis by IR spectroscopy[8] confirms that N_2O is a product in addition to NH_3 (0.175 equivalents of N_2O relative to the porphyrin complex were detected).

To further confirm that the product of the reaction of **1** and **2** with NH_2OBn is a ferrous porphyrin, EPR spectroscopy was employed. The EPR spectrum of **1** in toluene at 10 K, shown in Figure 2.2 (left), exhibits effective $g_\perp$ values of 5.8 and 4.6 and an effective $g_\parallel$ value of 2.0. This is indicative of a complex with a S = 5/2,

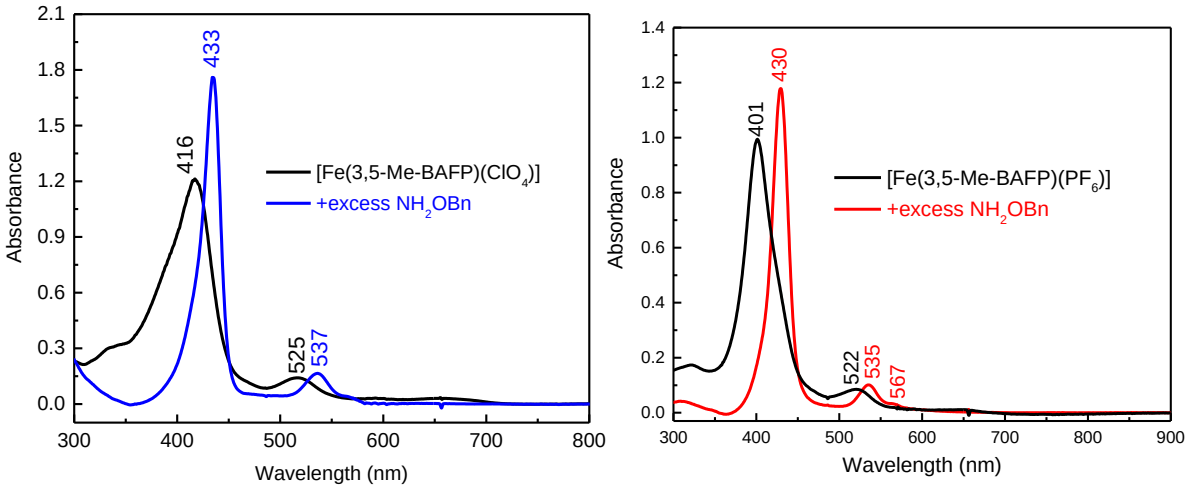

Figure 2.1. Left: UV-vis spectra of [Fe(3,5-Me-BAFP)(ClO_4)] (black) and of the product of the reaction of this complex with excess NH_2OBn (blue) in toluene at room temperature. Right: UV-vis spectra of [Fe(3,5-Me-BAFP)(PF_6)] (black) and of the product of the reaction of this complex with excess NH_2OBn (red) in toluene at room temperature.

3/2 spin-admixed ground state, which typically have effective $g_\perp$ values that range from 4 to 6 ($g_\parallel = 2$).[9,10] Also, these S = 5/2, 3/2 spin-admixed species are commonly observed for ferric porphyrin perchlorate complexes,[11,12] where the effective $g_\perp$ values then vary depending on the relative amounts of S = 5/2 and 3/2 in the ground state. For example, [Fe(TPP)(ClO_4)] (TPP = dianion of tetraphenylporphyrin), in toluene at 10 K has an effective $g_\perp$ of 4.70 ($g_\parallel = 1.98$),[11,12] while [Fe(OEP)(ClO_4)] (OEP = dianion of octaethylporphyrin), in a methylene chloride/toluene mixture at 77 K has a significantly shifted effective $g_\perp$ value of 3.83 ($g_\parallel = 1.97$).[12] Interestingly, the EPR spectrum of **2** in 2-Me-THF at 6 K shows a similar S=5/2, 3/2 spin-admixed ground state with effective $g_\perp$ values of 6.1 and 5.1 and an effective $g_\parallel$ value of 2.0 (see Figure 2.2, right). This is again in agreement with literature g-values for ferric porphyrin hexafluorophosphate complexes. For example, [Fe(TPP)(PF_6)] in toluene at 10 K with an effective $g_\perp$

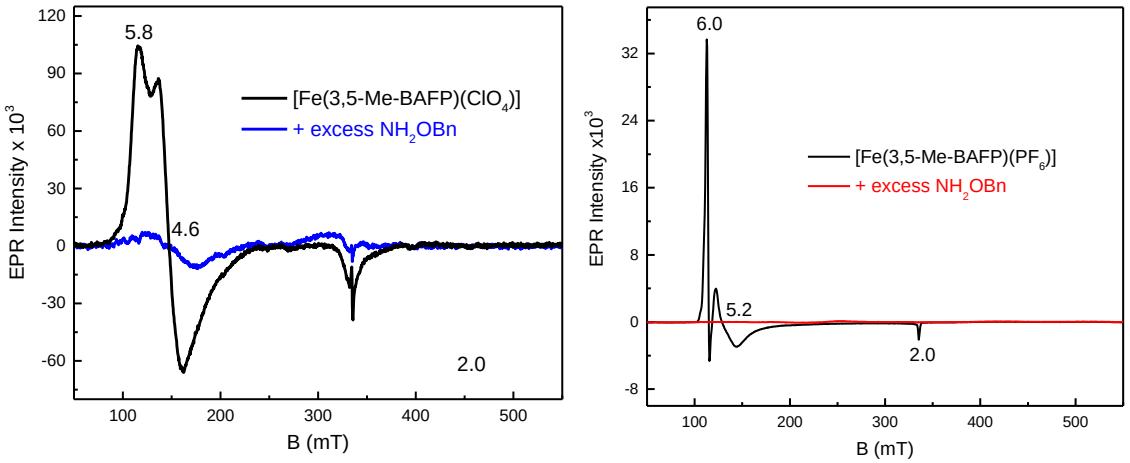

Figure 2.2. EPR spectra of [Fe(3,5-Me-BAFP)(ClO_4)] (black) and of the product of the reaction of this complex with excess NH_2OBn (blue) in toluene. Spectra were measured at 10 K. EPR spectra of [Fe(3,5-Me-BAFP)(PF_6)] (black) and of the product of the reaction of this complex with excess NH_2OBn (red) in 2-Me-THF. Spectra were measured at 6 K.

value of ~5.[11] This indicates that **2** has a dominant S = 5/2 contribution in the ground state, as the effective $g_\perp$ values are closer to those expected for high-spin ferric hemes.

Reaction with NH_2OBn (excess) with either ferric porphyrin complex results in a completely silent EPR spectrum, indicative of the formation of a ferrous porphyrin. This shows that the counter ion, ClO_4^- vs. PF_6^-, does not affect the formation of the ferrous reaction product. Feng and Ryan observed that the reaction of [Fe(TPP)(Cl)] with excess NH_2OH at -30 °C also led to the reduction of the complex, generating a ferrous product proposed to be [Fe(TPP)(NH_2OH)$_2$].[5] As such, we hypothesized that our reaction product was [Fe(3,5-Me-BAFP)(NH_2OBn)$_2$]. In order to further determine the nature of the product, in particular in the light of another paper that reported hydroxylamine disproportionation by ferrous hemes,[3] we set up crystallizations of **1** in the

presence of excess NH_2OBn. This resulted in the formation of brown prisms, suitable for X-ray crystallography.

The resulting crystal structure shows a six-coordinate heme complex with two small ligands, likely H_2O or NH_3 bound in the axial position to the heme. However, X-ray crystallography cannot differentiate between NH_3 and H_2O, so verification that the bound ligands were in fact both NH_3 was obtained from Russell's hypochlorite-phenol method for NH_3 quantification. A calibration curve was first generated by assaying NH_4Cl standards and measuring the absorbance of indophenolate at 630 nm by UV-visible spectroscopy.

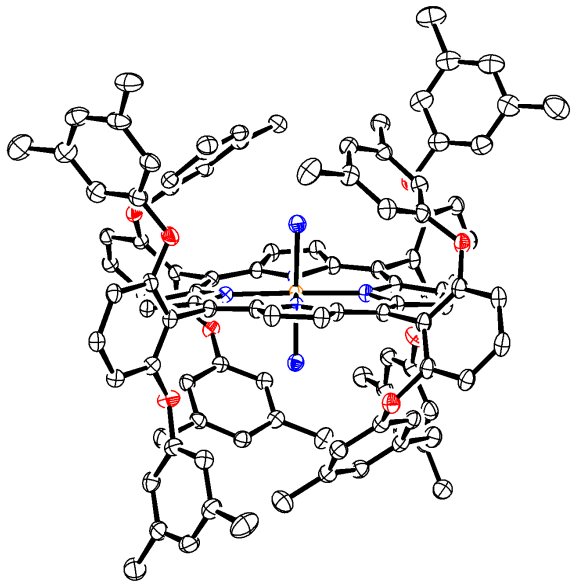

Figure 2.3. Crystal structure of [Fe(3,5-Me-BAFP)$(NH_3)_2$]. Hydrogen atoms and a solvent molecule (toluene) are omitted for clarity. Thermal ellipsoids are shown at 30% probability.

Since the ferrous product species is not water soluble, the assay was completed in toluene, and NH_4Cl standards were spiked with toluene to ensure that toluene does not interfere with NH_3 quantification (see Figure 2.25). To assay the potential product [Fe(3,5-Me-BAFP)$(NH_3)_2$] (**3**), the NH_3 is trapped by addition of excess dilute acid to a stirring solution of this complex on ice. The assay was carried out using bulk material of the reaction product and repeated three times. From this assay, we determined that two equivalents of NH_3 are bound to the ferrous porphyrin complex, as shown in Table 2.3. Hence, the product of the reaction is

clearly [Fe(3,5-Me-BAFP)(NH_3)$_2$], which is the first structurally characterized ferrous porphyrin ammonia complex.

The structure of the ferrous bis-ammonia complex **3** is shown in Figure 2.3. The two Fe-NH_3 bond lengths are 2.016 and 1.990 Å, and Fe-N bond lengths of the porphyrin are given in Table 2.1, which are in agreement with a low-spin ferrous heme (1.981-2.001 Å).[13] While the slight difference in Fe-NH_3 bond lengths was unexpected, the packing of the phenolate pickets of 3,5-Me-BAFP^{2-} (~3 Å away from the N-atom of NH_3) around the NH_3 ligands and minor saddling of the heme could modulate this difference. Surprisingly, there are no reported crystal structures of NH_3-bound ferrous (or ferric) porphyrin complexes in the Cambridge Structural Database. Crystal structures of water-bound ferrous[14] and ferric[15-19] porphyrin complexes are available, with Fe-OH_2 bonds lengths that range from 1.976 – 2.099 Å. For structural comparison, there is one reported crystal structure of a six-coordinate ferrous bis-aqua complex Fe[TDCP(NO_2)$_8$P(H_2O)$_2$] (where TDCP(NO_2)$_8$P = dianion of 2,6-dichlorophenyl-2,3,7,8,12,13,17,18-octanitro-porphyrin).[14] The Fe-OH_2 bond lengths are both 1.976 Å and the average Fe-N distances of the porphyrin are 1.945 Å, as shown in Table 2.1. The bound H_2O ligands are each hydrogen-bonded to one acetone molecule. Also, it should be mentioned that this ferrous porphyrin complex has a non-planar, ruffled structure and is likely intermediate spin based on the average Fe-N distances of the porphyrin.[13] In addition, there are reported crystal structures of six-coordinate bis(primary amine) ferrous porphyrins [Fe(TPP)(RNH_2)$_2$], where R = 1-butyl,

Table 2.1. Selected bond lengths for [Fe(3,5-Me-BAFP)$(NH_3)_2$][a], Fe[TDCP$(NO_2)_8$P$(H_2O)_2$], [Fe(TPP)(1-Bu$NH_2)_2$], [Fe(TPP)(Bz$NH_2)_2$], and [Fe(TPP)($PhCH_2CH_2NH_2)_2$].

Complex	ΔFe-N_{porph}[b]	ΔFe-L	ΔFe-L	Ref.
[Fe(3,5-Me-BAFP)$(NH_3)_2$]	1.992	1.990	2.016	t.w.
Fe[TDCP$(NO_2)_8$P$(H_2O)_2$] (distorted)	1.945	1.976	1.976	14
[Fe(TPP)(1-Bu$NH_2)_2$]	1.989	2.039	2.039	20
[Fe(TPP)(Bz$NH_2)_2$]	1.992	2.041	2.045	20
[Fe(TPP)($PhCH_2CH_2NH_2)_2$]	1.989	2.028	2.028	20

[a]All values are given in Å; [b]Average value

benzyl, and phenethyl.[20] These ferrous porphyrin complexes are low-spin and the Fe-NH_2R bond lengths (2.028 – 2.045 Å) are longer than the Fe-NH_3 bond lengths in **3** (see Table 2.1). The average Fe-N distances of the porphyrin for **3** and for these bis(primary amine) ferrous porphyrins are in good agreement with each other.

In addition, there are two reports of NH_3-bound iron porphyrin complexes with TPP^{2-} and OEP^{2-} co-ligands. The ferric complex [Fe(TPP)$(NH_3)_2]^+$ was characterized by ^{1}H-NMR, EPR, and Mössbauer spectroscopy. [Fe(TPP)$(NH_3)]^+$ is low spin and stable with respect to NH_3 loss. A broad resonance is observed at ~241 ppm for coordinated NH_3 in the ^{1}H-NMR spectrum.[20] With OEP^{2-}, the ferrous complex [Fe(OEP)$(NH_3)_2$] was prepared and studied in solution using Mössbauer spectroscopy.[21] This ferrous porphyrin complex is also low-spin as evident from the Mössbauer data. With this, our crystal structure of **3** is the first reported structure of an NH_3-bound ferrous heme model complex. One could envision that the bis-picket fence porphyrin could facilitate NH_3 binding by "trapping" it due to steric protection of the binding site by the picket fence.

Experimentally, the addition of excess NH_2OBn to our ferric porphyrin complexes at room temperature does not lead to the formation of a ferrous heme-nitrosyl product, as in Feng and Ryan's work who utilized NH_2OH In the latter case, the ferrous heme-nitrosyl is proposed to form via a reductive nitrosylation-type mechanism, for example:

$$[Fe(TPP)Cl] + 2NH_2OH \longrightarrow [Fe(TPP)(NH_2OH)_2]^+ + Cl^-$$

$$[Fe(TPP)(NH_2OH)_2]^+ + NH_2OH \longrightarrow [Fe(TPP)(NO)] + NH_3 + NH_3OH^+ + H_2O$$

In this mechanism, the coordinated NH_2OH ligand is oxidized to NO and an additional molecule of NH_2OH is reduced to NH_3.[5] This result differs from the report by Bari et al., who did not observe quantitative formation of the ferrous heme-nitrosyl from the reaction of $[Fe(TPPS)]^{3-}$ ($TPPS^{6-}$ = dianion of tetra(4-sulfanatophenyl)porphyrin) with excess NH_2OH, and the gaseous products N_2 and N_2O were also detected. The proposed mechanism of this reaction is shown in Scheme 2.4. In this case, Bari et al. suggest that NH_2OH is oxidized to generate the ferric intermediate $[Fe(TPPS)(HNO)(NH_3)]^{3-}$, followed by oxidation of the HNO ligand by the ferric heme and loss of coordinated NH_3 to give the corresponding ferrous heme-nitrosyl complex $[Fe(TPPS)(NO)]^{4-}$. However, there are other parallel

Scheme 2.4. Proposed disproportionation mechanism of NH_2OH by ferric porphyrin complexes, derived from the reaction of $[Fe(TPPS)]^{3-}$ with excess NH_2OH. This mechanism is adapted from reference 3.

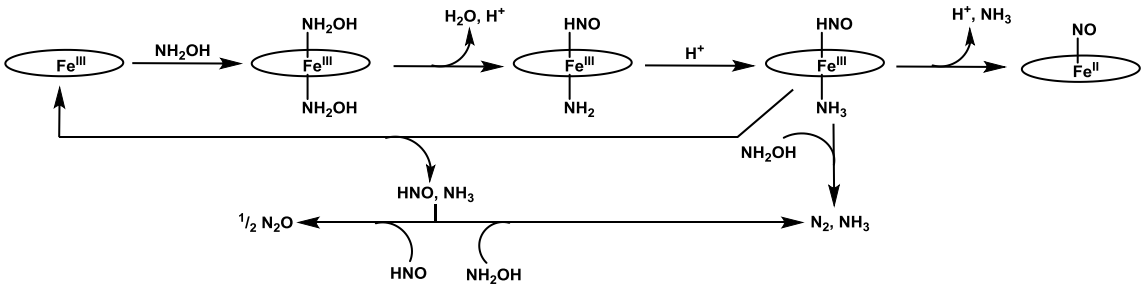

mechanistic pathways that must occur to generate N_2 and N_2O. For example, the HNO ligand from the ferric intermediate $[Fe(TPPS)(HNO)(NH_3)]^{3-}$ could react with excess NH_2OH to produce N_2. The generation of N_2O could occur by loss of coordinated HNO from $[Fe(TPPS)(HNO)(NH_3)]^{3-}$, followed by reaction of two molecules of HNO to form hyponitrous acid ($N_2O_2H_2$), which decomposes into N_2O and H_2O. The latter process regenerates the starting ferric porphyrin complex and the cycle can start over again.[3]

In contrast to these findings, a reduction of the ferric porphyrin to the ferrous state is observed, in our case followed by NH_2OBn disproportionation to generate NH_3 and benzyl alcohol and likely the additional gaseous products N_2 or N_2O. This leads ultimately to the formation of an ammonia bound ferrous heme complex, rather than $[Fe(3,5\text{-Me-BAFP})(NH_2OBn)_2]$ or [Fe(3,5-Me-BAFP)(NO)]. Therefore, the findings reported in this paper parallel observations by Bari et al., for the reaction of excess NH_2OH with the ferric heme complex $[Fe(TEPyP)]^{5+}$ ($TEPyP^{2+}$ = dianion of tetra(*N*-ethylpyridinium-2yl)porphyrin).[3] Interestingly, the UV-vis

Scheme 2.5. Proposed disproportionation mechanism of NH_2OH by ferric porphyrin complexes, derived from the reaction of $[Fe(TEPyP)]^{5+}$ with excess NH_2OH. This mechanism is adapted from reference 3.

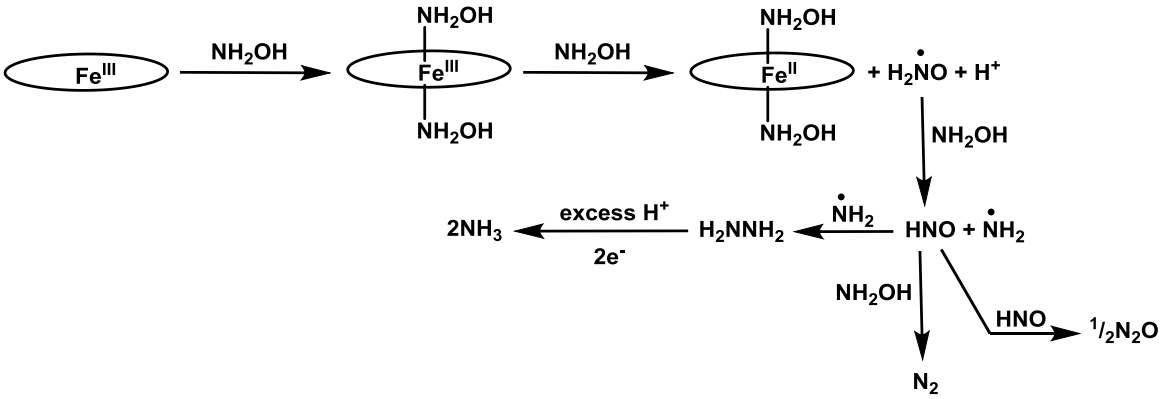

spectra after the addition of excess NH_2OBn to **1** or **2** are similar to the UV-vis spectrum that results from NH_2OH addition to $[Fe(TEPyP)]^{5+}$ with a Soret band at 425 nm and the main Q band at 535 nm. Therefore, addition of NH_2OH to $[Fe(TEPyP)]^{5+}$ results in a similar reduction of the iron from the ferric to the ferrous oxidation state as reported here, evidenced by UV-vis and ^{1}H-NMR spectroscopy. Also, Bari et al. showed free-radical formation in this reaction by the methylmetacrilate assay. In their proposed mechanism in Scheme 2.5, reduction of the ferric porphyrin complex generates a six-coordinate hydroxylamine-bound ferrous porphyrin complex and a nitrogen-containing radical species in the first step of the reaction. The nitrogen-containing radical species, NH_2O(radical), initiates the formation of HNO and other radical species, such as NH_2(radical). These species could then generate NH_3 as well as N_2 and N_2O as shown in Scheme 2.5. One could envision that the NH_2(radical) or N_2H_4 could also oxidize the ferrous porphyrin back to the ferric oxidation state, and the catalytic cycle could start over again. This is in accordance with the findings by Bari et al. for $[Fe(TEPyP)]^{5+}$, as they observe the porphyrin to be catalytically active in NH_2OH disproportionation. Overall, our findings are in good agreement with the work of Bari et al as previously reported.

In summary, the two new ferric bis-picket fence porphyrin complexes, [Fe(3,5-Me-BAFP)(ClO_4)] and [Fe(3,5-Me-BAFP)(PF_6)], have been prepared and characterized by UV-vis and EPR spectroscopy. The reactivity of these ferric porphyrin complexes with NH_2OBn was studied as a model for NH_2OH. When these ferric porphyrin complexes are reacted with excess NH_2OBn a reduction of

the iron from the ferric to ferrous oxidation state occurs, followed by disproportionation of NH_2OBn. The final product of this reaction is [Fe(3,5-Me-BAFP)$(NH_3)_2$], which was characterized by X-ray crystallography. This complex constitutes the first bis-ammonia complex of a ferrous or ferric heme structurally characterized to date.

2.2 Synthesis and Spectroscopic Characterization of [Fe(3,5-Me-BAFP)(NHOMe)]

As mentioned above there are no reports of ferric hydroxylamide heme complexes due to hydroxylamine disproportionation.[6] In Section 2.1 we found that although NH_2OR ligands are stable at room temperature, they undergo disproportionation reactions when reacted with iron porphyrins. We thought deprotonation of the NH_2OR ligands would impart more stability. We further speculated that hydroxylamide ($NHOR^-$) salts could be reacted with Fe(III)-X complexes (where X = weakly coordinated anions such as PF_6^-) to prepare Fe(III)-NHOR porphyrin complexes. The hydroxylamide salts were prepared by the deprotonation of NH_2OMe with methyllithium in dry diethyl ether at low temperature as previously reported.[22] The ferric hexafluorophosphate complex, [Fe(3,5-Me-BAFP)(PF_6)], was prepared as described in Section 2.1. Then, excess Li[NHOMe] was reacted with the iron(III)-PF_6^- complex in 2-Me-THF at room temperature to form the corresponding ferric hydroxylamide complex [Fe(3,5-Me-BAFP)(NHOMe)] in 81% yield. The UV-vis spectrum of the isolated product (Figure

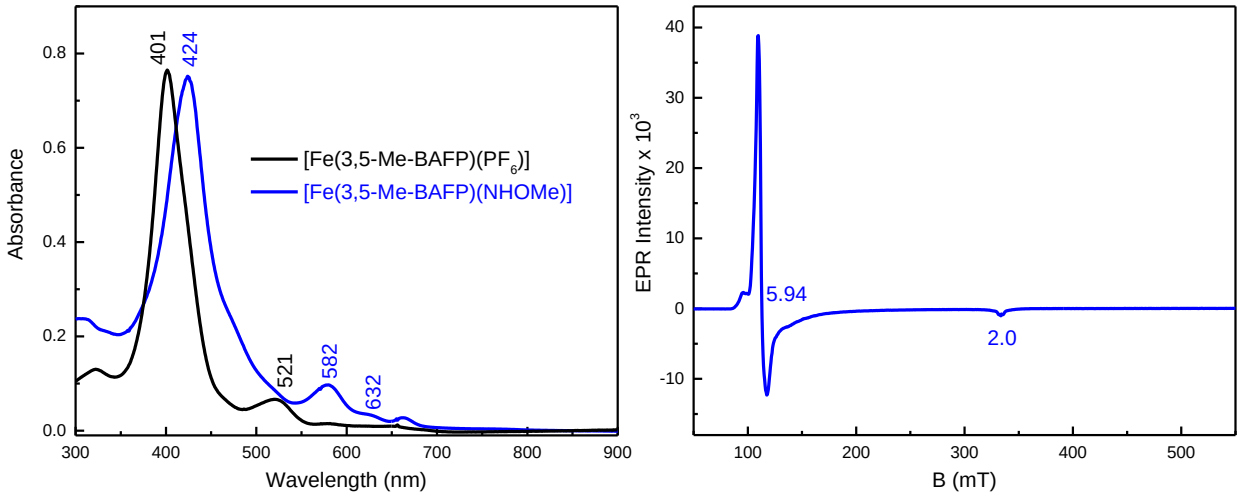

Figure 2.4. Left: UV-vis spectra of [Fe(3,5-Me-BAFP)(PF_6)] and of the isolated reaction product, [Fe(3,5-Me-BAFP)(NHOMe)] (blue), in 2-Me-THF at room temperature. Right: EPR spectrum of [Fe(3,5-Me-BAFP)(NHOMe)] in toluene at 6 K.

2.4, left) shows a broadening and a shift in the position of the Soret band from 401 to 424 nm and in the main Q band from 525 to 582 nm. The UV-vis of this product is indicative of an N-bound ferric reaction product such as [Fe(TPP)(4-MeIm)] ($\lambda = 416$, 576, and 621 nm in toluene).[23] To determine whether the ferric hydroxylamide complex was high- or low-spin EPR spectroscopy was employed. The EPR spectrum in toluene at 6 K in Figure 2.4 (right) shows that the complex is a high-spin (hs, S = 5/2) and 5-coordinate (5C) ferric complex, where $g_x = g_y =$ 5.94 and $g_z = 2.0$. In addition, the shift of the β-pyrrole proton NMR signals of the porphyrin co-ligand are correlated with the oxidation and spin state of the iron center. Our complex, [Fe(3,5-Me-BAFP)(NHOMe)], exhibits a broad signal at ~79

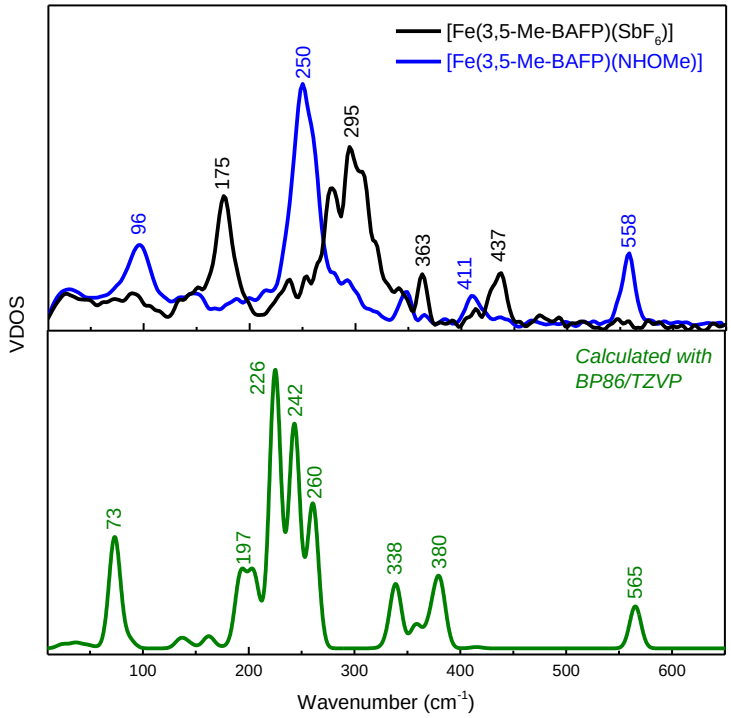

Figure 2.5. NRVS-derived vibrational density of states (VDOS) for the precursor, [^{57}Fe(TPP)(SbF_6)] (black), and the isolated reaction product, [^{57}Fe(3,5-Me-BAFP)(NHOMe)] (blue). Bottom: Calculated (BP86/TZVP) NRVS VDOS spectrum of [Fe(P)(NHOMe)].

ppm representative of a hs *S* = 5/2 complex. The remaining porphyrin proton NMR signals are found from 11.074 to 1.843 ppm. Interestingly, we also observed two broad signals from the bound $NHOMe^-$ ligand at -0.887 and -3.77 ppm, which are shifted upfield due to the ring current of the porphyrin. Lastly, we employed ^{57}Fe Nuclear Resonance Vibrational Spectroscopy (NRVS) to understand the electronic properties of [^{57}Fe(3,5-Me-BAFP)(NHOMe)]. The NRVS spectrum shown in Figure 2.5 contains notable features at 250 cm^{-1} and 558 cm^{-1}. The 250 cm^{-1} band is an Fe-porphyrin vibration, indicative of a high-spin ferric complex.[24,25] By comparison to the NRVS spectrum of precursor complex, [^{57}Fe(3,5-Me-BAFP)(SbF_6)], the 558

cm^{-1} feature in our complex seems like it is the Fe-N stretching frequency. Since we do not have the ^{15}NHOMe labeled complex data, we used DFT calculations to determine the nature of this vibration. The structure of [Fe(P)(NHOMe)] (where P = dianion of porphine) was optimized with BP86/TZVP and is in good agreement with the crystal structure data (see Table 2.2). The examination of the vibrational frequencies shows a similar energy vibration at 565 cm^{-1} that is the Fe-N stretching frequency. With this, we believe the 558 cm^{-1} vibration in the NRVS spectrum of [Fe(3,5-Me-BAFP)(NHOMe)] is the Fe-N stretching frequency, but the ^{15}NHOMe complex is needed to confirm this proposal.

Since this is the first iron-NHOMe^{-} type complex ever synthesized we wanted to ensure that the coordination of the NHOMe^{-} ligand was consistent with the proposed structure in Scheme 2.3. To answer this important question we obtained the crystal structure of the [Fe(3,5- Me-BAFP)(NHOMe)] complex in Figure 2.6.

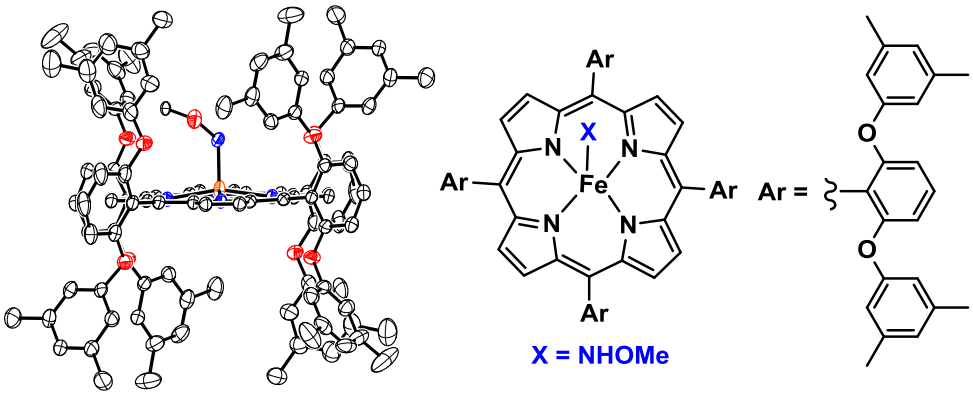

Figure 2.6. Left: Crystal structure of [Fe(3,5-Me-BAFP)(NHOMe)]. Hydrogen atoms and the disorder of the NHOMe ligand are omitted for clarity. The thermal ellipsoids are shown at 30% probability. Right: Schematic drawing of [Fe(3,5-Me-BAFP)(NHOMe)].

Table 2.2. Comparison of geometric parameters of selected iron porphyrin complexes to [Fe(3,5-Me-BAFP)(NHOMe)][a] and the calculated structure of this complex with BP86/TZVP (P^{2-} = porphine).

Complex	ΔFe-N_{porh}[b]	ΔFe-L[c]	ΔC-O	ΔN-O	<Fe-L	Ref.
[Fe(3,5-Me-BAFP)(NHOMe)]	2.069	1.929	1.489[d]	1.520[e]	125[f]	t.w.
[Fe(P)(NHOMe)], calculated	2.10	1.940	–	1.408	124	t.w.
[Fe(TPP)(N_3)]	2.066	1.953	–	–	122	26
[Fe(TPP)(OMe)]	2.082	1.816	1.393	–	129	27
[Fe(TPP)(Cl]	2.051	2.192	–	–	–	28

[a]Bond lengths are given in Å and the angle is given in degrees; [b]Average value; [c]L denotes the axial ligand bound to the iron center; [d]$NHOMe^-$ unit is disordered resulting in C-O bond lengths = 1.484, 1.437, 1.414, and 1.478 Å; [e]N-O bond lengths = 1.556, 1.4996, and 1.591 Å; [f]<Fe-NH-OMe = 116, 119, and 124°.

For clarity purposes the disorder of the $NHOMe^-$ unit above and below the heme plane and within the $NHOMe^-$ unit is not shown. The structure shows that the $NHOMe^-$ ligand is bound through the N-atom of the ligand and that the iron is located outside of the heme plane, indicating our complex is indeed five-coordinate. Also, the average Fe-N_{porph} bond length for our complex is 2.069 Å, which falls into the range of other high-spin (and 5C) ferric porphyrins (2.051 – 2.082 Å) as shown in Table 2.2.[26-28] Interestingly, the Fe-NHOMe bond length of 1.929 Å is similar to the [Fe(TPP)(N_3)] complex[26] with a Fe-N_3 bond length of 1.953 Å. However, our complex exhibits a much longer Fe-NHOMe bond than the Fe-OMe bond length of 1.816 Å in [Fe(TPP)(OMe)][27] and is significantly shorter than the Fe-Cl bond of 2.051 Å in [Fe(TPP)(Cl)].[28] It is also worth noting that because the iron sits outside of the heme plane in the crystal structure, ferric porphyrins usually have a small amount of a doming distortion. The doming distortion can be analyzed by measuring the iron atom displacement from the mean heme plane (toward the axial ligand). With our complex, the iron atom is displaced by 0.34 Å

from the mean heme plane, which, surprisingly, is just outside of the typical iron atom displacements values of 0.39 – 0.62 Å observed for five-coordinate (hs) ferric porphyrin complexes.[13] This indicates that our complex is less domed than other reported ferric heme complexes.

In summary, we synthesized the ferric hydroxylamide complex, [Fe(3,5-Me-BAP)(NHOMe)], in pure form and fully characterized this complex by UV-vis, EPR, and ^{1}H-NMR spectroscopy and NRVS. Additionally, we obtained the first X-ray structure of an iron-NHOR^{-} type species to date.

2.3 One-electron Oxidation of the Ferric Hydroxylamide Porphyrin Complex

Electrochemistry of [Fe(3,5-Me-BAFP)(NHOMe)]

The electrochemistry of the [Fe(3,5-Me-BAFP)(NHOMe)] complex, studied by Cyclic Voltammetry (CV), shows whether a one-electron oxidation reaction is accessible. The CV of the ferric hydroxylamide complex shows a chemically reversible one-electron oxidation at a reduction potential of +0.291 V vs. Fc/Fc^{+} (in 1,2-dichlorethane) as shown in Figure 2.7. Interestingly, the one-electron oxidation product appears to be stable on the timescale for CV measurements. This complex should exhibit an Fe(III)/Fe(IV) redox couple and two additional oxidations of the porphyrin macrocycle. Unfortunately, the solvent window cuts off in 1,2-dichloroethane around +1 V, but we still observe another quasi-reversible redox event at ~+0.90 V vs. Fc/Fc^{+}. In order to ensure that the first oxidative wave at

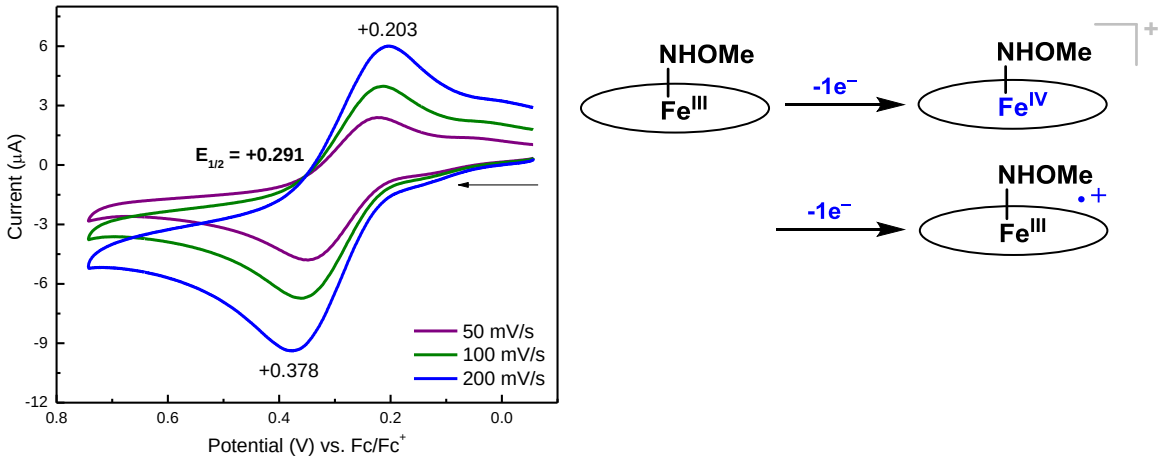

Figure 2.7. CV of a 3 mM solution of [Fe(3,5-Me-BAFP)(NHOMe)] in 1,2-DCE, where the working electrode is glassy carbon and the counter electrode is platinum with a Ag wire pseudo-reference at room temperature. Right: Schematic representation of the one-electron oxidation of [Fe(3,5-Me-BAFP)(NHOMe)], which could result in the oxidation of the iron-NHOMe unit, or the porphyrin co-ligand. The oval represents the porphyrin ligand.

~+0.3 V was indeed the Fe(III)/Fe(IV) couple rather than oxidation of the porphyrin co-ligand as depicted in Figure 2.12 (right), we investigated the later process further. This is discussed in the following section.

Chemical and Electrochemical Oxidation of [Fe(3,5-Me-BAFP)(Cl)]

In this section, we want to understand the spectroscopic features associated with oxidized porphyrin macrocycles, in order to compare these oxidized porphyrin features to the one-electron oxidation product of [Fe(3,5-Me-BAFP)(NHOMe)]. It was reported in that literature that the one-electron oxidation of ferric chloride heme complexes, [Fe(Porph)(Cl)] (Porph = dianion of porphyrin co-ligand), results in the oxidation of the porphyrin co-ligand to yield an iron(III) porphyrin^{+}(radical) complex (rather than oxidation of the iron center to an iron(IV) species).[29-31] To gain a spectroscopic handle on porphyrin oxidation with our 3,5-

Me-BAFP^{2-} co-ligand we carried out the one-electron oxidation of [Fe(3,5-Me-BAFP)(Cl)]. First, we measured the CV of the [Fe(3,5-Me-BAFP)(Cl)] complex as shown in Figure 2.17. The CV shows the first porphyrin oxidation at an $E_{1/2}$ value of +0.519 V vs. Fc/Fc$^+$ in 1,2-dichloroethane and is chemically reversible. This value is ~200 mV more negative than the $E_{1/2}$ value of [Fe(TPP)(Cl)] at +0.73 V (vs. Fc/Fc$^+$ in CH_2Cl_2). The redox potential of this complex is actually closer to the tetraphenylporphyrin derivative, [Fe(TPP-*p*-OCH_3)(Cl)] (TPP-*p*-OCH_3 = dianion of *p*-methoxytetraphenylporphyrin), which has an $E_{1/2}$ value of +0.64 V (vs. Fc/Fc$^+$ in CH_2Cl_2).[31]

Next, we employed UV-vis SpectroElectroChemistry (SEC) to determine whether we formed the oxidized porphyrin$^+$(radical) complex, [Fe(3,5-Me-BAFP)(Cl)]$^+$. The oxidation of a solution of [Fe(3,5-Me-BAFP)(Cl)] results in a significant decrease in the intensity of the Soret band at 425 nm, while the Cl to Fe charge transfer feature at 373 nm remains relatively unchanged resulting in a broad split Soret band. At the same time, the main Q band at 525 nm decreases as two new bands at 568 and 534 nm grow in. The oxidation is completely reversible as shown in Figure 2.8. In comparison to the TPP^{2-} macrocycle, the changes in the UV-vis are indicative of iron(III) porphyrin$^+$(radical) complexes.[29-31]

With a handle on the iron(III) porphyrin$^+$(radical) complex, [Fe(3,5-Me-BAFP)(Cl)]$^+$, we investigated bulk generation of this species at room temperature. The ferric chloride precursor, [Fe(3,5-Me-BAFP)(Cl)], was titrated with a solution of the oxidant tris(4-bromophenyl)ammoniumyl hexachloroantimonate, [N(C_6H_4Br-

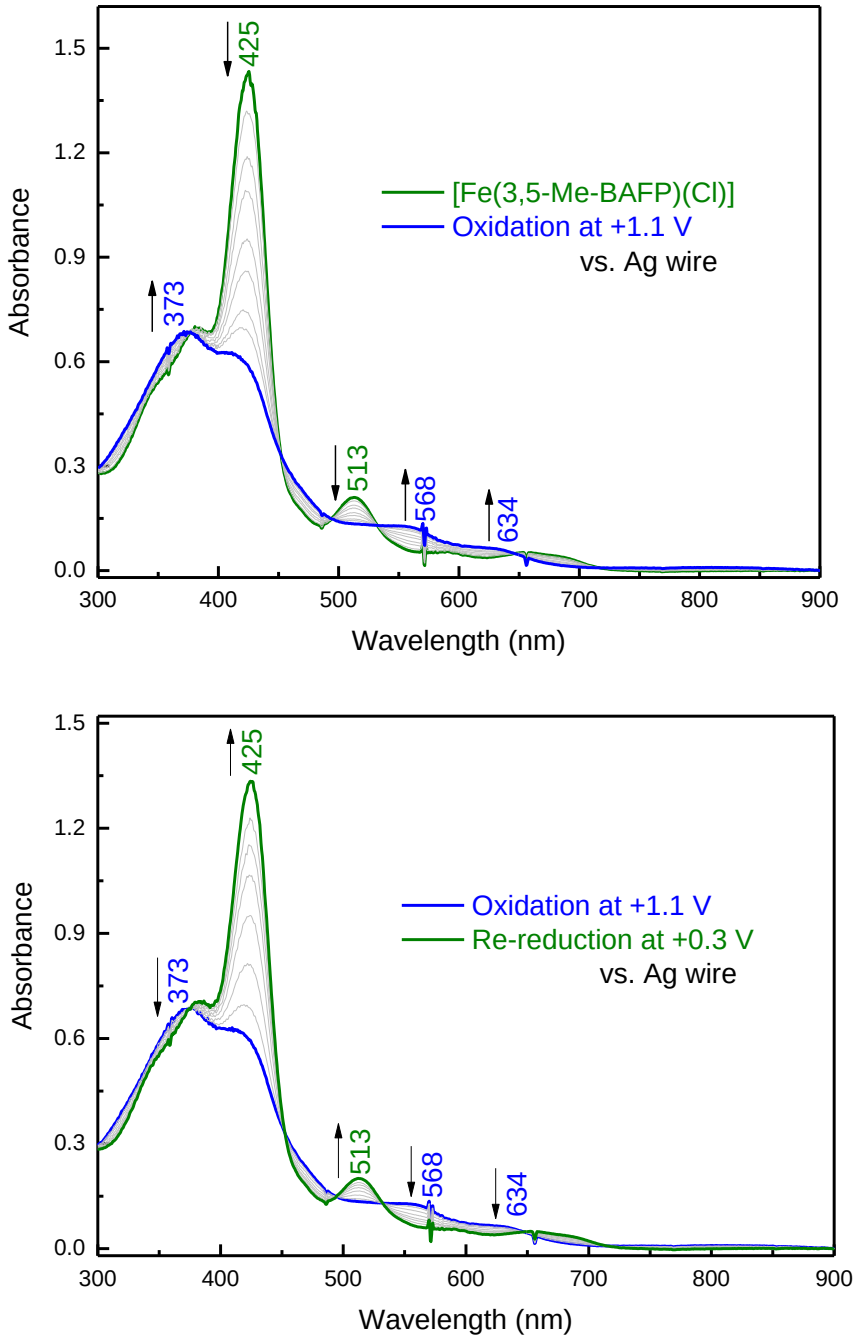

Figure 2.8. Top: UV-vis spectra for the SEC oxidation of [Fe(3,5-Me-BAFP)(Cl)] (green to blue) in an OTTLE UV-vis cell, taken in 0.10 M tetrabutylammonium hexaflourophosphate solution in 1,2-dichloroethane at room temperature. The working and counter electrodes are Pt mesh. Bottom: Re-reduction of the oxidation product (blue to green), showing that the oxidation is fully reversible.

4)$_3$][SbCl$_6$] ($E_{1/2}$ = +0.70 V vs. Fc/Fc$^+$ in CH_2Cl_2)[32] in dichloromethane. The reaction is complete upon ~1 equiv. of [N(C$_6$H$_4$Br-4)$_3$][SbCl$_6$] added to the solution as shown in Figure 2.9. The addition of more than 1 equiv. of oxidant solution results in an increase in the absorbance from bands of the oxidant itself at 373 and 728 nm. The UV-vis spectrum of the reaction product from the chemical oxidation is nearly identical to that of the UV-vis SEC generated species (see Figure 2.8). In addition, Figure 2.9 shows that the chemical oxidation is completely reversible upon the addition of excess ferrocene to the oxidized species [Fe(3,5-Me-BAFP)(Cl)]$^+$. To further access the purity of the bulk material, we utilized EPR and ^{1}H-NMR spectroscopy. For these experiments, the ferric chloride precursor was dissolved in dichloromethane (1 – 2 mM), added to excess solid oxidant, [N(C$_6$H$_4$Br-4)$_3$][SbCl$_6$], and then the solution was agitated until all of the solid

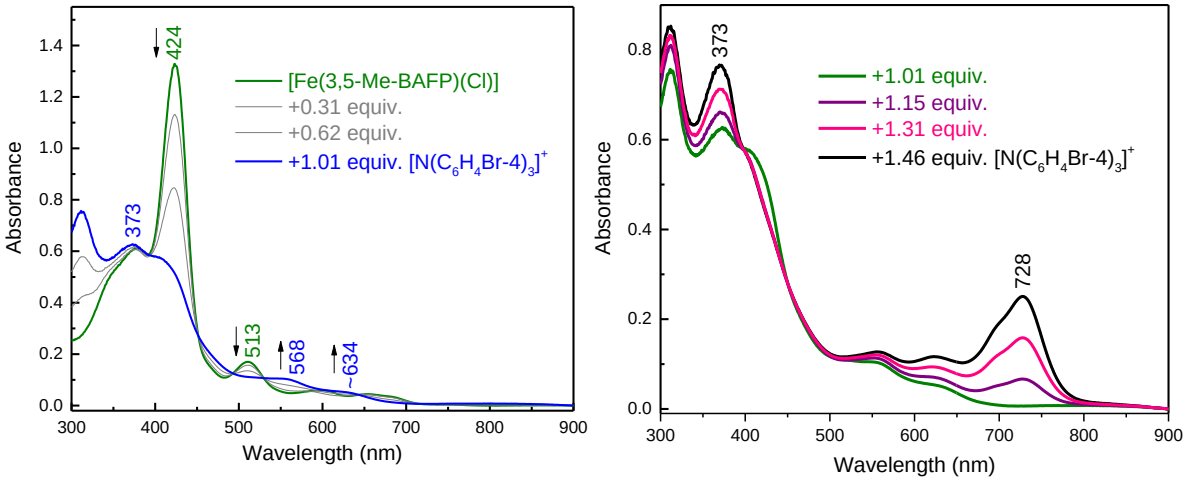

Figure 2.9. Left: UV-vis spectra of the titration of a ~11 μM solution of [Fe(3,5-Me-BAFP)(Cl)] (green) with the chemical oxidant [N(C$_6$H$_4$Br-4)$_3$][SbCl$_6$], in dichloromethane, to form the ferric porphyin radical complex, [Fe(3,5-Me-BAFP)(Cl)]$^+$ (green). Right: UV-vis spectra obtained upon addition of the excess oxidant, showing that the reaction is complete after the addition of one equivalent of oxidant. The peaks at 373 and 728 nm are from the oxidant [N(C$_6$H$_4$Br-4)$_3$][SbCl$_6$]. The reactions were carried out at room temperature.

dissolved. Progress was monitored by UV-vis spectroscopy. The EPR spectrum at 5 K of the ferric chloride precursor has a high-spin ferric signal where $g_X = g_y =$ 5.93 and $g_z = 2.0$. The addition of ~1.0 equiv. of oxidant to the ferric chloride solution results in a completely EPR silent spectrum shown as Figure 2.10. This indicates clean conversion to the oxidized species $[Fe(3,5\text{-Me-BAFP})(Cl)]^+$. Next, we used ^{1}H-NMR spectroscopy to determine the spin state of the oxidized porphyrin species. As previously mentioned, the β-pyrrole hydrogen atoms of the porphyrin co-ligand shift as a function of iron oxidation and spin state. For the ferric chloride precursor (hs, S = 5/2) the chemical shifts range from 2 to 80 ppm and are paramagnetically broadened in deuterated dichloromethane. The broad peak at ~80 ppm corresponds to the β-pyrrole hydrogen atoms of the porphyrin co-ligand (see Figure 2.18, top) and is indicative of a hs ferric heme complex. The addition of excess $[N(C_6H_4Br\text{-}4)_3][SbCl_6]$ to the ferric chloride complex results in a ^{1}H-NMR spectrum with chemical shifts that range from 80 to -11 ppm and that are still paramagnetically broadened as shown in Figure 2.18 (bottom). The shift of some of the porphyrin peaks up field is indicative of the oxidation of the porphyrin macrocycle.[33] Analogous to the ferric chloride precursor, there is a broad peak at ~83 ppm (the β-pyrrole hydrogen atoms). This would indicate $[Fe(3,5\text{-Me-BAFP})(Cl)]^+$ is a high-spin ferric complex with an oxidized porphyrin macrocycle. It should be noted that the electronic structure of $[Fe(TPP)(Cl)]^+$ has been studied in detail with magnetic techniques such as SQUID and Mössbauer spectroscopy to confirm the quintet (S = 2) ground state.[29] From this we can conclude that the electronic structure of the oxidized complex, $[Fe(3,5\text{-Me-BAFP})(Cl)]^+$, is best

described as a hs ferric complex (S = 5/2) that is antiferromagnetically (AFC) coupled to the porphyrin co-ligand (S = ½), resulting in total spin of S = 2. In summary, we generated a ferric porphyrin radical complex $[Fe(3,5\text{-}Me\text{-}BAP)(Cl)]^+$

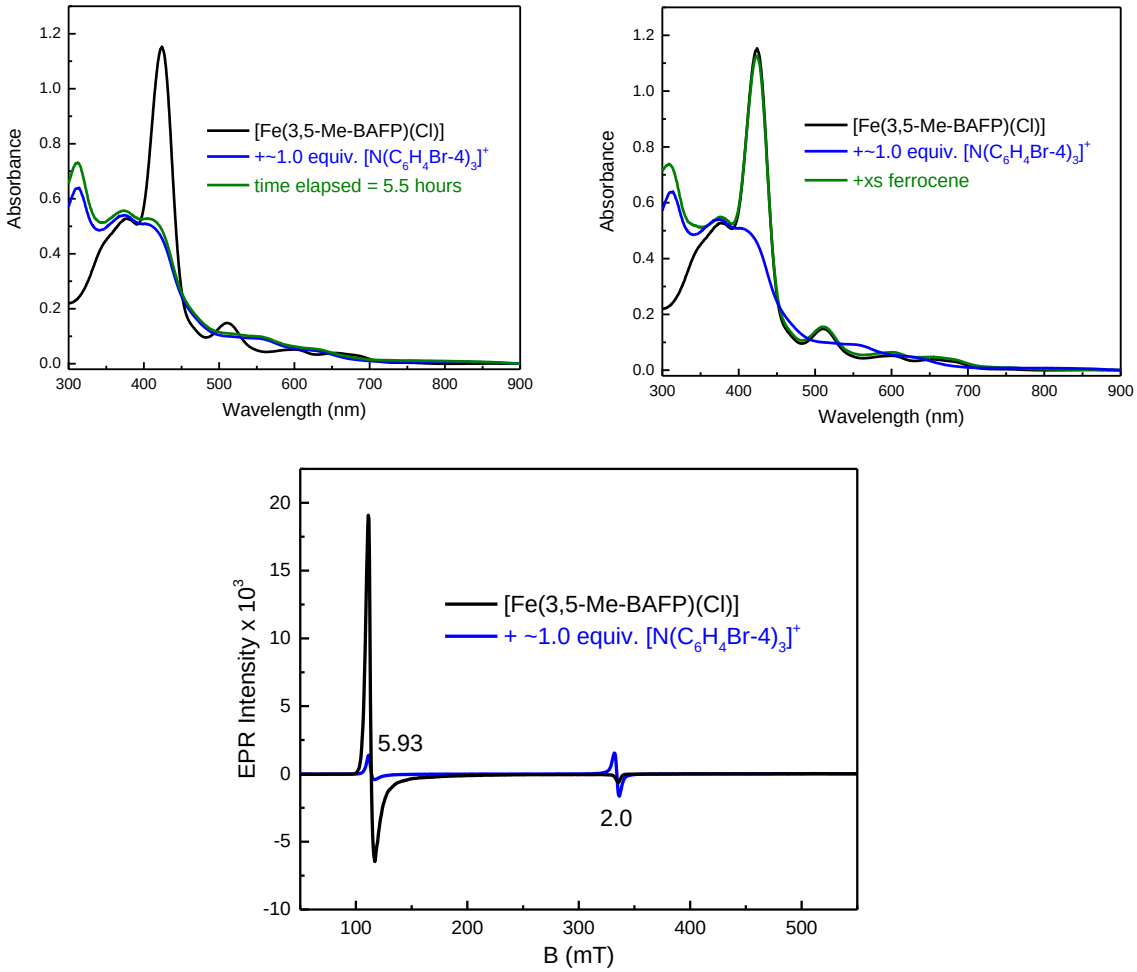

Figure 2.10. Top Left: UV-vis spectra of [Fe(3,5-Me-BAFP)(Cl)] (black) and after addition of ~1 equiv. $[N(C_6H_4Br\text{-}4)_3][SbCl_6]$, in dichloromethane, lead to the formation of the ferric porphyrin radical complex, $[Fe(3,5\text{-}Me\text{-}BAFP)(Cl)]^+$ (blue). The reaction product after stirring for 5.5 hours under an inert atmosphere at room temperature is shown in green. Top right: Subsequent reaction of the oxidized species with excess ferrocene reforms the [Fe(3,5-Me-BAFP)(Cl)] precursor (green). Bottom: EPR spectra of a 1.2 mM solution of the ferric chloride complex, [Fe(3,5-Me-BAFP)(Cl)], and of the reaction product upon addition of ~1 equiv. $[N(C_6H_4Br\text{-}4)_3][SbCl_6]$, measured at 5 K in dichloromethane.

in pure form and characterized this complex by UV-vis, EPR, and ^{1}H-NMR spectroscopy.

Formation of an Intermediate I Model Complex: [Fe(3,5-Me-BAFP)(NHOMe)]$^{+}$

First, the chemical oxidant, [DAcFc][SbF_6], as synthesized by reaction of 1,1'-diacetylferrocene with [thianthrene][SbF_6][34] in dichloromethane. The teal blue solid product precipitates from the solution and is used without further purification. For the following chemical oxidation studies the oxidant was dissolved in cold dimethoxyethane (DME) due to its poor solubility in toluene and dichloromethane.

Then, *in situ* UV-vis monitoring of the reaction of the Fe(III)-NHOMe complex with one equivalent of the chemical oxidant in toluene at room temperature shows a reaction product with a Soret band at 409 and the main Q band at 525 nm; see Figure 2.19 (left). This spectrum is identical to that of [Fe(3,5-Me-BAFP)(SbF_6)] (Figure 2.19, right). The EPR spectrum of the reaction product(s) also matches

Scheme 2.6. Chemical oxidation of [Fe(3,5-Me-BAFP)(NHOMe)] and the decomposition of the oxidized complex to [Fe(3,5-Me-BAFP)(SbF_6)].

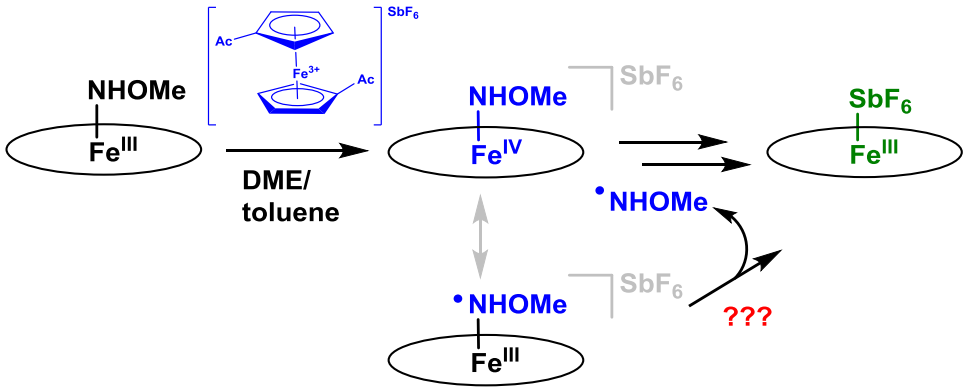

that of [Fe(3,5-Me-BAFP)(SbF_6)] with an additional minor signal from another rhombic iron species as shown in Figure 2.20. One possible route to form [Fe(3,5-Me-BAFP)(SbF_6)] is by NHOMe(radical) coming off the metal center as shown in Scheme 2.6. Based on previous reports (in the absence of a metal center),[35-37] the NHOMe(radical) molecule combines with another NHOMe(radical) molecule to form a hyponitrite-like compound, $N_2O_2Me_2$, which is known to decompose into dinitrogen and methanol. Further proof is needed to see if this happens in our reaction by detection of the reaction product(s). In summary, our results (by UV-vis) show that the porphyrin co-ligand is not oxidized and that the oxidation is likely of the iron-NHOMe unit (see Scheme 2.2).

At this point we speculated that due to the rapid decomposition of the oxidized species at room temperature, the iron(III)-NHOMe complex must be reacted with the oxidant at low temperatures to capture this reactive complex. Here, our experiments were performed at -80°C under inert atmosphere (in the glovebox) and monitored by *in situ* UV-vis spectroscopy with an immersion probe. The addition of ~1 equivalent of the oxidant, [DAcFc][SbF_6], to a solution of the ferric hydroxlyamide complex in toluene at -80°C results in a small decrease in the intensity of the Soret band at 424 nm along with a shift in the Q band region from 582 and 626 nm to 570 and 617 nm as shown in Figure 2.11. Importantly, the UV-vis spectrum looks different than the room temperature product [Fe(3,5-Me-BAFP)(SbF_6)] ($\lambda = 409$, 525 nm). Also, the spectrum of [Fe(3,5-Me-BAFP)(NHOMe)]$^+$ does not exhibit features associated with an oxidized porphyrin macrocycle. Then, we monitored (by UV-vis) the stability of the formed oxidized

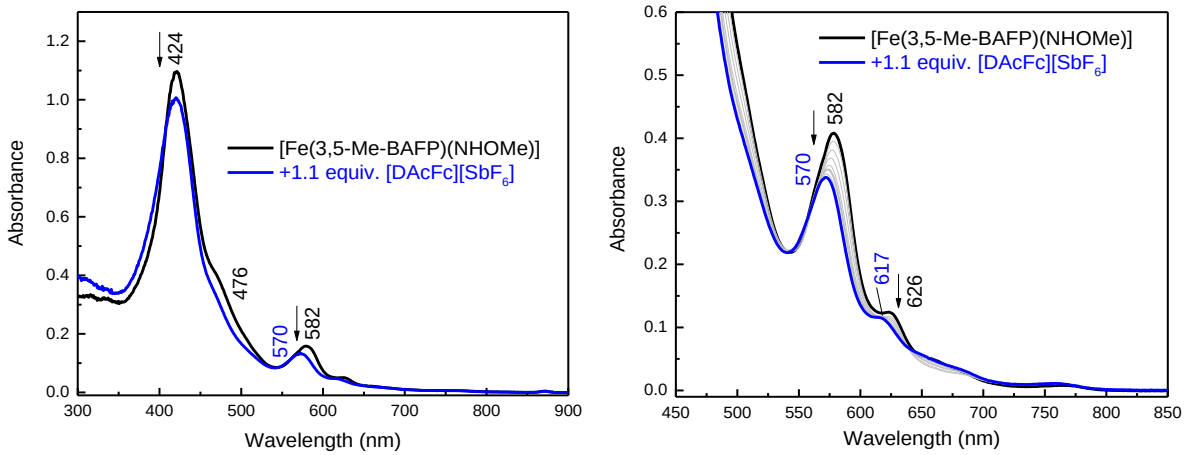

Figure 2.11. Left: UV-vis spectra of the reaction of a ~6 μM solution of [Fe(3,5-Me-BAFP)(NHOMe)] (black) with 1.1 equiv. [DAcFc][SbF_6] in toluene (blue). Right: UV-vis spectra of the reaction of a ~38 μM solution of [Fe(3,5-Me-BAFP)(NHOMe)] (black) with 1.1 equiv. [DAcFc][SbF_6] in toluene (blue). All reactions were carried out under an inert atmosphere at -80°C.

species, $[Fe(3,5\text{-Me-BAFP})(NHOMe)]^+$, at -80°C. Over a one hour time period, the 570 nm band slowly decreases in intensity while a new band grows in at 525 nm; see Figure 2.21 (left). The decay of the Q band at 570 nm plotted versus time is fit to a single exponential (see Figure 2.21, right) with a k_{obs} = 1.7 x 10^{-4} s^{-1} and a half-life of 68 minutes. This means the oxidized species is mostly decomposed within a 3 hour time period at -80°C. Then, the solution of the oxidized species was warmed to room temperature and found that this species rapidly decomposes into the iron(III)-SbF_6 complex in ~10 minutes. This product is the same as the room temperature decomposition product. Interestingly, Intermediate *I* in P450nor also decays into a ferric complex.[38] Though this oxidized species is quite *unstable* this work has shown that there is a modest time window to obtain samples for further spectroscopic characterization. To determine the purity of our oxidized species, $[Fe(3,5\text{-Me-BAFP})(NHOMe)]^+$, EPR spectroscopy was employed. The

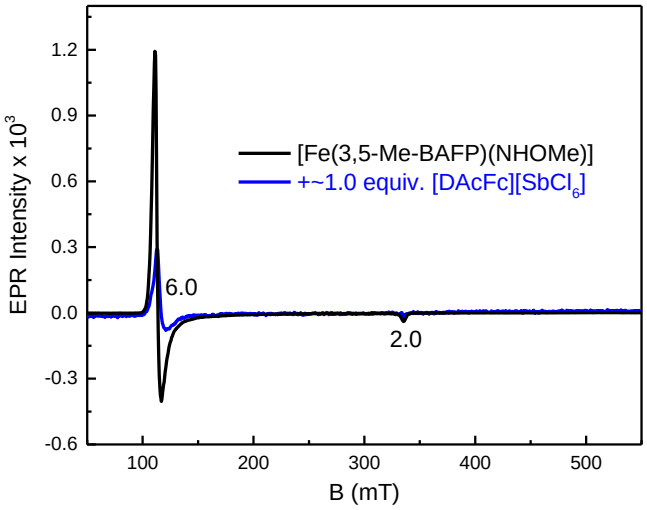

Figure 2.12. EPR spectra of a 0.1 mM solution of the ferric complex, [Fe(3,5-Me-BAFP)(NHOMe)], and of the reaction product upon addition of ~1.0 equiv. [DAcFc][$SbCl_6$], measured at 5 K in dichloromethane.

iron(III)-NHOMe precursor is EPR active with an *S* = 5/2 ground state as previously mentioned and upon oxidation the complex is integer spin (*S* = 1, or 2) and EPR silent. The EPR spectra in Figure 2.12 shows that the oxidizes species is ~90% pure.

In summary, chemical oxidation at room temperature results in direct decomposition of $[Fe(3,5\text{-Me-BAFP})(NHOMe)]^+$ to [Fe(3,5-Me-BAFP)(SbF_6)] and no porphyrin oxidation is observed. However, at low temperature we observe a new species that we believe is $[Fe(3,5\text{-Me-BAFP})(NHOMe)]^+$. Preliminary characterization shows that the one-electron oxidation of [Fe(3,5-Me-BAFP)(NHOMe)] results in oxidation of the iron-NHOMe unit, rather than the porphyrin ligand.

2.4 Electronic Structure of the Intermediate *I* Model Complex

In order to gain insight into the oxidation and spin state of the oxidized species, [Fe(3,5-Me-BAFP)(NHOMe)]$^{+}$, we utilized rRaman (rR) spectroscopy. The two ways to describe the electronic structure of this oxidized complex are either an iron(IV)-NHOMe^{-}, or an iron(III)-NHOMe(radical) species. It has been established that some of the core vibrations from the porphyrin co-ligand are sensitive to the oxidation and spin state of the iron center, measured by rRaman.[39,40] For example, the symmetric C-$N_{pyrrole}$ stretching frequency represents the oxidation state marker band (ν_4),[41] depicted in Scheme 2.7. This oxidation state marker band ranges from ~1340 – 1370 cm^{-1}.[42] First we measured the rRaman spectrum of the ferric precursor, [Fe(3,5-Me-BAFP)(NHOMe)], in toluene at 77 K. The ν_4 marker band is found at 1364 cm^{-1} with a small shoulder at 1348 cm^{-1} as shown in Figure 2.13. In the spectrum of [Fe(3,5-Me-BAFP)(NHOMe)]$^{+}$ (formed with ~1 equiv. of [DAcFc][SbF_6]) the 1364 cm^{-1} band is more symmetric with loss of the shoulder observed in the precursor. As a control, we warmed the solution of the oxidized species to room temperature and measured its corresponding rRaman spectrum, which we believe is [Fe(3,5-Me-BAFP)(SbF_6)]. This sample has a split oxidation state marker band at 1347 and 1364 cm^{-1}. The splitting in the oxidation state marker band is a characteristic

Scheme 2.7. Bond vectors showing the C-N stretching frequency mode of the porphyrin core, which is known as the oxidation state marker band (ν_4). Adapted from reference 41.

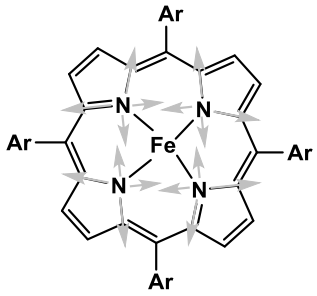

feature of spin-admixed (S = 3/2, 5/2) ground state ferric heme complexes.[43,44] To further confirm this, the spectrum of an independently prepared sample of [Fe(3,5-Me-BAFP)(SbF_6)] in a toluene/DME was measured, which looks very similar to the decomposed product (see Figure 2.22). From these data, we hypothesize that the

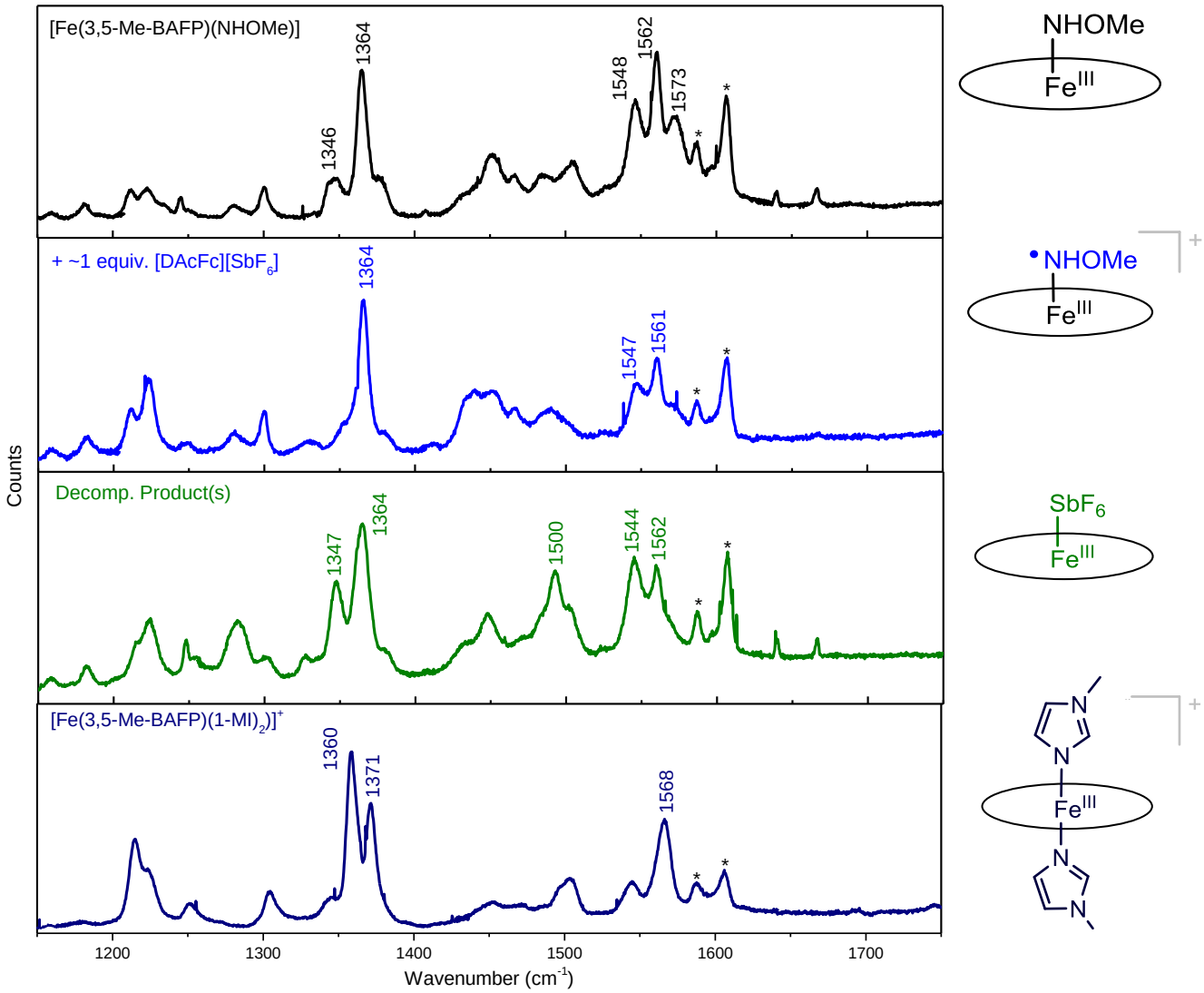

Figure 2.13. rRaman spectra of frozen solutions of [Fe(3,5-Me-BAFP)(NHOMe)] (black), the reaction product upon addition ~1 equiv. [DAcFc][SbF_6] (blue), the reaction product(s) after the solution is warmed to room temperature (green), and a low-spin ferric complex, [Fe(3,5-Me-BAFP)(1-MI)$_2$]SbF_6 (black) in a 5:1 ratio of toluene/DME (power = 28 mW). The * denotes bands from toluene.

oxidized species is a ferric complex with a bound NHOMe(radical) ligand rather than an iron(IV) complex.

Furthermore, we can determine whether the oxidized complex is high- or low-spin based on examination of the spin state marker band (ν_2) that ranges from ~1537 – 1568 cm^{-1}.[42] In the precursor iron(III)-NHOMe complex there is a three band pattern observed at 1548, 1562, and 1573 cm^{-1} (not observed in the toluene/DME blank) with the 1562 cm^{-1} band being the most intense. For comparison, in the high-spin complex [Fe(3,5-Me-BAFP)(Cl)] there is a single band at 1561 cm^{-1}. This implies there may be some distortion of the porphyrin co-ligand in [Fe(3,5-Me-BAFP)(NHOMe)] in solution causing this unusual three band pattern. Nevertheless, in the oxidized complex the 1573 cm^{-1} band disappears while two bands at 1547 and 1561 cm^{-1} appear again, with the 1561 cm^{-1} feature being most intense. For comparison to a low-spin complex, we prepared a solution of the ferric bis-imidazole complex, [Fe(3,5-Me-BAFP)(MI)]SbF_6 (MI = 1-methylimdazole). In this complex the ν_2 band is shifted to 1568 cm^{-1}. This leads us to believe our oxidized complex is a high-spin ferric species.

Along with rRaman studies, Mössbauer spectroscopy was employed to investigate the electronic structure of the oxidized species [Fe(3,5-Me-BAFP)(NHOMe)]$^+$. The Mössbauer spectrum of [Fe(3,5-Me-BAFP)(NHOMe)] is magnetically split and can be fit with δ = 0.50 mm/s and ΔE_Q = -0.413 mm/s (Figure 2.14). The addition of oxidant to [Fe(3,5-Me-BAFP)(NHOMe)] results in a Mössbauer spectrum with a quadrupole doublet with δ = 0.427 mm/s and ΔE_Q =

0.752 mm/s (Figure 2.15). The isomer shift is altered only slightly from that of the precursor, which suggests the oxidized complex is still a high-spin ferric species. Also, the isomer shift values are in good agreement with other high-spin ferric species that range from 0.35 – 45 mm/s, whereas the high-spin iron(IV) species range from 0 – 0.1 mm/s.[45-49]

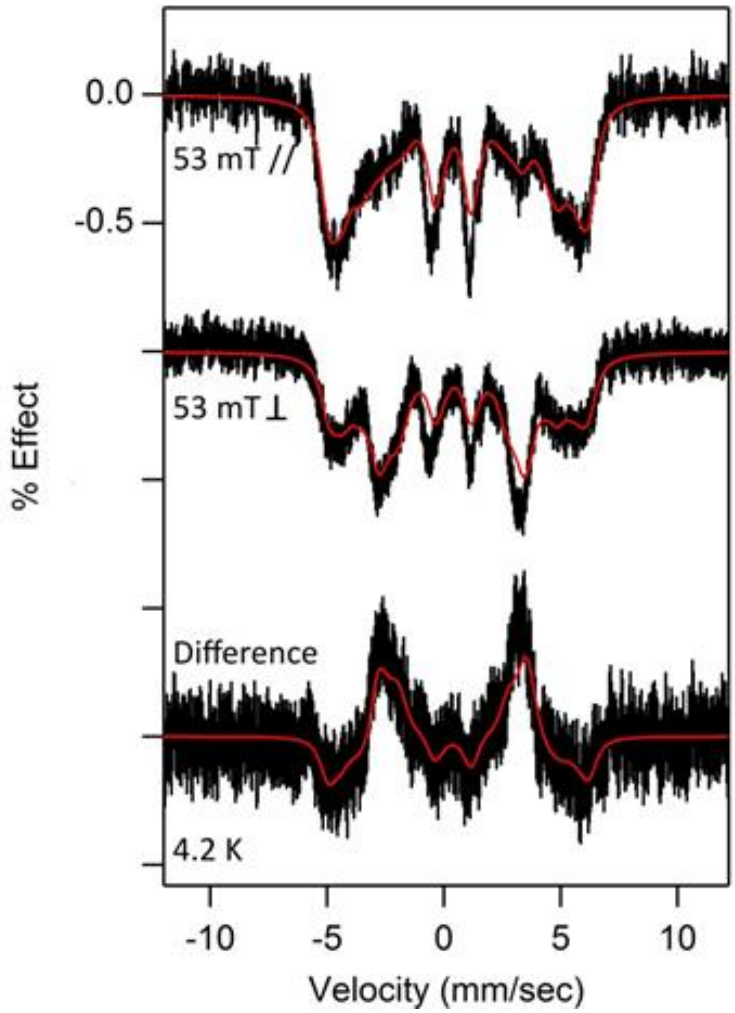

Figure 2.14. 4.2 K low-field (53 mT) Mössbauer spectrum of a ~2 mM solution of [Fe(3,5-Me-BAFP)(NHOMe)] frozen in a 5:1 ratio of toluene/DME, where the γ-beam was applied parallel or perpendicular to the applied magnetic field. Spectra (and the // - ⊥ difference spectrum) are shown as black bars, and the simulations are in red. Simulation parameters used are given as follows: D = 3 cm^{-1}; E/D = 0.05; ΔE_Q) = -0.413 mm/s; δ) = 0.50 mm/s; asymmetry parameter (η) = 0.154; Ax, Ay, Az = -200 kG

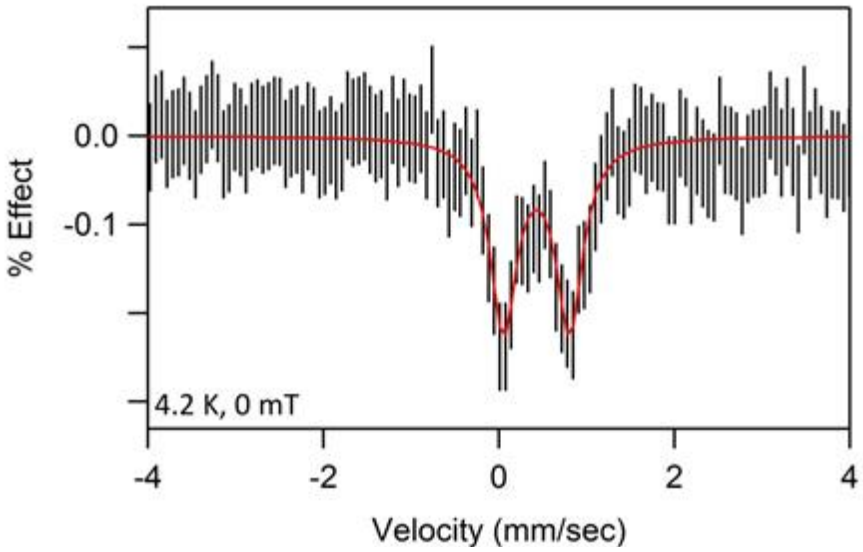

Figure 2.15. 4.2 K Mössbauer spectrum of a ~0.3 mM solution of [Fe(3,5-Me-BAFP)(NHOMe)]$^{+}$ frozen in a 5:1 ratio of toluene/DME in no applied field (black bars), with the corresponding simulation in red. Simulation parameters used are given as follows: δ = 0.427 mm/s; ΔE_Q = 0.752 mm/s. All of the Mössbauer data were collected and analyzed by Dr. Elizabeth Blaesi (Penn State University).

In summary, rRaman and Mössbauer spectroscopy provide insight into the oxidation and spin state of our [Fe(3,5-Me-BAFP)(NHOMe)]$^{+}$ model complex, which we propose is a high-spin iron(III) complex with a bound NHOMe(radical) ligand.

2.5 Reactivity of [Fe(3,5-Me-BAFP)(NHOMe)]$^{+}$ with NO

Finally, we studied the reactivity of the oxidized species, [Fe(3,5-Me-BAFP)(NHOMe)]$^{+}$, with NO to determine if this reaction is catalytically competent in P450nor. First, using *in situ* UV-vis we monitored the reaction of the oxidized species at -80°C with low equivalents of NO gas. This resulted in facile formation

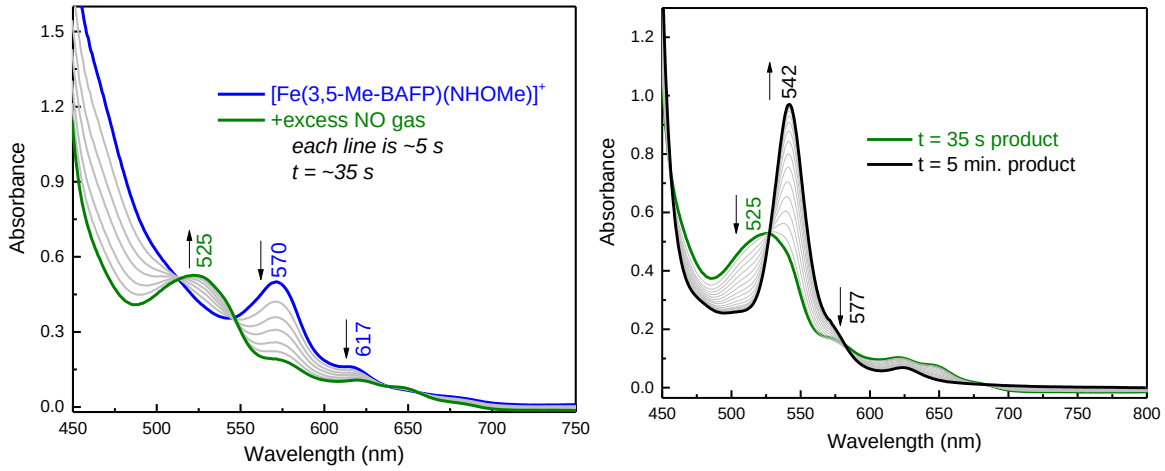

Figure 2.16. Left: *In situ* UV-vis monitoring of the reaction of $[Fe(3,5\text{-}Me\text{-}BAFP)(NHOMe)]^+$ (blue) with excess NO gas in green, which is indicative of $[Fe(3,5\text{-}Me\text{-}BAFP)(SbF_6)]$. Right: Further reaction with NO gas to form a six-coordinate ferric heme-nitrosyl complex, $[Fe(3,5\text{-}Me\text{-}BAFP)(NO)(L)]^+$, where L is a neutral ligand.

(t = ~35 s) of a 525 nm species, indicative of $[Fe(3,5\text{-}Me\text{-}BAFP)(SbF_6)]$, as shown in Figure 2.16 (left). After ~5 minutes at -80°C, the solution turns bright red along with a shift in the Q band from 525 to 542 nm; see Figure 2.16 (left). We propose that this species is a 6-coordinate ferric heme-nitrosyl complex, $[Fe(3,5\text{-}Me\text{-}BAFP)(NO)(L)]^+$, which forms due to excess NO gas in the solution as shown in Scheme 2.8. At this point, we envision that an N-N bond was formed because we see the formation of an iron(III)-SbF_6 complex rather than (1) simple displacement of the NHOMe(radical) ligand, or (2) binding of NO to the open coordinate site at the iron center. If this were the case we would not observe $[Fe(3,5\text{-}Me\text{-}BAFP)(SbF_6)]$, and instead we would observe direct formation of $[Fe(3,5\text{-}Me\text{-}BAFP)(NO)(L)]^+$. Because of this we hypothesized that an N-N bond is formed, resulting in an analogous ferric hyponitrous acid ($N_2O_2H_2$) species as in P450nor. Hyponitrous acid is known to decompose into N_2O and water. In my case, with

Scheme 2.8. Proposed reaction mechanism of the reaction of [Fe(3,5-Me-BAFP)(NHOMe)]$^+$ with low equivalents of NO gas at -80°C.

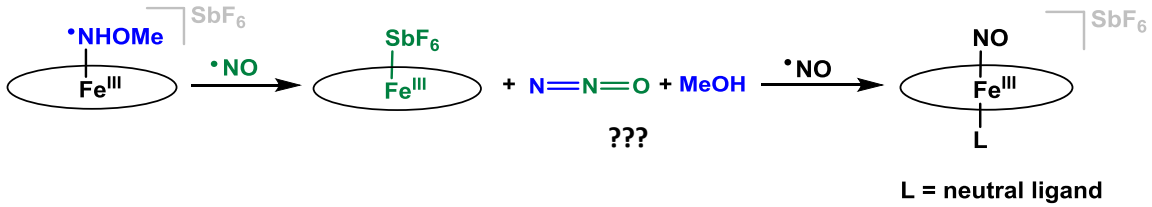

NHOMe(radical) as the ligand (rather than NHOH(radical) in P450nor) I expect to make a ferric N_2O_2MeH type species as the product, and we speculated that it should decompose in the same way (as P450nor) into N_2O, methanol, and a ferric complex. However, head space analysis via cannula transfer from the reaction mixture of [Fe(3,5-Me-BAFP)(NHOMe)]$^+$ with NO gas into a gas IR cell showed that there is no N_2O gas formed; see Figure 2.24 (right). It should be noted that N_2O gas was detectable using our experimental setup and reaction conditions (shown in Figure 2.24). Additionally, we speculated that acid may be necessary to aid in the proton transfer and decomposition of this hyponitrite-like species (N_2O_2MeH) to form N_2O (and methanol). This hypothesis was tested by reaction of [Fe(3,5-Me-BAFP)(NHOMe)]$^+$ with NO gas followed by addition of ~3 equiv. of trifluoroacetic acid, but gas head space analysis again showed no N_2O gas; see Figure 2.24 (left). Despite these results, it is not clear whether an N-N bond is being formed, since there is very little known about the properties of N_2O_2MeH type compounds. This makes it difficult to understand what respective products would ultimately form from an N_2O_2MeH type species. On the other hand, one could imagine that the oxidized species, [Fe(3,5-Me-BAFP)(NHOMe)]$^+$, could oxidize NO to NO^+. However, this can immediately be ruled out since the reduction potential

of our complex (+0.291 V vs. Fc/Fc^+) is not positive enough to oxidize NO (+1 V vs. Fc/Fc+ in dichloromethane).[32] Another feasible reaction that we have ruled out based on gas head space analysis is the production of NO_2 gas, following the reaction:

$$NHOMe(radical) + NO \longrightarrow NO_2 + MeOH$$

For future studies I believe that a ^{13}C-labeled hydroxylamide ligand and ^{15}NO gas could provide great insight into the nature of the N-containing products. We plan to synthesize a ^{13}C-labeled $NHOMe^-$ ligand to track the methyl group with ^1H- and ^{13}C-NMR spectroscopy. The reaction of $[Fe(3,5\text{-Me-BAFP})(NHOMe)]^+$ with ^{15}NO gas would indicate if any dinitrogen was formed by GC-MS.

In summary, we generated $[Fe(3,5\text{-Me-BAFP})(NHOMe)]^+$ as a chemical model for Intermediate *I* in P450nor and, using spectroscopy, determined the electronic structure of this complex, which corresponds to an iron(III)-NHOMe(radical) species. The oxidized species reacts with NO to make $[Fe(3,5\text{-Me-BAFP})(SbF_6)]$, which implies N-N bond formation, but we so far we have been unable to identify the N-containing product(s).

2.6 Experimental Section

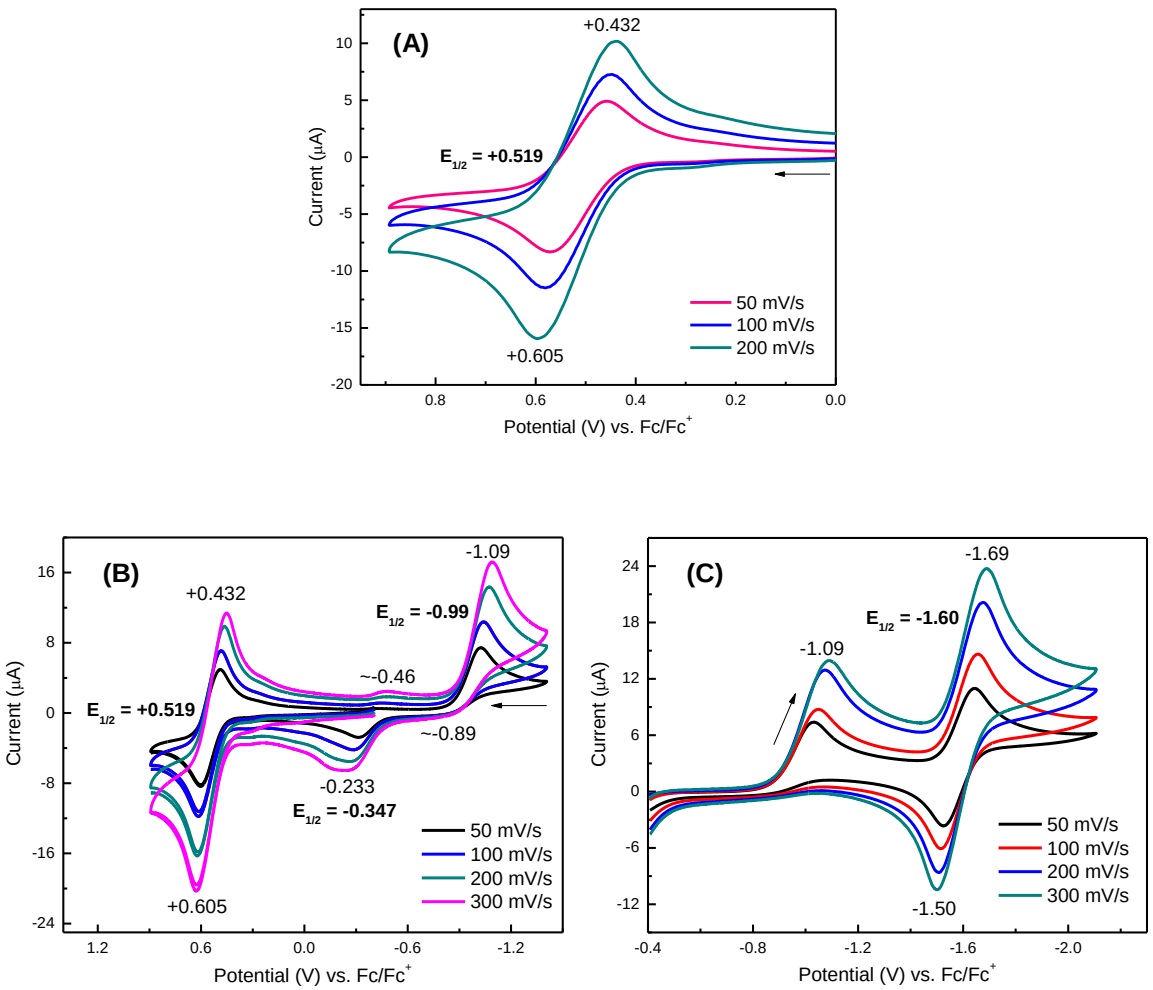

Figure 2.17. CVs of a ~3 mM solution of [Fe(3,5-Me-BAFP)(Cl)] in 1,2-dichloroethane where the working electrode is glassy carbon and the counter electrode is platinum with a Ag wire pseudo-reference at room temperature.

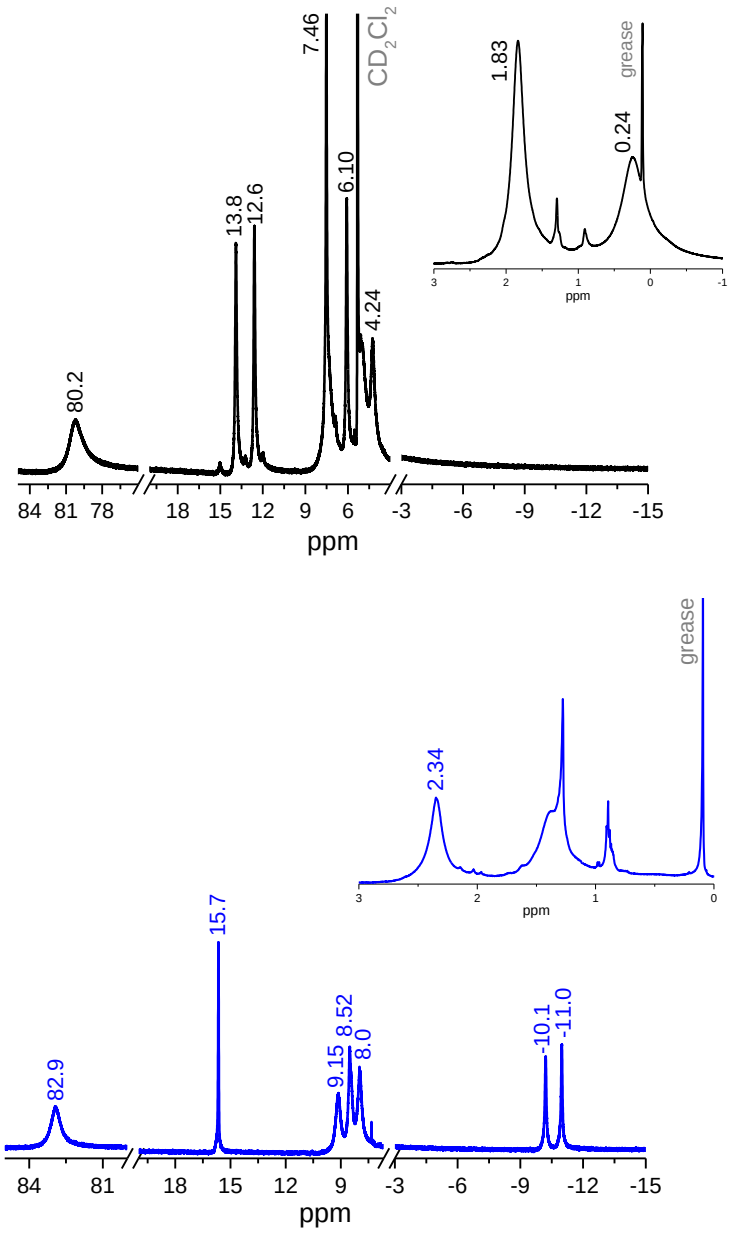

Figure 2.18. Top: ^{1}H-NMR spectra of the ferric chloride complex, [Fe(3,5-Me-BAFP)(Cl)], measured in CD_2Cl_2 with the line width set to 0.3 Hz. Bottom: The reaction product upon addition of ~1.0 equiv. $[N(C_6H_4Br\text{-}4)_3][SbCl_6]$ in deuterated dichloromethane to form $[Fe(3,5\text{-}Me\text{-}BAFP)(Cl)]^+$.

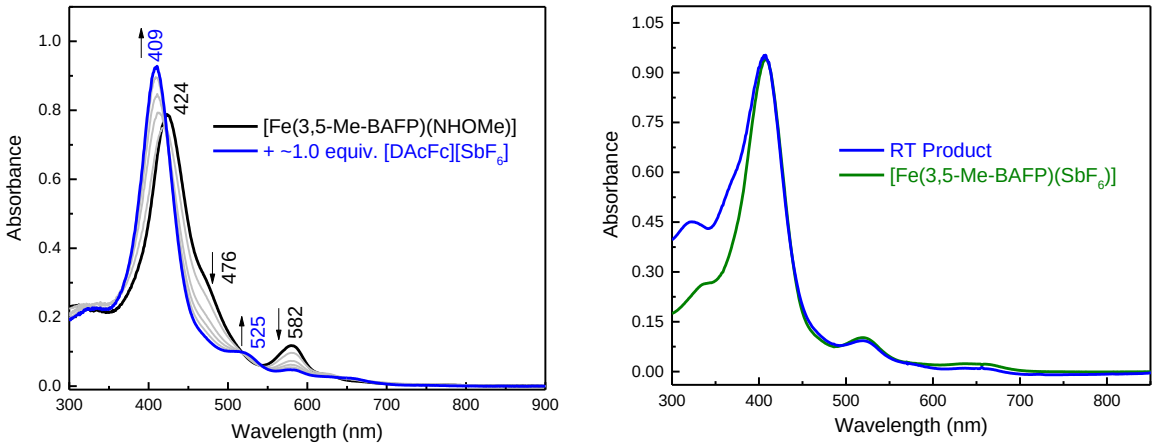

Figure 2.19. Left: UV-vis spectra of a solution of [Fe(3,5-Me-BAFP)(NHOMe)] (black) and the reaction product upon addition of ~1 equiv. [DAcFc][SbF_6] in toluene (blue). Note that the oxidant is dissolved in DME. Right: Comparison of the reaction product (blue) and [Fe(3,5-Me-BAFP)(SbF_6)] in toluene (green). All spectra were recorded at room temperature.

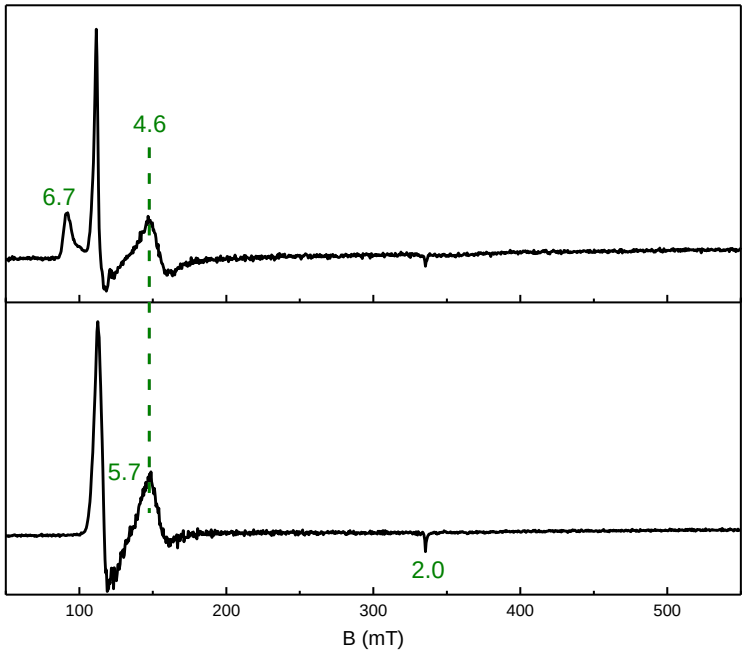

Figure 2.20. Top: EPR spectrum of the reaction of [Fe(3,5-Me-BAFP)(NHOMe)] with ~1 equiv. [DAcFc][SbF_6] in a 5:1 toluene/DME mixture at room temperature. Bottom: EPR spectrum of [Fe(3,5-Me-BAFP)(SbF_6)] in a 5:1 toluene/DME mixture. Both EPR spectra were taken at 5 K.

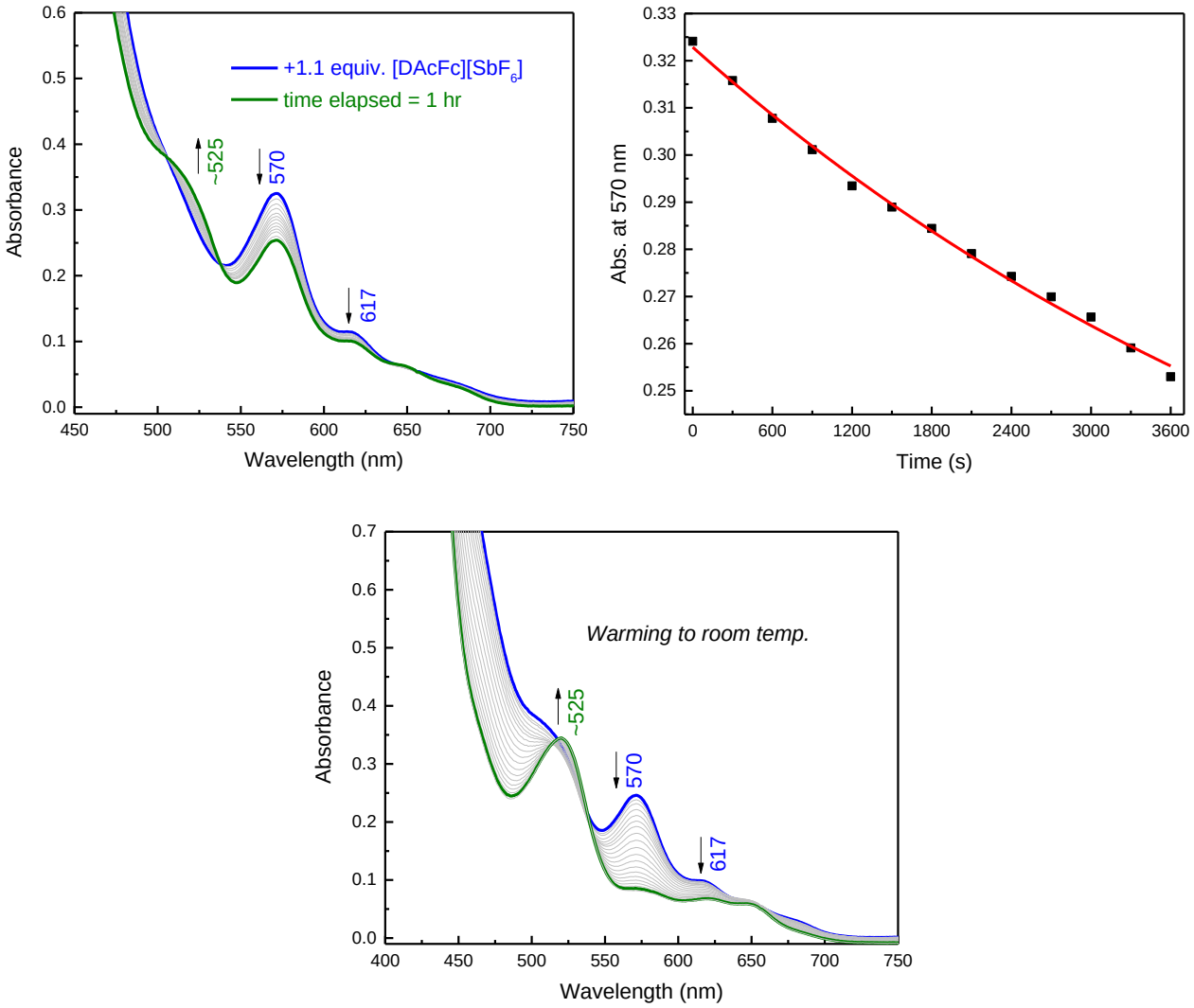

Figure 2.21. Top left: *In situ* UV-vis monitoring of the decomposition of [Fe(3,5-Me-BAFP)(NHOMe)]$^{+}$ (blue) over a one hour time period (green). Top right: Fit of the UV-vis band at 570 nm over time. The data are fit to a single exponential function with $k_{obs} = 1.7 \times 10^{-4}$ s^{-1} ($t_{1/2}$ = 68 minutes). Bottom: *In situ* UV-vis monitoring of the warming of the oxidized species (shown in top left graph; blue) over a 10 minute time period to the final product [Fe(3,5-Me-BAFP)(SbF_6)] (green).

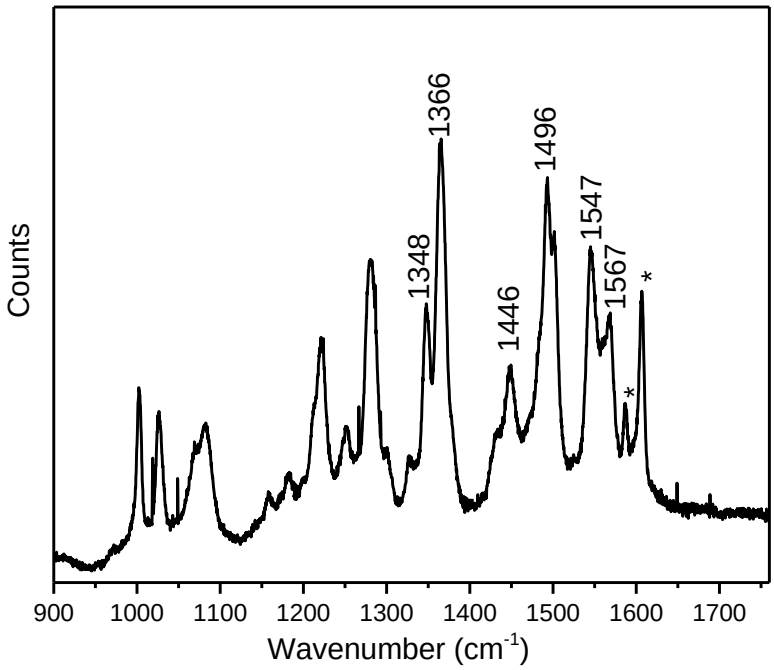

Figure 2.22. rRaman spectrum of a frozen solution of 0.94 mM of [Fe(3,5-Me-BAFP)(SbF_6)] in a 5:1 toluene/DME mixture measured at 77 K (power = 30 mW). The * denotes bands from toluene.

Synthesis

All reactions were performed under insert conditions using Schlenk techniques. Preparation and handling of air sensitive materials was carried out under a nitrogen atmosphere in an MBraun glovebox equipped with a circulating purifier (O_2, H_2O < 0.1 ppm). Nitric oxide (Cryogenic Gases Inc., 99.5%) was purified by passage through an ascarite II column (NaOH on silica) followed by a cold trap at -80°C to remove higher order nitrogen oxide impurities. All solvents (including deuterated solvents) and 1-methylimidazole (MI) were distilled from CaH_2 under nitrogen, then degassed via five freeze-pump-thaw cycles. Tetrabutylammonium hexafluorophosphate was recrystallized from ethanol. The purified solvents were stored over appropriate sized activated molecular sieves in the glovebox until used. 1,1'-diacetylferrocene was purchased from Fisher Scientific, tris(4-bromophenyl)ammoniumyl hexachloroantimonate was purchased from Sigma Aldrich, and O-Methylhydoxylamine and O-Benzylhydroxylamine hydrochloride was purchased from TCI America. All of these materials were used without further purification. Deprotonation of O-Methylhydroxylamine to the corresponding lithium salt, Li[NHOMe], was carried out as previously reported.[22] [Fe(3,5-Me-BAFP)(Cl)],[7] [Fe(3,5-Me-BAFP)(X)][6] where X = PF_6^- or SbF_6^-, and O-Benzylhydroxylamine[50] were synthesized as previously reported. ^{57}Fe complexes were synthesized in the same way as the natural abundance complexes using the $^{57}FeCl_2$ dimethanol salt as the iron source.

O-Methylhydroxylamine: 11.2 g O-Methylhydroxylamine hydrochloride (0.134 mmol) was dissolved in 95 mL sodium hydroxide solution (5M). Then, the product O-Methylhydroxylamine was distilled off under nitrogen as a clear oil. Yield: 4.53 g (0.096 mol, 72%) ^{1}H-NMR ($CDCl_3$, 400 MHz): δ: 3.554 (s, 3H); 5.437 (b, 2H).

Synthesis of [Fe(3,5-Me-BAFP)(ClO_4)]. 286 mg [Fe(3,5-Me-BAFP)(Cl)] (0.172 mmol) and 36 mg silver perchlorate (0.172 mmol) were dissolved in 17 mL 2-methyltetrahydrofuran. The reaction mixture was refluxed for 1 hour and filtered hot through a fine frit. The filtrate was layered with 30 mL hexanes and allowed to precipitate at -30^{o}C. After 20 hours, the resulting purple crystalline material was filtered off and vacuum dried for 4 hours. Yield: 185 mg (62%). UV-vis (CH_2Cl_2): 405, 524, 593, 623 nm. UV-vis (toluene): 416, 515, 597, 661 nm. IR (KBr): v(ClO_4): 1096, 623 cm^{-1}.

Synthesis of [Fe(3,5-Me-BAFP)(PF_6)]. 695 mg [Fe(3,5-Me-BAFP)(Cl)] (0.417 mmol) and 106 mg silver hexafluorophosphate (0.419 mmol) were dissolved in 30 mL 2-methyltetrahydrofuran. The reaction mixture was refluxed for 2 hours and filtered through a fine frit. The filtrate was layered with 90 mL hexanes and allowed to precipitate at -30 ^{o}C. After 24 hours, the resulting purple crystalline solid was filtered off and vacuum dried overnight. Yield: 580 mg (78%). UV-vis (toluene): 414, 517, 596, 663 nm. UV-vis (2-Me-THF): 401, 523, 589, 655 nm. IR (KBr): v(PF_6): 842, 557 cm^{-1}. ^{19}F{^{1}H} NMR ($CDCl_3$): -81.17 (d, J_{PF} = 713 Hz).

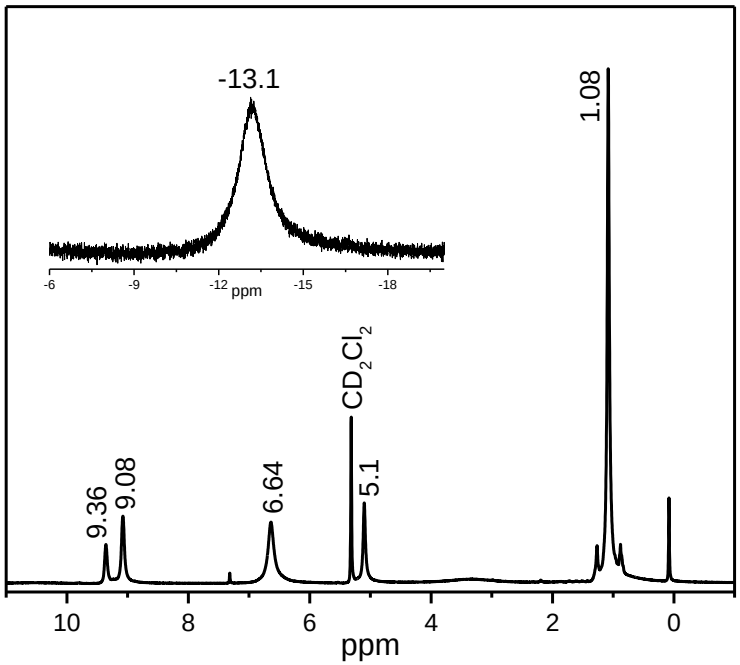

Figure 2.23. ^{1}H-NMR spectra of [Fe(3,5-Me-BAFP)(SbF_6)] recorded in CD_2Cl_2 with the line width set to 1 Hz. The inset graph shows the β-pyrrole hydrogens of the porphyrin co-ligand.

Crystallization of [Fe(3,5-Me-BAFP)(NH_3)$_2$]. In a 5 mm diameter glass tube, 5 mg of [Fe(3,5-Me-BAFP)(ClO_4)] and ~5 equivalents O-benzylhydroxylamine were dissolved in 0.2 mL toluene. The mixture was layered carefully with 1.5 mL hexanes and closed with a rubber septum. After 5 days, brown prisms suitable for X-ray analysis were collected.

Synthesis of [Fe(3,5-Me-BAFP)(NHOMe)]: The same procedure was followed when using the precursor [Fe(3,5-Me-BAFP)(X)] where X = ClO_4^- or SbF_6^-. Under an inert atmosphere, 244 mg [Fe(3,5-Me-BAFP)(PF_6)] (0.137 mmol) was dissolved

in 5 mL dry 2-methyltetrahydrofuran (the reaction also works in toluene). Then, 22 mg Li[NHOMe] (0.75 mmol) was added to the solution and the reaction was allowed to stir until it looked complete by UV-vis spectroscopy. Based on the UV-vis conversion, more ligand can be added (typically up to ~5 equiv.) due to the poor solubility of the lithium salt. Note: You can ensure the reaction is complete by evaporation of the solvent under vacuum, and then measure the ^{1}H-NMR spectrum of the crude product to look for the protons from the precursor complex. Typical reaction times are ~24 hours. The solution was filtered through a 0.2 μM PTFE filter, layered with hexanes, and allowed to precipitate in the -33°C freezer. After two days, the reaction was filtered through a frit to give a dark purple powder. Yield: 185 mg (0.110 mmol, 81%) UV-vis (2-Me-THF): 421, 582, 631 nm. UV-vis (toluene): 424, 582, 632 nm. ^{1}H-NMR (CD_2Cl_2, 400 MHz): $\delta = -0.887$ (b); -3.77 (b); 1.843 (b); 6.172 (b); 6.539 (b); 7.558 (b); 10.285 (b); 11.074 (b); 79.41 (b). Anal. Calcd. for $C_{109}H_{96}FeN_5O$: C, 78.12; H, 5.77; N, 4.18. Found: C, 77.05; H, 5.87; N, 3.21.

Brown plates suitable for X-ray diffraction were grown by layering a concentrated 2-Me-THF solution of [Fe(3,5-Me-BAFP)(NHOMe)] in a 5 mm diameter glass tube with penates at room temperature for 3 days.

Synthesis of [Fe(η^5-$C_5H_4COMe)_2$][SbF_6]: In the glovebox, 72 mg (0.267 mmol) 1,1'-diacetylferrocene and 118.6 mg (0.262 mmol) [thianthrene][SbF_6] were dissolved in 5 mL dichloromethane, which caused a light blue solid to precipitate

from the reaction mixture. The reaction was allowed to stir for ~30 minutes and at this point was vacuum filtered through a frit to give a teal blue powder. This powder was washed with dichloromethane and hexanes, and then stored in the glovebox freezer. Yield: 59 mg (0.117 mmol, 44%) UV-vis (CH_2Cl_2): 655 nm. Anal. Calcd. for $C_{14}H_{14}F_6FeO_2Sb$: C, 33.24; H, 2.79; N, 0.00. Found: C, 33.28; H, 2.71; N, 0.00. No peaks from the oxidant are observed in the ^{1}H-NMR spectrum. $^{19}F\{^1H\}$ NMR (471 MHz): –123.96 (m). IR (KBr): ν(CO) = 1701 cm^{-1}, $\nu(SbF_6)$ = 659 cm^{-1}.

Chemical Oxidation of [Fe(3,5-Me-BAFP)(Cl)]: Under an inert atmosphere, 7.2 mg [Fe(3,5-Me-BAFP)(Cl)] (0.0043 mmol) was dissolved in 2 mL dry dichloromethane. The solution was added to 5.6 mg of solid $[N(C_6H_4Br\text{-}4)_3][SbCl_6]$ (0.0068 mmol) and agitated until all of the solid had dissolved, forming [Fe(3,5-Me-BAFP)(Cl)]$SbCl_6$. Typical reaction concentrations were 1 – 2 mM. UV-vis (CH_2Cl_2): 373, 411, 568, 634 nm. ^{1}H-NMR (CD_2Cl_2, 500 MHz): $\delta = -10.22$ (s); -11.00 (s); 2.34 (b); 7.97 (b); 8.49 (b); 9.11 (b); 15.642 (s); 83.08 (b).

Chemical Oxidation of [Fe(3,5-Me-BAFP)(NHOMe)]: Typical concentrations of [Fe(3,5-Me-BAFP)(NHOMe)] used were from ~5 μM – 0.3 mM. Under an inert atmosphere, the stirring dry toluene solution of [Fe(3,5-Me-BAFP)(NHOMe)] in a custom designed flask fitted with a UV-vis immersion probe (with its metal cover) was cooled to -80°C in a dry ice/hexanes bath. The syringes, needles, and oxidant solution were pre-chilled in dry ice. The oxidant $[DAcFc][SbF_6]$ was dissolved in

cold dimethoxyethane (typical concentrations were ~1 mM), and slowly added to the [Fe(3,5-Me-BAFP)(NHOMe)] toluene solution. The reaction completion to the oxidized species, $[Fe(3,5\text{-}Me\text{-}BAFP)(NHOMe)]^{+}$, was monitored by *in situ* UV-vis spectroscopy measurements. Then, this solution was transferred to precooled quartz tubes (in a dewar with a dry ice/hexanes bath) for EPR and rRaman measurements. For Mössbauer spectroscopy, the cups were cooled inside of a custom designed aluminum block that contained dry ice.

N_2O detection. Under an inset atmosphere, a stirring dry toluene solution of [Fe(3,5-Me-BAFP)(NHOMe)] in a custom designed air-tight flask fitted with an *in situ* UV-vis immersion probe (without its metal cover) was cooled to -80°C in a dry ice/hexanes bath. The NO gas (from a bomb flask) was added to a solution of $[Fe(3,5\text{-}Me\text{-}BAFP)(NHOMe)]^{+}$ at -80°C via syringe. The reaction progress was monitored using *in situ* UV-vis (coupled to the kinetics program settings). Once the spectral features of the oxidized species, $[Fe(3.5\text{-}Me\text{-}BAFP)(NHOMe)]^{+}$, had disappeared (typical reaction times are less than 1 min.; I usually waited for ~5 minutes before the next step) the solution was warmed to room temperature for 30 minutes. At this point, the UV-vis looks like a six-coordinate ferric heme-nitrosyl complex. The headspace of the flask was pulled via cannula into a gas IR cell.

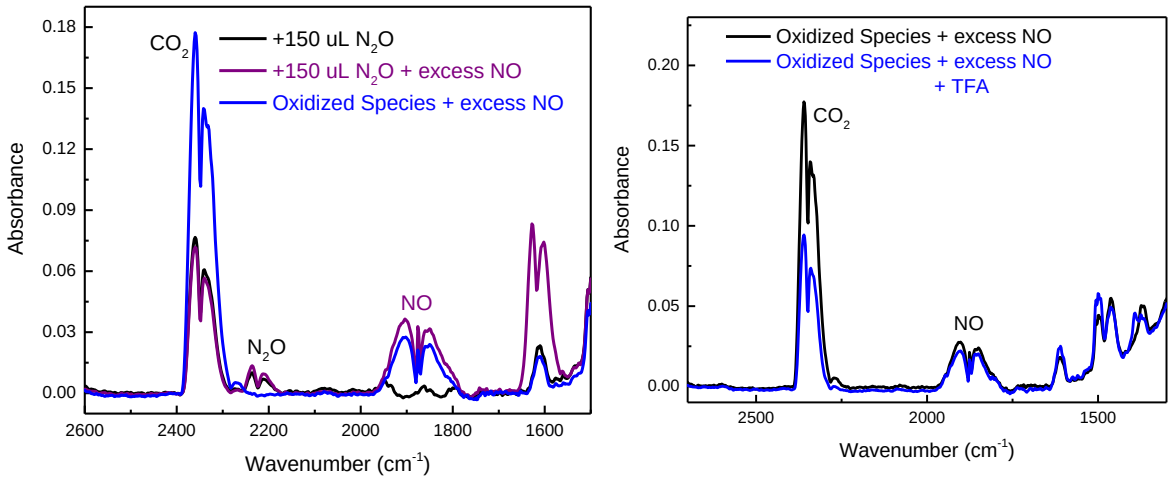

Figure 2.24. Left: Gas IR spectra of the reaction of a solution of 0.28 mM [Fe(3,5-Me-BAFP)(NHOMe)]$^{+}$ with excess NO gas in a 5:1 toluene/DME mixture (blue) and control reactions under same conditions with 150 µL N_2O (black) and NO gas (purple) added in a 5:1 toluene/DME mixture. The headspace of the flask was transferred to a gas IR cell at room temperature. Right: Comparison of the gas IR spectra of 0.28 mM [Fe(3,5-Me-BAFP)(NHOMe)] with excess NO gas in a 5:1 toluene/DME mixture (black) and with the addition of 3 equiv. trifluoroacetic acid. 150 µL of N_2O is a 100% N_2O yield

Analysis of NH_3. The reagents for Russell's hypochlorite-phenol method for NH_3 quantification were prepared as previously reported.[51] The assay was carried out using the modified procedure by Ryan and co-workers described below.[52] A calibration curve was generated by assaying NH_4Cl standards and measuring the absorbance of indophenolate at 630 nm by UV-visible spectroscopy (see Figure S1). Since the assay is normally carried out in water, but [Fe(3,5-Me-BAFP)$(NH_3)_2$] is not water-soluble, the assay was conducted in a mixture of toluene and water. To ensure that toluene does not interfere with the assay, NH_4Cl standards were spiked with 0.5 mL of toluene and a calibration curve was generated for these modified conditions. As shown in Figure 2.23, toluene does not affect the assay.

[Fe(3,5-Me-BAFP)(NH_3)$_2$] was prepared by the reaction of 50 mg of [Fe(3,5-Me-BAFP)(PF_6)] and ~10 equivalents of NH_2OBn in 3 mL of toluene by stirring the reaction mixture for ~2 hours in the glovebox. The solution was then carefully layered with 9 mL of hexanes and allowed to precipitate at -30 °C. The next day, the resulting dark red powder was filtered off through a fine frit. The red powder was washed with hexanes to remove any remaining NH_2OBn. NH_3 determination was carried out with bulk material of [Fe(3,5-Me-BAFP)(NH_3)$_2$] by the following method. In a typical experiment, 5 mg of [Fe(3,5-Me-BAFP)(NH_3)$_2$] was dissolved in 0.5 mL of toluene in a round bottom flask, which was sealed with a septum in the glovebox. Then the solution was brought out of the glovebox and stirred on ice. In the next step, 3.3 mL 0.01 M HCl, 250 µL of 0.003 M manganese chloride tetrahydrate solution, 0.25 mL hypochlorite solution (2.1 M), and 0.5 mL phenol solution (3.0 M) were added via syringe resulting in the formation of a dark blue solution. Next, the solution (still stirring) was placed in a hot water bath for ~5 minutes. Once cooled to room temperature, an aliquot of the aqueous layer was removed and the absorbance at 630 nm was measured. The concentration of NH_3 was calculated using the calibration curve shown below in Figure 2.23. The bulk material was assayed three times.

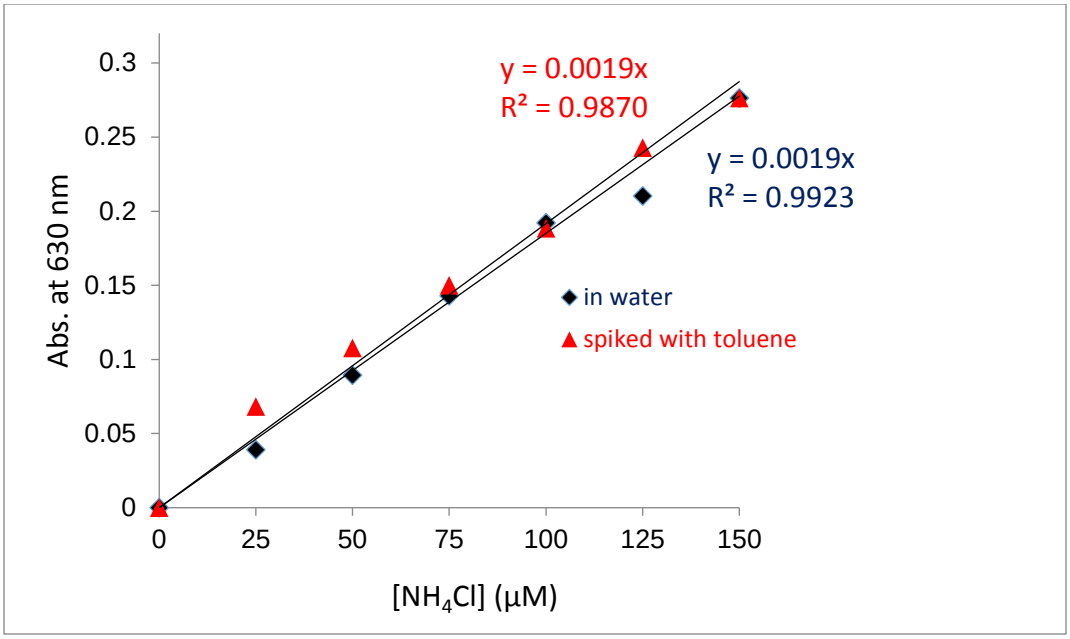

Figure 2.25. Calibration curve of absorbance versus NH_4Cl concentration (µM) in water (blue) and water-toluene mixtures (red).

Table 2.3 NH_3 concentrations (mM) determined from the assay of the bulk material of [Fe(3,5-Me-BAFP)$(NH_3)_2$]. The theoretical [NH_3] is based on the amount of [Fe(3,5-Me-BAFP)$(NH_3)_2$] used in the assay.

Theoretical [NH_3] / mM	Detected [NH_3] / mM	Equiv. of NH_3
6.48	6.39	1.97
6.73	6.53	1.94
8.42	8.25	1.96

Physical Methods

Infrared spectra were obtained from KBr disks on Perkin-Elmer BX spectrometer at room temperature. Electronic absorption spectra were measured using an Analytical Jena Specord S600 instrument at room temperature. Electron paramagnetic resonance spectra were recorded on a Bruker X-band EMX spectrometer equipped with Oxford Instruments liquid nitrogen and helium

cryostats. EPR spectra were typically obtained on frozen solutions using 20 mW microwave power and 100 kHz field modulation with the amplitude set to 1 G. Sample concentrations were ~1 – 3 mM. Proton NMR spectra were recorded on a Varian MR 400 MHz instrument or a Varian NMRS 500 MHz spectrometer at room temperature. *In situ* UV-vis measurements were taken with a Hellma quartz immersion problem with a 10 mm path length. Cyclic voltammograms were obtained using a CH insruments CHI600E electrochemical workstation with a three component electrochemical cell consisting of a glassy carbon working electrode, platinum counter electrode, and silver wire pseudo-reference electrode. All potentials were corrected to Fc/Fc^+. UV-vis spectroelecrochemical measurements were performed using custom-built thin layer electrochemical cells as previously described.[7] All electrochemical and spectroelectrochemical measurements were carried out in the presence of 0.1 M tetrabutylammonium hexafluorophosphate. Nuclear Resonance Vibrational spectroscopy (NRVS) was carried out as previously described[53] at beamline 3-ID-XOR at the Advanced Photon Source (APS) at Argonne National Laboratory. This beamline provides about 2.5 x 10^9 photons/sec in ~1 meV bandwidth (8 cm^{-1}) at 14.4125 keV in a 0.5 mm (vertical) x 0.5 mm (horizontal) spot. Samples were loaded into 4 x 7 x 1 mm copper cells. The final spectra represent averages of 4 scans. The program Phoenix was used to convert the NRVS raw data to the Vibrational Density of States (VDOS).[54,55] The resonance Raman measurements were performed using the 413.13 nm excitation line from a Kr^+ ion laser (Spectra Physics Beam Lok 2060-RS). Raman spectra were recorded at 77 K using an Acton two-stage TriVista 555 monochromator

connected to a liquid nitrogen cooled CCD camera (Princeton instruments Spec-10:400B/LN). The total exposure time of the samples to the laser radiation was 3 minutes using 1-2 accumulations, and typical laser powers were in the 20 – 30 mW range.

Mössbauer spectroscopy: Mössbauer spectra were recorded on a spectrometer from WEB Research, equipped with a Janis SVT-400 variable-temperature cryostat. The external magnetic field (53 mT) was absent, parallel, or perpendicular to the γ-beam. All isomer shifts are quoted relative to the centroid of the spectrum of α-Fe at room temperature. Simulation of the Mössbauer spectra was conducted in the WMOSS spectral analysis package, using the spin-Hamiltonian shown in the following equation:

$$\mathbf{H} = \beta \mathbf{S} \cdot \mathbf{g} \cdot \mathbf{B} + \mathrm{D}\left(\mathbf{S_z^2} - \frac{\mathrm{S}(\mathrm{S}+1)}{3}\right) + \mathrm{E}\left(\mathbf{S_x^2} - \mathbf{S_y^2}\right) + \frac{\mathbf{eQV_{zz}}}{4}\left[\mathrm{I_z^2} - \frac{\mathrm{I}(\mathrm{I}+1)}{3} + \frac{\eta}{3}\left(\mathrm{I_x^2} - \mathrm{I_y^2}\right)\right] + \mathbf{S} \cdot \mathbf{A} \cdot \mathbf{I} - \mathrm{g_n}\beta_\mathrm{n}\mathbf{B} \cdot \mathbf{I}$$

The first three terms represent the electron Zeeman and the zero field splitting (ZFS) of the spin-spin ground state, the fourth term describes the interaction between the nuclear quadrupole moment and the electric field gradient, the fifth term represents the magnetic hyperfine interaction of the electronic spin with the ^{57}Fe nucleus, and the last term describes the ^{57}Fe nuclear Zeeman interaction.

Crystal Structure Determination. A brown prism of [Fe(3,5-Me-BAFP)(NH_3)$_2$] of dimensions 0.18 x 0.09 x 0.09 mm was mounted on a Rigaku AFC10K Saturn 944+ CCD-based X-ray diffractometer equipped with a low temperature device and Micromax-007HF Cu-target micro-focus rotating anode (λ = 1.54187 Å) operated at 1.2 kW power (40 kV, 30 mA). The X-ray intensities were measured at 85 K with the detector placed at a distance 42.00 mm from the crystal. A total of 3803 images were collected with an oscillation width of 1.0° in ω. The exposure time was 5 sec. for the low angle images, 15 sec. for high angle. The integration of the data yielded a total of 245071 reflections to a maximum 2θ value of 136.48° of which 16890 were independent and 15237 were greater than 2σ(I). The final cell constants were based on the xyz centroids 117456 reflections above 10σ(I). Analysis of the data showed negligible decay during data collection; the data were processed with CrystalClear 2.0 and corrected for absorption. The structure was solved and refined with the Bruker SHELXTL (version 2008/4) software package,[56] using the space group P2(1)/c with Z = 4 for the formula $C_{108}H_{98}N_6O_8FeC_7H_8$. Full matrix least-squares refinement based on F^2 converged at R1 = 0.0520 and wR2 = 0.1503 [based on I > 2σ(I)], R1 = 0.0559 and wR2 = 0.1537 for all data.

[Fe(3,5-Me-BAFP)(NHOMe)]: A brown plate of [Fe(3,5-Me-BAFP)(NHOMe)] of dimensions 0.22 x 0.15 x 0.02 mm was mounted on a Rigaku AFC10K Saturn 944+ CCD-based X-ray diffractometer equipped with a low temperature device and Micromax-007HF Cu-target micro-focus rotating anode (λ = 1.54187 Å) operated

at 1.2 kW power (40 kV, 30 mA). The X-ray intensities were measured at 85 K with the detector placed at a distance 42.00 mm from the crystal. A total of 3461 images were collected with an oscillation width of 1.0° in ω. The exposure time was 5 sec. for the low angle images, 20 sec. for high angle. The integration of the data yielded a total of 58575 reflections to a maximum 2θ value of 136.48° of which 8776 were independent and 6733 were greater than $2\sigma(I)$. The final cell constants were based on the xyz centroids 23732 reflections above 10 $\sigma(I)$. Analysis of the data showed negligible decay during data collection; the data were processed with CrystalClear 2.0 and corrected for absorption. The structure was solved and refined with the Bruker SHELXTL (version 2008/4) software package,[56] using the space group P1bar with Z = 1 for the formula $C_{110}H_{100}N_6O_{10}Fe$. All non-hydrogen atoms were refined anisotropically with the hydrogen atoms placed in idealized positions. Full matrix least-squares refinement based on F^2 converged at R1 = 0.1059 and wR2 = 0.3008 [based on I > 2 $\sigma(I)$], R1 = 0.1192 and wR2 = 0.3178 for all data.

DFT calculations: The structure of [Fe(3,5-Me-BAFP)(NHOMe)] was fully optimized for the sextet (*S* = 5/2) ground state of this complex, using the BP86 functional[57,58] and the TZVP basis set.[59,60] Vibrational frequencies calculated for the [Fe(3,5-Me-BAFP)(NHOMe)] structure showed no imaginary frequencies. In all calculations, convergence was reached when the relative change in the density matrix between subsequent iterations was less than 1×10^{-8}. All of these calculations were performed using the program package Gaussian 09.[61]

2.7 References

1. Nast, R.; Föppl, I. *Z. Anorg. Allg. Chem.* **1950**, *263*, 310-315.
2. Bonner, F. T.; Dzelzkalns, L. S.; Bonucci, J. A. *Inorg. Chem.* **1978**, *17*, 2487-2494.
3. Bari, S. E.; Amorebieta, V. T.; Gutiérrez, M. M.; Olabe, J. A.; Doctorovich, F. *J. Inorg. Biochem.* **2010**, *104*, 30-36.
4. Choi, I.-K.; Liu, Y.; Wei, Z.; Ryan, M. D. *Inorg. Chem.* **1997**, *36*, 3113-3118.
5. Feng, D. W.; Ryan, M. D. *Inorg. Chem.* **1987**, *26*, 2480-2483.
6. McQuarters, A. B.; Goodrich, L. E.; Goodrich, C. M.; Lehnert, N. *Z. Anorg. Allg. Chem.* **2013**, *639*, 1520-1526.
7. Goodrich, L. E.; Roy, S.; Alp, E. E.; Zhao, J.; Hu, M. Y.; Lehnert, N. *Inorg. Chem.* **2013**, *52*, 7766-7780.
8. Zheng, S.; Berto, T. C.; Dahl, E. W.; Hoffman, M. B.; Speelman, A. L.; Lehnert, N. *J. Am. Chem. Soc.* **2013**, *135*, 4902-4905.
9. Evans, D. R.; Reed, C. A. *J. Am. Chem. Soc.* **2000**, *122*, 4660-4667.
10. Blumberg, W. E. In *Methods Enzymol.*; Academic Press: 1981; Vol. Volume 76, p 312-329.
11. Reed, C. A.; Mashiko, T.; Bentley, S. P.; Kastner, M. E.; Scheidt, W. R.; Spartalian, K.; Lang, G. *J. Am. Chem. Soc.* **1979**, *101*, 2948-2958.
12. Kintner, E. T.; Dawson, J. H. *Inorg. Chem.* **1991**, *30*, 4892-4897.
13. Scheidt, W. R.; Reed, C. A. *Chem. Rev.* **1981**, *81*, 543-555.
14. Barkigia, K. M.; Palacio, M.; Sun, Y.; Nogues, M.; Renner, M. W.; Varret, F.; Battioni, P.; Mansuy, D.; Fajer, J. *Inorg. Chem.* **2002**, *41*, 5647-5649.
15. Kastner, M. E.; Scheidt, W. R.; Mashiko, T.; Reed, C. A. *J. Am. Chem. Soc.* **1978**, *100*, 666-667.
16. Patra, R.; Chaudhary, A.; Ghosh, S. K.; Rath, S. P. *Inorg. Chem.* **2008**, *47*, 8324-8335.
17. La, T.; Miskelly, G. M.; Bau, R. *Inorg. Chem.* **1997**, *36*, 5321-5328.
18. Hijazi, I.; Roisnel, T.; Even-Hernandez, P.; Geneste, F.; Cador, O.; Guizouarn, T.; Boitrel, B. *Inorg. Chem.* **2010**, *49*, 7536-7544.
19. Korber, F. C. F.; Smith, J. R. L.; Prince, S.; Rizkallah, P.; Reynolds, C. D.; Shawcross, D. R. *J. Chem. Soc., Dalton Trans.* **1991**, 3291-3294.
20. Munro, O. Q.; Madlala, P. S.; Warby, R. A. F.; Seda, T. B.; Hearne, G. *Inorg. Chem.* **1999**, *38*, 4724-4736.
21. Kim, Y. O.; Goff, H. M. *Inorg. Chem.* **1990**, *29*, 3907-3908.
22. Beak, P.; Basha, A.; Kokko, B.; Loo, D. *J. Am. Chem. Soc.* **1986**, *108*, 6016-6023.
23. Quinn, R.; Nappa, M.; Valentine, J. S. *J. Am. Chem. Soc.* **1982**, *104*, 2588-2595.
24. Scheidt, W. R.; Durbin, S. M.; Sage, J. T. *J. Inorg. Biochem.* **2005**, *99*, 60-71.

25. Rai, B. K.; Durbin, S. M.; Prohofsky, E. W.; Timothy Sage, J.; Ellison, M. K.; Robert Scheidt, W.; Sturhahn, W.; Ercan Alp, E. *Physical Review E* **2002**, *66*, 051904.
26. Zhang, Y.; Hallows, W. A.; Ryan, W. J.; Jones, J. G.; Carpenter, G. B.; Sweigart, D. A. *Inorg. Chem.* **1994**, *33*, 3306-3312.
27. Lecomte, C.; Chadwick, D. L.; Coppens, P.; Stevens, E. D. *Inorg. Chem.* **1983**, *22*, 2982-2992.
28. Grande, L. M.; Noll, B. C.; Oliver, A. G.; Scheidt, W. R. *Inorg. Chem.* **2010**, *49*, 6552-6557.
29. Reed, C. A. In *Electrochemical and Spectrochemical Studies of Biological Redox Components*; AMERICAN CHEMICAL SOCIETY: 1982; Vol. 201, p 333-356.
30. Felton, R. H.; Owen, G. S.; Dolphin, D.; Fajer, J. *J. Am. Chem. Soc.* **1971**, *93*, 6332-6334.
31. Phillippi, M. A.; Goff, H. M. *J. Am. Chem. Soc.* **1982**, *104*, 6026-6034.
32. Connelly, N. G.; Geiger, W. E. *Chem. Rev.* **1996**, *96*, 877-910.
33. Ikezaki, A.; Ohgo, Y.; Nakamura, M. *Coord. Chem. Rev.* **2009**, *253*, 2056-2069.
34. Boduszek, B.; Shine, H. J. *The Journal of Organic Chemistry* **1988**, *53*, 5142-5143.
35. Carey, F. A.; Hayes, L. J. *The Journal of Organic Chemistry* **1973**, *38*, 3107-3114.
36. Kaba, R. A.; Ingold, K. U. *J. Am. Chem. Soc.* **1976**, *98*, 7375-7380.
37. Malatesta, V.; Ingold, K. U. *J. Am. Chem. Soc.* **1974**, *96*, 3949-3954.
38. Riplinger, C.; Bill, E.; Daiber, A.; Ullrich, V.; Shoun, H.; Neese, F. *Chemistry – A European Journal* **2014**, *20*, 1602-1614.
39. Kitagawa, T.; Ozaki, Y. In *Metal Complexes with Tetrapyrrole Ligands I*; Buchler, J. W., Ed.; Springer Berlin Heidelberg: Berlin, Heidelberg, 1987, p 71-114.
40. Spiro, T. G.; Strekas, T. C. *J. Am. Chem. Soc.* **1974**, *96*, 338-345.
41. Biju, V.; Pan, D.; Gorby, Y. A.; Fredrickson, J.; McLean, J.; Saffarini, D.; Lu, H. P. *Langmuir* **2007**, *23*, 1333-1338.
42. Das, P. K.; Samanta, S.; McQuarters, A. B.; Lehnert, N.; Dey, A. *Proceedings of the National Academy of Sciences* **2016**, *113*, 6611-6616.
43. Hobbs, J. D.; Larsen, R. W.; Meyer, T. E.; Hazzard, J. H.; Cusanovich, M. A.; Ondrias, M. R. *Biochemistry* **1990**, *29*, 4166-4174.
44. Teraoka, J.; Kitagawa, T. *The Journal of Physical Chemistry* **1980**, *84*, 1928-1935.
45. Epstein, L. M.; Straub, D. K.; Maricondi, C. *Inorg. Chem.* **1967**, *6*, 1720-1724.
46. Abu-soud, H. M.; Silver, J. *Inorg. Chim. Acta* **1989**, *161*, 139-141.
47. Schulz, C. E.; Rutter, R.; Sage, J. T.; Debrunner, P. G.; Hager, L. P. *Biochemistry* **1984**, *23*, 4743-4754.
48. Rittle, J.; Green, M. T. *Science* **2010**, *330*, 933.
49. Stone, K. L.; Hoffart, L. M.; Behan, R. K.; Krebs, C.; Green, M. T. *J. Am. Chem. Soc.* **2006**, *128*, 6147-6153.
50. Falborg, L.; Jorgensen, K. A. *J. Chem. Soc., Perkin Trans. 1* **1996**, 2823-2826.
51. Russell, J. *J. Biol. Chem.* **1944**, *156*, 457-462.

52. Choi, I. K.; Liu, Y.; Feng, D.; Paeng, K. J.; Ryan, M. D. *Inorg. Chem.* **1991**, *30*, 1832-1839.
53. Paulat, F.; Berto, T. C.; DeBeer George, S.; Goodrich, L.; Praneeth, V. K. K.; Sulok, C. D.; Lehnert, N. *Inorg. Chem.* **2008**, *47*, 11449-11451.
54. Sage, J. T.; Paxson, C.; Wyllie, G. R. A.; Sturhahn, W.; Durbin, S. M.; Champion, P. M.; Alp, E. E.; Scheidt, W. R. *J. Phys.: Condens. Matter* **2001**, *13*, 7707.
55. Sturhahn, W. *Hyperfine Interact.* **2000**, *125*, 149-172.
56. Sheldrick, G. M.; v. 2008/4 ed.; Bruker Analytical X-ray: Madison, WI, 2008.
57. Perdew, J. P. *Physical Review B* **1986**, *33*, 8822-8824.
58. Becke, A. D. *Physical Review A* **1988**, *38*, 3098-3100.
59. Schäfer, A.; Horn, H.; Ahlrichs, R. *The Journal of Chemical Physics* **1992**, *97*, 2571-2577.
60. Schäfer, A.; Huber, C.; Ahlrichs, R. *The Journal of Chemical Physics* **1994**, *100*, 5829-5835.
61. Frisch, M. J.; Trucks, G. W.; Schlegel, H. B.; Scuseria, G. E.; Robb, M. A.; Cheeseman, J. R.; Scalmani, G.; Barone, V.; Mennucci, B.; Petersson, G. A.; Nakatsuji, H.; Caricato, M.; Li, X.; Hratchian, H. P.; Izmaylov, A. F.; Bloino, J.; Zheng, G.; Sonnenberg, J. L.; Hada, M.; Ehara, M.; Toyota, K.; Fukuda, R.; Hasegawa, J.; Ishida, M.; Nakajima, T.; Honda, Y.; Kitao, O.; Nakai, H.; Vreven, T.; Montgomery Jr., J. A.; Peralta, J. E.; Ogliaro, F.; Bearpark, M. J.; Heyd, J.; Brothers, E. N.; Kudin, K. N.; Staroverov, V. N.; Kobayashi, R.; Normand, J.; Raghavachari, K.; Rendell, A. P.; Burant, J. C.; Iyengar, S. S.; Tomasi, J.; Cossi, M.; Rega, N.; Millam, N. J.; Klene, M.; Knox, J. E.; Cross, J. B.; Bakken, V.; Adamo, C.; Jaramillo, J.; Gomperts, R.; Stratmann, R. E.; Yazyev, O.; Austin, A. J.; Cammi, R.; Pomelli, C.; Ochterski, J. W.; Martin, R. L.; Morokuma, K.; Zakrzewski, V. G.; Voth, G. A.; Salvador, P.; Dannenberg, J. J.; Dapprich, S.; Daniels, A. D.; Farkas, Ö.; Foresman, J. B.; Ortiz, J. V.; Cioslowski, J.; Fox, D. J.; Gaussian, Inc.: Wallingford, CT, USA, 2009.

Chapter 3

Stable Analogues for Ferrous HNO Complexes: Characterization and Reactivity of Heme-Nitrosoalkane Complexes

C-nitroso compounds (RNO, R = alkyl, aryl) are formed as byproduct of the oxidative metabolism of drugs (or xenobiotics) that contain an amine, or hydroxylamine functional group, and through the reduction of nitroalkanes (or nitrosoarenes, RNO_2):[1-3]

$$RNH_2 \longrightarrow RNHOH \longrightarrow RNO$$

In mammals, *C*-nitroso compounds bind to heme proteins in the ferrous oxidation state, such as myoglobin/hemoglobin (Mb/Hb), Cytochrome P450, and soluble guanylate cyclase (sGC), which inhibits these proteins from carrying out important functions. This generally makes nitro-containing compounds quite toxic to cells because they can be reduced to *C*-nitroso derivatives.[4] Interestingly, nitrosoarenes react with thiols like glutathione in red blood cells to form sulfonamide as a defense mechanism against these toxic molecules, before they are metabolized in the liver.[5] Alternatively, RNOs also react with cyseinate residues in proteins.[6-10]. In addition, ferrous heme RNO complexes are isoelectronic to ferrous nitroxyl complexes, or $\{FeN(H)O\}^8$ in the Enemark-Feltham

notation (the superscript “8” represents the number of iron d electrons plus the unpaired electrons in the π^* orbitals of NO).[11] On the basis of QM/MM calculations it has been proposed that the ferrous NHO complex in P450nor could react with NO directly to form an N-N bond, yielding a ferric hyponitrite species, as the central step of P450nor catalysis, as discussed in Chapter 1 (see Scheme 1.1)[12,13] Model complexes are ideally suited to study the reactivity of this proposed intermediate. However, until recently, there were no heme model complexes available that could generate a stable {FeNHO}^{8} species in order to investigate its reactivity. This is due to disproportionation of the bound HNO ligand in simple [Fe(Porph)(NHO)] complexes as observed by Ryan and co-workers.[14] This yields H_2 and the corresponding {FeNO}^{7} complex:

$$[Fe(Porph)(NHO)] \longrightarrow [Fe(Porph)(NO)] + H_2$$

Recently, however, our group prepared a long-lived five-coordinate {FeNHO}^{8} heme complex that incorporates steric bulk around the iron center, utilizing the bis-picket fence porphyrin co-ligand (3,5-Me-BAFP^{2-}), at room temperature.[15] In this case, the picket fence greatly slows down the disproportionation reaction of the bound HNO ligand. Though this HNO complex is stable, it is prepared electrochemically and contains molar electrolyte in concentration, which makes it challenging to isolate this complex. Hence, we synthesized a stable HNO analogue by substituting the N-atom of the HNO ligand with an alkyl group to form ferrous porphyrin RNO complexes. We studied the reactivity of these complexes with NO

Scheme 3.1. Proposed reactions of iron(II)-RNO complexes with (1) NO to make a ferric hyponitrite type species and (2) acid to form an analogue of Intermediate *I*. The oval represents a generic porphyrin ligand.

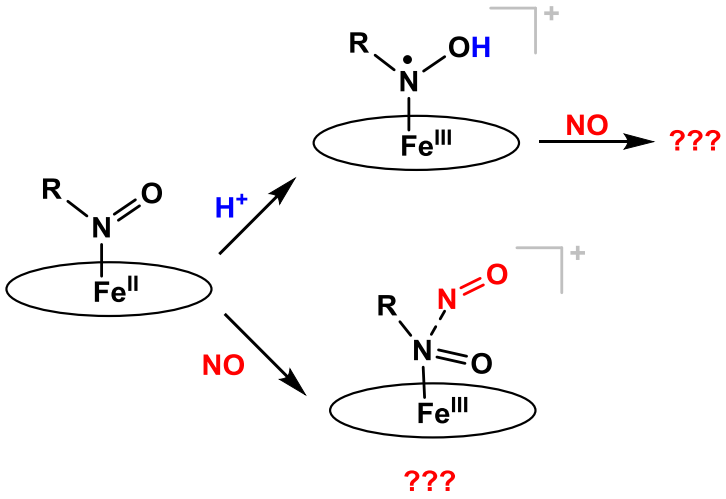

to determine whether N-N bond formation was possible in this case, as shown in Scheme 3.1. Further, we envisioned that the reaction of the iron(II)-RNO complexes with strong acids would protonate the Fe-RNO unit, resulting in an iron(IV)-NOHR^{-}, or iron(III)-NOHR(radical) type complex (see Scheme 3.1). This species is an analogue for Intermediate *I* in P450nor, and will provide insight into whether the singly or doubly protonated intermediate of P450nor is catalytically competent for NO reduction.

This chapter focuses on ferrous heme RNO complexes and their reactivity as a model for P450nor. Section 3.1 will address the synthesis and characterization of ferrous porphyrin RNO (where R = iPr, Ph) complexes with tetraphenylporphyrin and the bis-picket fence porphyrin (3,5-Me-BAFP^{2-}). Section 3.2 discusses the vibrational assignments of [Fe(TPP)(iPrNO)]. Section 3.3 describes the reactivity of our ferrous RNO complexes towards NO and acid.

The studies summarized in this chapter are in part adapted from a manuscript in preparation for the journal Inorganic Chemistry. [Fe(TPP)(iPrNO)] and the corresponding ^{15}N-labeled complex were synthesized and characterized by undergraduate student Diamond Thomas. The reactivity studies of the complex [Fe(TPP)(iPrNO)] with NO and acid were conducted together.

3.1 Characterization of Ferrous Porphyrin RNO Complexes

Ferrous porphyrin RNO complexes are synthesized via two different methods in the literature.[16,17] The first method is the reaction of the ferric complex, [Fe(Porph)(Cl)] (where Porph = dianion of a generic porphyrin ligand), with excess N-alkylhydroxlamines (RNHOH, R = alkyl, aryl), which undergoes a disproportionation reaction to give the ferrous RNO complex, as shown in equation (1). The second method of preparation is the reaction of the ferrous porphyrin, [Fe(Porph)], with nitrosoalkane ligands (RNO, R = alkyl, aryl) to directly form the ferrous RNO complex. These reactions are usually carried out in the presence of excess neutral ligand (L), such as the N-donor ligand MI (MI = 1-methylimidazole), to form the corresponding six-coordinate complex, [Fe(Porph)(RNO)(MI)] as shown in equation (2).

$$[Fe(Porph)(Cl)] + 2RNHOH \longrightarrow [Fe(TPP)(RNO)] + 0.5RNH_2 + 0.5H_2O + HCl \quad (1)$$

$$[Fe(Porph)] + RNO \xrightarrow{\text{excess L}} [Fe(Porph)(RNO)(L)] \quad (2)$$

In this work, we used modified versions of both methods to synthesize our ferrous porphyrin RNO model complexes (where R = iPr, Ph).

Ferrous Porphyrin PhNO Complexes

Using the method according to equation (1) we reacted [Fe(TPP)(BF_4)] with excess N-Phenylhydroxylamine (PhNHOH) in tetrahydrofuran (THF) to yield the corresponding PhNO complex in 89% yield. The UV-vis spectrum of the reaction product (in CH_2Cl_2) exhibits a Soret band at 412 nm and the main Q band at 523 nm, indicative of a ferrous species as shown in Figure 3.1 (in THF Soret band shifts to 420 nm and the main Q band is observed at 535 nm). Interestingly, when a

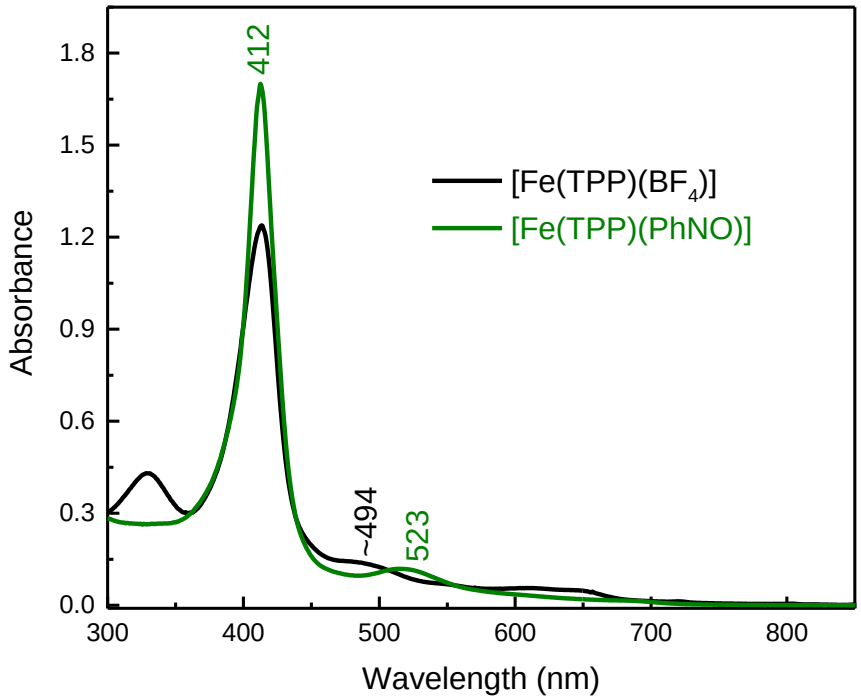

Figure 3.1. UV-vis spectra of the precursor, [Fe(TPP)(BF_4)] (black), and of the isolated reaction product, [Fe(TPP)(PhNO)] (green), in dichloromethane at room temperature.

solution of [Fe(TPP)(PhNO)] is exposed to air for one hour it does not show any signs of oxidation (by UV-vis spectroscopy). This air stability is quite different than that of ferrous tetraphenylporphyrin [Fe(TPP)], which oxidizes immediately upon air exposure. Next, we further characterized the product by ^{1}H-NMR spectroscopy. The iron complex shows a multiplet of peaks from 6.04 – 6.51 ppm that originate from the bound PhNO ligand, and the porphyrin ligand peaks range from 7.72 – 8.58 ppm; see Figure 3.20. These chemical shifts indicate that the product is pure and are characteristic of a diamagnetic, low-spin (ls) ferrous porphyrin complex (the precursor is paramagnetic). It should be noted that these peaks were assigned based on the reported ^{1}H-NMR spectrum of [Fe(TPP)(PhNO)$_2$].[18]

Though there are five reported crystal structures for ferrous porphyrin PhNO complexes with the TPP^{2-} and OEP^{2-} co-ligands (OEP = dianion of octaethylporpyhrin), the only published N-O stretching frequency was reported for the bis-PhNO complex, [Fe(TPP)(PhNO)$_2$]. To determine the N-O stretch of our mono-PhNO complex, we synthesized the corresponding Ph^{15}NO complex using the method according to equation (2). The IR spectra in Figure 3.2 of the natural abundance isotopes (n.a.i.) and the ^{15}N-complex show that there are two isotope sensitive features at 1350 and 1368 cm^{-1}, where the latter band is significantly lower in intensity than the 1350 cm^{-1} feature. This observation prompted investigation into whether other ferrous PhNO-containing complexes could be present in our reaction product. As previously mentioned, the reported N-O stretching frequency for [Fe(TPP)(PhNO)$_2$] is 1353 cm^{-1}.[18] This would imply that we obtained a mixture of the ferrous mono- and bis-PhNO complexes in our

Table 3.1. Comparison of geometric and vibrational parameters and BP86/TZVP calculated structures of ferrous porphyrin PhNO complexes (P = porphine^{2-}).

Complex	Geometric Parameters (Å) (°)				ν(N-O) (cm^{-1})
	ΔFe-N[a]	ΔFe-L[b]	ΔN-O	<Fe-N-O	
Crystal Structures					
[Fe(TPP)(PhNO)(MI)][c]	1.80 1.802,1.807 1.812[d]	2.029 2.03	1.254 1.267, 1.263, 1.26[b]	125	n.d.
[Fe(TPP)(PhNO)$_2$]	1.874	1.899	1.227, 1.237	123, 124	1353
[Fe(TPP)(*o*-tolPhNO)(MI)]	1.841	2.066	1.257	123	1366
Calculated Structures					
[Fe(P)(PhNO)]	1.779	–	1.245	123	1383
[Fe(P)(PhNO)(THF)]	1.795	2.220	1.245	124	1386
[Fe(P)(PhNO)(MI)]	1.830	2.084	1.246	124	1380
[Fe(P)(PhNO)$_2$]	1.936	1.936	1.239	121	1382
[Fe(P)(PhNO)(PhNHOH)]	1.814	2.223	1.245, 1.456	110, 123	1386

[a]N represents the PhNO ligand; [b]L represents the ligand trans to the PhNO ligand; PhNO [c]Two different molecules in the unit cell; [d]Data from the disordered structural components.

isolated product. Since the IR spectrum of [Fe(TPP)(PhNO)$_2$] is not shown in the literature report, we synthesized [Fe(TPP)(PhNO)$_2$] using the reported method of preparation.[18] The IR spectrum of the ferrous bis-PhNO complex has a very intense N-O band at 1353 cm^{-1} that shifts to 1336 cm^{-1} with Ph^{15}NO (Δ = 17 cm^{-1}), as shown in Figure 3.3 (bottom). The 1350 cm^{-1} band (and its relative intensity) in [Fe(TPP)(PhNO)$_2$] matches one of the bands in the IR spectrum of our complex, which implies that our product contains some ferrous bis-PhNO complex. Additionally, we find that the reaction of [Fe(TPP)] with one equivalent or excess Ph^{15}NO ligand makes no difference on the formation of the iron PhNO products; see IR spectra in Figure 3.3 (top). On the other hand, a crystal structure was reported by Richter-Addo and co-workers for a similar iron complex, [Fe(TPP)(*o*-tolNO)(MI)], that has an N-O stretching frequency of 1366 cm^{-1} (IR spectrum is not shown in the report). This value is very close to the other N-O band of 1368 cm^{-1}

in our PhNO complex. Based on this, we conclude that the bis- and mono-PhNO complexes have in fact different N-O stretching frequencies. To gain further insight into the vibrational properties of these PhNO complexes we employed DFT calculations. We optimized a series of ferrous porphyrin PhNO complexes as shown in Table 3.1 using BP86/TZVP. Comparison of the optimized structures to the crystal structures in the literature and show good agreement with deviations in bond lengths <0.06 Å. Unfortunately, the experimental difference in the N-O stretching frequencies (~10 cm^{-1}) between the mono- and bis-PhNO complexes is not reproduced by the DFT calculations. The calculated N-O stretching frequencies of [Fe(P)(PhNO)(MI)] and [Fe(P)$(PhNO)_2$] are 1380 and 1382 cm^{-1}, respectively (P = dianion of porphine). It should be noted that the 1382 cm^{-1} band of the [Fe(P)$(PhNO)_2$] complex is the antisymmetric mode of the N-O stretching frequencies, while the symmetric mode is not IR active (predicted to be at 1403 cm^{-1}). Based on this, we hypothesize that the 1368 cm^{-1} band in the IR spectrum of the product belongs to the ferrous mono-PhNO complex (with a THF molecule bound to the iron center) and that the 1350 cm^{-1} band is the ferrous bis-PhNO complex, [Fe(TPP)$(PhNO)_2$]. In order to complete our understanding of the N-O vibrations of ferrous porphyrin mono-PhNO complexes, we plan to synthesize the MI bound iron complex, [Fe(TPP)(PhNO)(MI)], in future work.

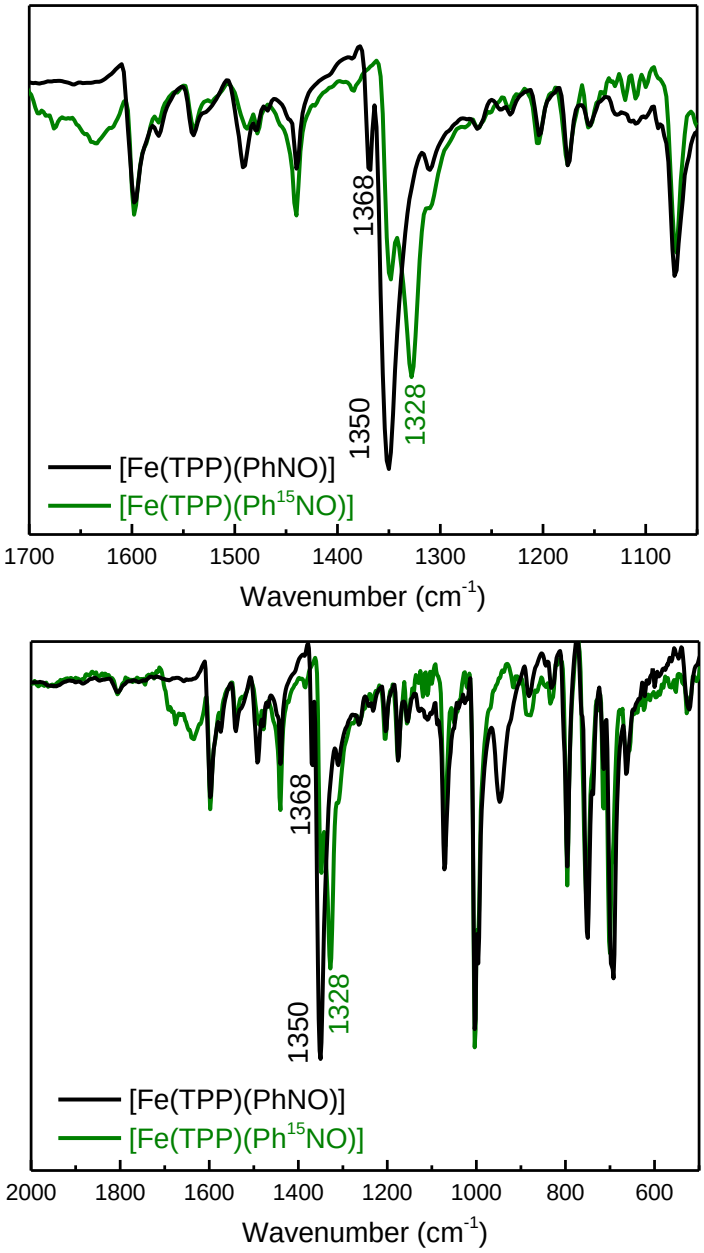

Figure 3.2. Top: Overlay of the IR spectra of [Fe(TPP)(PhNO)] (black), and the ^{15}N-labeled complex, [Fe(TPP)(Ph^{15}NO)] (green), measured in KBr pellets. Bottom: Zoom into the N-O stretching frequency region of the IR spectra.

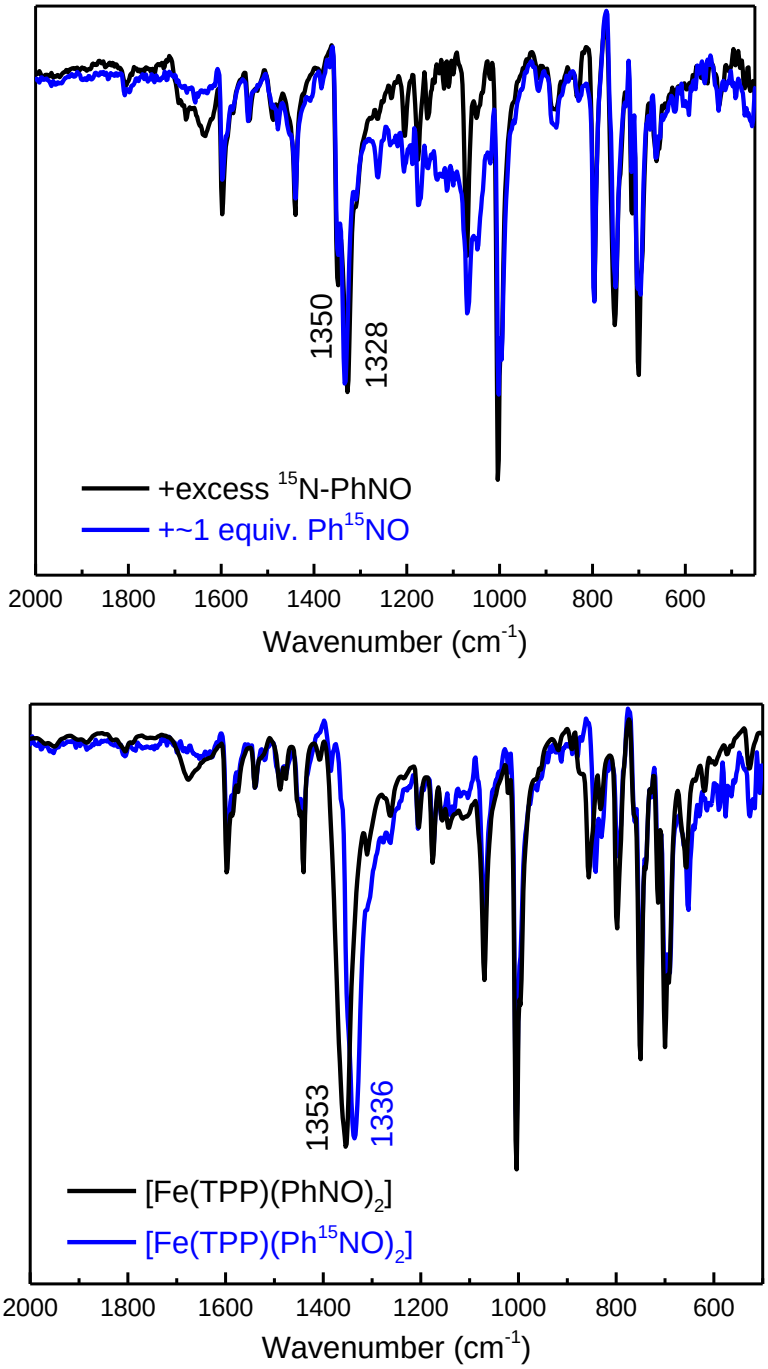

Figure 3.3. Top: Comparison of the IR spectra of the isolated product, [Fe(TPP)(Ph^{15}NO)], prepared by reacting [Fe(TPP)] with different equivalents of Ph^{15}NO. The N-O stretching frequency region is identical when excess Ph^{15}NO (black) versus ~1 equiv. Ph^{15}NO (blue) is used. Bottom: Overlay of the IR spectra of [Fe(TPP)(PhNO)$_2$] (black) and the ^{15}N-labeled complex, [Fe(TPP)(PhNO)$_2$] (blue), measured in KBr pellets.

[Fe(3,5-Me-BAFP)(PhNO)]

[Fe(3,5-Me-BAFP)] was synthesized according to a previous report.[15] Then, [Fe(3,5-Me-BAFP)] was reacted with excess PhNO to form the PhNO complex in 40% yield (see Scheme 3.2). The UV-vis spectrum of the product in THF shows typical ferrous porphyrin absorption features with a Soret band at 426 nm and the main Q band at 543 nm, as shown in Figure 3.4. The UV-vis spectrum of the product looks similar to that of [Fe(TPP)(PhNO)], but the Soret band is shifted by ~6 nm (likely an effect of using a different porphyrin ligand). In addition, the UV-vis spectrum closely resembles that of the {FeNHO}^{8} complex in [Fe(3,5-Me-BAFP)(NHO)]$^-$, which exhibits a Soret band at 426 and a Q band at 545 nm in THF.[15] It is also similar to the Mb(II)-NHO adduct prepared by Farmers and co-workers (Soret band at 423 nm).[19] The ^{1}H-NMR spectrum of the product contains peaks that range from 1.93 – 8.91 ppm, indicating that the heme is in the low-spin ferrous state. Lastly, in comparison to the precursor, [Fe(3,5-Me-BAFP)], the IR spectrum of the product has two new low-intensity bands at 1344 and 1357 cm^{-1} as shown in Figure 3.18. We do not observe an intense N-O stretch from a bis-PhNO complex as in the case of the TPP^{2-} co-ligand. This implies that the reaction

Scheme 3.2. Schematic drawing of [Fe(3,5-Me-BAFP)(PhNO)].

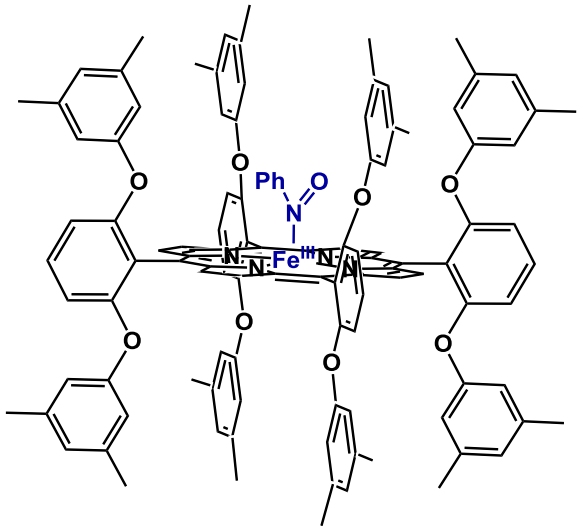

product is a ferrous mono-PhNO species, which could be due to the sterics of the picket fence of the porphyrin. To confirm this hypothesis, the corresponding $Ph^{15}NO$ complex will be synthesized in future studies.

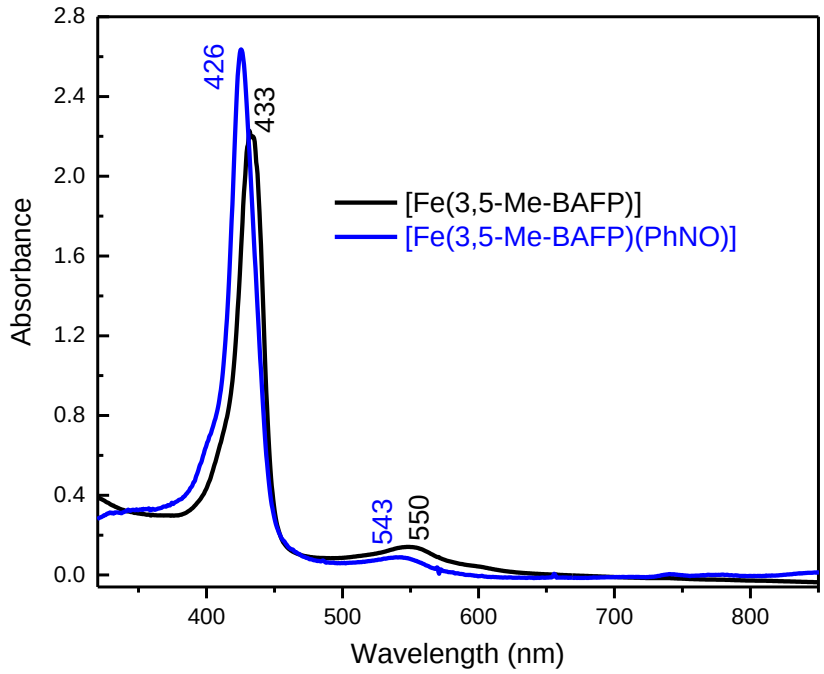

Figure 3.4. UV-vis spectra of the precursor, [Fe(3,5-Me-BAFP)] (black), and of the isolated reaction product, [Fe(3,5-Me-BAFP)(PhNO)] (blue), in THF at room temperature. Note that complex likely has THF bound to the iron center.

Ferrous Porphyrin iPrNO Complexes

We envisioned that changing the R group of the RNO ligand to an isopropyl group would be a better model for a ferrous NHO complex. Using method (2) we reacted [Fe(TPP)] with a slight excess of iPrNO to form [Fe(TPP)(iPrNO)] in a 67% yield. In the UV-vis spectra in Figure 3.5, the Soret band of the precursor, [Fe(TPP)], shifts from 426 to 417 nm upon coordination of iPrNO but remains very

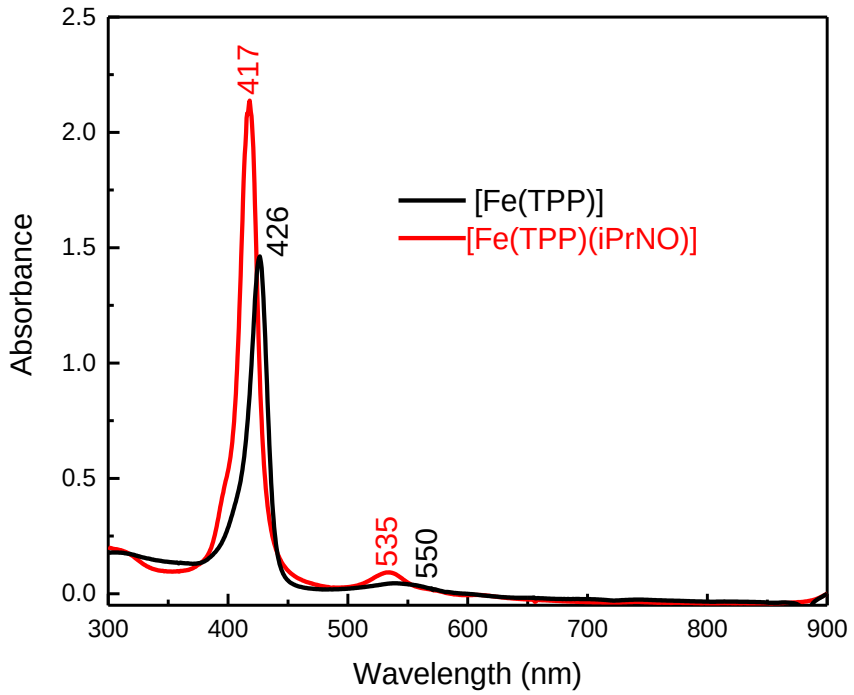

Figure 3.5. UV-vis spectra of the precursor, [Fe(TPP)] (black), and of the isolated reaction product, [Fe(TPP)(iPrNO)] (red), in THF at room temperature. Note that complex likely has THF bound to the iron center.

symmetric, which is a feature characteristic of ferrous porphyrins. At the same time, the main Q band of [Fe(TPP)] shifts from 550 to 535 nm. The resulting UV-vis spectrum of [Fe(TPP)(iPrNO)] is similar to that of [Fe(TPP)(PhNO)]. Also, like the ferrous PhNO complex, the product does not oxidize upon exposure to air for several hours. The ^{1}H-NMR spectrum of the isolated product exhibits peaks that range from 7.70 – 8.73 ppm for the porphyrin ligand, which is indicative of a diamagnetic ferrous heme complex (the precursor is paramagnetic). Additionally, there are two peaks shifted upfield to -0.61 and -2.07 ppm that originate from the bound iPrNO ligand (due to the ring current of the porphyrin). The ^{1}H-NMR spectrum of [Fe(TPP)(iPrNO)] was assigned based on a previous paper that

reported the synthesis of the complex using method (1).[16] Unlike the ferrous PhNO complexes, the literature reports the N-O stretching frequencies of six-coordinate ferrous heme iPrNO complexes with MI (MI = 1-methylimidazole), pyridine, or methanol bound to the iron center, which range from 1423 – 1433 cm^{-1} (see Table 3.2).[16,17,20]. However, these N-O stretching vibrations were not assigned based on isotope-labeled complexes. To accurately determine the N-O stretch, we synthesized the ^{15}N-labeled analogue of [Fe(TPP)(iPrNO)]. This revealed the N-O stretching frequency of the n.a.i. complex to be 1440 cm^{-1}, which shifts to 1417 cm^{-1} with ^{15}N-labeling (Δ = 23 cm^{-1}), as shown in Figure 3.6. The N-O stretch of the n.a.i. complex is consistent with the previous report[16] for [Fe(TPP)(iPrNO)] of 1445 cm^{-1}. Importantly, our work has finally lead to the unambiguous assignment of the N-O stretching frequency of [Fe(TPP)(iPrNO)] and has validated that other

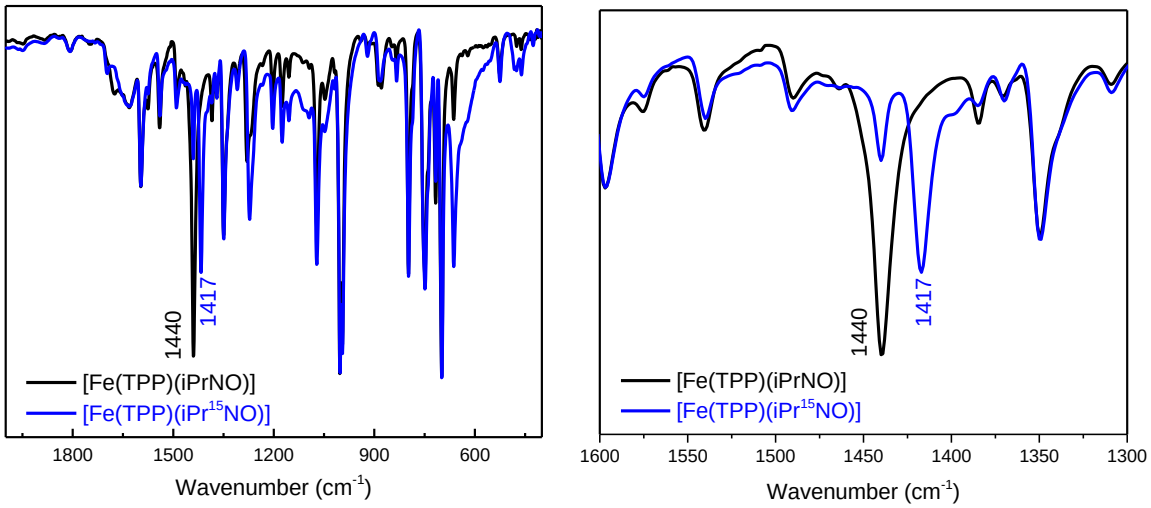

Figure 3.6. Left: Overlay of the IR spectra of [Fe(TPP)(iPrNO)] (black), and of the ^{15}N-labled complex, [Fe(TPP)(iPr^{15}NO)] (blue), measured in KBr pellets. Right: Zoom into the N-O stretching frequency region of the IR spectra.

reports have correctly assigned the N-O stretches of their corresponding ferrous iPrNO complexes. Furthermore, we isolated a pure complex that does not show a mixture of ferrous mono- and bis-RNO complexes, as observed with the PhNO ligand.

Crystallography Studies

With the long-term stability of ferrous heme RNO complexes established, we obtained crystal structures of the complexes, [Fe(TPP)(PhNO)], [Fe(TPP)(iPrNO)] and [Fe(3,5-Me-BAFP)(PhNO)]. From this, we can learn how the RNO ligands are coordinated to the iron center and whether they have THF bound in the trans position to the RNO ligand (originating from the synthesis).

X-ray quality crystals of [Fe(TPP)(PhNO)] were obtained by vapor diffusion of hexanes into a concentrated THF solution of the complex in the -33°C glovebox freezer. This resulted in a co-crystal with two different PhNO complexes in the unit cell, as shown in Figure 3.7 (top). One of the heme complexes in the unit cell is [Fe(TPP)(PhNO)(THF)], which has a THF molecule bound to the iron center as predicted. The crystal structure exhibits an Fe-N bond length of 1.813 Å and an Fe-N-O angle of 122°. These geometric parameters are very similar to that of [Fe(TPP)(PhNO)(MI)] that has an Fe-N(Ph)O bond length of 1.80 Å and an Fe-N-O bond angle of 125° (see Table 3.2). The other heme complex in the unit cell is the phenylamine ($PhNH_2$) bound complex, [Fe(TPP)(PhNO)($PhNH_2$)]. The phenylamine is formed during the disproportionation reaction of the ferric heme

complex with excess PhNHOH, reflected in equation (1). This was a surprise, as we did not expect the $PhNH_2$ to be bound since the reaction was carried out in the coordinating solvent THF. This structure shows disorder of the bound PhNO and $PhNH_2$ ligands above and below the heme plane, resulting in corresponding Fe-N bond lengths of 1.963 and 1.994 Å from the structural fit. However, these bond lengths are significantly longer than the Fe-N and Fe-O bond lengths in of

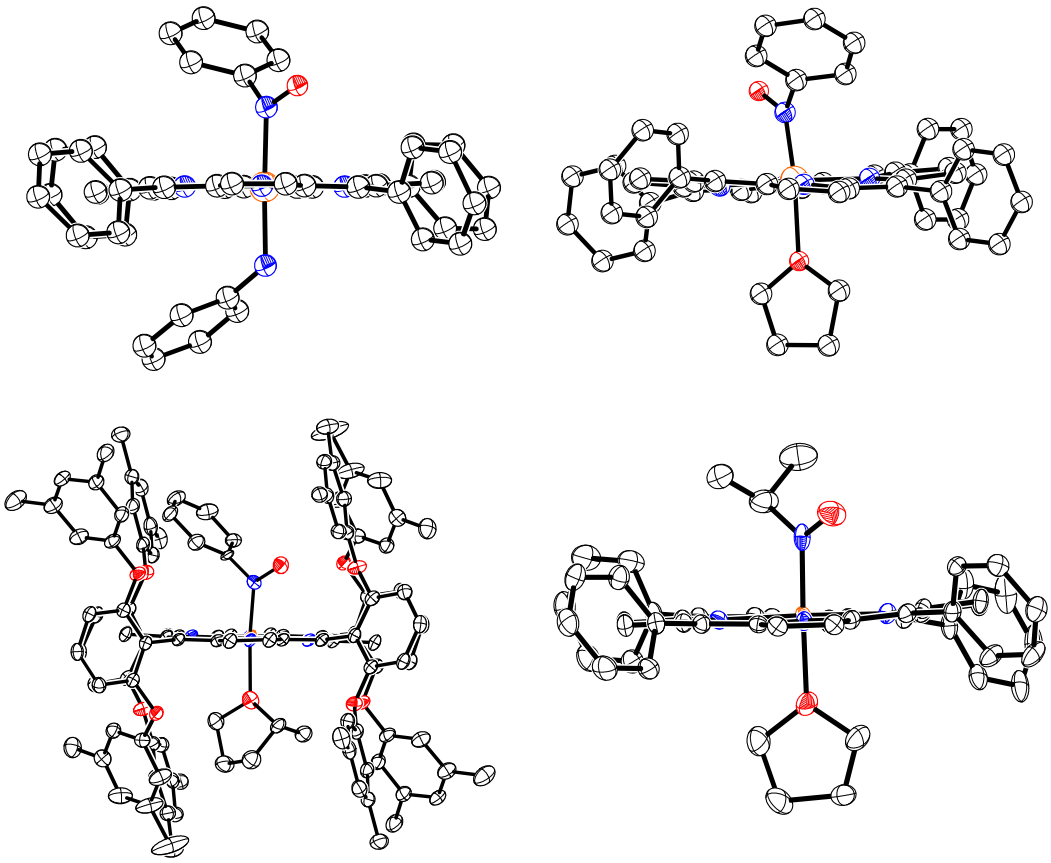

Figure 3.7. Top: Crystal structures of the two unique ferrous PhNO complexes in the unit cell of the co-crystallized compounds [Fe(TPP)(PhNO)($PhNH_2$)] (left) and [Fe(TPP)(PhNO)(THF)] (right). Bottom: Crystal structures of [Fe(3,5-Me-BAFP)(PhNO)(2-Me-THF)] (left) and [Fe(TPP)(iPrNO)(THF)] (right). In the structures, the hydrogen atoms, disorder, and solvent molecules are omitted for clarity. Thermal ellipsoids are shown at 50% probability.

[Fe(TPP)(PhNO)(THF)]. They are also much longer than of all of the other reported Fe-N distances in other ferrous heme RNO complexes (1.80 – 1.90 Å), as shown in Table 3.2.[16-18,21] On the other hand, the Fe-N(amine) bond length is shorter than that in bis(primary amine) ferrous porphyrins, where the Fe-NH_2R bond lengths range from 2.028 – 2.045 Å[22] (see Chapter 2, Table 2.1). Based on these considerations, we feel that the Fe-N bond distances in [Fe(TPP)(PhNO)($PhNH_2$)] are partially less well defined due to the disorder, and should be treated with care.

X-ray quality crystals of [Fe(TPP)(iPrNO)] were obtained by layering a concentrated solution of the complex with hexanes at room temperature. The structure of [Fe(TPP)(iPrNO)(THF)] has a THF molecule bound to the iron center as shown in Figure 3.7. In the structure, the Fe-NO bond length is 1.853 Å and the Fe-NO bond angle of 121°. This is in good agreement with other 6C heme iPrNO complexes that have Fe-NO bond lengths between 1.80 – 1.89 Å and Fe-N-O bond angles from 116 – 124°, as shown in Table 3.2.[16,17] The Fe-NO bond length of this complex is slightly longer than that of the MI adduct, [Fe(TPP)(iPrNO)(MI)] at 1.81 Å, but the Fe-N-O angle is quite similar (122°). These geometric parameters are consistent with the crystal structure of the $\{FeNO\}^8$ complex, $[Fe(TFPPBr_8)(NO)]^-$ (where $TFPPBr_8$ = dianion of 2,3,7,8,12,13,17,18-octabromo-5,10,15,20-(tetra-(pentrafluorophenyl)porphyrin), which exhibits an Fe-NO bond length of 1.814 Å and an Fe-N-O angle of 122°.[23] Also, all of these values compare well with the Mb(II)-NHO adduct where XAFS fitting determined the Fe-NHO bond length to be 1.82 Å.[24] On the other hand, $\{FeNO\}^7$ complexes, such as [Fe(TPP)(NO)] and

[Fe(TPP)(NO)(MI)], exhibit much shorter Fe-NO bond lengths of 1.72[25] and 1.750 Å,[26] respectively, than ferrous heme RNO complexes.

Figure 3.8. View looking down the *meso* carbon group of the heme plane in [Fe(TPP)(PhNO)(THF)]. All of the hydrogen atoms and phenyl groups of the porphyrin ligand are omitted for clarity.

For the last crystal structure, we obtained crystals from a concentrated solution of [Fe(3,5-Me-BAFP)(PhNO)] in 2-methyl-tetrahydrofuran (2-Me-THF). The structure revealed that the complex is six-coordinate with 2-Me-THF bound to the iron center, as shown in Figure 3.7 (bottom). All three of the RNO crystal structures obtained here have either THF or 2-Me-THF bound, which shows that these ferrous RNO complexes prefer to be six-coordinate. This is in agreement with previous findings that HNO does not rise to a significant trans effect in ferrous heme complexes.[27] In contrast to our other THF-bound structures, [Fe(3,5-Me-BAFP)(PhNO)(2-Me-THF)] has an elongated Fe-NO bond length of 1.90 Å, but it still falls within the range of crystal structures of ferrous heme PhNO complexes (see Table 3.2). For further comparison, the {FeNO}^{7} complex [Fe(3,5-Me-BAFP)(NO)] that has a significantly shorter Fe-NO bond length of 1.712 Å.[15]

The heme is completely planar in all of our RNO crystal structures, except in [Fe(TPP)(PhNO)(THF)] where the porphyrin shows some ruffling distortion as illustrated in Figure 3.8. This distortion is unusual for 6C ferrous porphyrins since the iron is located in the heme plane. A ruffling distortion is characterized by the rotation of *trans* pyrrole rings in the opposite direction around the Fe-$N_{pyrrole}$ bonds

of the porphyrin co-ligand. This out-of-plane distortion is measured by the root mean square deviation (RMSD) of the porphyrin atoms from the heme plane. The 25-atom core displacement of [Fe(TPP)(PhNO)(THF)] is 0.15 Å, whereas planar hemes are defined by a 25-atom core displacement of less than 0.10 Å.[28] For example, the completely planar complex $[Fe(TMP)(MI)_2]ClO_4$ (TMP = dianion of tetramesitylporphyrin) has a 25-atom core displacement of 0.02 Å,[29] which is 7.5 times smaller than that of [Fe(TPP)(PhNO)(THF)]. The RMSD for the 4-atom *meso* carbon displacement in [Fe(TPP)(PhNO)(THF)] is 0.15 Å.

Lastly, all of our crystal structures exhibit average $Fe\text{-}N_{pyrrole}$ bond distances of ~2.0 Å. This bond length is indicative of low-spin ferrous hemes, which exhibit average $Fe\text{-}N_{pyrrole}$ bond distances between 1.981 – 2.008 Å.[30]

Table 3.2. Comparison of geometric parameters and vibrational frequencies for selected ferrous porphyrin complexes.[a]

Complex	ΔFe-Nporph[b]	ΔFe-N(RNO)	ΔFe-Axial	ΔN-O	<Fe-N-O	ν(N-O)	Ref.
[Fe(3,5-Me-BAFP)(PhNO)(2-Me-THF)]	2.003	1.904	2.089	1.265	125	1356	t.w.
[Fe(TPP)(PhNO)(THF)]	1.998	1.813	2.141	1.253	122	1368/ 1347	t.w.
[Fe(TPP)(PhNO)($PhNH_2$)][c]	2.002	1.994, 1.963	1.994, 1.963	1.172, 1.194	119, 120	1353	t.w.
[Fe(TPP)($PhNO)_2$]	1.9975	1.874, 1.899	-	1.237, 1.227	124, 123	1353	18
[Fe(TPP)(PhNO)(Pyr)][d]	1.9900	1.819	2.106	1.249	124	n.d.	21
[Fe(TPP)(PhNO)(MI)][c]	1.9855	1.800	2.029	1.254	125	n.d.	21
	2.004	1.802, 1.807, 1.812	2.03	1.267, 1.263, 1.26	123, 124, 124		
[Fe(TPP)(*o*-tolNO)(MI)]	2.007	1.841	2.066	1.257	123	1366	20
[Fe(TPP)(NODMA)(Pyr)][e]	1.981	1.859	2.095	1.252	120	n.d.	21
[Fe(OEP)(PhNO)(MI)][c]	2.002	1.809, 1.802	2.092, 2.094	1.269, 1.258	123, 124	n.d.	21
[Fe(TPP)(iPrNO)(THF)]	1.998	1.853	2.090	1.212	120.8	1440	t.w.
[Fe(TPP)(iPrNO)(MI)]	1.996	1.81	2.050	1.24	122	1433	17
[Fe(TPP)(iPrNO)($iPrNH_2$)][c]	1.993	1.86, 1.87	2.105, 2.094	1.26	124	1432	16
[Fe(TTP)(iPrNO)(MI)][c]	1.997	1.81, 1.86	2.05, 2.03	1.25, 1.28	123, 121	1428	17
[Fe(OEP)(iPrNO)(MeOH)]	2.010	1.890	2.15	1.26	116	1433	17
[Fe(OEP)(iPrNO)(MI)][c]	2.014	1.80	2.03, 2.11	1.26	123	1423	17
[Fe(OEP)(iPrNO)(Pyr)]	2.009	1.84	2.12	1.23	124	1429	17

[a]All values are given in Å and °; [b]Average value; [c]Data from the disordered structural components; [d]Two different molecules in the unit cell; [e]NODMA = 4-nitroso-*N*,*N*-dimethylaniline.

3.2 Vibrational Analysis of [Fe(TPP)(iPrNO)]

In addition, there are several crystal structures of ferrous heme-nitrosoalkane (and nitrosoarene) complexes reported in the literature[16-18,20,21]. However, previous vibrational assignments of these complexes, such as the ferrous NHO adduct of Mb are ambiguous. This HNO adduct exhibits a feature at 649 cm^{-1}, but the exact nature of this vibration is not understood. To look further into this, we measured the Fe-NO stretching and bending frequencies of [Fe(TPP)(iPrNO)] using Nuclear Resonance Vibrational Spectroscopy (NRVS). The NRVS data of the ^{57}Fe-labeled iPrNO/iPr^{15}NO complexes are shown in Figure 3.9. Two isotope sensitive bands are identified in the NRVS data. The first feature is observed 426 cm^{-1}, which shifts to 418 cm^{-1} with iPr^{15}NO ($\Delta = 8$ cm^{-1}). The second band is significantly lower in intensity and is found at 633 cm^{-1}. This feature shifts to 627 cm^{-1} with iPr^{15}NO ($\Delta = 6$ cm^{-1}). To determine the nature of these Fe-NO based vibrations we employed DFT computations. The BP86/TZVP calculated geometric parameters of the ferrous iPrNO complexes are listed in Table 3.3. Overall, the calculated structure of [Fe(P)(iPrNO)(THF)] (where P = dianion of porphine) is in good agreement with the crystal structure of [Fe(TPP)(iPrNO)(THF)]. The N-O stretching frequency is also within ~20 cm^{-1} of the experimental value for this complex. With this, we predicted the NRVS data of the [Fe(P)(iPrNO)] and [Fe(P)(iPrNO)(THF)] complexes, as shown in Figure 3.9 (bottom). Interestingly, the five-coordinate complex [Fe(TPP)(iPrNO)], shows an Fe-NO based feature at 608 cm^{-1}, which increases in the energy (646 cm^{-1}) in the

THF bound complex. The calculated NRVS data of the THF bound complex, [Fe(TPP)(iPrNO)(THF)], shown in Figure 3.9, nicely reproduce the intensity pattern of the 633 and 426 cm^{-1} bands observed in our experimental data. We find that the low intensity feature at 633 cm^{-1} corresponds to the Fe-N-O bend, while the 426 cm^{-1} feature is the Fe-NO stretching frequency. In comparison, Farmer and co-workers reported the Fe-N(H)O stretching frequency for the Mb(II)-NHO complex to be 649 cm^{-1} (shifts to 636 cm^{-1} with $H^{15}NO$; measured by rRaman spectroscopy). This was determined by comparison to the Fe-NO stretching frequency of the $\{FeNO\}^7$ complex of Mb at 551 cm^{-1}. It should be noted that later work revealed that this assignment was not correct and that the 551 cm^{-1} feature is the Fe-N-O bending frequency.[31,32] In addition, ferrous heme RNO proteins (sGC, Hb, and Mb, where R = Me, Pentyl, and Octyl)[33-38] have Fe-NO stretches that range from 543 – 554 cm^{-1} (measured by rRaman spectroscopy). These values were assigned to the Fe-NO stretch merely based on their similarity to the Fe-NO stretches of 6C $\{FeNO\}^7$ porphyrin complexes (554 – 558 cm^{-1}), but no further analysis was provided to make these assignments.[39] As previously mentioned, at that time it was thought that the higher energy feature was the Fe-NO stretching frequency, which, however, is wrong.[31,32]

To further analyze this, we optimized the structures of [Fe(P)(NHO)(L)], where L = THF and MI, using MI is a model for histidine (see Table 3.3). The calculated structure of [Fe(P)(NHO)(MI)] agrees well with the fitted XAFS data for the Mb(II)-HNO species. However, the N-O stretching frequency for the HNO complex is overestimated by 81 cm^{-1}. It should be noted that the experimentally derived N-O

stretch in the Mb-NHO adduct was measured via rRaman spectroscopy. The feature assigned to the N-O stretch is buried under a very intense porphyrin band. Hence, the energy of this feature was derived from a difference spectrum of the data for the ferrous ^{14}NHO/^{15}NHO complexes, which could lead to artifacts. On the other hand, it is possible that the hydrogen bonding interactions between the HNO ligand and the distal histidine in the active site of Mb need to be included in order to accurately predict the N-O stretch. This is likely the case as Zhang and co-workers showed this hydrogen bonding interaction is important for reproducing experimental data of the NHO complex with computational models.[40,41] Despite this, the experimental Fe-N(H)O vibration (649 cm^{-1}) is much closer in energy to the DFT calculated feature at 653 cm^{-1}, as shown in Table 3.3. The calculated NRVS data of the HNO adducts are shown in Figure 3.10. The calculated vibrational frequencies of the iron(II)-NHO complex reveal that the Fe-N(H)O stretch is located at 653 cm^{-1} and the Fe-N(H)-O bend is predicted at 447 cm^{-1}. The stretching and bending frequencies are opposite to [Fe(P)(iPrNO)(THF)], where the calculated Fe-NO stretch is at 447 cm^{-1} and the Fe-N-O bend is predicted at 646 cm^{-1}. Our assignments of [Fe(TPP)(iPrNO)] should be further confirmed by Single-Crystal NRVS for future studies.

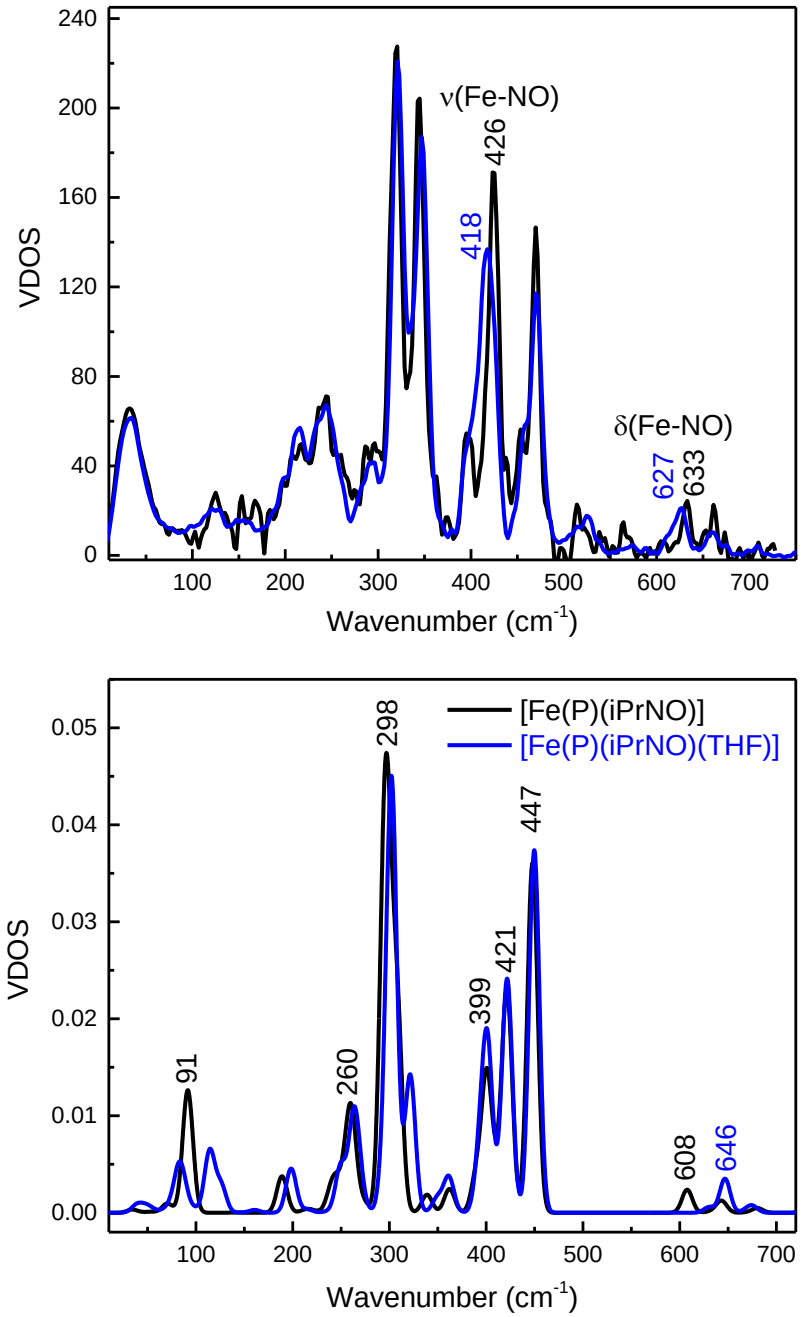

Figure 3.9. Top: NRVS-derived vibrational density of states (VDOS) for [^{57}Fe(TPP)(iPrNO))] (black) and the ^{15}N-labeled iPrNO complex (blue). Bottom: BP86/TZVP calculated NRVS VDOS for [Fe(P)(iPrNO)] (black) and [Fe(P)(iPrNO)(THF)] (blue).

Table 3.3. Comparison of geometric and vibrational parameter and BP86/TZVP calculated structures of selected ferrous iPrNO/NHO heme complexes (P = porphine^{2-}).

Complex	Geometric Parameters (Å) (°)				Vibrational Frequencies (cm^{-1})		
	ΔFe-NO	ΔFe-L[a]	ΔN-O	<Fe-N-O	ν(N-O)	δ(Fe-NO)	ν(Fe-NO)
[Fe(TPP)(iPrNO)(THF)], crystal struct.	1.853	2.09	1.212	121	1445	633	426
[Fe(TPP)(iPrNO)(MI)]	1.81	2.050	1.26	124	1433	n.d.	
Mb(II)-NHO[b]	1.82	2.09	1.24	131	1385	649	
BP86/TZVP							
[Fe(P)(iPrNO)]	1.770	–	1.235	124	1464/1468/1261[c]	608	448
[Fe(P)(iPrNO)(THF)]	1.795	2.245	1.236	124	1461/1466/1265[c]	646	447
[Fe(P)(iPrNO)(MI)]	1.831	2.089	1.237	124	1457/1464/1268[c]	676/660	414
[Fe(P)(NHO)]	1.741	–	1.235	132	1466	440	685
[Fe(P)(NHO)(THF)]	1.762	2.219	1.235	132	1466	462	663/678
[Fe(P)(NHO)(MI)]	1.788	2.08254	1.236	132	1459	463	653/672

[a]L represents the ligand trans to the iPrNO or HNO ligand; [b]Bond lengths derived from fitted XAFS data; [c]Other vibrations that are coupled to the N-O stretching frequency

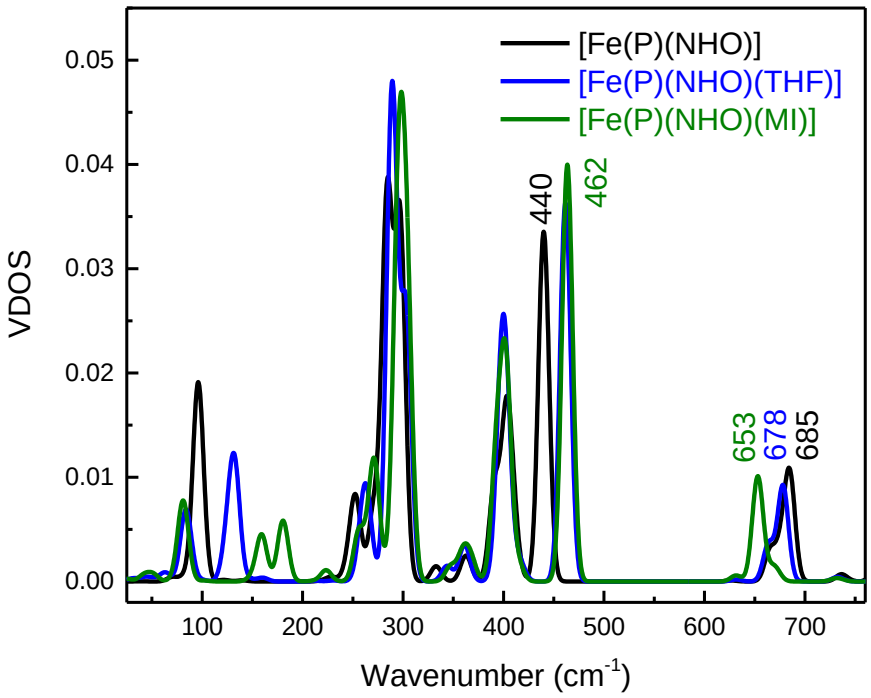

Figure 3.10. BP86/TZVP calculated NRVS VDOS for [Fe(P)(NHO)] (black), [Fe(P)(NHO)(THF)] (blue), and [Fe(P)(NHO)(MI)] (green).

3.3 Reactivity of Ferrous Heme-Nitrosoalkane Complexes

In Section 3.1 we showed that ferrous heme RNO complexes are good structural models for {FeN(H)O}^{8} complexes. With this, we further investigated the reactivity of our ferrous porphyrin PhNO and iPrNO model complexes with NO and strong acids (see Scheme 3.1)

NO reactivity

The reactivity of ferrous heme RNO complexes with NO gas has not been previously studied. First, we saturated a solution of dichloromethane with NO gas. Then, we titrated a solution of cobalt tetraphenylporphyrin [Co(TPP)] in THF with the NO/CH_2Cl_2 solution to form the corresponding [Co(TPP)(NO)] complex. From this we approximated the NO concentration of the solution (typically ~1 mM). The UV-vis spectra in Figure 3.11 show the titration of [Fe(TPP)(PhNO)] in THF with the NO saturated CH_2Cl_2 solution at room temperature. The reaction is complete with ~1 equiv. of the NO solution and the UV-vis data of the reaction product exhibits features at 412, 476, and 540 nm that are identical to that of the {FeNO}^{7} complex, [Fe(TPP)(NO)]. We hypothesized that this {FeNO}^{7} complex is generated by formation of the intermediate, [Fe(TPP)(NO)(PhNO)], which, due to the strong *trans* effect of NO, causes the PhNO ligand to dissociate, as shown in Scheme 3.3. It is important to point out that the proposed intermediate, [Fe(TPP)(PhNO)(NO)], would likely not be observed at room temperature, due to high binding constants of NO to a ferrous heme (Keq = $10^{10\text{-}12}$ M^{-1}).[42-44] With this

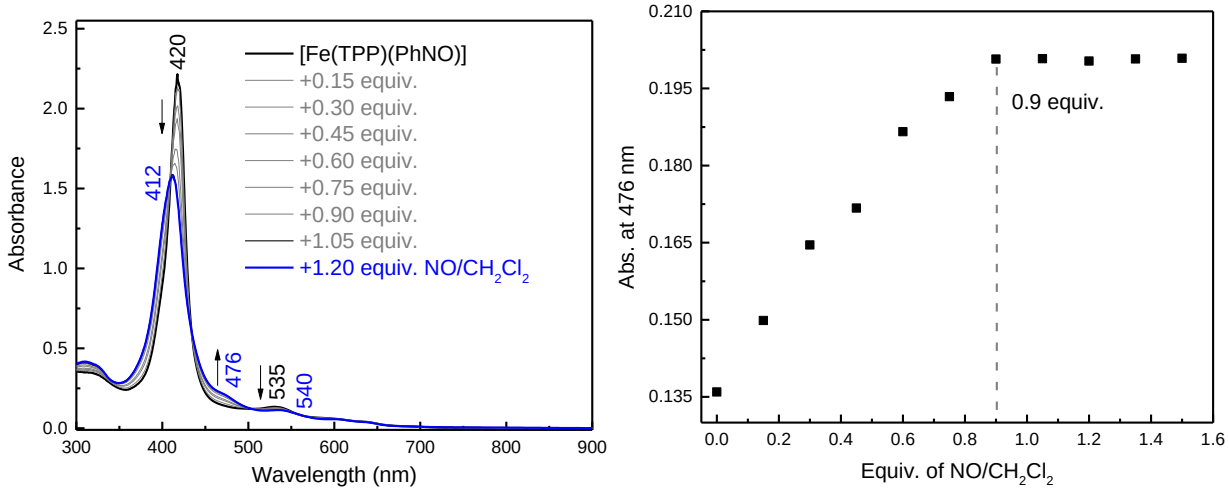

Figure 3.11. UV-vis spectra of the titration of ~14 μM [Fe(TPP)(PhNO)] (black) in THF with a NO saturated solution of dichloromethane, forming the ferrous NO complex [Fe(TPP)(NO)] (blue). Right: Changes in the absorption at 476 nm upon addition of the NO solution, showing that the reaction is complete after the addition of ~0.90 equivalent of the NO saturated dichloromethane solution.

result, we hypothesized that binding of an N-donor ligand, MI, to the iron center, leading to the corresponding 6C complex, [Fe(TPP)(PhNO)(MI)], could force the NO to react with the PhNO ligand, rather than NO simply binding to the iron center and displacing the RNO ligand. The [Fe(TPP)(PhNO)] complex in dichloromethane binds ~1 equivalent of MI to form the six-coordinate complex, [Fe(TPP)(PhNO)(MI)], as shown in Figure 3.12. The UV-vis spectra show that the Soret band shifts from 412 to 426 nm and the Q band at 523 shifts to 540 nm upon MI binding. Interestingly, this implies that heme RNO complexes have no *trans* effect, whereas {FeNO}^{7} complexes have a strong *trans* effect. This result compares well with a DFT study from our laboratory that predicts heme HNO complexes to have a significantly weaker σ-*trans* effect than that of NO, more comparable to that of CO.[27]

Scheme 3.3. Summary of the reactivity observed with five- and six-coordinate ferrous heme RNO (R = IPr, PhNO) complexes and NO with the TPP^{2-} co-ligand.

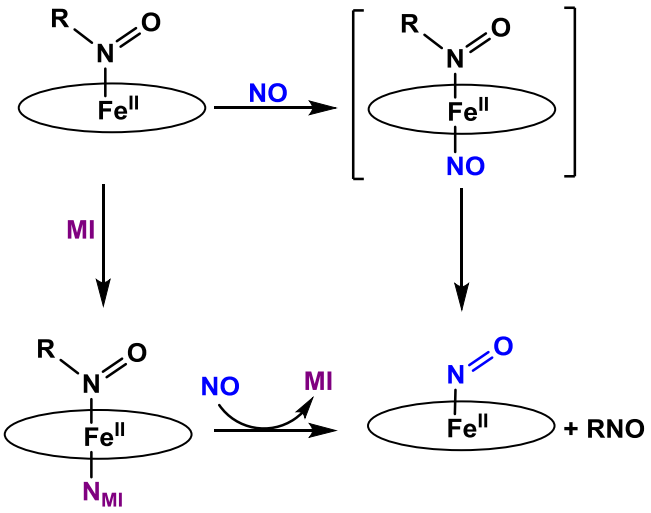

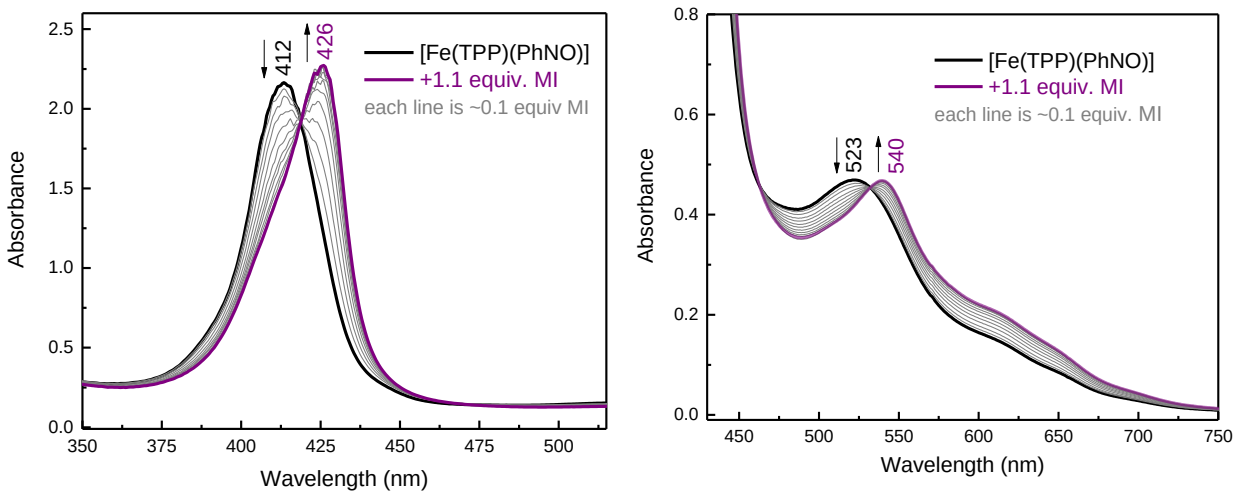

Figure 3.12. Left: UV-vis spectra of the titration of ~13 μM [Fe(TPP)(PhNO)] (black) with a solution of MI in dichloromethane, forming the six-coordinate complex [Fe(TPP)(PhNO)(MI)] (purple). Right: UV-vis spectra of the titration of ~51 μM [Fe(TPP)(PhNO)] (black) with a solution of MI in dichloromethane, forming the six-coordinate complex [Fe(TPP)(PhNO)(MI)] (purple). In both cases, the reaction is complete after the addition of ~1.0 equivalent MI to the solution.

We then reacted the six-coordinate adduct with low equivalents of NO gas in dichloromethane at room temperature. The UV-vis spectra of the products formed, shown Figure 3.13, are again identical to that of [Fe(TPP)(NO)]. We envisioned this could arise from (1) a weak Fe-RNO bond, or (2) the NO ligand having a higher binding constant than MI. Hypothesis (1) was tested by adding excess MI to a solution of [Fe(TPP)(PhNO)] in dichloromethane. In Figure 3.14, the UV-vis spectra show that the addition of 1 equiv. or 50 equiv. of MI results in no change in the UV-vis spectrum. We expected the formation of a ferrous bis-imidazole complex if the Fe-RNO bond is “weak”, but this is not the case (the ferrous bis-imidazole adduct has UV-vis bands at 430 and 536 nm). In summary, ferrous RNO complexes have strong Fe-NO bonds like ferrous heme-nitrosyls ($\{FeNO\}^7$) and ferrous heme CO complexes. Based on these findings, we can rule out hypothesis (1) and we believe that the NO ligand has a higher binding affinity for the iron center than the MI ligand (see Scheme 3.3).

Finally, we investigated the reactivity of [Fe(TPP)(iPrNO)] with excess NO gas. Unfortunately, we observed the same general findings as with the ferrous PhNO complex. In summary, even in the presence of MI we observe [Fe(TPP)(NO)] as the product of both reactions (see Figures 3.16 – 3.17). Overall, this shows that heme RNO complexes with the $TPP^{2=}$ porphyrin are generally unreactive toward NO and do not form N-N bonds.

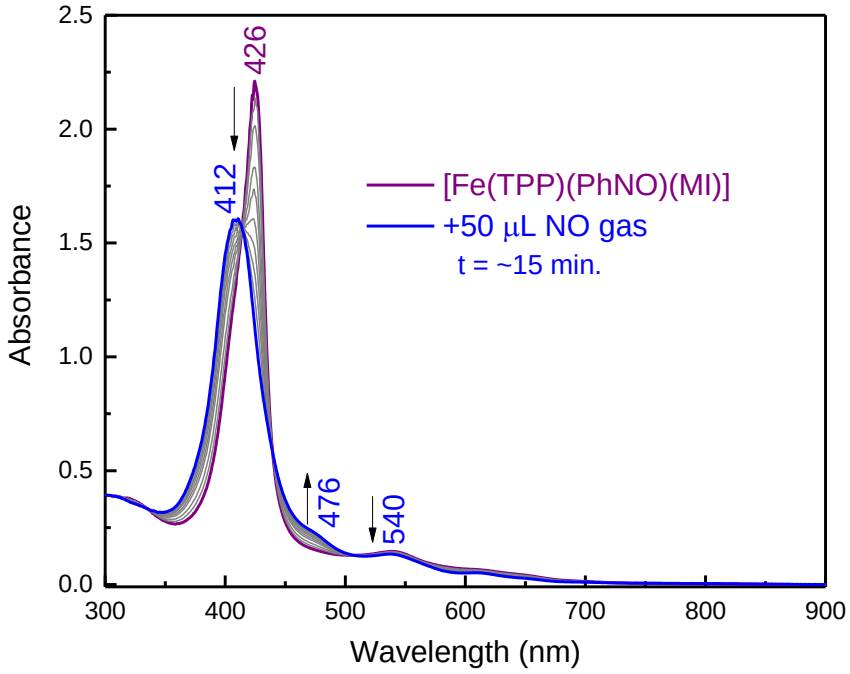

Figure 3.13. UV-vis spectra of [Fe(TPP)(PhNO)(MI)] (purple) and of the reaction product upon addition of 50 μL of NO gas (~6 equiv.) in dichloromethane, which is the ferrous NO complex, [Fe(TPP)(NO)] (blue).

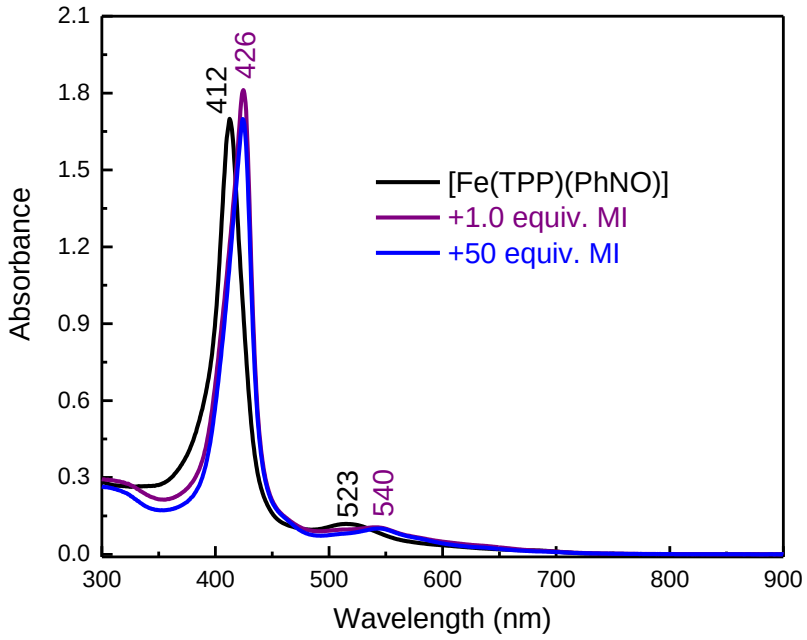

Figure 3.14. UV-vis spectra of a solution of [Fe(TPP)(PhNO)] (black), with ~1 equiv. MI added to the solution (purple), and 50 equiv. MI added to the same solution (blue).

Acid reactivity

We speculated that reaction of these iron(II)-RNO complexes with a strong acid could protonate the O-atom of the nitrosoalkane ligand, resulting in a formally iron(IV)-NORH complex as shown in Scheme 3.1. This species is an analogue for Intermediate *I* in P450nor and the oxidized species, formally Fe(IV)-$NHOMe^{-}$, as previously discussed. Since iPrNO leads to a better model (than PhNO) for ferrous HNO complexes, we investigated the reactivity of these compounds with acid.

The reaction of excess *p*-toluenesulfonic acid with [Fe(TPP)(iPrNO)] in dichloromethane resulted in no reaction by UV-vis spectroscopy in THF (even in the presence of >100 equiv. of acid). However, the reaction of [Fe(TPP)(iPrNO)] with excess (~18 equiv.) glacial acetic acid (AcOH) in dichloromethane resulted in a ferric complex with a bound acetate (OAc^{-}) ligand, as shown in Figure 3.15 (left). We initially confirmed the ferric product via ^{1}H-NMR spectroscopy. The formation of the ferric product is extremely slow and the reactions are stirred for ~24 hours to ensure full conversion to the ferric acetate complex. To further confirm the oxidation state of the product, we used EPR spectroscopy. [Fe(TPP)(iPrNO)] is diamagnetic and EPR silent, but the product (after acid addition and stirred for ~24 hours) exhibits an EPR spectrum that is characteristic of a high-spin ferric species ($g_x = g_y = 5.8$ and $g_z = 2.0$), as shown in Figure 3.15 (right). The spin quantification of this signal was 78% versus the [Fe(TPP)(Cl)] standard.

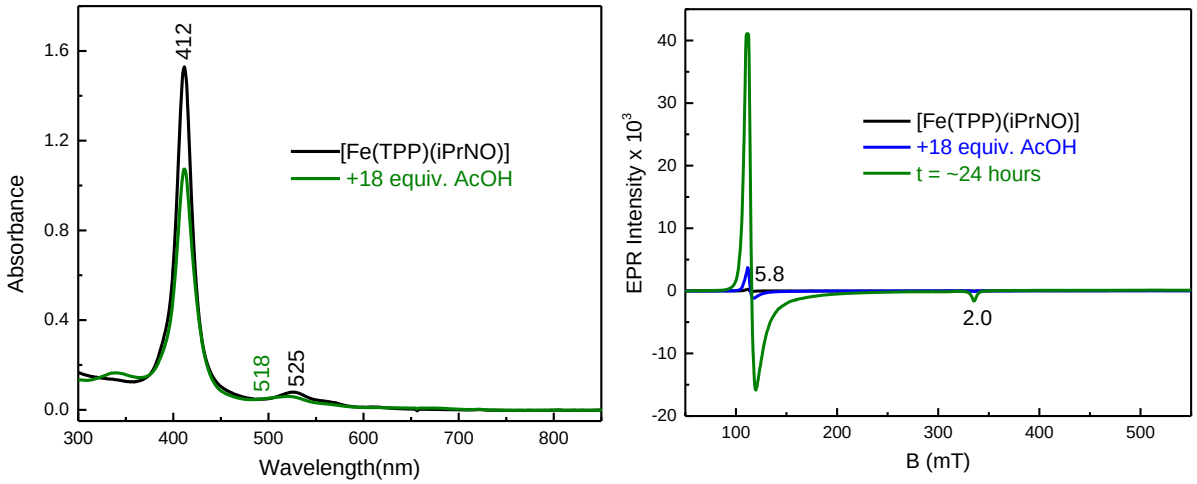

Figure 3.15. UV-vis spectra of [Fe(TPP)(iPrNO)] (black) and of the reaction of this complex with 18 equiv. of acetic acid after stirring for ~24 hours (green) in CH_2Cl_2. Right: EPR spectra of a ~4 mM solution of [Fe(TPP)(iPrNO)] (black) and of the product after reaction with 18 equiv. of acetic acid and stirring for ~24 hours (green; 18 equiv.) in CH_2Cl_2 measured at 4.2 K. The EPR signals are indicative of the formation of a high-spin ferric complex.

At this point, due to the large excess of AcOH required for the reaction to proceed, we tested using a stronger acid, trifluoroacetic acid (TFA), which resulted in the reaction to proceeding significantly faster with only ~4 equiv. of TFA needed. The UV-vis spectra shown in Figure 3.19 show a reaction product with features at 372, 411, and 510 nm. This left us with the question of what the organic reaction products are. We speculated that if the acid would protonate the RNO ligand, the product would likely be an iron(III)-NOHR(radical) complex, analogous to our observations in Chapter 2 A previous report in the literature found that NHOMe(radical) type molecules combine in solution to give a hyponitrous acid type species. It is farther proposed this species decomposes to give dinitrogen and

methanol as products.[45-47] Based on this report, we initially assumed that the reaction of the iron(II)-iPrNO complex with triflouroacetic acid results in protonation of the O-atom of the iPrNO ligand, generating an iron(III)-iPrNOH(radical) complex (based on the findings regarding the electronic structure of the Intermediate *I* model complex in Chapter 2), which then rapidly decomposes to a ferric trifluoroacetate complex, dinitrogen, and isopropanol (iPrOH). To check for iPrOH we used ^{1}H-NMR spectroscopy, since this molecule has a unique septet from the *CH*$(CH_3)_2$NO hydrogen and a doublet from the CH$(CH_3)_2$NO hydrogens of the isopropyl group. In the ^{1}H-NMR spectrum we observed an IPrX containing molecule; however, when the solution is spiked with iPrOH it does not line up with the IPrX species from our reaction. At this point, we speculated that iPrOH in the presence of TFA (and the iron complex) could make diisopropyl ether, or the corresponding ester, isopropyl trifluoroacetate. We obtained authentic standards of diisopropyl ether and isopropyl trifluooacetate and spiked our product solutions with them. Curiously, the chemical shifts of diisoproyl ether and isopropyl trifluoroacetate do not line up with our iPrX containing product either. It should also be noted that the iPrNO ligand does not decompose in the presence of excess TFA over a 24 hour time period by ^{1}H-NMR spectroscopy. Also, in the same time frame (~24 hours) the addition of excess TFA to a solution of iPrOH results in a tiny amount of isopropyl trifluoacetate (by ^{1}H-NMR spectroscopy). Based on these results, the product(s) if the reaction of [Fe(TPP)(iPrNO)] with excess TFA are not clear. In the next step, we tested whether the N-atom of iPrNO was present in the

Scheme 3.4. Proposed reactivity of [Fe(TPP)(iPrNO)] with acid resulting in an Intermediate *I* type model, which then decomposes into a ferric species, N_2O, and iPrOH.

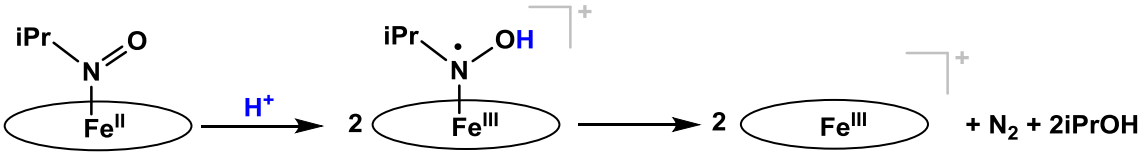

IPrX product. Since we do not observe any iPrOH (or related products) with *p*-toluenesulfonic acid this implies that the reaction might be driven by the carboxylate acid. We thought that the carboxylic acids react with the iPrNO ligand (bound to the iron complex) rather than undergoing the biologically relevant reaction that we initially proposed (see Scheme 3.4). To investigate this further, we carried out the reaction with the ^{15}N-labeled complex, [Fe(TPP)(iPr^{15}NO)] with excess HCl. The ^{15}N-nucleus couples to the protons of the methyl groups of iPrNO to give a quartet in the ^{1}H-NMR spectrum, rather than the usual doublet in the n.a.i. ligand. The ^{1}H-NMR spectrum of the reaction product revealed a quartet resonance, therefore indicating that the N-atom is still attached to the isopropyl group in the product. In future studies, the identification of the iPrNX containing species will be further pursued by GC-MS.

Discussion

In this work, we prepared the ferrous RNO complexes (where R = iPr, Ph) with the TPP^{2-} and 3,5-Me-BAFP^{2-} porphyrin co-ligands using established literature methods, and we fully characterized these complexes using UV-vis, IR, and ^{1}H-NMR spectroscopy. In addition, we obtained a series of new crystal structures for

these complexes. We have shown by UV-vis spectroscopy that the [Fe(TPP)(RNO)] complexes (R = iPr, Ph) in the presence of ~1 equiv. of MI generate the corresponding 6C complexes, [Fe(TPP)(RNO)(MI)]. This new finding shows that RNO ligands in ferrous heme complexes have do not elicit a significant *trans* effect, unlike the NO ligand in ferrous heme-nitrosyl complexes. This is further supported by crystal structures of [Fe(TPP)(RNO)(MI)] (R = iPr, PhNO), [Fe(TPP)(NO)(MI)], and [Fe(TPP)(CO)(MI)], which exhibit Fe-N_{MI} bond lengths of 2.05/2.03 Å, 2.173 Å, and 2.071 Å, respectively. By comparison, in [Fe(TPP)$(MI)_2$], where no *trans* interaction exists, the Fe-N_{MI} bond length is 1.997 Å.[48] Hence, ferrous heme RNO complexes are most similar to ferrous heme CO complexes that bind to ferrous hemes predominately via strong π-backbonds, which do not result in a strong *trans* effect. This provides strong support for previous, computational work on ferrous heme NHO complexes.[27]

In addition, we found that ferrous heme RNO complexes are unreactive toward NO, resulting in the formation of $\{FeNO\}^7$ complexes rather than N-N bond formation. This finding is consistent with previous work by our group that showed that the reaction of [Fe(3,5-Me-BAFP)(NHO)] with NO gas (in THF at room temperature) resulted in the formation of an $\{FeNO\}^7$ complex. However, we still cannot rule out ferrous heme NHO complexes as intermediates in P450nor, because a *trans* thiolate ligand (like in P450nor) may result in the activation of these complexes toward N-N bond formation by reaction with NO. For future studies, a ferrous RNO complex with a neutral thiol ligand could be synthesized to examine this point further. In addition, recent work by Richter-Addo and co-workers

provides evidence that the ferrous NHO complex, [Fe(OEP)(NHO)(5-MI)], reacts with NO at low temperature to generate N_2O (determined via gas head space analysis at room temperature).[49] The N_2O formed was not quantified, but mixed isotope labeling studies imply the produced N_2O indeed comes from a N-N bond forming reaction rather than simple HNO dimerization. Further proof is needed to validate these findings, but there results certainly indicate that ferrous HNO complexes may be catalytically competent in N-N bond formation in P450nor.

3.4 Experimental Section

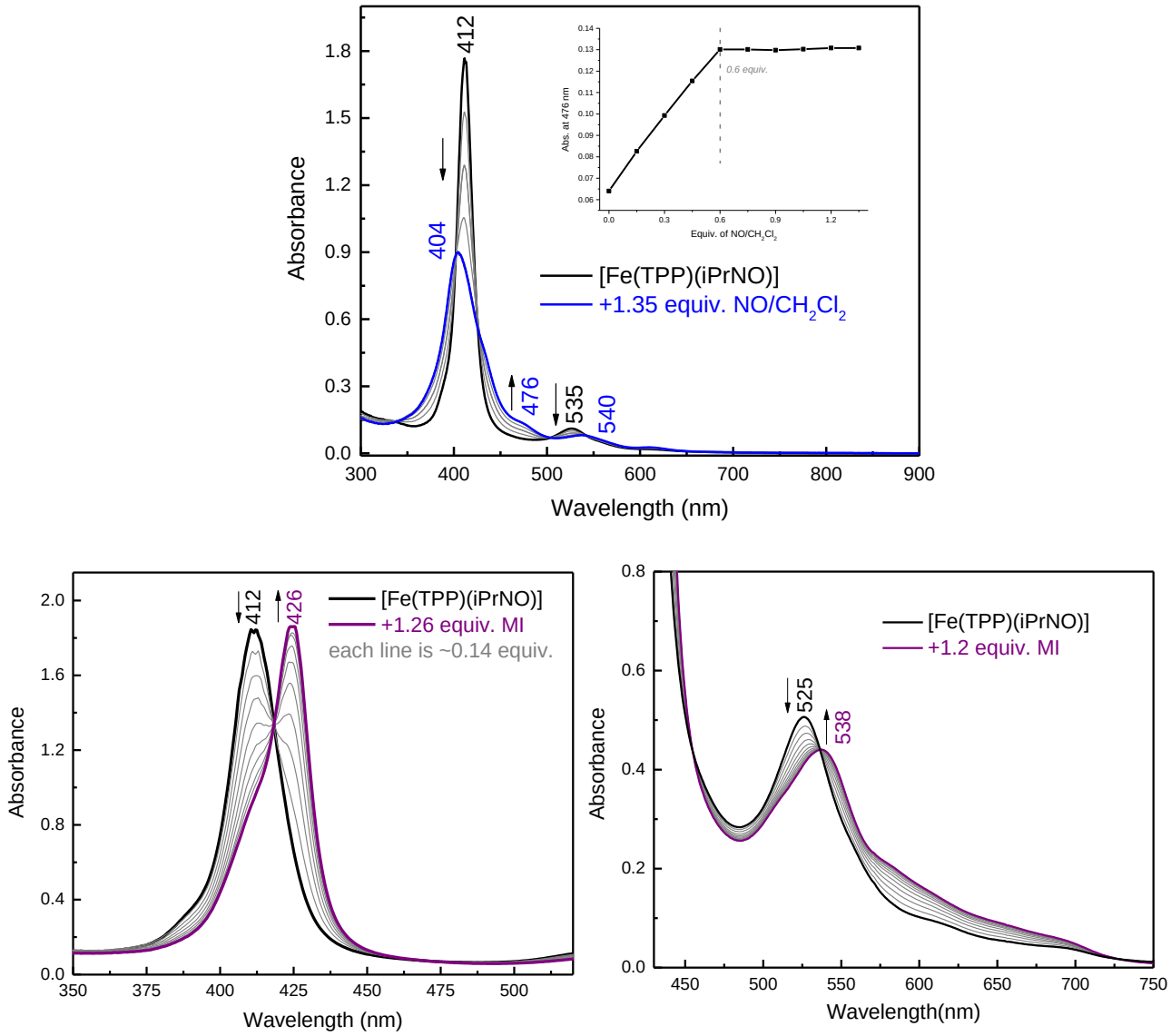

Figure 3.16. Top: UV-vis spectra of the titration of ~16 μM [Fe(TPP)(iPrNO)] (black) in CH_2Cl_2 with a NO saturated solution of dichloromethane, forming the ferrous NO complex [Fe(TPP)(NO)] (blue). Inset: Changes in the absorption at 476 nm upon addition of NO solution, showing that the reaction is complete after the addition of ~0.60 equivalent of the NO saturated dichloromethane solution. Bottom left: UV-vis spectra of the titration of ~16 μM [Fe(TPP)(iPrNO)] (black) with a solution of MI in dichloromethane, forming the six-coordinate complex [Fe(TPP)(iPrNO)(MI)] (purple). Bottom right: UV-vis spectra of the titration of ~74 μM [Fe(TPP)(iPrNO)] (black) with a solution of MI in dichloromethane, forming the six-coordinate complex [Fe(TPP)(PhNO)(MI)] (purple). The reaction is complete after the addition of ~1.0 equivalent MI to the solution.

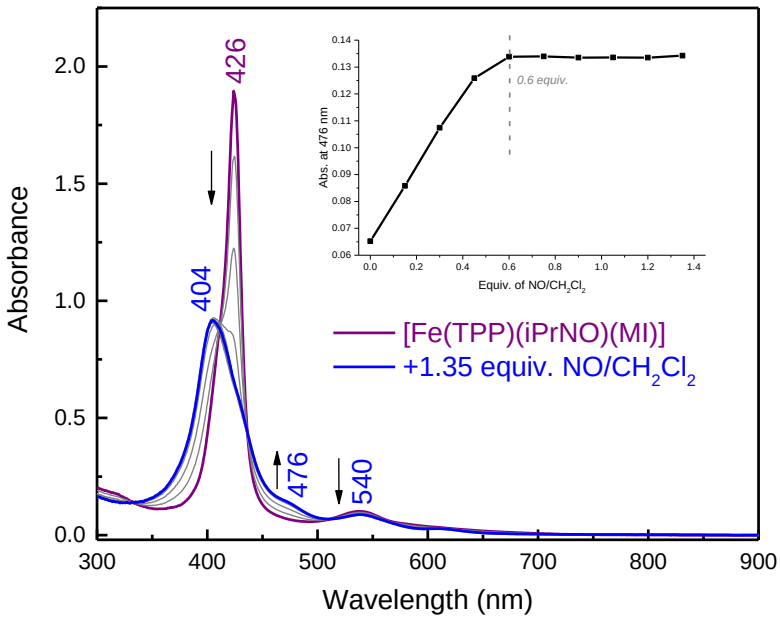

Figure 3.17. UV-vis spectra of the titration of ~16 μM [Fe(TPP)(iPrNO)(MI)] (purple) in CH_2Cl_2 with a NO saturated solution of dichloromethane, forming the ferrous NO complex [Fe(TPP)(NO)] (blue). Inset: Changes in the absorption at 476 nm upon addition of NO solution, showing that the reaction is complete after the addition of ~0.60 equivalent of the NO saturated dichloromethane solution.

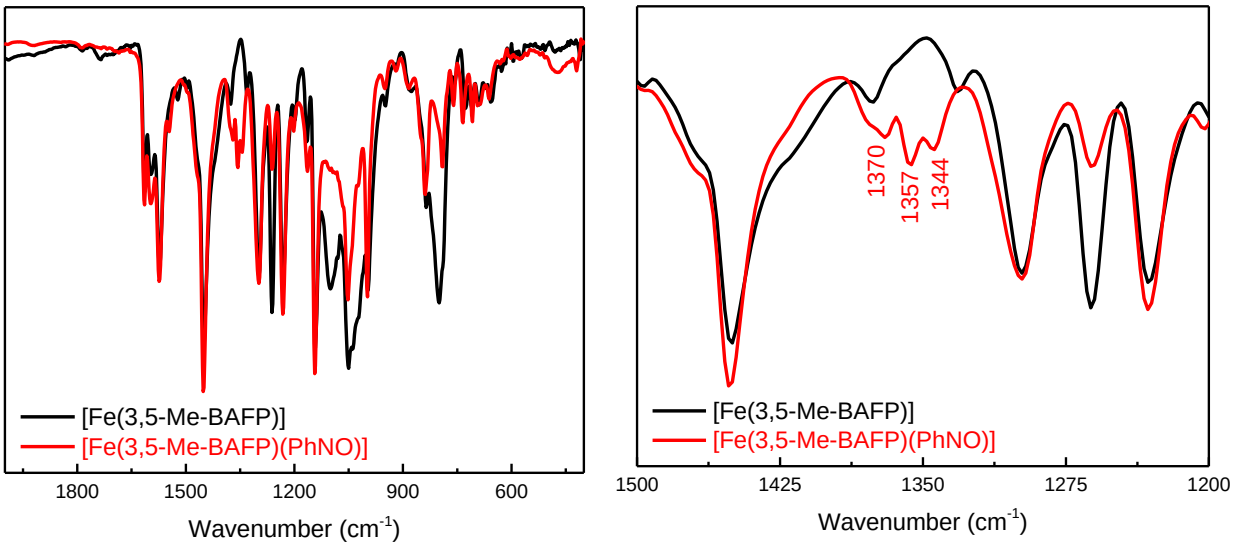

Figure 3.18. Left: Overlay of the IR spectra of the precursor, [Fe(3,5-Me-BAFP)] (black), and of the reaction product, [Fe(3,5-Me-BAFP)(PhNO)] (red), measured in KBr pellets. Right: Zoom into the N-O stretching frequency region of the IR spectra.

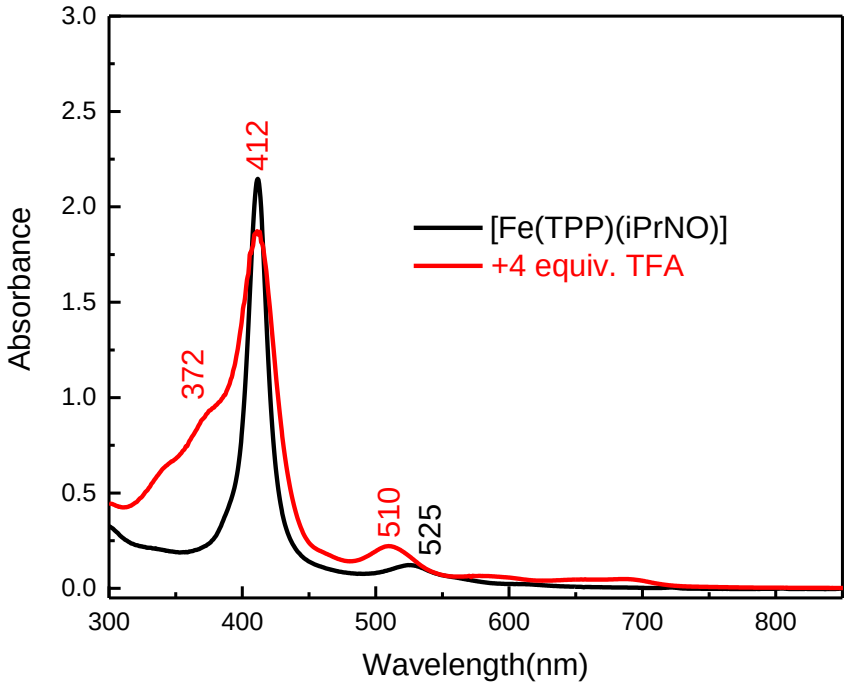

Figure 3.19. UV-vis spectra of [Fe(TPP)(iPrNO)] (black) and of the reaction product of this complex with excess trifluoroacetic acid (red; 4 equiv.) in CH_2Cl_2.

Synthesis

All reactions were performed under insert conditions using Schlenk techniques. Preparation and handling of air sensitive materials was carried out under a dinitrogen atmosphere in an MBraun glovebox equipped with a circulating purifier (O_2, H_2O < 0.1 ppm). Nitric oxide (Cryogenic Gases Inc., 99.5%) was purified by passage through an ascarite II column (NaOH on silica) followed by a cold trap at -80°C to remove higher order nitrogen oxide impurities. All solvents (including deuterated solvents) and 1-methylimidazole were distilled from CaH_2 under nitrogen, then degassed via five freeze-pump-thaw cycles. The purified solvents were stored over appropriate sized activated molecular sieves in the glovebox until used. N-isopropylhydroxylamine hydrochloride was purchased from TCI America and used without further purification. N-phenylhydroxylamine, ^{15}N-aniline, and ^{15}N-sodium nitrite were purchased from Sigma Aldrich and used without any further purification. [Fe(TPP)(Cl)], [Fe(TPP)(X)] where X = BF_4^-, PF_6^-, and SbF_6^-,[50] [Fe(TPP)],[15] and [Fe(TPP)$(PhNO)_2$][18] were synthesized as previously reported. Analogous ^{57}Fe complexes were synthesized in the same way using $^{57}FeCl_2$ dimethanol salt as the iron source.

Root Mean Square Deviation Determination. The RMSD is calculated by the following equation:[28]

$$RMSD = \sqrt{\frac{1}{N}\sum(dist)^2}$$

where *N* corresponds to the number of atoms that constitute the mean heme plane and *dist* is the distance (in Å) of a specific atom to the mean heme plane. The RMSD can be calculated from the 25-atom core displacement or the 4-atom *meso* carbon displacement.

Synthesis of Nitrosobenzene: Nitrosobenzene was synthesized using a modified literature procedure.[51] A 4.6 mL portion of aniline (50.4 mmol) was stirred in a mixture of 15 mL methanol and 23 mL water in an ice bath. To this solution, 28 mL H_2O_2 (30% w/v) was slowly added and the reaction mixture was stirred for 10 minutes. Then, 0.76 g MoO_3 (5.28 mmol) was added followed by 5 mL KOH (1 M), which caused the solution to turn orange-brown in color. The solution was allowed to stir for 6 hours in an ice bath. When the reaction was complete the solid was filtered off and washed with water (15 mL) and cold methanol (15 mL) to give a light yellow solid. The light yellow solid was dissolved in 50 mL absolute ethanol and allowed to precipitate in the -33°C freezer overnight. The following day the solution was vacuum filtered through a frit to give a white solid. Yield: 4.23 g (82%). ^{1}H-NMR (CD_2Cl_2, 400 MHz): δ = 7.621-7.906 (m, 5H). ^{13}C-NMR: ($CDCl_3$, 126 MHz) δ = 121.2 (s), 129.7 (s), 136.1 (s), 166.4 (s). IR ν(N-O) = 1589 cm^{-1}. UV-vis (CH_2Cl_2): 282, 304, 750 nm.

The corresponding ^{15}N-labeled nitrosobenzene compound was synthesized in the same way starting from ^{15}N-labeled aniline.

Synthesis of N-isopropylhydroxylamine: 1.0 g N-isopropylhydroxylamine hydrochloride (9 mmol) and 0.694 g potassium methoxide (9.9 mmol) were dispersed in 30 mL dichloromethane and allowed to stir for several hours. The next day the white precipitate (KCl) was filtered off and the filtrate was dried via rotary evaporation to give a white solid. Yield: 0.686 g (100%) ^{1}H-NMR ($CDCl_3$, 400 MHz): δ: 3.379 – 3.412 (sep, 1H); 1.276, 1.292 (d, 6H); ^{13}C-NMR ($CDCl_3$, 126 MHz): δ: 53.240 (s), 17.522 (s).

Synthesis of ^{15}N-Ispropylhydroxylamine: The first step of this reaction was carried out according to a previous report.[52] Reaction of 2-iodopropane and ^{15}N-sodium nitrite delivers a crude product that contains ^{15}N-2-nitropropane which, according to the literature, is purified via vacuum distillation to remove the impurities. We used the crude product for the following reaction based on a modified patent procedure. Here, ~0.5 g of crude ^{15}N-iPrNO_2 (~5.6 mmol), 96 μL acetic acid (16.8 mmol), and 0.550 g Zn powder (8.4 mmol) was added to 100 mL 95% ethanol and allowed to stir for 3 hours at 0°C. Then, the solvent was evaporated under vacuum to give a grey powder. The grey solid was washed with dichloromethane (to dissolve the product) and the filtrate was dried by rotary evaporation. Crude Yield: ~0.357g (~89%). The ^{1}H-NMR spectrum shows that a large amount of acetic acid is present in the solid, so the product was further purified. For this purpose, ~0.375 g of crude ^{15}N-Isopropylhydroxylamine (~5 mmol) and 0.351 g KOMe (5 mmol) were stirred in 10 mL dichloromethane for 2

hours. Then, the reaction was filtered through a cotton plug and the solvent was evaporated via rotary evaporation. The resulting oil was redissolved in 2 mL dichloromethane and layered with 48 mL hexanes and placed in the -33°C freezer. The next day the solution was filtered through a frit to give a white needle-like microcrystalline solid. The product was dried under vacuum for a few hours before further use. ^{1}H-NMR ($CDCl_3$, 400 MHz): δ: 3.150-3.118 (sep, 1H); 1.044, 1.067 (dd, 6H).

Synthesis of 2-methyl-2-nitrosopropane: 2-methyl-2-nitrosopropane was synthesized according to a modified literature procedure.[53] Under an inert atmosphere, 0.10 g (1.3 mmol) N-isopropylhydroxylamine was dissolved in 10 mL of dry methylene chloride and 0.404 g Ag_2CO_3 (1.46 mmol) was added, causing a black precipitate to form. Then, the reaction was brought outside the glovebox and stirred for one hour. The solution was filtered through a celite pad in a frit and the resulting filtrate was dried to an oil via rotary evaporation. The crude material was chromatographed on silica gel with CH_2Cl_2 as the eluent (in a 9 inch Pasteur pipet). The solvent was removed via rotary evaporation and the product was further dried under vacuum to give a white solid (the solid is assumed to be in the dimer form based on previous literature reports).[54,55] Yield: 32 mg (15%). ^{1}H-NMR ($CDCl_3$, 400 MHz): δ: 5.315-5.347 (sep, 2H); 1.35, 1.36 (d, 6H).

Synthesis of [Fe(TPP)(PhNO)]: There are two literature methods[16,17] reported to synthesize ferrous porphyrin RNO complexes: (1) reaction of a ferric porphyrin

chloride complex with excess RNHOH, and (2) reaction of a ferrous porphyrin complex with excess of the RNO ligand. In this work, we synthesized our ferrous heme RNO complexes using modified versions of these methods as described below to obtain the ferrous PhNO/Ph^{15}NO complexes. For the natural abundance isotopes (n.a.i.) complex, a 132 mg (0.175 mmol) portion of [Fe(TPP)(BF_4)] (also works with the PF_6^- or SbF_6^- counterions) and 95 mg N-Phenylhydroxylamine (0.880 mmol) were dissolved in 5 mL tetrahydrofuran. The solution was allowed to stir in the glovebox overnight and the reaction progress was monitored by UV-vis spectroscopy. The following day, the solution was layered with 40 mL hexanes and placed in the -33°C glovebox freezer. The next day the reaction mixture was vacuum filtered through a frit and washed with hexanes to give a dark purple powder. Yield: 120 mg (0.208 mmol, 89%). UV-vis (CH_2Cl_2): 412, 523 nm. UV-vis (THF): 420, 535 nm. ^{1}H-NMR (CD_2Cl_2, 400 MHz): $\delta =$ 8.58 (s); 8.014 (s); 7.72 (s); 6.339 – 6.509 (m); 6.014 (s). Anal. Calcd. for $C_{50}H_{33}FeN_5O$: C, 77.42; H, 4.29; N, 9.03. Found: C, 75.57; H, 4.59; N, 9.42. IR (KBr): ν(NO) = 1350, 1368 cm^{-1}.

Crystals suitable for X-ray diffraction were grown by vapor diffusion of hexanes into a concentrated THF solution of [Fe(TPP)(PhNO)] in the -33°C glovebox freezer.

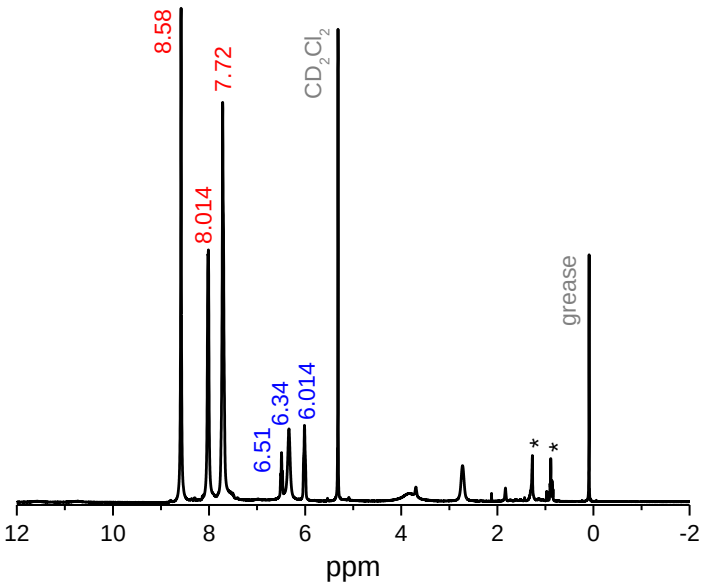

Figure 3.20. ^{1}H-NMR spectrum of [Fe(TPP)(PhNO)] in CD_2Cl_2 with the line width set to 0.3 Hz at room temperature. The *denotes residual hexanes from the recrystallization.

Synthesis of [Fe(TPP)(Ph^{15}NO)]: A 14 mg (0.021 mmol) portion of [Fe(TPP)] and 9 mg nitrosobenzene (0.083 mmol) were dissolved in 1 mL tetrahydrofuran and the resulting mixture was allowed to stir in the glovebox. The reaction progress was monitored by UV-vis spectroscopy. After one hour, the solution was layered with 15 mL hexanes and left in the -33°C freezer. After 2 days, the solution was filtered through a frit to give a dark purple powder. Yield: 11 mg (0.0142 mmol, 68%). The UV-vis data is identical to that of the n.a.i complex in THF: 420, 535 nm. $\nu(^{15}NO)$ = 1328, 1348 cm^{-1}.

Synthesis of [Fe(TPP)(iPrNO)]: Under inert atmosphere, 100 mg [Fe(TPP)] (0.15 mmol) and 21 mg iPrNO (0.3 mmol) were dissolved in 2 mL dry tetrahydrofuran. The reaction was stirred for one hour, and then was layered with 48 mL heptanes and placed in the -33°C glovebox freezer. The following day, the reaction was filtered through a frit and washed with cold heptanes to give a dark purple solid. Yield: 81.7 mg (67%). UV-vis (CH_2Cl_2): 412, 525 nm. UV-vis (THF): 417, 535 nm. ^{1}H-NMR (CD_2Cl_2, 400 MHz): $\delta = 8.73$ (s, β pyrrole H); 8.11 (s, *ortho*-H); 7.70 (s, *para*-, meta-H); -0.71 (s, $(CH_3)_2CH$NO); -2.07 (s, $(CH_3)_2$CHNO). The peaks were assigned based on a previous literature report.[16] Anal. Calcd. for $C_{47}H_{35}N_5O$ with one molecule of THF: C, 75.27; H, 5.33; N, 8.61. Found: C, 74.99; H, 5.11; N, 8.43. Crystals were grown by dissolving ~18 mg [Fe(TPP)(iPrNO)] in 0.2 mL THF and placing the solution in a 5 mm diameter glass tube. The solution was carefully layered with 2 mL hexanes, the tube was sealed with a septum, and left at room temperature in the glovebox. After 4 days crystals suitable for X-ray analysis were collected.

Synthesis of [Fe(TPP)(iPr^{15}NO)]: 70 mg [^{57}Fe(TPP)(SbF_6)] (0.077 mmol) were dissolved in 5 mL THF in the glovebox. To this solution, 29 mg (0.39 mmol) ^{15}N-isopropylhydroxylamine were added and the reaction mixture was allowed to stir overnight. The reaction progress was monitored by UV-vis spectroscopy. When the reaction was complete, the solution was layered with heptanes and placed in the glovebox -33°C freezer. The following day the solution was filtered through a

frit and washed with cold heptanes to give a dark purple solid. Yield: 62 mg (100%). The UV-vis and ^{1}H-NMR spectra are analogous to that of the n.a.i [Fe(TPP)(iPrNO)] complex.

The ^{57}Fe-labeled complex, [^{57}Fe(TPP)(iPrNO)], was synthesized using the same method, except that the precursor complex [^{57}Fe(TPP)(Cl)] was used.

Synthesis of [Fe(3,5-Me-BAFP)(PhNO)]: Under inert atmosphere, 117 mg [Fe(TPP)] (0.072 mixture) and 47 mg nitrosobenzene (0.44 mmol) were dissolved in 5 mL tetrahydrofuran. The reaction was stirred for 5 hours, and then was layered with 20 mL hexanes and placed in the -33°C glovebox freezer. The following day, the reaction was filtered through a frit to give a bright purple solid. Yield: 50 mg (0.029 mmol, 40%). UV-vis (THF): 426, 543 nm. ^{1}H-NMR (CD_2Cl_2, 400 MHz): $\delta =$ 8.91 (s, β pyrrole H); 7.51 – 7.55 (t); 6.89 (d); 6.38 (s); 1.93 (s).

Crystals were grown by dissolving ~5 mg [Fe(3,5-Me-BAFP)(PhNO)] in 0.2 mL 2-methyltetrahydrofuran and placing the solution in a 5 mm diameter glass tube. The solution was carefully layered with 1 mL hexanes, the tube was sealed with a septum, and left at room temperature in the glovebox. After 6 days crystals suitable for X-ray analysis were collected.

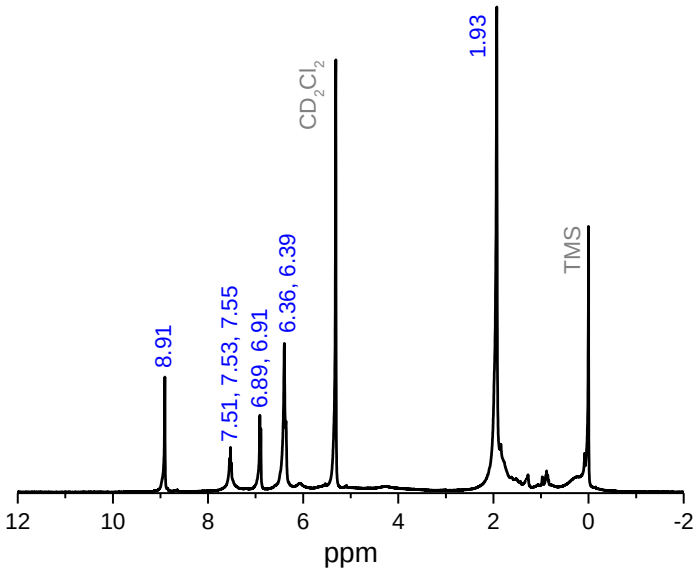

Figure 3.21. ^{1}H-NMR spectrum of [Fe(3,5-Me-BAFP)(PhNO)] in CD_2Cl_2 (with TMS) with the line width set to 0.3 Hz at room temperature.

Physical Methods

Infrared spectra were obtained from KBr disks on Perkin-Elmer BX or GX spectrometers at room temperature. Electronic absorption spectra were measured using an Analytical Jena Specord S600 instrument at room temperature. *In situ* UV-vis measurements were taken with a Hellma quartz immersion probe with a 10 mm path length. ^{1}H- and ^{13}C-NMR spectra were recorded on a Varian MR 400 MHz instrument or a Varian NMRS 500 MHz spectrometer at room temperature. Electron paramagnetic resonance spectra were recorded on a Bruker X-band EMX spectrometer equipped with Oxford Instruments liquid nitrogen and helium cryostats. EPR spectra were typically obtained on frozen solutions using 20 mW microwave power and 100 kHz field modulation with the amplitude set to 1 G. Sample concentrations were ~1 – 3 mM. Nuclear Resonance Vibrational

spectroscopy (NRVS) was carried out as previously described[56] at beamline 3-ID-XOR at the Advanced Photon Source (APS) at Argonne National Laboratory. This beamline provides about 2.5 x 10^9 photons/sec in ~1 meV bandwidth (8 cm^{-1}) at 14.4125 keV in a 0.5 mm (vertical) x 0.5 mm (horizontal) spot. Samples were loaded into 4 x 7 x 1 mm copper cells. The final spectra represent averages of 4 scans. The program Phoenix was used to convert the NRVS raw data to the Vibrational Density of States (VDOS).[57,58]

Crystal Structure Determination: A brown plate of [Fe(TPP)(iPrNO)] of dimensions 0.24 x 0.14 x 0.12 mm was mounted on a Rigaku AFC10K Saturn 944+ CCD-based X-ray diffractometer equipped with a low temperature device and Micromax-007HF Cu-target micro-focus rotating anode (λ = 1.54187 Å) operated at 1.2 kW power (40 kV, 30 mA). The X-ray intensities were measured at 85 K with the detector placed at a distance 42.00 mm from the crystal. A total of 3857 images were collected with an oscillation width of 1.0° in ω. The exposure times were 5 sec. for the low angle images, 30 sec. for high angle. The integration of the data yielded a total of 103181 reflections to a maximum 2θ value of 136.38° of which 7302 were independent and 7094 were greater than $2\sigma(I)$. The final cell constants were based on the xyz centroids 56915 reflections above $10\sigma(I)$. Analysis of the data showed negligible decay during data collection; the data were processed with CrystalClear 2.0 and corrected for absorption. The structure was solved and refined with the Bruker SHELXTL (version 2008/4) software package,[59] using the

space group P2(1)/c with Z = 4 for the formula $C_{51}H_{43}N_5O_2Fe$. All non-hydrogen atoms were refined anisotropically with the hydrogen atoms placed in idealized positions. Full matrix least-squares refinement based on F^2 converged at R1 = 0.0612 and wR2 = 0.1627 [based on $I > 2\sigma(I)$], R1 = 0.0621 and wR2 = 0.1635 for all data.

[Fe(TPP)(PhNO)]: A brown plate of [Fe(TPP)(PhNO)] of dimensions 0.22 x 0.14 x 0.12 mm was mounted on a Rigaku AFC10K Saturn 944+ CCD-based X-ray diffractometer equipped with a low temperature device and Micromax-007HF Cu-target micro-focus rotating anode (λ = 1.54184 Å) operated at 1.2 kW power (40 kV, 30 mA). The X-ray intensities were measured at 85 K with the detector placed at a distance 42.00 mm from the crystal. A total of 4223 images were collected with an oscillation width of 1.0° in w. The exposure times were 2 sec. for the low angle images, 12 sec. for high angle. Rigaku d*trek images were exported to CrysAlisPro for processing and corrected for absorption. The integration of the data yielded a total of 137394 reflections to a maximum 2q value of 147.91° of which 17016 were independent and 16662 were greater than $2\sigma(I)$. The final cell constants were based on the xyz centroids 67011 reflections above 10s(I). Analysis of the data showed negligible decay during data collection; the data were processed with CrystalClear 2.0 and corrected for absorption. The structure was solved and refined with the Bruker SHELXTL (version 2014/6) software package,[59] using the space group P1bar with Z = 2 for the formula $C_{114}H_{89}N_{11}O_4Fe_2$. All non-

hydrogen atoms were refined anisotropically with the hydrogen atoms placed in idealized positions. Full matrix least-squares refinement based on F^2 converged at R1 = 0.0436 and wR2 = 0.1159 [based on $I > 2\sigma(I)$], R1 = 0.0444 and wR2 = 0.1169 for all data.

[Fe(3,5-Me-BAFP)(PhNO)]: A brown block-like crystal of [Fe(3,5-Me-BAFP)(PhNO)] of dimensions 0.12 x 0.12 x 0.10 mm was mounted on a Rigaku AFC10K Saturn 944+ CCD-based X-ray diffractometer equipped with a low temperature device and Micromax-007HF Cu-target micro-focus rotating anode (λ = 1.54187 Å) operated at 1.2 kW power (40 kV, 30 mA). The X-ray intensities were measured at 85(1) K with the detector placed at a distance 42.00 mm from the crystal. A total of 4005 images were collected with an oscillation width of 1.0° in ω. The exposure time was 2 sec. for the low angle images, 10 sec. for high angle. The integration of the data yielded a total of 127465 reflections to a maximum 2θ value of 136.46° of which 8510 were independent and 8187 were greater than $2\sigma(I)$. The final cell constants were based on the xyz centroids 78234 reflections above $10\sigma(I)$. Analysis of the data showed negligible decay during data collection; the data were processed with CrystalClear 2.0 and corrected for absorption. The structure was solved and refined with the Bruker SHELXTL (version 2008/4) software package,[59] using the space group P2(1)/c with Z = 2 for the formula $C_{119}H_{107}N_5O_{10}Fe$. All non-hydrogen atoms were refined anisotropically with the hydrogen atoms placed in idealized positions. The complex lies on an inversion

center of the crystal lattice. The axial positions of the core iron atom have coordinated 2-Me-THF and nitrosobenzene molecules in a 1:1 ratio disordered over the inversion center. Full matrix least-squares refinement based on F^2 converged at R1 = 0.0428 and wR2 = 0.1112 [based on $I > 2\sigma(I)$], R1 = 0.0440 and wR2 = 0.1122 for all data.

DFT calculations. The structures were all optimized for the singlet ($S = 0$) ground states, using the BP86 functional[60,61] and the TZVP basis set.[62,63] Vibrational frequencies calculated for the structures showed no imaginary frequencies. In all calculations, convergence was reached when the relative change in the density matrix between subsequent iterations was less than 1×10^{-8}. All of these calculations were performed using the program package Gaussian 09.[64]

3.5 References

1. Mansuy, D.; Rouer, E.; Bacot, C.; Gans, P.; Chottard, J. C.; Leroux, J. P. *Biochem. Pharmacol.* **1978**, *27*, 1229-1237.

2. Bensoussan, C.; Delaforge, M.; Mansuy, D. *Biochem. Pharmacol.* **1995**, *49*, 591-602.

3. Delaforge, M.; Jaouen, M.; Mansuy, D. *Biochem. Pharmacol.* **1983**, *32*, 2309-2318.

4. O'Brien, P. J.; Wong, W. C.; Silva, J.; Khan, S. *Xenobiotica* **1990**, *20*, 945-955.

5. Belisario, M. A.; Pecce, R.; Garofalo, A.; Sannolo, N.; Malorni, A. *Toxicology* **1996**, *108*, 101-108.

6. Ringe, D.; Turesky, R. J.; Skipper, P. L.; Tannenbaum, S. R. *Chem. Res. Toxicol.* **1988**, *1*, 22-24.

7. Eyer, P. *Chem. Biol. Interact.* **1979**, *24*, 227-239.

8. Dölle, B.; Töpner, W.; Neumann, H. G. *Xenobiotica* **1980**, *10*, 527-536.

9. Klehr, H.; Eyer, P.; Schäfer, W. *Biol. Chem. Hoppe-Seyler* **1985**, *366*, 755-760.

10. Eyer, P.; Lierheimer, E. *Xenobiotica* **1980**, *10*, 517-526.

11. Enemark, J. H.; Feltham, R. D. *Coord. Chem. Rev.* **1974**, *13*, 339-406.

12. Riplinger, C.; Neese, F. *ChemPhysChem* **2011**, *12*, 3192-3203.

13. McQuarters, A. B.; Wirgau, N. E.; Lehnert, N. *Curr. Opin. Chem. Biol.* **2014**, *19*, 82-89.

14. Choi, I.-K.; Liu, Y.; Feng, D.; Paeng, K.-J.; Ryan, M. D. *Inorg. Chem.* **1991**, *30*, 1832-1839.

15. Goodrich, L. E.; Roy, S.; Alp, E. E.; Zhao, J.; Hu, M. Y.; Lehnert, N. *Inorg. Chem.* **2013**, *52*, 7766-7780.

16. Mansuy, D.; Battioni, P.; Chottard, J. C.; Riche, C.; Chiaroni, A. *J. Am. Chem. Soc.* **1983**, *105*, 455-463.

17. Sohl, C. D.; Lee, J.; Alguindigue, S. S.; Khan, M. A.; Richter-Addo, G. B. *J. Inorg. Biochem.* **2004**, *98*, 1238-1246.

18. Wang, L.-S.; Chen, L.; Khan, M. A.; Richter-Addo, G. B. *Chem. Commun.* **1996**, 323-324.

19. Lin, R.; Farmer, P. J. *J. Am. Chem. Soc.* **2000**, *122*, 2393-2394.

20. Abucayon, E. G.; Awasabisah, D.; Powell, D. R.; Richter-Addo, G. B. *Acta Crystallographica Section E* **2014**, *70*, m51-m52.

21. Godbout, N.; Sanders, L. K.; Salzmann, R.; Havlin, R. H.; Wojdelski, M.; Oldfield, E. *J. Am. Chem. Soc.* **1999**, *121*, 3829-3844.

22. Munro, O. Q.; Madlala, P. S.; Warby, R. A. F.; Seda, T. B.; Hearne, G. *Inorg. Chem.* **1999**, *38*, 4724-4736.

23. Hu, B.; Li, J. *Angew. Chem. Int. Ed.* **2015**, *54*, 10579-10582.

24. Immoos, C. E.; Sulc, F.; Farmer, P. J.; Czarnecki, K.; Bocian, D. F.; Levina, A.; Aitken, J. B.; Armstrong, R. S.; Lay, P. A. *J. Am. Chem. Soc.* **2005**, *127*, 814-815.

25. Scheidt, W. R.; Frisse, M. E. *J. Am. Chem. Soc.* **1975**, *97*, 17-21.
26. Wyllie, G. R. A.; Schulz, C. E.; Scheidt, W. R. *Inorg. Chem.* **2003**, *42*, 5722-5734.
27. Goodrich, L. E.; Lehnert, N. *J. Inorg. Biochem.* **2013**, *118*, 179-186.
28. Walker, F. A. *J. Inorg. Biochem.* **2005**, *99*, 216-236.
29. Safo, M. K.; Walker, F. A.; Raitsimring, A. M.; Walters, W. P.; Dolata, D. P.; Debrunner, P. G.; Scheidt, W. R. *J. Am. Chem. Soc.* **1994**, *116*, 7760-7770.
30. Scheidt, W. R.; Reed, C. A. *Chem. Rev.* **1981**, *81*, 543-555.
31. Lehnert, N.; Scheidt, W. R.; Wolf, M. W. In *Nitrosyl Complexes in Inorganic Chemistry, Biochemistry and Medicine II*; Mingos, D. M. P., Ed.; Springer Berlin Heidelberg: Berlin, Heidelberg, 2014, p 155-223.
32. Lehnert, N.; Sage, J. T.; Silvernail, N.; Scheidt, W. R.; Alp, E. E.; Sturhahn, W.; Zhao, J. *Inorg. Chem.* **2010**, *49*, 7197-7215.
33. Derbyshire, E. R.; Tran, R.; Mathies, R. A.; Marletta, M. A. *Biochemistry* **2005**, *44*, 16257-16265.
34. Denninger, J. W.; Marletta, M. A. *Biochim. Biophys. Acta* **1999**, *1411*, 334-350.
35. Karow, D. S.; Pan, D.; Davis, J. H.; Behrends, S.; Mathies, R. A.; Marletta, M. A. *Biochemistry* **2005**, *44*, 16266-16274.
36. Mansuy, D.; Chottard, J. C.; Chottard, G. *Eur. J. Biochem.* **1977**, *76*, 617-623.
37. Stone, J. R.; Marletta, M. A. *Biochemistry* **1995**, *34*, 16397-16403.
38. Romberg, R. W.; Kassner, R. J. *Biochemistry* **1979**, *18*, 5387-5392.
39. Lukat-Rodgers, G. S.; Rodgers, K. R. *Biochemistry* **1997**, *36*, 4178-4187.
40. Yang, L.; Ling, Y.; Zhang, Y. *J. Am. Chem. Soc.* **2011**, *133*, 13814-13817.
41. Van Stappen, C.; Goodrich, L. E.; Lehnert, N. In *The Chemistry and Biology of Nitroxyl (HNO)*; Farmer, P. J., Marti, M. A., Eds.; Elsevier: Boston, 2017, p 155-192.
42. Lehnert, N.; Berto, T. C.; Galinato, M. G. I.; Goodrich, L. E. In *The Handbook of Porphyrin Science*; Kadish, K. M., Smith, K. M., Guilard, R., Eds.; World Scientific: New Jersey, 2011; Vol. 14, p 1-247.
43. Cooper, C. E. *Biochim. Biophys. Acta* **1999**, *1411*, 290-309.
44. Hoshino, M.; Ozawa, K.; Seki, H.; Ford, P. C. *J. Am. Chem. Soc.* **1993**, *115*, 9568-9575.
45. Carey, F. A.; Hayes, L. J. *The Journal of Organic Chemistry* **1973**, *38*, 3107-3114.
46. Kaba, R. A.; Ingold, K. U. *J. Am. Chem. Soc.* **1976**, *98*, 7375-7380.
47. Malatesta, V.; Ingold, K. U. *J. Am. Chem. Soc.* **1974**, *96*, 3949-3954.
48. Li, J.; Nair, S. M.; Noll, B. C.; Schulz, C. E.; Scheidt, W. R. *Inorg. Chem.* **2008**, *47*, 3841-3850.
49. Abucayon, E. G.; Khade, R. L.; Powell, D. R.; Zhang, Y.; Richter-Addo, G. B. *J. Am. Chem. Soc.* **2016**, *138*, 104-107.

50. McQuarters, A. B.; Goodrich, L. E.; Goodrich, C. M.; Lehnert, N. *Z. Anorg. Allg. Chem.* **2013**, *639*, 1520-1526.

51. Defoin, A. *Synthesis* **2004**, *2004*, 706-710.

52. Leinisch, F.; Jiang, J.; Deterding, L. J.; Mason, R. P. *Molecules* **2011**, *16*.

53. Maassen, J. A.; de Boer, T. J. *Recl. Trav. Chim. Pays-Bas* **1971**, *90*, 373-376.

54. Gowenlock, B. G.; Luttke, W. *Quarterly Reviews, Chemical Society* **1958**, *12*, 321-340.

55. Emmons, W. D. *J. Am. Chem. Soc.* **1957**, *79*, 6522-6524.

56. Paulat, F.; Berto, T. C.; DeBeer George, S.; Goodrich, L.; Praneeth, V. K. K.; Sulok, C. D.; Lehnert, N. *Inorg. Chem.* **2008**, *47*, 11449-11451.

57. Sage, J. T.; Paxson, C.; Wyllie, G. R. A.; Sturhahn, W.; Durbin, S. M.; Champion, P. M.; Alp, E. E.; Scheidt, W. R. *J. Phys.: Condens. Matter* **2001**, *13*, 7707.

58. Sturhahn, W. *Hyperfine Interact.* **2000**, *125*, 149-172.

59. Sheldrick, G. M. In *SHELXTL*; v. 2008/4 ed.; Bruker Analytical X-ray: Madison, WI, 2008.

60. Perdew, J. P. *Physical Review B* **1986**, *33*, 8822-8824.

61. Becke, A. D. *Physical Review A* **1988**, *38*, 3098-3100.

62. Schäfer, A.; Horn, H.; Ahlrichs, R. *The Journal of Chemical Physics* **1992**, *97*, 2571-2577.

63. Schäfer, A.; Huber, C.; Ahlrichs, R. *The Journal of Chemical Physics* **1994**, *100*, 5829-5835.

64. Frisch, M. J.; Trucks, G. W.; Schlegel, H. B.; Scuseria, G. E.; Robb, M. A.; Cheeseman, J. R.; Scalmani, G.; Barone, V.; Mennucci, B.; Petersson, G. A.; Nakatsuji, H.; Caricato, M.; Li, X.; Hratchian, H. P.; Izmaylov, A. F.; Bloino, J.; Zheng, G.; Sonnenberg, J. L.; Hada, M.; Ehara, M.; Toyota, K.; Fukuda, R.; Hasegawa, J.; Ishida, M.; Nakajima, T.; Honda, Y.; Kitao, O.; Nakai, H.; Vreven, T.; Montgomery Jr., J. A.; Peralta, J. E.; Ogliaro, F.; Bearpark, M. J.; Heyd, J.; Brothers, E. N.; Kudin, K. N.; Staroverov, V. N.; Kobayashi, R.; Normand, J.; Raghavachari, K.; Rendell, A. P.; Burant, J. C.; Iyengar, S. S.; Tomasi, J.; Cossi, M.; Rega, N.; Millam, N. J.; Klene, M.; Knox, J. E.; Cross, J. B.; Bakken, V.; Adamo, C.; Jaramillo, J.; Gomperts, R.; Stratmann, R. E.; Yazyev, O.; Austin, A. J.; Cammi, R.; Pomelli, C.; Ochterski, J. W.; Martin, R. L.; Morokuma, K.; Zakrzewski, V. G.; Voth, G. A.; Salvador, P.; Dannenberg, J. J.; Dapprich, S.; Daniels, A. D.; Farkas, Ö.; Foresman, J. B.; Ortiz, J. V.; Cioslowski, J.; Fox, D. J.; Gaussian, Inc.: Wallingford, CT, USA, 2009.

Chapter 4

Ferric Heme-Nitrosyl Complexes: Synthesis, Spectroscopic Properties, and Stabilities

Nitric oxide (NO) is a toxic gas that has surprisingly important roles in biological systems. In mammals, NO plays a crucial role in nerve signal transduction, vasodilation, and immune response by white blood cells.[1-3] NO is produced *in vivo* by the nitric oxide synthase (NOS) family of enzymes.[4,5] In mammals, NO produced by endothelial NOS in the cardiovascular system is sensed by and subsequently activates soluble guanylate cyclase (sGC) and in this way, modulates arterial vasodilation.[6] Interestingly, certain blood-sucking insects such as *Rhodnius proxlixus* (known as the "kissing bug") and *Cimex lectularius* (known as the "bed bug") are taking advantage of NO's vasodilating effect. When these insects bite a victim, they use small NO-carrier proteins called nitrophorins (Nps) to inject NO into the bite to increase their blood meal.[7] Nps use ferric heme-nitrosyl complexes, or $\{FeNO\}^6$ in the Enemark-Feltham notation (where the superscript 6 represents the number of iron d electrons plus the unpaired electrons in the π* orbitals of NO),[8] for NO transport. Ferric heme-nitrosyl complexes are also important intermediates in dissimilatory denitrification.[9-11] Heme $\{FeNO\}^6$

complexes in proteins are generally six-coordinate (6C) and use either a neutral N-donor ligand such as histidine (His), or an anionic S-donor ligand such as cysteinate (Cys) as *trans* ligand to NO. Due to the significance of ferric heme-nitrosyl complexes in biology, it is important to understand their basic properties and reactivity. Synthetic model complexes are a great tool to study the fundamental properties of these complexes, and in comparison to the proteins, identify the different roles that the protein matrix plays in modulating their geometric and electronic structures, properties and reactivities. In the case of $\{FeNO\}^6$ complexes, proteins usually show NO binding constants in the $10^3 – 10^5$ range,[12-15] whereas corresponding model complexes are often times only stable in the presence of excess NO in solution. It is therefore believed that the protein matrix plays a significant role in stabilizing these species. As our work presented in this paper shows, this general conclusion is in fact incorrect.

The generally applied method for the preparation of ferric heme-NO complexes in the literature is the reaction of ferric heme precursors with weakly coordinating anions, [Fe(Porph)(X)] (X = BF_4^-, ClO_4^-, etc.; Porph = general porphyrin^{2-} ligand), with excess NO gas as shown in Scheme 4.1. This results in the formation of the respective five-coordinate (5C) ferric heme-nitrosyl complexes, [Fe(Porph)(NO)]X, and in the presence of an N-donor ligand (L), 6C complexes [Fe(Porph)(NO)(L)]X are formed. These $\{FeNO\}^6$ model systems are typically handled, stored, and redissolved under NO saturated conditions due to their inherent propensity to lose NO from the iron center.[16-20] Also, using this

method, the formed iron(III)-NO complexes react with any trace water (or bases such as methanol) in the presence of excess NO gas to form corresponding ferrous heme-NO, or {FeNO}^{7}, complexes. This process is called reductive nitrosylation, and has been studied in detail in the literature.[21-23] This frequently results in isolated mixtures of {FeNO}$^{6/7}$ complexes. Despite these difficulties, Scheidt and co-workers prepared and crystallized a series of 5C and 6C ferric heme-nitrosyl complexes with the OEP^{2-} (octaethylporphyrin^{2-}) co-ligand using this approach, and characterized these complexes by UV-Vis (in an NO atmosphere) and IR spectroscopy (in the solid state).[17,18,24,25] Besides OEP^{2-}, another synthetic porphyrin frequently applied in model complex studies is TPP^{2-} (tetraphenyl-porphyrin^{2-}). In the latter case, however, there are only three crystal structures of {FeNO}^{6} complexes available: [Fe(TPP)(NO)(H_2O)],[19] [Fe(TPP)(NO)(NO_2)],[25] and [Fe(TPP)(NO)(CO_2CF_3)].[26] Since model complex studies performed in our and many other laboratories are heavily based on TPP^{2-} and its derivatives,[16,27-38] we therefore set out to fill this knowledge gap and study the 5C and biologically relevant 6C {FeNO}^{6} complexes with the TPP^{2-} ligand.

In this work, we first prepared the {FeNO}^{6} complexes $[Fe(TPP)(NO)]^{+}$ and $[Fe(TPP)(NO)(MI)]^{+}$ using the established literature method, and we fully characterized these compounds using UV-Vis, IR, NMR and Nuclear Resonance Vibrational Spectroscopy (NRVS). In addition, we obtained the first crystal structures for these complexes. We further devised a new synthetic route to synthesize these {FeNO}^{6} complexes via chemical oxidation of the corresponding

{FeNO}^{7} precursor [Fe(TPP)(NO)], which can be accomplished by both chemical and electrochemical means as shown in Scheme 4.1. Using this method of preparation results in a surprisingly solution stable 5C {FeNO}^{6} complex that very slowly loses NO over a long period of time. With this notable stability, we also show that the oxidation of [Fe(TPP)(NO)] in the presence of ~1 equiv. MI generates the 6C {FeNO}^{6} complex [Fe(TPP)(NO)(MI)]$^+$ in pure form. The {FeNO}^{6} complexes generated via chemical oxidation have identical spectroscopic features to those made via the traditional method of preparation. The remarkable stability of the {FeNO}^{6} complexes against NO loss observed here differs from many previous reports in the literature. We attribute the accelerated NO loss in the latter cases to halide impurities, and we demonstrate that addition of halide to solutions of our {FeNO}^{6} complexes indeed leads to fast NO loss. In fact, the {FeNO}^{6} complexes obtained here via {FeNO}^{7} oxidation are stable enough to perform further studies on them in the absence of excess NO gas, which opens up the door for future reactivity studies on these complexes with reagents that would otherwise be susceptible to reaction with excess, free NO in solution.

Furthermore, as previously discussed, {FeNO}^{7} complexes are frequently synthesized by reductive nitrosylation (or commonly referred to as “autoreduction”) of ferric precursors. In many cases, this reaction is started from a ferric chloride complex, [Fe(Porph)(Cl)], that is reacted with excess NO gas in the presence of base (such as methanol). In the first step of the proposed mechanism, the ferric chloride complex binds NO to form the intermediate, [Fe(Porph)(NO)(Cl)], which

then reacts with the base resulting in a ferrous porphyrin complex (see Scheme 4.2). This autoreduction has been studied in detail, but there has been limited characterization of the elusive chloride-bound {FeNO}^{6} intermediate.[39] To learn more about this process, we synthesized the complex [Fe(TPP)(NO)(Cl)] and characterized it using different spectroscopic methods. We found that this complex loses NO from the iron center very easily and needs to be handled under an NO-

Scheme 4.1. Synthesis of iron NO complexes (MI = 1-methylimidazole) The oval represents the porphyrin ligand.

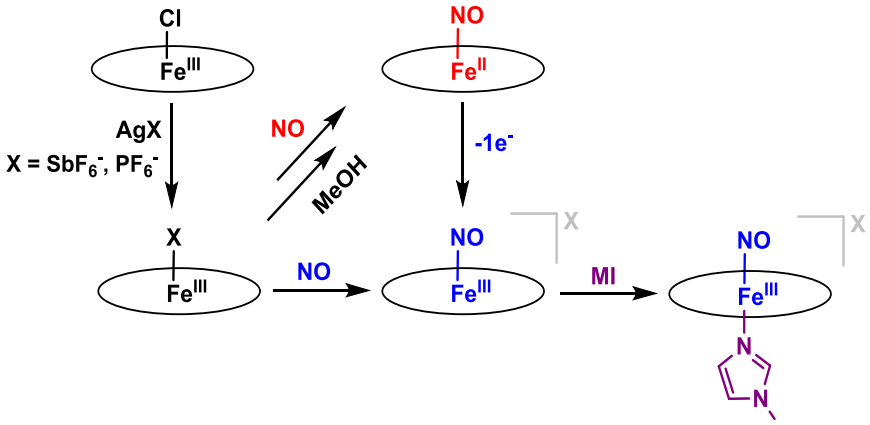

saturated atmosphere at all times. Finally, we also characterized this species using X-ray crystallography, which represents the first crystal structure of any [Fe(Porph)(NO)(Cl)] complex reported to this date.

This chapter focuses on the synthesis and spectroscopic characterization of a new series of ferric heme-nitrosyl complexes with the TPP^{2-} porphyrin ligand. Section 4.1 discusses the spectroscopic properties of {FeNO}^{6} complexes prepared by the two different methods (see Scheme 4.1). Section 4.2 investigates the stability of the {FeNO}^{6} complexes prepared by chemical oxidation of the

{FeNO}^{7} precursor. Section 4.3 discusses the crystallographic data of our series of {FeNO}^{6} complexes. Section 4.4 investigates the effect of halide salts on the stability of ferric heme-nitrosyl complexes. Section 4.5 discusses the electronic properties of {FeNO}^{6} complexes using NRVS. The studies described in this chapter are in part adapted with from a manuscript in preparation for Journal of the American Chemical Society.

4.1 Synthesis and Characterization of Ferric Heme-Nitrosyl Complexes

Preparation of {FeNO}^{6} Complexes using NO gas

Using standard literature procedures,[16,17] we reacted ferric porphyrins with the TPP^{2-} co-ligand, for example [Fe(TPP)(SbF_6)], with excess NO gas to form the corresponding five-coordinate (5C) {FeNO}^{6} complex, [Fe(TPP)(NO)]SbF_6. In the solid state, this compound has an N-O stretching frequency of 1850 cm^{-1} as shown in Figure 4.1 (bottom), which is consistent with the analogous OEP^{2-} complex (N-O stretching frequency is 1862 cm^{-1}).[19] The dissolution of the solid {FeNO}^{6} complex in dichloromethane (Figure 4.1, top) results in a UV-vis spectrum with a split Soret band at 370 and 411 nm and a Q band at 550 nm. The ^{1}H-NMR spectrum of the redissolved solid contains a multiplet of peaks from 7.70 – 7.88 ppm as shown in Figure 4.31, which is indicative of a diamagnetic iron heme complex, demonstrating that the complex is pure (NO loss results in a paramagnetic species). However, monitoring the solution over time by *in situ* UV-vis and solution IR experiments shows that the complex is *not stable*, and shows

signs of decomposition into a ferrous heme-nitrosyl complex after 2 hours (Figure 4.18). The Fe-NO unit is reduced by one-electron and the source of the electron is likely an impurity or potentially the solvent. Next, we synthesized the six-coordinate (6C) ferric heme-nitrosyl complex [Fe(TPP)(NO)(MI)]X (X = PF_6^-, SbF_6^-), and characterized this complex by UV-vis and IR spectroscopy. The UV-vis spectrum was obtained by reacting the ferric precursor complex with excess NO gas in the presence of ~1 equiv. 1-methylimidazole (MI), resulting in features at 430, 544, and 580 nm (see Figure 4.33, top). The UV-vis spectrum of this $\{FeNO\}^6$ complex is generally similar to that of [Fe(TPP)(NO)(NO_2)], previously reported by Scheidt and co-workers.[25] The IR of our 6C complex in the solid state shows a very intense N-O stretching frequency at 1918 cm^{-1}, and no feature at 1676 cm^{-1}, which would indicate the presence of an $\{FeNO\}^7$ impurity (see Figure 4.32). The dissolution of this $\{FeNO\}^6$ complex in dichloromethane (see Figure 4.33, bottom), monitored by UV-vis spectroscopy, shows decomposition of the complex into a ferric bis-imdazole complex, [Fe(TPP)($MI)_2$]SbF_6, and to ferric complex [Fe(TPP)(SbF_6)] via NO loss.

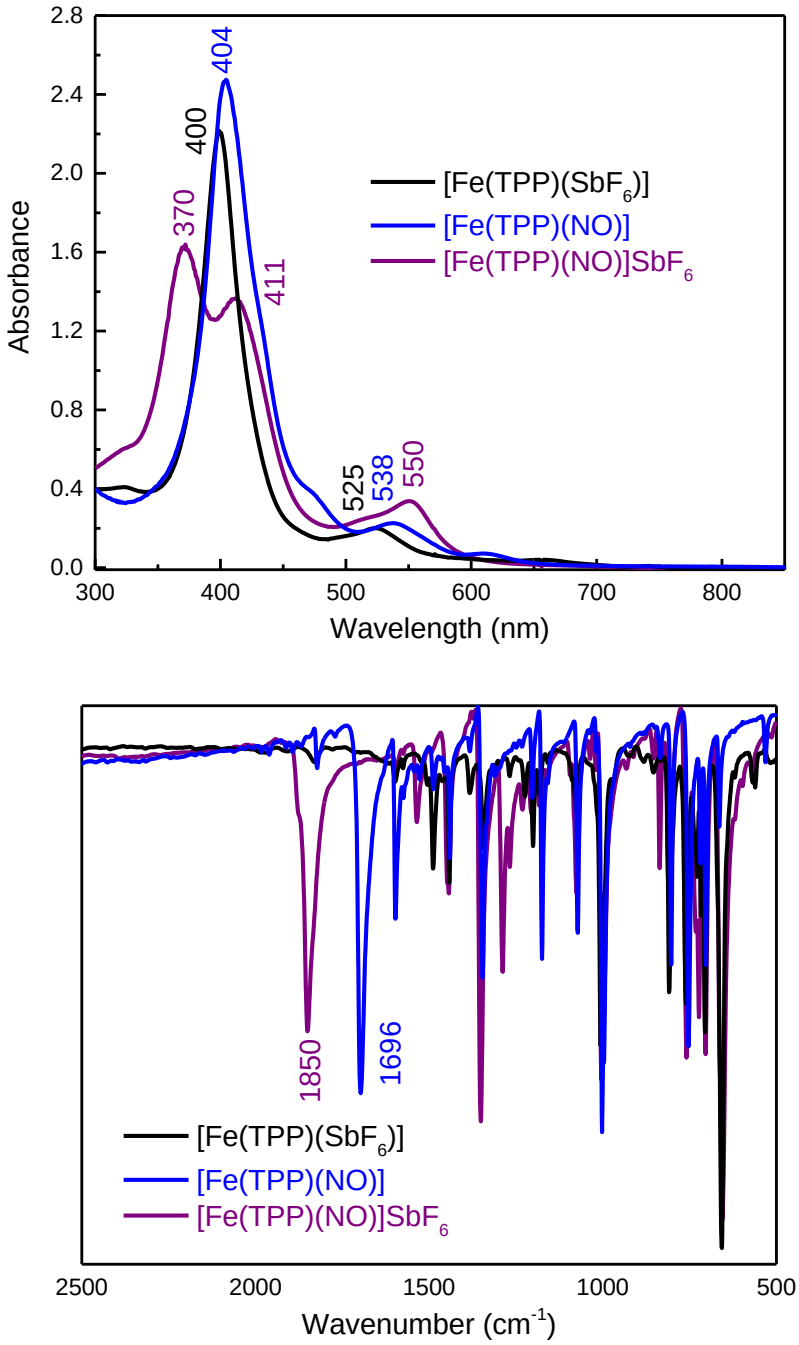

Figure 4.1. Top: Comparison of the UV-vis spectra of the precursor, [Fe(TPP)(SbF_6)] (black), the {FeNO}^{7} complex [Fe(TPP)(NO)] (blue), and the {FeNO}^{6} complex [Fe(TPP)(NO)]SbF_6 (purple, redissolved under non-NO saturated conditions), isolated from the reaction of the iron(III)-SbF_6 complex with excess NO gas in dichloromethane. All spectra recorded at room temperature. Bottom: Overlay of the IR spectra of the precursor, [Fe(TPP)(SbF_6)] (black), [Fe(TPP)(NO)] (blue), and [Fe(TPP)(NO)]SbF_6 (purple) measured in KBr pellets.

Preparation of {FeNO}^{6} Complexes via {FeNO}^{7} Oxidation

To overcome the problems with autoreduction and purity, we devised an alternative route to synthesize ferric NO complexes that was inspired by previous studies by Kadish and co-workers.[40] In their work, Cylic Voltammetry (CV) experiments on iron-NO complexes, such as [Fe(TPP)(NO)], were performed, and it was found that the one-electron oxidation of this complex is chemically reversible. Additionally, IR and UV-vis SpectroElectroChemical (SEC) studies of the 5C {FeNO}^{7} complex showed clean formation of the oxidized product, for example [Fe(TPP)(NO)]$^+$, at least on the CV timescale. In the presence of ~1 equiv. of N-donor ligands (such as pyridine), [Fe(TPP)(NO)(Py)]$^+$ and analogous complexes were formed. However, attempts to obtain {FeNO}^{6} heme complexes *on the preparative scale* by bulk electrolysis of the {FeNO}^{7} precursors resulted in direct decomposition, generating a ferric porphyrin complex with a weakly coordinating anion (determined by UV-Vis spectroscopy).[40] Since these pioneering studies, there have been no other attempts to synthesize {FeNO}^{6} complexes via one-electron oxidation of an {FeNO}^{7} precursor. With this in mind, we investigated the one-electron oxidation of the {FeNO}^{7} complex [Fe(TPP)(NO)], which itself was synthesized by reductive nitrosylation of [Fe(TPP)(SbF_6)] in a solution of methanol/dichloromethane that was exposed to excess NO gas. This reaction generates [Fe(TPP)(NO)] in pure form as judged by IR and ^{1}H-NMR spectroscopy (see Figure 4.30). Next, we measured the CV of the {FeNO}^{7} complex as shown in Figure 4.2. The CV shows the {FeNO}$^{7/8}$ reduction at an $E_{1/2}$ value of –1.37 V vs.

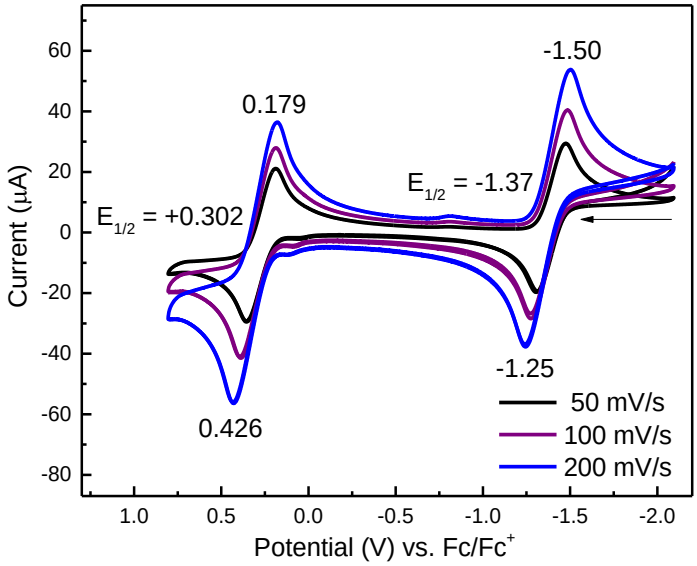

Figure 4.2. CV of ~6.6 mM [Fe(TPP)(NO)] in CH_2Cl_2 at room temperature. The working electrode was a glassy carbon and the counter electrode was a platinum electrode with a Ag wire pseudo-reference with tetrabutylammonium hexafluorophosphate was used as the electrolyte.

Fc/Fc^+ in CH_2Cl_2, which is chemically reversible and consistent with the literature value of -1.42 V (vs. Fc/Fc^+ in CH_2Cl_2).[28] The one-electron oxidation of the $\{FeNO\}^7$ complex is observed at an $E_{1/2}$ value of +0.302 V vs. Fc/Fc^+ in dichloromethane (+0.932 V vs. NHE). The $\{FeNO\}^{7/6}$ oxidation is also chemically reversible, and our results are consistent with the literature ($E_{1/2}$ = +0.356 V vs. Fc/Fc^+ in CH_2Cl_2).[40] In order to determine whether oxidation indeed produces the $\{FeNO\}^6$ complex, $[Fe(TPP)(NO)]^+$, we then carried out the corresponding UV-vis and IR SEC studies on the $\{FeNO\}^7$ complex. We can reversibly form the 5C $\{FeNO\}^6$ complex by SEC, and the spectroscopic data are consistent with the literature reports (see Figure 4.19 for UV-vis SEC and Figure 4.20 for IR SEC), and also the material that we obtained by reaction of [Fe(TPP)(X)] (X = PF_6^-, SbF_6^-) with NO gas (see above

and Table 4.1). In particular, the IR SEC data show the N-O stretching vibration at 1676 cm^{-1} in the starting $\{FeNO\}^7$ complex (in CH_2Cl_2), which decreases in intensity upon oxidation as a new band at 1850 cm^{-1} appears. Additionally, the UV-vis and IR SEC oxidations were completed in the presence of ~1 equiv. 1-methylimidazole (MI; as a model for His in proteins). Whereas ferrous heme-NO complexes have a strong σ trans effect, leading to low binding constants of N-donor ligands to 5C ferrous heme-nitrosyls,[29] the corresponding ferric complexes do not show this effect.[14] Hence, in the SEC experiments, oxidation of the 5C $\{FeNO\}^7$ complex generates the corresponding 6C complex $[Fe(TPP)(NO)(MI)]^+$ in the presence of MI (UV-Vis and IR SEC data for these transformations are shown in Figures 4.21 and 4.22). Interestingly, the re-reduction of the $\{FeNO\}^6$ complex at UV-Vis concentrations is not completely reversible and results in a mixture of the starting $\{FeNO\}^7$ complex and the ferric complex $[Fe(TPP)(MI)_2]^+$. To show this, we oxidized the [Fe(TPP)(NO)] complex in the presence of a large excess of MI, and observed a UV-vis spectrum that is identical to the ferric bis-imidazole complex $[Fe(TPP)(MI)_2]^+$. In the IR SEC experiments, the N-O stretching vibration of [Fe(TPP)(NO)] at 1676 cm^{-1} disappears upon oxidation, as new bands at 1920 and 1850 cm^{-1} appear (see Figure 4.22). The band at 1850 cm^{-1} corresponds to a small amount of the 5C $\{FeNO\}^6$ complex, $[Fe(TPP)(NO)]^+$, that does not have MI bound to the iron center.

With spectroscopic handles on 5C and 6C $\{FeNO\}^6$ complexes with the TPP^{2-} co-ligand established, we investigated whether the bulk generation of these complexes is possible via one-electron chemical oxidation of the corresponding $\{FeNO\}^7$ precursor. The UV-vis spectra in Figure 4.3 show the titration of [Fe(TPP)(NO)] (in CH_2Cl_2 solution) with the chemical oxidant 1,1'-diacetylferrocenium hexafluoroantimonate ($E_{1/2}$ = +0.49 V vs. Fc/Fc^+ in CH_2Cl_2),[41] abbreviated as [DAcFc][SbF_6] (dissolved in dimethoxyethane (DME)) at room temperature. The reaction is complete with ~1 equiv. of the oxidant and the UV-Vis data of the product exhibit features at 372, 404, and 550 nm that are identical to those of the UV-Vis SEC generated species (see overlay in Figure 4.4). The addition of excess ferrocene to the $\{FeNO\}^6$ solution reduces the complex back to

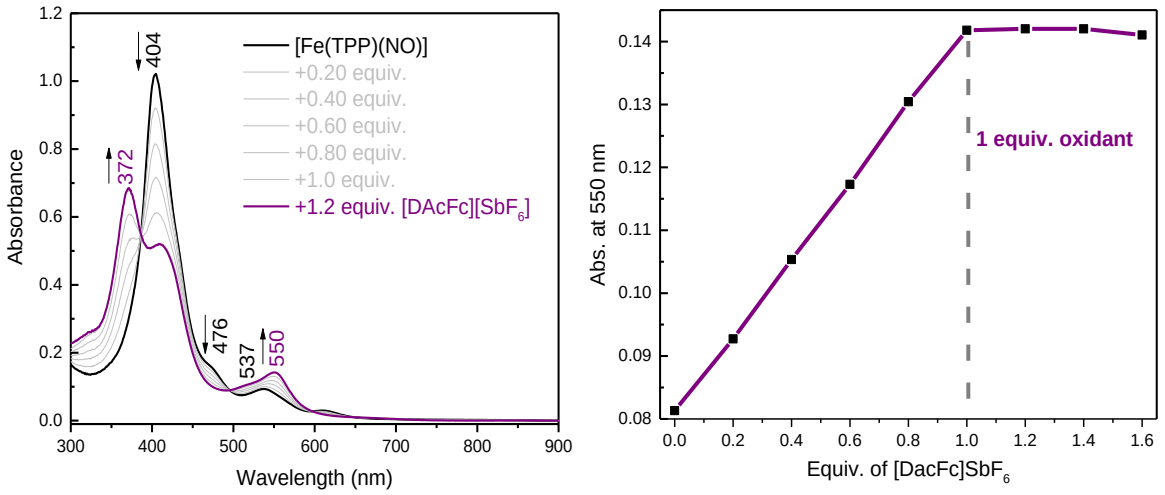

Figure 4.3. Left: UV-vis spectra of the titration of ~10 μM [Fe(TPP)(NO)] (black) with the chemical oxidant [DAcFc][SbF_6] (dissolved in dimethoxyethane) in dichloromethane, forming the ferric NO complex $[Fe(TPP)(NO)]^+$ (purple). Right: Changes of the absorption at 550 nm upon addition of the oxidant, showing that the reaction is complete after the addition of one equivalent of oxidant.

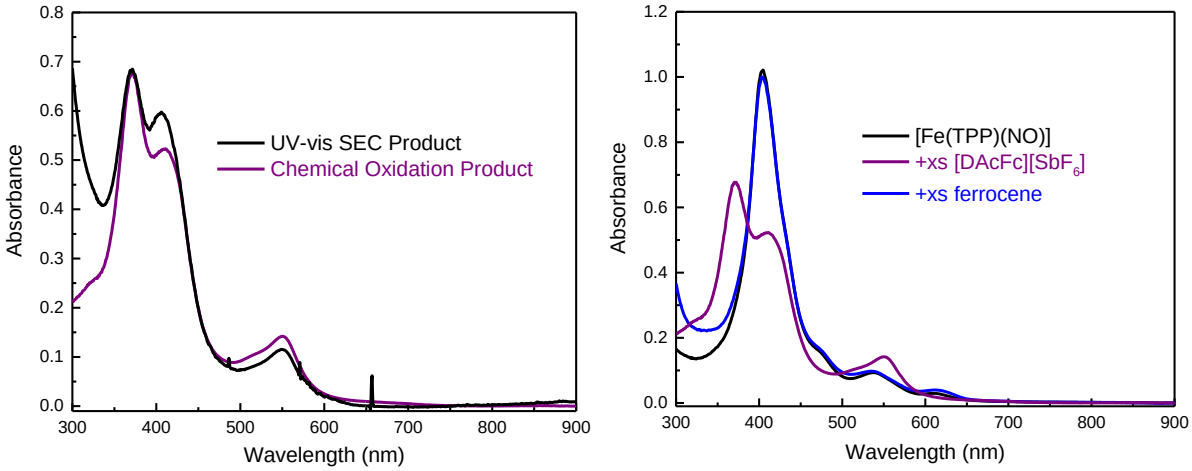

Figure 4.4. Left: UV-vis SEC used for the formation of $[Fe(TPP)(NO)]^+$ (black), compared to $[Fe(TPP)(NO)]^+$ (purple) generated by chemical oxidation, both recorded in dichloromethane. These data show that identical species are formed by both methods. Right: UV-vis spectra of [Fe(TPP)(NO)] before (black) and after addition of the chemical oxidant $[DAcFc][SbF_6]$ (dissolved in dimethoxyethane) in dichloromethane, leading to the formation of the ferric NO complex, $[Fe(TPP)(NO)]^+$ (purple). Subsequent reaction of the oxidized species with ferrocene reforms the $\{FeNO\}^7$ precursor (blue).

the starting ferrous NO complex, as shown in the UV-vis spectra in Figure 4.4. The 5C $\{FeNO\}^6$ complex can also be generated at higher concentrations (2 – 6 mM range) for characterization by solution IR spectroscopy. For these experiments, the $\{FeNO\}^7$ complex, [Fe(TPP)(NO)], was dissolved in dichloromethane and the resulting solution was then added to a slight excess of the solid oxidant, $[DAcFc][SbF_6]$, causing the solution to change color from orange-brown to bright red. The $\{FeNO\}^7$ precursor exhibits an intense N-O stretching vibration in dichloromethane at 1676 cm^{-1}, which shifts to 1850 cm^{-1} ($\Delta = 174$ cm^{-1}) upon oxidation as shown in Figure 4.5. Intense C-O stretching bands from the $[DAcFc]^{0/+}$ oxidant are also observed in the IR spectrum at 1672 and 1702 cm^{-1}, respectively. Finally, we followed the conversion of the $\{FeNO\}^7$ precursor to the $\{FeNO\}^6$

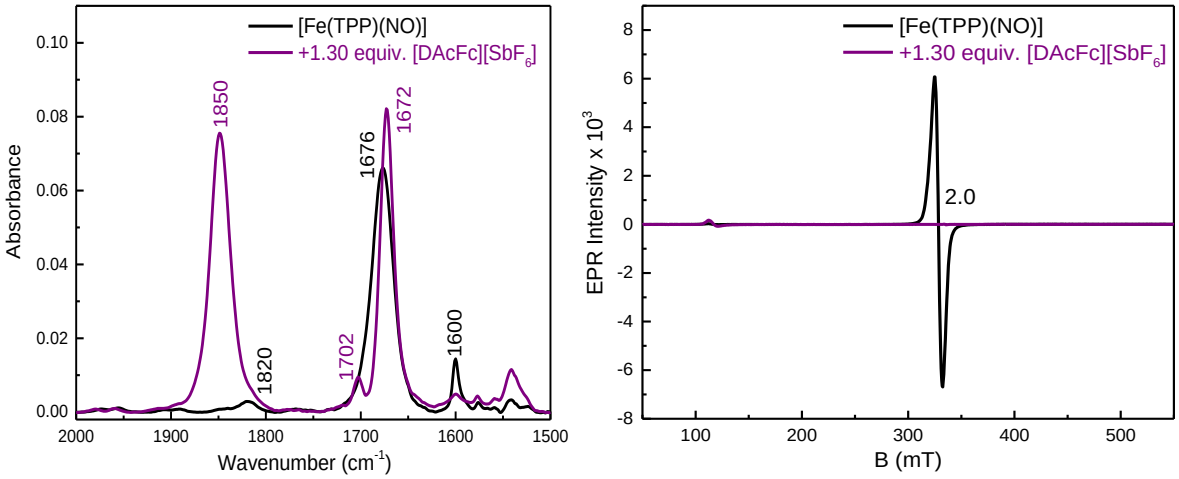

Figure 4.5. Left: Solution IR spectra of 1.8 mM [Fe(TPP)(NO)] (black) in CH_2Cl_2 and of the reaction product (purple) after the addition of ~1.30 equiv. [DAcFc][SbF_6] to the solution. The N-O stretch at 1676 cm^{-1} shifts to 1850 cm^{-1} upon oxidation. The bands at 1702 and 1672 cm^{-1} are the C-O stretching frequencies (ester groups) of the respective $DAcFc^{0/+}$ reagents. Right: EPR spectra of the same solution used for the solution IR experiments (on the left) at 4K. The black spectrum represents the $\{FeNO\}^7$ complex with a broad, isotropic S = 1/2 signal at g = 2.0, and the purple spectrum represents the solution of the corresponding oxidized species, $[Fe(TPP)(NO)]^+$, which is EPR silent and contains a minor g = 6 signal that spin integrates to <5% of a ferric impurity. The sample was spin integrated against [Fe(TPP)(Cl)] using SpinCount.

species by EPR spectroscopy. EPR spectra at 4K show that upon addition of the oxidant to the [Fe(TPP)(NO)] solution an EPR silent species is generated with a very minor high-spin ferric impurity that shows g values of ~5.7 (<5% from spin integration against [Fe(TPP)(Cl)]).

We further reacted the 5C $\{FeNO\}^6$ complex with ~1 equiv. of MI to form the 6C complex $[Fe(TPP)(NO)(MI)]^+$. The UV-vis spectrum of $[Fe(TPP(NO)(MI)]^+$, shown in Figure 4.36, has features at 430, 544, and 580 nm, which matches the spectra of the complex made from iron(III)-X with excess NO gas and 1 equiv. MI, and also the UV-vis SEC generated data (see Figure 4.23). Based on the UV-Vis data shown in Figure 4.36, the $[Fe(TPP)(NO)(MI)]^+$ complex can also be formed

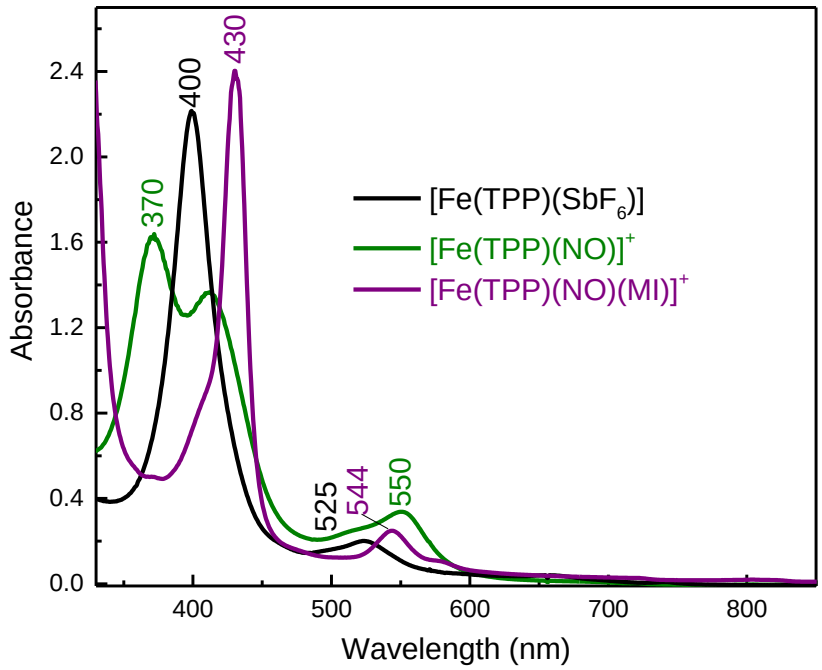

Figure 4.6. Comparison of the UV-vis spectra of the five-coordinate $\{FeNO\}^6$ complex $[Fe(TPP)(NO)]^+$ (green), to the six-coordinate complex $[Fe(TPP)(NO)(MI)]^+$ (purple), and the $[Fe(TPP)(SbF_6)]$ precursor in dichloromethane. All spectra recorded at room temperature.

by addition of ~1 equiv. MI to the $\{FeNO\}^7$ solution, followed by the addition of $[DAcFc][SbF_6]$, dissolved in DME. Figure 4.6 shows a comparison of the UV-Vis spectra of all relevant complexes. For the preparation of 2 – 6 mM solutions, the $\{FeNO\}^7$ complex, [Fe(TPP)(NO)], was dissolved in dichloromethane with ~1 equiv. MI and the resulting solution was then added to a slight excess of the solid oxidant, $[DAcFc][SbF_6]$, causing the solution to change color from orange-brown to deep red with a pink hue. The $\{FeNO\}^7$ precursor exhibits an intense N-O stretching band in dichloromethane at 1676 cm^{-1}, which shifts to 1920 cm^{-1} ($\Delta = 244$ cm^{-1}) upon oxidation in the presence of MI as shown in Figure 4.37. The small band at 1850 cm^{-1} can be attributed to the $[Fe(TPP)(NO)]^+$ complex. As

previously mentioned, intense C-O stretching bands from the $[DAcFc]^{0/+}$ oxidant are also observed in the IR spectrum at 1672 and 1702 cm^{-1}, respectively. Lastly, the conversion to the $\{FeNO\}^6$ complex was quantified by EPR spectroscopy. The oxidation product is EPR silent with only a small (~5%) high-spin ferric heme impurity (integrated against [Fe(TPP)(Cl)]).

In summary, we developed a new and convenient method to make preparative amounts of ferric heme-nitrosyl complexes via chemical oxidation of iron(II)-NO precursors at room temperature, and we characterized all products using different spectroscopic methods.

4.2 Stability of $\{FeNO\}^6$ Complexes

As mentioned above, the generally used literature method to synthesize both 5C and 6C ferric NO model complexes often results in inherently unstable species in solution that have a high propensity to lose NO over time (in the absence of excess NO gas). This is surprising, considering that analogous 6C ferric heme-NO complexes in protein active sites (where the proximal ligand is a histidine or cysteinate) are quite stable under NO-limited conditions.[12] The instability of the $\{FeNO\}^6$ heme model complexes makes studies of their basic properties and reactivity difficult in solution, since such studies require the presence of excess NO gas, which by itself is very reactive and can interfere with the desired reactivity studies. In contrast to these observations, we noticed that the $\{FeNO\}^6$ complexes, when generated via oxidation of the corresponding $\{FeNO\}^7$ precursors, are

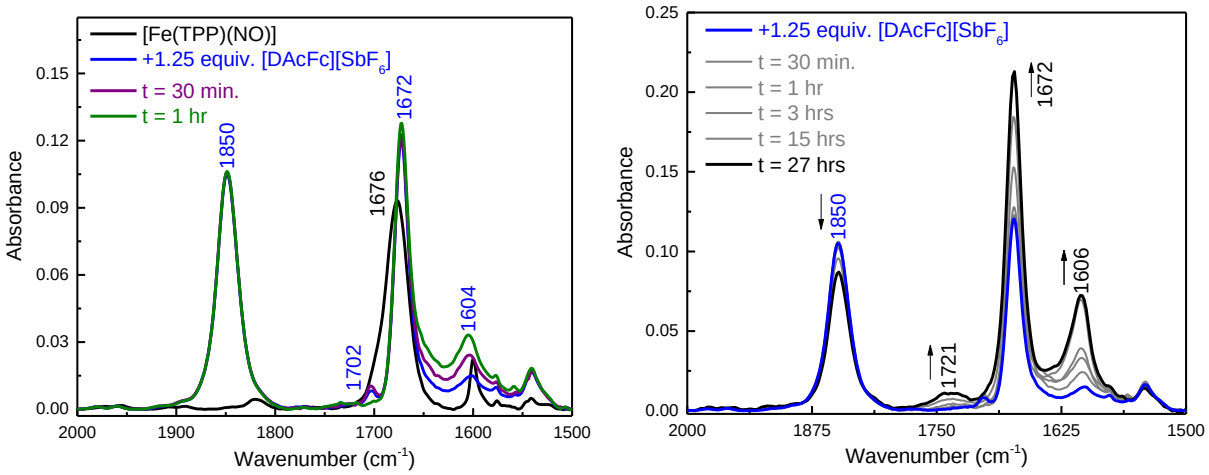

Figure 4.7. Left: Solution IR spectra of a 2.4 mM solution of [Fe(TPP)(NO)] (black) in CH_2Cl_2 and of the reaction product after the addition of ~1.25 equiv. [DAcFc][SbF_6] to the solution (shown in blue). The N-O stretching frequency of the {FeNO}^{6} complex at 1850 cm^{-1} remains unchanged after one hour of stirring in solution (green). The bands at 1672/1702 cm^{-1} belong to the DAcFc$^{0/+}$ oxidant. Right: Continued monitoring of the {FeNO}^{6} complex over a 27 hour time period shows minimal NO loss. For these experiments, aliquots were taken from a stirring solution and transferred into a solution IR cell.

surprisingly stable. To investigate this further, we took aliquots from the oxidation reaction solutions and monitored the changes in the IR spectra over a ~24 hour time period at room temperature. After a few hours, the N-O stretching frequency at 1850 cm^{-1} of the 5C complex completely overlayed with the initial IR spectrum, indicating minimal NO loss (see Figure 4.7). After >15 hours, the 1850 cm^{-1} band starts to slowly decrease in intensity; however, this change is very small indicating that the {FeNO}^{6} complex is quite stable in solution in the absence of excess NO. At the same time, the intensity of the C-O stretching band of reduced DAcFc at 1672 cm^{-1} increases notably. Since excess [DAcFc][SbF_6] oxidant is present in solution, we tested whether [DAcFc][SbF_6] is stable in DME (the oxidant is not soluble enough in dichloromethane for solution IR measurements). The IR spectra

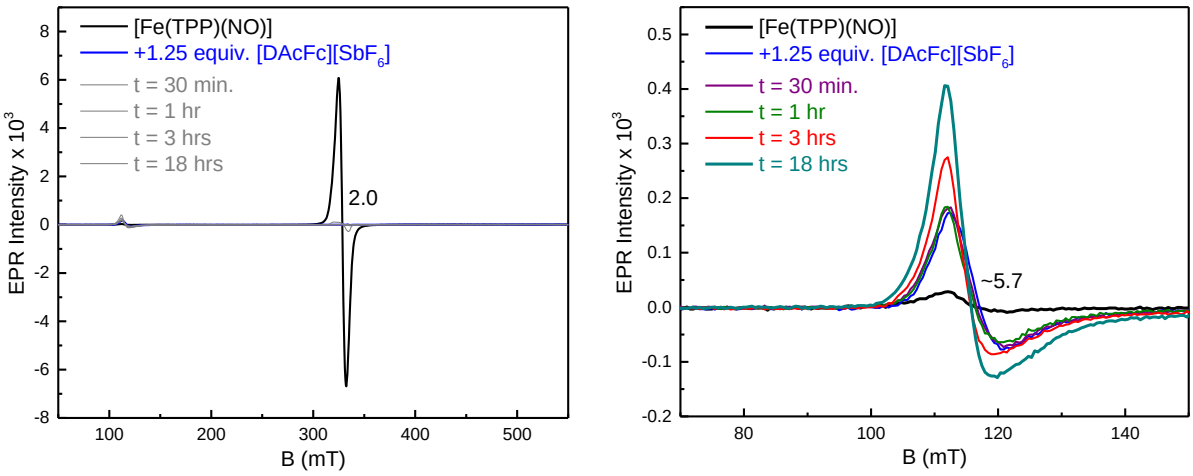

Figure 4.8. EPR spectra of the same sample measured in the solution IR experiments shown in Figure S19, obtained at 4K. The black spectrum represents the {FeNO}^{7} precursor with a broad, isotropic *S* = 1/2 signal at g = 2.0, and the blue spectrum represents the corresponding oxidized species, [Fe(TPP)(NO)]$^+$, which is EPR silent and contains a minor g = 6 signal that spin integrates to <5% of a ferric species. The sample was spin integrated against [Fe(TPP)(Cl)] using SpinCount.

in Figure 4.24 show that the oxidant [DAcFc][SbF_6] decomposes within 2 hours to form DAcFc and other decomposition products. Therefore, we believe that the increasing intensity of the band at 1672 cm^{-1} can be attributed to excess oxidant that decomposes over time. Another possibility is that some amount of {FeNO}^{7} complex is formed over time. This complex shows the N-O stretch at 1676 cm^{-1}, which could contribute to the intensity increase of the 1672 cm^{-1} feature. In order to test this further, EPR spectroscopy was used (Figure 4.8). In order to ensure consistency, we used the same solutions for solution IR and EPR spectroscopy (Figure 4.7 and Figure 4.8). At cryogenic temperatures of ~4 K, the {FeNO}^{7} precursor has a broad *S* = 1/2 signal with a g-value centered at 2.0 (note: when the temperature is raised to 77 K the typical rhombic spectrum with hyperfining coupling from the ^{14}N-atom of NO appears), and the addition of a slight excess of

[DAcFc][SbF_6] results in a completely EPR silent spectrum as shown in Figure 4.8. Over time (t = >15 hours), a small signal around g = ~6 appears in the EPR spectrum, which is indicative of a hs ferric heme complex resulting from NO loss. Spin integration of this signal against [Fe(TPP)(Cl)] shows that it corresponds to ~5% ferric complex. No formation of the {FeNO}^{7} complex is observed. In summary, the 5C {FeNO}^{6} complex is stable over extended periods of time in solution as shown by UV-vis, solution IR, and EPR spectroscopy. Analysis of the UV-vis data in Figure 4.25 estimates the k_{off} rate of NO for $[Fe(TPP)(NO)]^+$ to be ~4.7 x $10^{-5}s^{-1}$. For the six-coordinate adduct, $[Fe(TPP)(NO)(MI)]^+$, we monitored the stability of the complex by solution IR experiments shown in Figure 4.6. Over ~6 hours there a decrease in the intensity of NO band of the complex at 1920 cm^{-1} and an increase in the band at 1850 cm^{-1} from the five-coordinate complex, $[Fe(TPP)(NO)]^+$, as shown in (1). The imidazole complex, $[Fe(TPP)(MI)]^+$, has an extremely high binding affinity for another MI ligand resulting in bis-imdazole complex, $[Fe(TPP)(MI)_2]^+$ shown in (2).[42]

$$[Fe(TPP)(NO)(MI)]^+ \underset{}{\overset{k_1}{\rightleftharpoons}} [Fe(TPP)(MI)]^+ + NO \qquad (1)$$

$$[Fe(TPP)(MI)]^+ + [Fe(TPP)(NO)(MI)]^+ \xrightarrow{k_2} [Fe(TPP)(MI)_2]^+ + [Fe(TPP)(NO)]^+ \qquad (2)$$

Analysis of the UV-vis after the addition of MI to the solution of $[Fe(TPP)(NO)]^+$ results in a significantly faster k_{off} of 1.9 x 10^{-4} s^{-1} (Figure 4.26) than that of $[Fe(TPP)(NO)]^+$. The observed rate constant for $[Fe(TPP)(NO)(MI)]^+$ is consistent

with ferric heme NO complexes in protein environments, which have k_{off} rate constants that range from ~10^1 – 10^{-2} s^{-1} (includes Mb/Hb, NPs, HRP, NOS, and Cyt. P450s) .[12] In contrast, previous work with other model complexes shows much faster k_{off} rates of ~10^1 - 10^3 s^{-1}.[43,44]

4.3 Crystallographic Studies

With the long-term stability of $[Fe(TPP)(NO)]^+$ in solution established, we prepared the 5C $\{FeNO\}^6$ complex as described above from the chemical oxidant, [DAcFc][BF_4], and then layered the solution with hexanes and placed it in the -33°C freezer to obtain X-ray quality crystals (in the absence of excess NO gas!). The crystal structure of [Fe(TPP)(NO)]BF_4 is shown in Figure 4.9. In the unit cell, there are two unique $\{FeNO\}^6$ complexes with slightly different geometric parameters (see Table 4.1). The crystal structure of the complex exhibits a linear Fe-N-O unit and Fe-NO bond lengths of 1.640/1.665 Å. These bond lengths are in agreement with the crystal structure of [Fe(OEP)(NO]ClO_4, which exhibits an Fe-NO bond length of 1.644 Å.[19] Interestingly, the porphyrin is completely planar in the crystal structure of the 5C $\{FeNO\}^6$ complex with the OEP^{2-} co-ligand, but the heme plane is ruffled in our crystal structure of [Fe(TPP)(NO)]BF_4. A ruffling distortion is characterized by the rotation of *trans* pyrrole rings in the opposite direction around the Fe-$N_{pyrrole}$ bonds of the porphyrin co-ligand. This distortion is commonly observed in 5C ferric porphyrins because the iron sits above the heme plane. This out-of-plane distortion is measured by the root mean square deviation

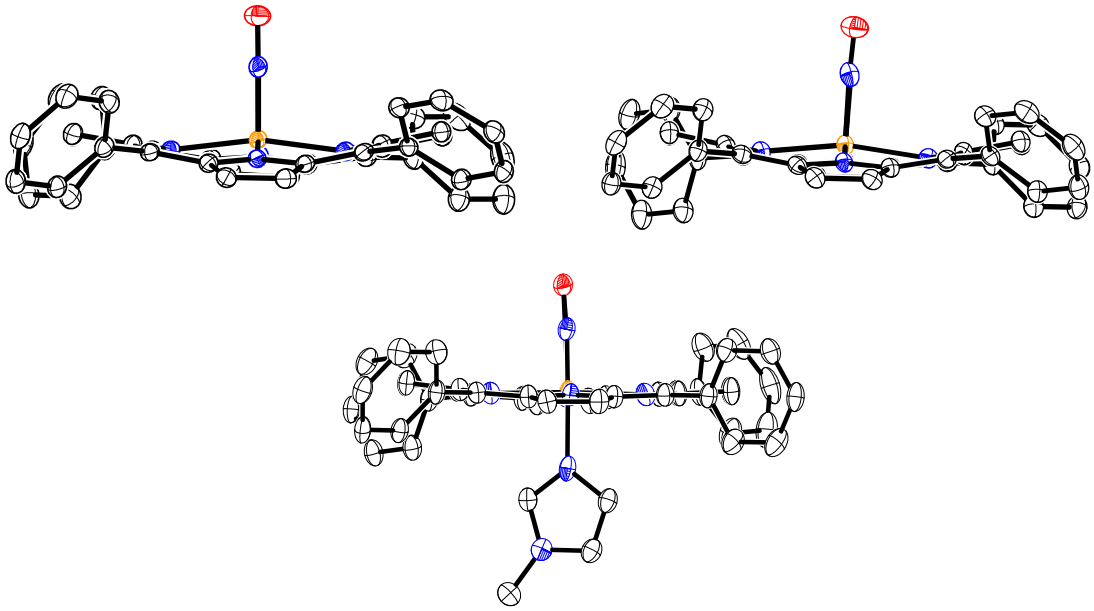

Figure 4.9. Top: Crystal structures of the two different 5C {FeNO}^{6} complexes in the unit cell for [Fe(TPP)(NO)]BF_4. Bottom: Crystal structure of [Fe(TPP)(NO)(MI)]PO_2F_2. In all structures, the hydrogen atoms, solvent molecules, and counterions are omitted for clarity. Thermal ellipsoids are shown at 40% probability.

(RMSD) of the porphyrin atoms from the heme plane. The 25-atom core displacement of [Fe(TPP)(NO)]BF_4 is 0.31 Å, whereas planar hemes are defined by a 25-atom core displacement of less than 0.10 Å.[7] For example, the completely planar complex [Fe(TMP)$(MI)_2$]ClO_4 (TMP^{2-} = tetramesitylporphyrin) has a 25-atom core displacement of 0.02 Å,[45] which is 15 times smaller than that of [Fe(TPP)(NO)]BF_4. The RMSD for the 4-atom *meso* carbon displacement of [Fe(TPP)(NO)]BF_4 is 0.077 Å. In addition, we crystallized the analogous {FeNO}^{6} complex with MI bound to the iron center. The bulk material, [Fe(TPP)(NO)(MI)]PF_6, was prepared by reaction of the ferric precursor with excess NO gas in dichloromethane. The dissolution of [Fe(TPP)(NO)(MI)]PF_6 in

Table 4.1. Comparison of geometric parameters for selected {FeNO}^{6} complexes.[a]

Complex	ΔFe-N_p[b]	ΔFe-NO	ΔFe-L	ΔN-O	<Fe-N-O[c]	Ref.
[Fe(TPP)(NO)]BF_4	1.986/1.990	1.640/1.665	-	1.153/1.124	178/177	t.w.
[Fe(OEP)(NO)]ClO_4	1.994	1.644	-	1.112	177	19
[Fe(TPP)(NO)(MI)]PO_2F_2	2.001	1.6275	1.973	1.148	176	t.w.
[Fe(TPP)(NO)(H_2O)]ClO_4	1.999	1.652	2.001	1.15	174	19
[Fe(TPP)(NO)(*i*-$C_5H_{11}OH$)]ClO_4	2.013	1.776	2.063	0.925	177	20
[Fe(OEP)(NO)(MI)]ClO_4	2.003	1.647	1.989	1.135	177	17
[Fe(OEP)(NO)(Pz)]ClO_4	2.004	1.627	1.988	1.141	177	17
[Fe(OEP)(NO)(Iz)]ClO_4	1.996	1.632	2.01	1.136	178	17
[Fe(TPP)(NO)(Cl)]	2.011	1.6685	2.013	1.201	180	t.w.
[Fe(TPP)(NO)(NO_2)]	1.996	1.671	1.998	1.144	169	25
[Fe(TPP)(NO)(CO_2CF_3)]	2.011	1.618	1.899	1.151	176	26
[Fe(OEP)(NO)(SR-H_2)[d]]	2.010	1.671	2.356	1.187	160	54

[a]All values given in Å or °; [b]Average value; [c]All values are given in degrees; [d]SR-H_2 = S-2,6-$(CF_3CONH)_2C_6H_3$.

dichloromethane, layered with hexanes under an NO atmosphere at -33°C, results in needle-like crystals. The crystal structure of this complex is shown in Figure 4.9. It should be noted that the counterion in this structure is $PO_2F_2^-$ as further discussed in the Experimental Section. This is the first crystal structure of a 6C ferric heme-nitrosyl complex with an N-donor ligand using TPP^{2-} as the porphyrin. In the crystal structure of [Fe(TPP)(NO)(MI)]PO_2F_2, the porphyrin co-ligand is completely planar, unlike the ruffled conformation of the heme in the 5C complex [Fe(TPP)(NO)]BF_4. The complex exhibits a linear Fe-N-O unit and the Fe-NO bond length is 1.628 Å, which is similar to other 6C ferric heme-nitrosyl complexes with neutral N-donor ligands that exhibit Fe-NO bond lengths ranging from 1.627 – 1.647 Å (Table 4.1).[17] It should be noted that this {FeNO}^{6} complex has a Fe-N_{MI} bond length of 1.973 Å that is slightly shorter than that in other neutral N-donor coordinated {FeNO}^{6} complexes with the OEP^{2-} co-ligand, which show Fe-N bond

lengths ranging from 1.996 – 2.003 Å as shown in Table 4.1. Finally, the average Fe-$N_{pyrrole}$ bond distance is 2.001 Å, similar to other 6C ferric heme-nitrosyl complexes.[17]

4.4 The Roles of Halides for Stability

With a stable 5C {FeNO}^{6} complex in hand, we further investigated the stability of this complex in the presence of halides. First, we generated the {FeNO}^{6} complex via chemical oxidation of the {FeNO}^{7} complex with [DAFc][SbF_6], and then reacted it with ~1 equiv. of tetrabutylammonium chloride (TBACl) and monitored the reaction using *in situ* UV-vis spectroscopy. Addition of [TBA][Cl] to the {FeNO}^{6} solution resulted in immediate formation of the ferric chloride complex

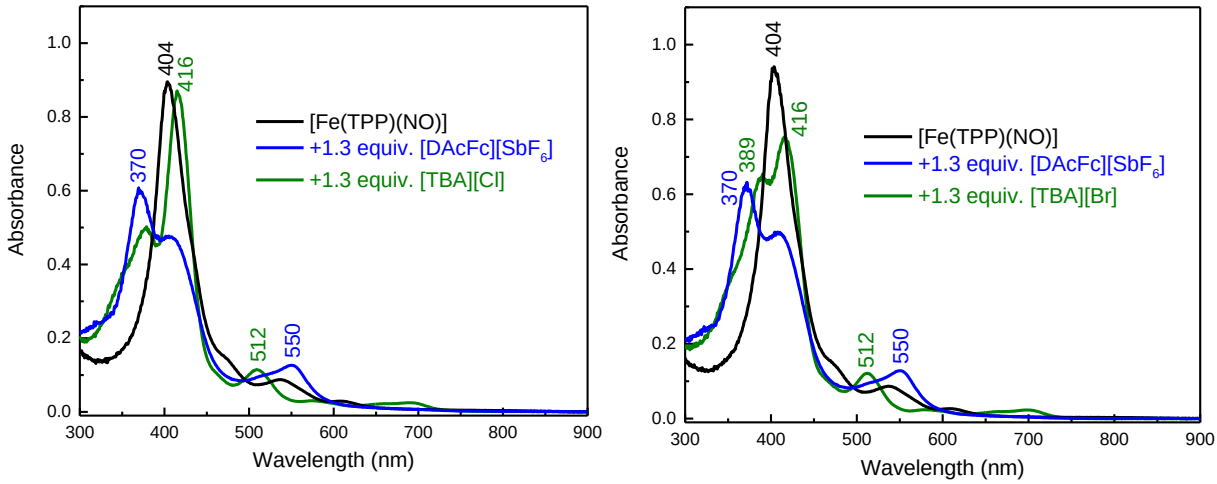

Figure 4.10. Top: Overlay of the UV-vis spectra of [Fe(TPP)(NO)] (black) and of the reaction product after the addition of ~1.30 equiv. [DAcFc][SbF_6] to the solution (blue), and of the product of the subsequent reaction with ~1.3 equivalent [TBA][Cl] (green). The later spectrum is identical to that of [Fe(TPP)(Cl)]. Bottom: Overlay of the UV-vis spectra of [Fe(TPP)(NO)] (black) and of the reaction product after the addition of ~1.30 equiv. [DAcFc][SbF_6] to the solution (blue), and of the product of the subsequent reaction with ~1.3 equivalent [TBA][Br] (green). The later species is likely [Fe(TPP)(Br)].

[Fe(TPP)(Cl)] and NO release as shown in Figure 4.10 (left). The same result is also obtained when $[Fe(TPP)(NO)]^+$ is reacted with [TBA][Br] forming a ferric bromide complex (Figure 4.10, right). This is consistent with previous work by Olson and co-workers, and shows that the $\{FeNO\}^6$ complex, [Fe(TPP)(NO)(Cl)], is not stable under non-NO saturated conditions. For future studies we plan to use stopped-flow UV-Vis measurements to determine the rates of the reaction of $[Fe(TPP)(NO)]^+$ with [TBA][Cl] and [TBA][Br].

The Quest for the Elusive Complex [Fe(TPP)(Cl)(NO)] – The Critical Intermediate in Reductive Nitrosylation

Ferrous heme-nitrosyl complexes, $\{FeNO\}^7$, are typically synthesized by reductive nitrosylation as mentioned in the Introduction. In reductive nitrosylation, a ferric chloride complex, [Fe(Porph)(Cl)] (where $Porph^{2-}$ = a $porphyrin^{2-}$ co-ligand), is typically reacted with excess NO gas in the presence of a base (such as methanol). In the first step, as shown in Scheme 4.2, the ferric chloride complex binds NO to the iron center to form a 6C ferric heme-nitrosyl complex, [Fe(Porph)(NO)(Cl)], which then reacts with the base to form HCl, RNO_2, and a ferrous porphyrin complex. The ferrous heme then binds

Scheme 4.2. The reductive nitrosylation mechanism (or known as autoreduction).

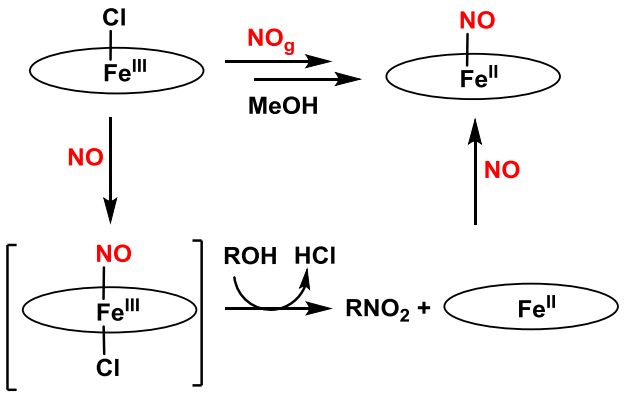

another equivalent of NO to generate the respective {FeNO}^{7} complex.[12] The key intermediate for this process, [Fe(Porph)(NO)(Cl)], has so far only been poorly characterized in the literature. In a previous report over 30 years ago, Olson and co-workers describe the reaction of [Fe(TPP)(Cl)] with excess NO gas to form [Fe(TPP)(Cl)(NO)], monitored by *in situ* UV-vis spectroscopy. The isolated reaction product was characterized in the solid state by IR spectroscopy.[39] Additionally, Kadish and co-workers carried out the IR SEC oxidation of [Fe(TPP)(NO)] in the presence of [TBA][Cl], [TBA][Br], and [TBA][I], resulting in the formation of the corresponding {FeNO}^{6} complexes [Fe(TPP)(NO) (X)] where X = Cl^-, Br^-, and I^-. The N-O stretching frequencies of these complexes were reported to occur at 1886, 1883, and 1879 cm^{-1}, respectively.[40] We generated [Fe(TPP)(NO)(Cl)] by reacting the ferric chloride complex with excess NO gas. Under an NO atmosphere, hexanes was added to precipitate the target complex. Characterization of the isolated complex in the solid state by IR spectroscopy showed an N-O stretching frequency of 1880 cm^{-1} (Figure 4.34, left). This ferric chloride NO complex shows minimal NO loss over a 3 month time period in the solid state when stored in the glovebox freezer at -33°C (Figure 4.34, right). The dissolution of the NO complex results in immediate NO loss from the iron center, and reformation of the ferric chloride precursor. Due to the facile NO loss from the iron center, the ferric chloride complex, [Fe(TPP)(Cl)], was reacted with excess NO gas in dichloromethane directly in a Schlenk cuvette in order to obtain a UV-vis spectrum of [Fe(TPP)(NO)(Cl)]. The resulting spectrum shows features at 430,

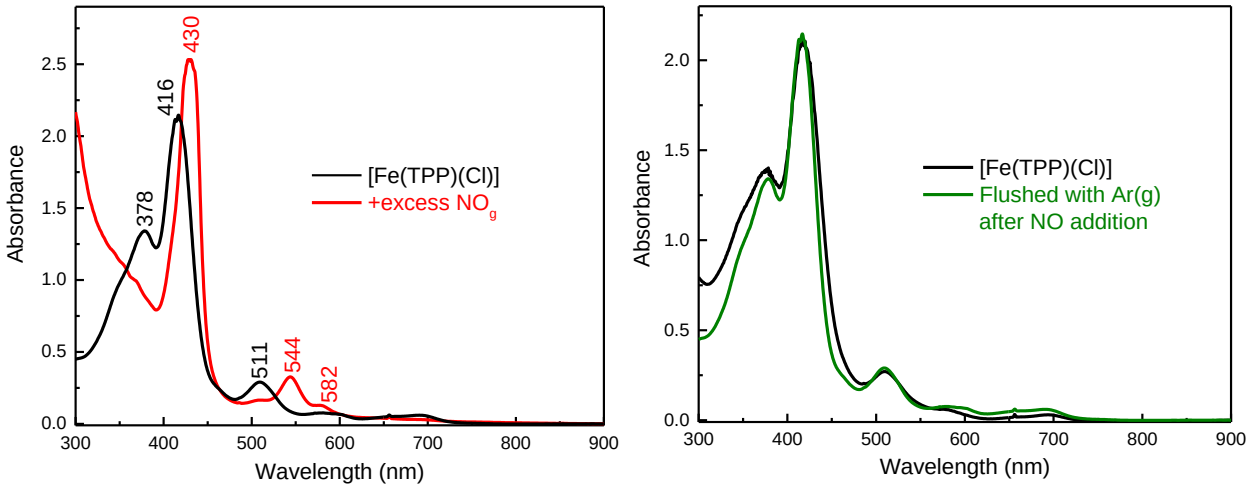

Figure 4.11. Left: UV-vis spectra of the ferric precursor, [Fe(TPP)(Cl)] (black), and of the corresponding reaction product after bubbling the solution with NOg to form [Fe(TPP)(NO)(Cl)] (red), in CH_2Cl_2. Right: The reaction product after flushing the solution with argon gas (green), which results in reformation of the starting material [Fe(TPP)(Cl] (black).

544, and 582 nm (left, Figure 4.11) that are similar to spectral features observed for the 6C $\{FeNO\}^6$ complex, $[Fe(TPP)(NO)(MI)]^+$, see Figure 4.6. Upon flushing the cuvette with argon gas the ferric chloride precursor is reformed, indicating again that NO binding is reversible (Figure 4.11, right). In addition, under an NO-rich environment, we were able to grow crystals of [Fe(TPP)(NO)(Cl)] and solve the crystal structure of this complex, which is displayed in Figure 4.12. It should be noted that the crystal structure is disordered with respect to the NO and Cl^- ligands, which makes the heme plane appear atypically planar. The crystal structure of this complex exhibits a linear Fe-N-O unit and an Fe-N-O bond length of 1.6685 Å and Fe-Cl distance of 2.013 Å (the Fe-Cl bond length in [Fe(TPP)(Cl)] is 2.192 Å).[46]

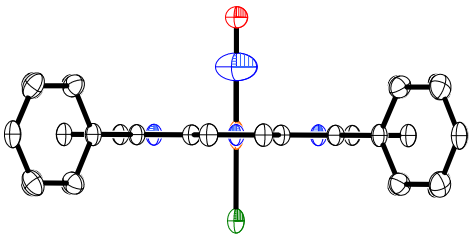

Figure 4.12 Crystal structure of [Fe(TPP)(NO)(Cl)]. The hydrogen atoms are omitted for clarity and thermal ellipsoids are shown at 40% probability.

Finally, we reacted the 5C $\{FeNO\}^6$ complex with other halides to form the corresponding halide-bound complexes, [Fe(TPP)(NO)(X)], X = Br^-, I^- under an NO saturated atmosphere. The reaction of $[Fe(TPP)(NO)]^+$ with [TBA][Br] results in the corresponding bromide-coordinated NO complex, [Fe(TPP)(NO)(Br)] and [TBA][SbF_6]. The N-O stretching frequency of [Fe(TPP)(Br)(NO)] is 1870 cm^{-1} as shown in Figure 4.35. Interestingly, in our hands the reaction of $[Fe(TPP)(NO)]^+$ with [TBA][I] results in reduction of the Fe-NO unit to form the ferrous-heme nitrosyl

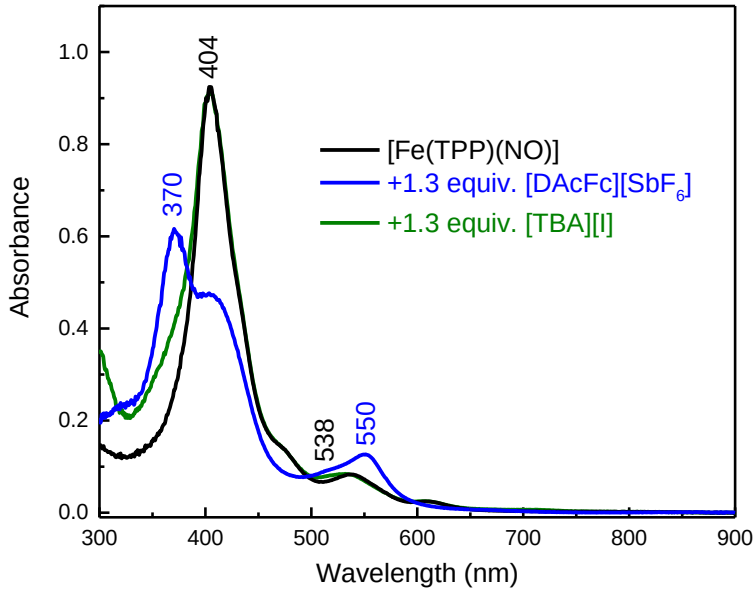

Figure 4.13. Overlay of the UV-vis spectra of [Fe(TPP)(NO)] (black) and of the reaction product after the addition of ~1.30 equiv. [DAcFc][SbF_6] to the solution (blue), and of the product of the subsequent reaction with ~1.3 equivalent [TBA][I] (green). The product from the later reaction is identical to the precursor [Fe(TPP)(NO)].

complex, [Fe(TPP)(NO)] (N-O stretching frequency = 1696 cm^{-1}), I_2, and [TBA][SbF_6] (see Figure 4.28). Further, when a solution of $[Fe(TPP)(NO)]^+$ in dichloromethane in the absence of NO gas is reacted with [TBA][I] there is immediate formation of the [Fe(TPP)(NO)] complex as shown in Figure 4.13.

Table 4.2. Comparison of vibrational frequencies for selected $\{FeNO\}^6$ complexes.

Complex	ν(N-O) cm^{-1}	ν/δ(Fe-NO) cm^{-1}	Ref
[Fe(TPP)(NO)]SbF_6	1850	δ: 393, ν: 585	t.w.
[Fe(OEP)(NO)]ClO_4	1862	δ: 402, ν: 595	19
[Fe(TPP)(NO)(MI)]SbF_6	1920	589	t.w.
[Fe(TPP)(NO)(H_2O)]ClO_4	1862	–	19
[Fe(TPP)(NO)(*i*-$C_5H_{11}OH$)]ClO_4	1935	–	20
[Fe(OEP)(NO)(MI)]ClO_4	1921	–	17
[Fe(OEP)(NO)(2-MI)]ClO_4	–	δ: 574, 580 ν: 600	24
[Fe(OEP)(NO)(Pz)]ClO_4	1909	–	17
[Fe(OEP)(NO)(Iz)]ClO_4	1914	–	17
Mb(III)-NO	1927	δ: 572, ν: 595	51, 59, 60
Hb(III)-NO	1925	594	51, 61, 62
rNP1(III)-NO	1917	δ: 578, ν: 591	52, 63
[Fe(TPP)(NO)(Cl)]	1880	563	t.w.
[Fe(TPP)(NO)(Br)]	1870	–	t.w.
[Fe(TPP)(NO)(NO_2)]ClO_4	1874	–	25
[Fe(TPP)(NO)(CO_2CF_3)]	1907	–	26
[Fe(OEP)(NO)(SR-H_2)][a]	1850	549	53, 54
[Fe(SPorph)(NO)][b]	1828	510	12
[Fe(SPoprh-HB)(NO)][c]	1837	515	12
P450nor(III)-NO	1851	530	56
P450cam(III)-NO	1806	528	55, 56
P450cam(III)-NO + camphor	1806	522	56, 57
P450cam(III)-NO + norcamphor	1818	524	56, 57
P450cam + adamantanone	1818	520	56, 57
CPO(III)-NO[d]	1868	538	56, 58

[a]SR-H_2 = S-2,6-($(CF_3CONH)_2C_6H_3$; [b]SPorph = *meso-a,a,a,a*-[o[[(acetylthio)methyl]phenoxy]acetamido]phenyl]tris(o-pivalamidophenyl)porphyrin^{2-}; [c]SPorph-HB = SPorph with proposed hydrogen bonding; [d]CPO denotes chloroperoxidase.

4.5 Nuclear Resonance Vibrational Spectroscopy (NRVS)

To gain further insight into the electronic properties of our new {FeNO}^{6} complexes, we measured their Fe-NO stretching frequencies applying NRVS. In correlation to the N-O stretching frequencies, this provides key insight into changes in Fe-NO bonding along a series of complexes as we and others have previously shown.[16,29,47-50] In linear {FeNO}^{6} complexes, the Fe-N-O unit gives rise to one Fe-NO stretch and two degenerate Fe-N-O linear bends, which, in the case of corresponding six-coordinate complexes, are very similar in energy,[16,24] which complicates assignments.

Previous work by Scheidt and co-workers reported the resonance Raman (rRaman) spectrum of [Fe(OEP)(NO)]ClO_4, which shows one broad, isotope-sensitive feature at 600 cm^{-1} (which shifts to 593 cm^{-1} with ^{15}NO).[50] In this work, it was not possible to discern the Fe-NO stretch from the Fe-N-O linear bends. Later work by our group employed NRVS, coupled to Normal Coordinate Analysis (NCA) and Density Functional Theory computations (DFT), to examine [^{57}Fe(TPP)(NO)(MI)]BF_4. In this case, the NRVS data exhibit a broad, $^{15}N^{18}O$ sensitive, feature at 578/586 cm^{-1}.[16] In conjunction with NCA and DFT calculations we assigned the Fe-NO stretch to the 578 cm^{-1} band and the Fe-N-O linear bends to the feature at 586 cm^{-1}. Further work by Scheidt and co-workers utilized oriented singe-crystal NRVS to provide definitive assignments of the stretching and bending modes of the Fe-N-O moiety in the ^{57}Fe labeled complexes [Fe(OEP(NO)]ClO_4 and [Fe(OEP)(MO)(2-MI)]ClO_4 (2-MI = 2-methylimidazole).[24] It should be pointed

out that single-crystal NRVS only works for select complexes, since it requires a crystalline form of the compound where all of the porphyrin planes are parallel and all of the molecules have the same orientation.

The NRVS data of the 5C $\{FeNO\}^6$ complex, $[^{57}Fe(TPP)(NO)]SbF_6$, show the Fe-N-O bends at 393 cm^{-1}, which shift to 386 cm^{-1} upon $^{15}N^{18}O$ labeling (Δ = 7 cm^{-1}). This finding is fully consistent with the results for $[Fe(OEP)(NO)]ClO_4$, where the linear Fe-N-O bends are found at 402 cm^{-1}. To higher energy, there are two peaks observed at 559 and 585 cm^{-1} that are isotope sensitive. As shown in Figure 4.14, the spectrum of the $^{15}N^{18}O$ complex shows a significant decrease in the intensity of the peak at 585 cm^{-1} while at the same time the peak at 559 cm^{-1}increases in intensity. This implies that the Fe-NO stretch is located at 585 cm^{-1}, and coupled with a porphyrin-based vibration around 559 cm^{-1}. This is consistent with work by Scheidt and co-workers on $[Fe(OEP)(NO)]ClO_4$ where the Fe-NO stretch is observed at 595 cm^{-1}. This would also explain the very large (apparent) isotope shift (Δ = 26 cm^{-1}) observed for this feature.

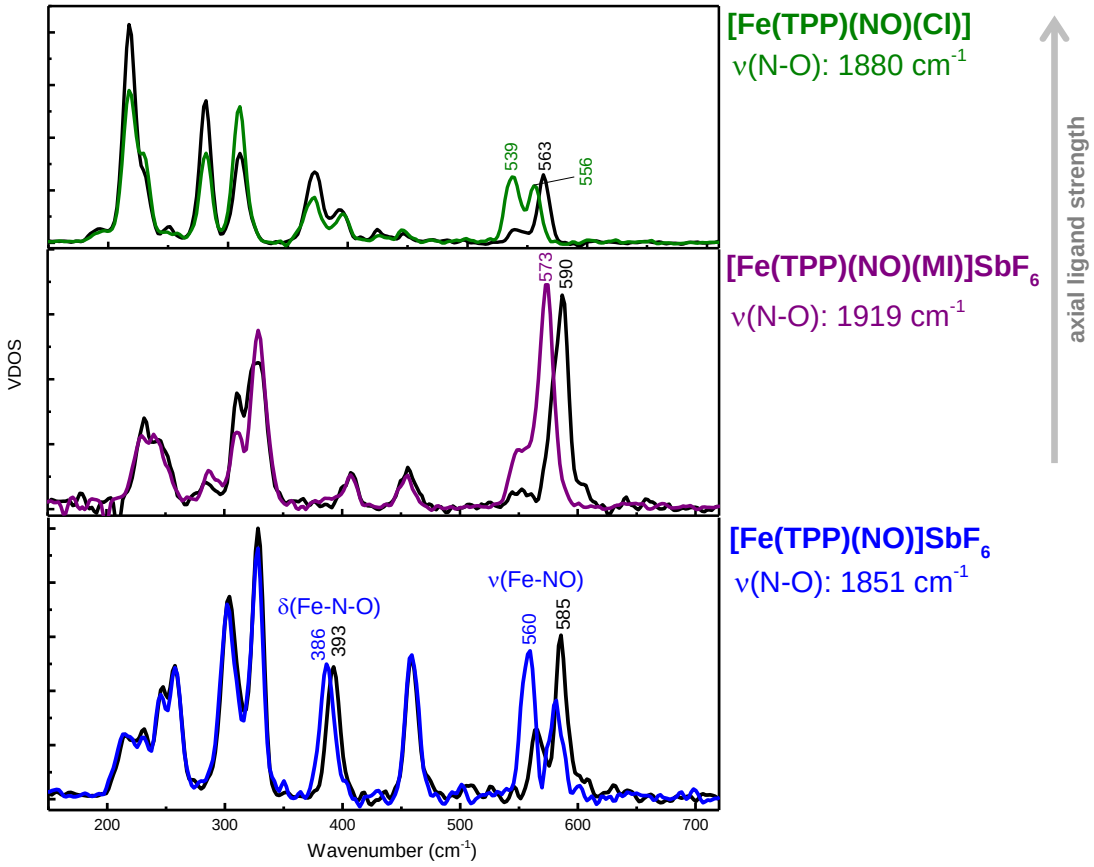

Figure 4.14. Top: NRVS-derived ibrational density of states (VDOS) for [^{57}Fe(TPP)(NO)(Cl)] (black) and the ^{15}N^{18}O labeled complex (green). Middle: NRVS VDOS for [^{57}Fe(TPP)(NO)(MI)]SbF$_6$ (black) and the ^{15}N^{18}O labeled complex (purple). Bottom: NRVS VDOS for [^{57}Fe(TPP)(NO)]SbF$_6$ (black) and the ^{15}N^{18}O labeled complex (green).

In the 6C case, we measured the resonance Raman (rR) spectrum of the [Fe(TPP)(NO)(MI)]SbF$_6$ complex. For this purpose, the precursor [Fe(TPP)(SbF$_6$)] was dissolved in dichloromethane in the presence of ~1 equiv. MI and was exposed to NO gas. The NO-saturated solution was then transferred to a quartz EPR tube. In the rRaman spectrum shown in Figure 4.15, the oxidation state marker band (ν_4) is observed at 1370 cm^{-1} and the spin state marker band (ν_2) is found at 1569 cm^{-1}, both consistent with other ferric heme-NO complexes.[51,52]

Interestingly, the ν_4 and ν_2 bands are identical to the {FeNO}^{7} complex [Fe(TPP)(NO)] (ν_4 = 1370, ν_2 = 1568 cm^{-1}), indicating that the heme is in the low-spin ferrous state.[29] In the low energy region of the spectrum, the natural abundance isotopes (n.a.i.) complex exhibits a broad band at ~598 cm^{-1} (see Figure 4.16, top) that downshifts to 586 cm^{-1} ($\Delta = 12$ cm^{-1}) upon isotope labeling with $^{15}N^{18}O$ gas (Figure 4.16, bottom). In contrast to our complex, six-coordinate

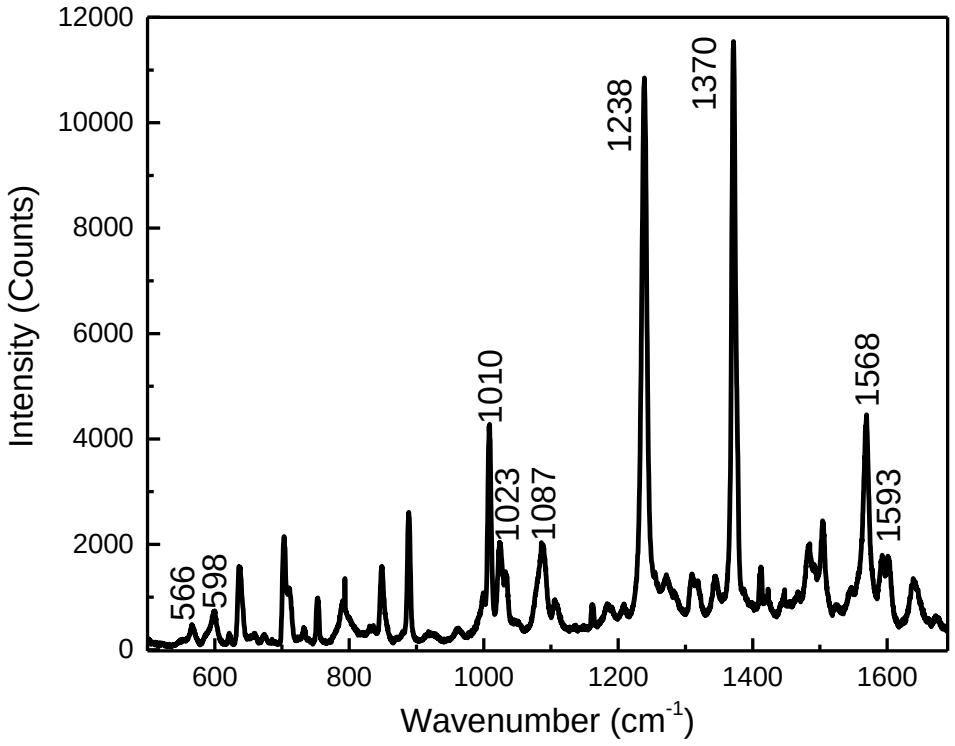

Figure 4.15. rRaman spectrum of a 2 mM solution of [Fe(TPP)(NO)(MI)]SbF_6 in dichloromethane (power = 31 mW). Note: The {FeNO}^{6} complex was formed by the reaction of [Fe(TPP)(SbF_6)] with excess NO gas in the presence of ~1 equiv. MI. While the solution was under an NO atmosphere, an aliquot was transferred into a quartz EPR tube for rRaman measurements.

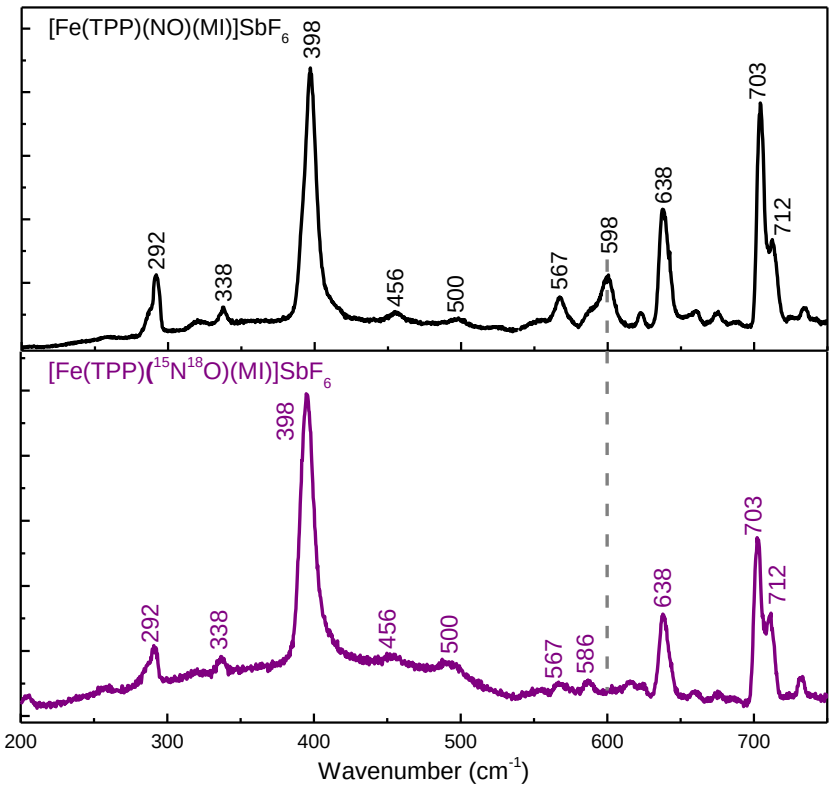

Figure 4.16. Top: rRaman spectrum of a ~2 mM solution of [Fe(TPP)(NO)(MI)]SbF_6 (power = 31 mW). Bottom: rRaman spectrum of a ~2 mM solution of the corresponding $^{15}N^{18}O$-labeled complex, [Fe(TPP)($^{15}N^{18}O$)(MI)]SbF_6 (bottom; power = 28 mW). There is one isotope sensitive feature at 598 cm^{-1} that shifts to 586 cm^{-1} upon $^{15}N^{18}O$ labeling. Note: The {Fe$^{15}N^{18}O$}^{6} complex was formed by the reaction of [Fe(TPP)(SbF_6)] with excess $^{15}N^{18}O$ gas in the presence of ~1 equiv. MI. The solution was allowed to stir for ~45 minutes under an NO atmosphere and then an aliquot was transferred into a quartz EPR tube for Raman measurements.

ferric heme NO proteins (such as myoglobin) the Fe-NO stretching and bending modes are resolved (measured via rRaman; see Table 4.2).[49]

We also obtained NRVS data for the 6C complex, [^{57}Fe(TPP)(NO)(MI)]SbF_6, which show one isotope sensitive feature at 589 cm^{-1} that downshifts to 573 cm^{-1} upon $^{15}N^{18}O$ labeling (Δ = 16 cm^{-1}). This complex exhibits a much sharper Fe-NO band in the NRVS spectrum than [Fe(TPP)(NO)(MI)]BF_4 reported by us previously, but again the Fe-NO stretch and

the Fe-N-O bends are not resolved. Finally, in the [^{57}Fe(TPP)(NO)(Cl)] complex, the IR of the natural abundance isotopes (n.a.i.) species shows two isotope sensitive features, the main band at 1880 and a minor feature at 1829 cm^{-1} (see Figure 4.29). Isotope labeling with $^{15}N^{18}O$ results in a downshift of the N-O stretching frequency to 1802 (Δ = 78 cm^{-1}), whereas the 1829 cm^{-1} feature actually shifts to higher energy at 1844 cm^{-1} (Δ = 15 cm^{-1}). We believe this is due to Fermi resonance, since the 182/1844 cm^{-1} band is to lower energy of the N-O stretch in the n.a.i. complex, but to higher energy of the N-O stretch in the $^{15}N^{18}O$ labeled complex. The NRVS spectrum contains one isotope sensitive band at 563 cm^{-1}, which shifts to 556 cm^{-1} upon $^{15}N^{18}O$ labeling (Δ = 7 cm^{-1}). There is another band at 539 cm^{-1} in the n.a.i. complex that significantly increases in intensity in the $^{15}N^{18}O$ labeled complex. We believe that this feature at 539 cm^{-1} is a Fe-porphyrin related vibration that steals some intensity from the Fe-NO stretch. In summary, we can resolve the Fe-NO stretch from the linear Fe-N-O bends from in the 5C complex, [Fe(TPP)(NO)]SbF_6; however, both 6C {FeNO}^{6} complexes only show one combined band for these features.

Discussion

In this chapter, we developed a new method to synthesize ferric heme-nitrosyl complexes by chemical and electrochemical oxidation of {FeNO}^{7} precursors, and demonstrated this for complexes with the TPP^{2-} ligand. When generated in this way, the 5C {FeNO}^{6} complex is solution stable and slowly loses

NO over time and the k_{off} rate is 4.7 x 10^{-5} s^{-1}, which means the half-life is ~4 hours. The addition of ~1 equiv. MI to the solution results in the formation of the 6C complex $[Fe(TPP)(NO)(MI)]^+$, which is also solution stable, but shows a significantly enhanced rate for NO loss (k_{off} = 1.9 x 10^{-4} s^{-1} with a half-life of ~1 hour). We further characterized our series of $\{FeNO\}^6$ complexes via UV-vis, IR, and NMR spectroscopy and NRVS. The $\{FeNO\}^6$ complexes obtained in this way have identical spectroscopic features to those prepared via the traditional method shown in Scheme 4.1. The complexes are also more stable, which is likely due to less impurities in the precursor complex such as halides. We avoid halide impurities by synthesizing a pure form of the $\{FeNO\}^7$ complex by a reductive nitrosylation reaction from an iron(III)-X complex (where X is a weakly coordinating anion). This finding is breakthrough that allows one to handle $\{FeNO\}^6$ complexes in the absence of NO gas.

Next, we determined that [Fe(TPP)(NO)(Cl)] can be made as proposed in previous studies.[39,40] The complex reversibly binds NO, but quickly loses NO upon dissolution of the isolated material. We can also generate the halide-bound $\{FeNO\}^6$ complexes by addition of [TBA][X] (where X = Cl^- or Br^-) to a solution of $[Fe(TPP)(NO)]^+$ under an NO atmosphere. However, the reaction of [TBA][I] with $[Fe(TPP)(NO)]^+$ results in one-electron reduction of the Fe-NO unit to generate the ferrous heme-nitrosyl complex, [Fe(TPP)(NO)]. This is in not in agreement with a previous literature report that presents the IR SEC oxidation of [Fe(TPP)(NO)] in the presence of [TBA][I], which was thought to result in the generation of

[Fe(TPP)(NO)(I)] with an N-O stretching frequency of 1879 cm^{-1}.[40] To further illustrate this contradiction, we can examine the reduction potentials of the reported species in CH_3CN (vs Fc/Fc^+): for the oxidation of Cl^-/Cl_2, Br^-/Br_2, and I^-/I_2 redox potentials of +0.18, +0.07, and –0.14 V, respectively,[41] have been determined. Importantly, the oxidation potential of I^- to I_2 is ~440 mV more negative than that of the [Fe(TPP)(NO)] complex (note: the reduction potential of [Fe(TPP)(NO)] is measured in CH_2Cl_2), which means the complex will easily oxidize I^- to I_2. This is also consistent with the fact that the ferric complex FeI_3 does not exist (due to conversion to $FeI_2 + I_2$).

Lastly, we obtained the crystal structures for our new series of $\{FeNO\}^6$ complexes. In our 5C complex, $[Fe(TPP)(NO)]BF_4$, has a linear Fe-N-O unit and a similar Fe-NO bond length to $[Fe(OEP)(NO)]ClO_4$ complex shown in Table 4.1. The only notable difference between these complexes is that our 5C $\{FeNO\}^6$ complex has a slightly lower N-O stretching frequency of 1850 cm^{-1} in comparison to the OEP^{2-} analogue at 1862 cm^{-1} (see Table 4.2).[19] The Fe-NO stretching and bending vibrations are 585 and 393 cm^{-1}, which are slightly lower than those of the $[Fe(OEP)(NO)]ClO_4$ complex at 595 and 402 cm^{-1}, respectively (see Table 4.2).[19] Ferric heme-nitrosyl complexes with axial neutral N-donors (ie. imidazole, pyridine, and pyrazole) also have linear Fe-N-O units and N-O and Fe-NO stretching frequencies in the 1890 - 1935 cm^{-1} and 580 - 600 cm^{-1} range.[11] Our 6C complex $[Fe(TPP)(NO)(MI)]^+$ exhibits a linear Fe-N-O moiety (see Table 4.1) with N-O and Fe-NO stretching frequency values of 1920 and 589 cm^{-1} shown in Table 4.2.

Interestingly, ferric heme-nitrosyl species with histidine ligation, such as myoglobin/hemoglobin and nitrophorins, have N-O (1917 – 1927 cm^{-1}) and Fe-NO stretching frequencies (591 – 595 cm^{-1}) similar to our 6C N-donor $\{FeNO\}^6$ complex shown in Table 4.2. For six-coordinate $\{FeNO\}^6$ complexes with anionic ligands, a correlation of the donor strength and the Fe-N-O bond angle has been derived.[53] For example, with a weak donor like trifluoroacetate [Fe(TPP)(NO)(CO_2CF_3)], exhibits a slightly bent Fe-N-O unit of 176°.[26] Upon increasing the donor strength the Fe-N-O units bends in [Fe(TPP)(NO)(NO_2)] with an Fe-N-O bond angle of 169°.[25] Further, in the presence of an S-donor, [Fe(OEP)(NO)(SR-H_2)] (where SR-H_2 = S-2,6-$(CF_3CONH)_2C_6H_3$), the Fe-N-O moiety is bends even more at 160°.[54] By comparison to our chloride bound $\{FeNO\}^6$ complex, [Fe(TPP)(NO)(Cl)], has a linear Fe-N-O unit (180°), which would make Cl^- a very weak donor by this classification (similar to the acetate ligated complex). However, donor strength is also correlated with N-O and Fe-NO stretches as depicted in Figure 4.17. Interestingly, [Fe(TPP)(NO)(Cl)] falls in the region between the neutral N-donor and thiolate ligated complexes on the graph (Figure 4.17). This would indicate the Cl^- ligand is a moderate donor, but does not explain the fact that the Fe-N-O unit is completely linear. The most notable difference between the anionic ligands discussed here is that they are *anisotropic* donors, whereas chloride is an *isotropic* donor. Thiolates cause bending of the Fe-N-O unit by inducing a s-trans effect on the bound NO via population of an Fe-N-O σ^* antibonding orbital. This implies that this type of antibonding Fe-N-O interaction is not present in [Fe(TPP)(NO)(Cl)],

similar to $[Fe(Porph)(NO)(IM)]^+$ complexes (IM = imidazole derivatives), and as result the Fe-N-O unit is linear. In summary, the Cl^- ligand is a moderate *isotropic* donor that causes a weakening of the Fe-NO bond evidenced by spectroscopy, but the *isotropic* nature of Cl^- results in the linearity of the Fe-N-O unit unlike other *anisotropic* donor ligands.

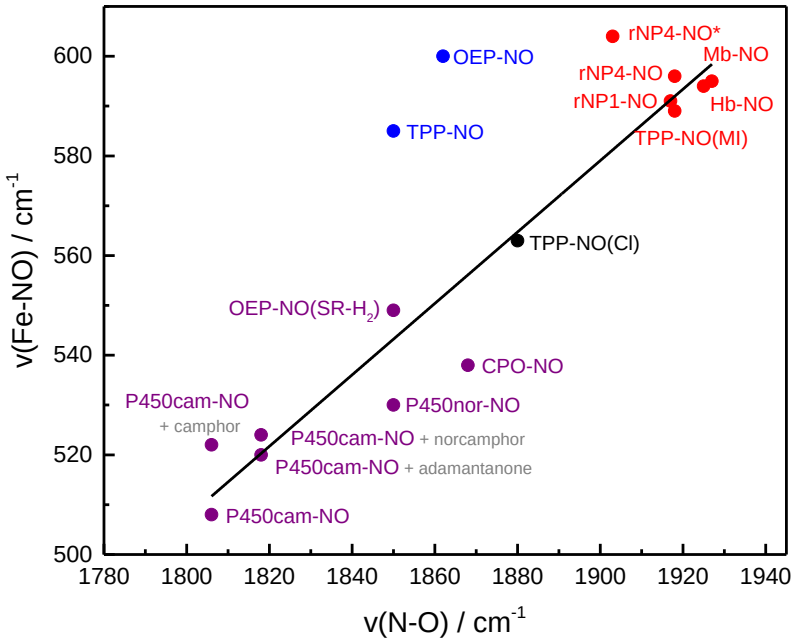

Figure 4.17. Experimental vibrational stretching frequency correlation of the Fe-NO stretching frequency versus the N-O stretching frequency based on this work and published data. 5C $\{FeNO\}^6$ complexes $[Fe(TPP)(NO)]BF_4$ and $[Fe(OEP)(NO)]ClO_4$ are depicted in blue. 6C $\{FeNO\}^6$ complexes with an axial thiolate ligand *trans* to the NO are shown in purple: Cyt. P450cam[55,56] (+camphor, norcamphor, and adamantanone),[56,57] Cyt. P450nor,[56] CPO,[56,58] and $[Fe(OEP)(NO)(SR\text{-}H_2)]ClO_4$.[53,54] $[Fe(TPP)(NO)(Cl)]$ is shown in black and 6C $\{FeNO\}^6$ complexes with an axial histidine (Mb,[51,59,60] Hb,[51,61,62] and rNP1[52,63]) or MI ligand *trans* to the NO are shown in red. MI denotes 1-methylimdiazole, $SR\text{-}H_2$ denotes the S-2,6-$(CF_3CONH)_2C_6H_3$ ligand, CPO denotes chloroperoxidase, Mb denotes myoglobin, Hb denotes hemoglobin, and rNP1 denotes nitrophorin 1 from *Rhodnius prolixus*.

4.6 Experimental Section

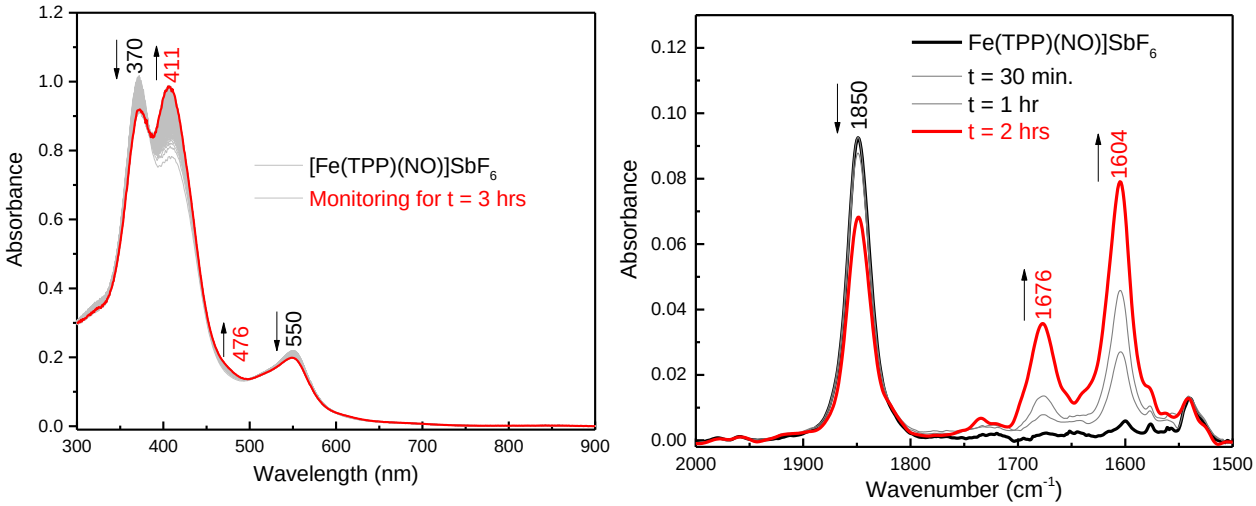

Figure 4.18. Left: UV-vis spectra monitoring the stability of [Fe(TPP)(NO)]SbF_6 for 3 hours in dichloromethane at room temperature. Right: IR spectra monitoring the stability of [Fe(TPP)(NO)]SbF_6 for 2 hours in dichloromethane at room temperature. For these experiments, solid [Fe(TPP)(NO)]SbF_6 (obtained by reaction of [Fe(TPP)(SbF_6)] with excess NO gas) was dissolved in dichloromethane, and monitored by taking aliquots from a stirring solution that were transferred into a solution IR cell.

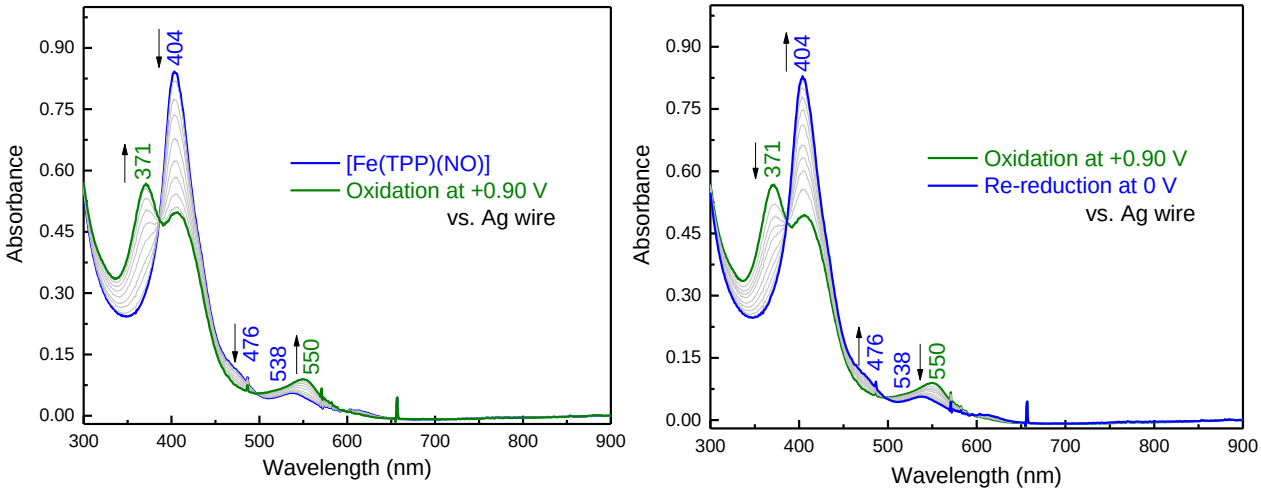

Figure 4.19. Left: UV-vis spectra for the SEC oxidation of [Fe(TPP)(NO)] (green to blue) in an OTTLE UV-vis cell, measured in a 0.10 M tetrabutylammonium hexafluorophosphate solution in dry CH_2Cl_2 at room temperature. The working and counter electrodes were both a Pt mesh. Right: Re-reduction of the oxidation product (blue to green), showing that the oxidation is fully reversible.

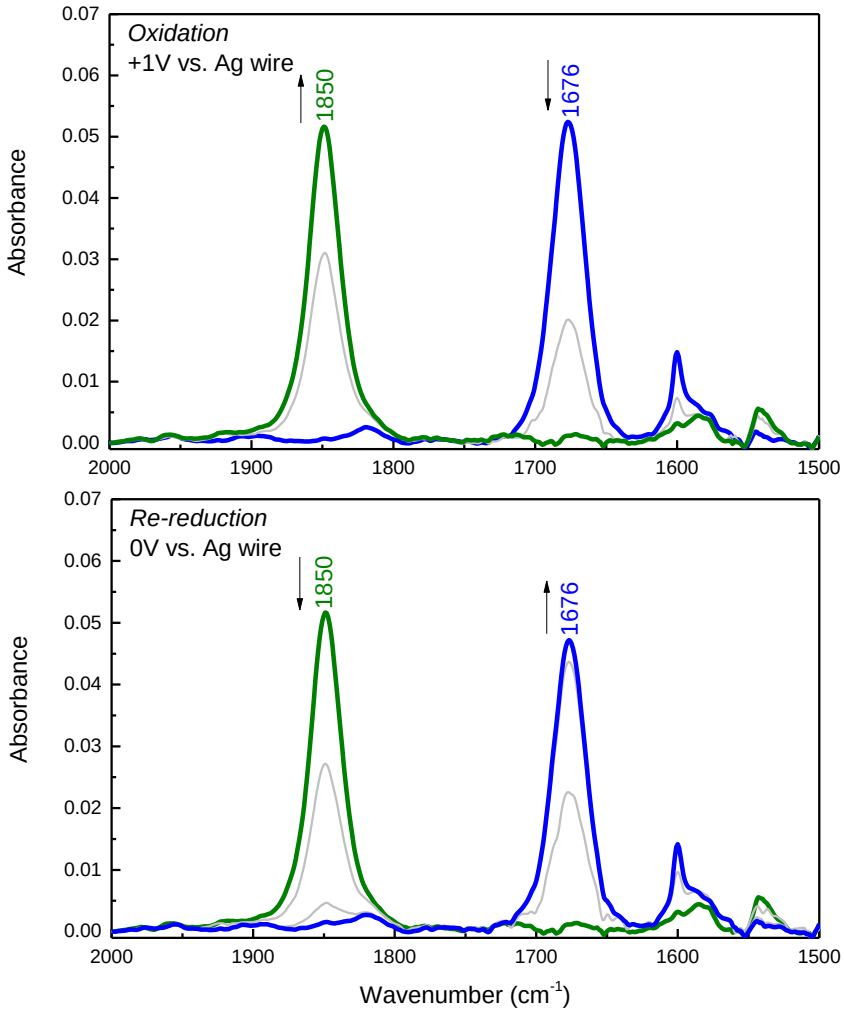

Figure 4.20. Top: IR spectra for the SEC oxidation of [Fe(TPP)(NO)] (blue to green), measured in a 0.30 M tetrabutylammonium hexafluorophosphate solution in dry CH_2Cl_2 at room temperature. Bottom: Re-reduction of the oxidation product (green to blue), which shows that the oxidation is fully reversible. The working and counter electrodes were both a Pt mesh.

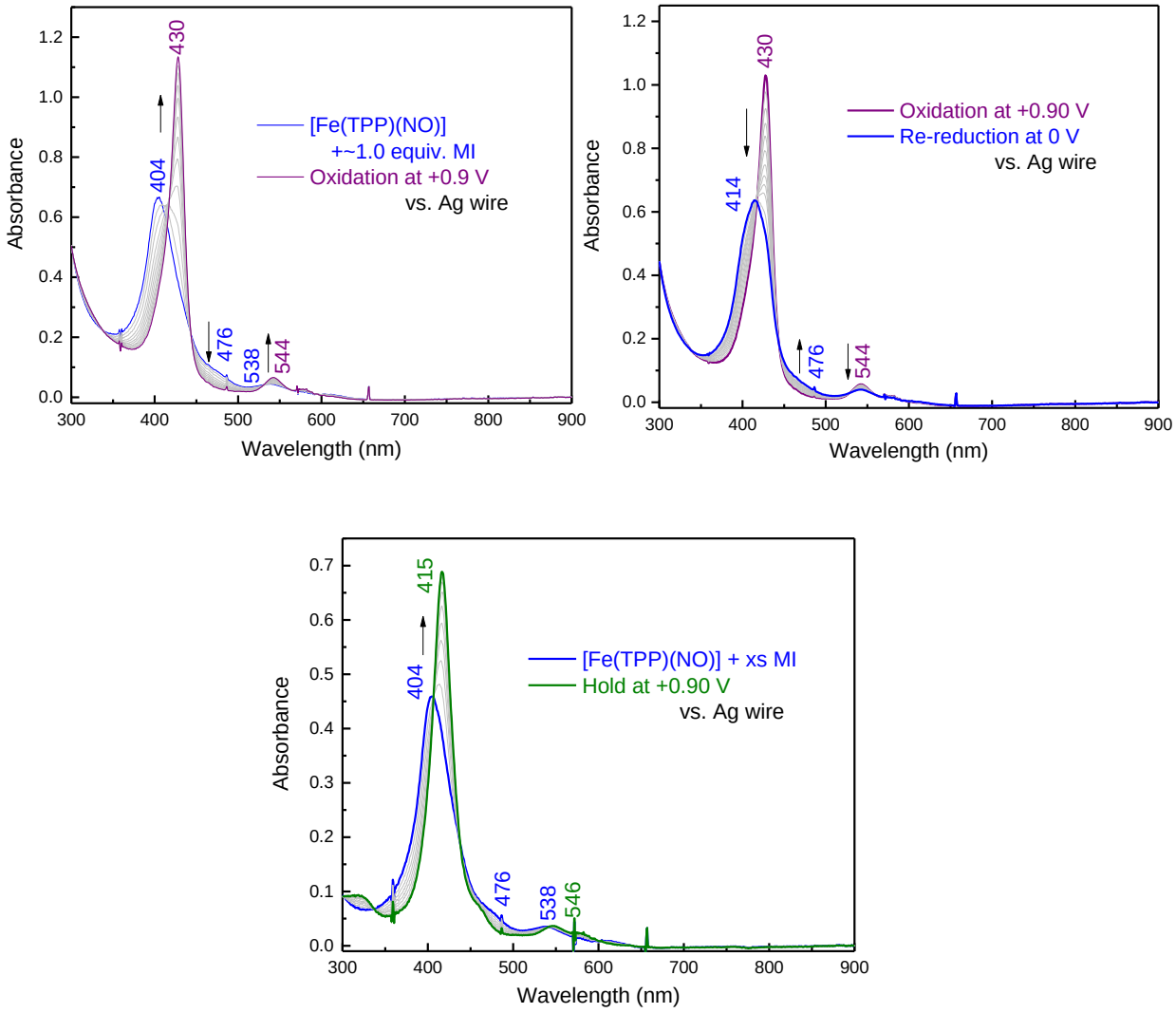

Figure 4.21. Top left: UV-vis spectra for the SEC oxidation of [Fe(TPP)(NO)] in the presence of **~1 equiv.** MI (blue to purple) in an OTTLE UV-vis cell, measured in a 0.10 M tetrabutylammonium hexafluorophosphate solution in dry CH_2Cl_2 at room temperature. The working and counter electrodes were both a Pt mesh. Top right: Re-reduction of the oxidation product (blue to green) shows that the oxidation is not reversible, resulting in the generation of the starting [Fe(TPP)(NO)] complex and a ferric bis imidazole (MI) complex. Bottom: UV-vis spectra for the SEC oxidation of [Fe(TPP)(NO)] in the presence of **excess** MI (blue to green) in an OTTLE UV-vis cell, measured in a 0.10 M n-Bu_4PF_6 solution in dry CH_2Cl_2 at room temperature. The working and counter electrodes were both a Pt mesh. The oxidation product is the ferric bis-imidazole complex, $[Fe(TPP)(MI)_2]^+$, and hence, the oxidation is irreversible.

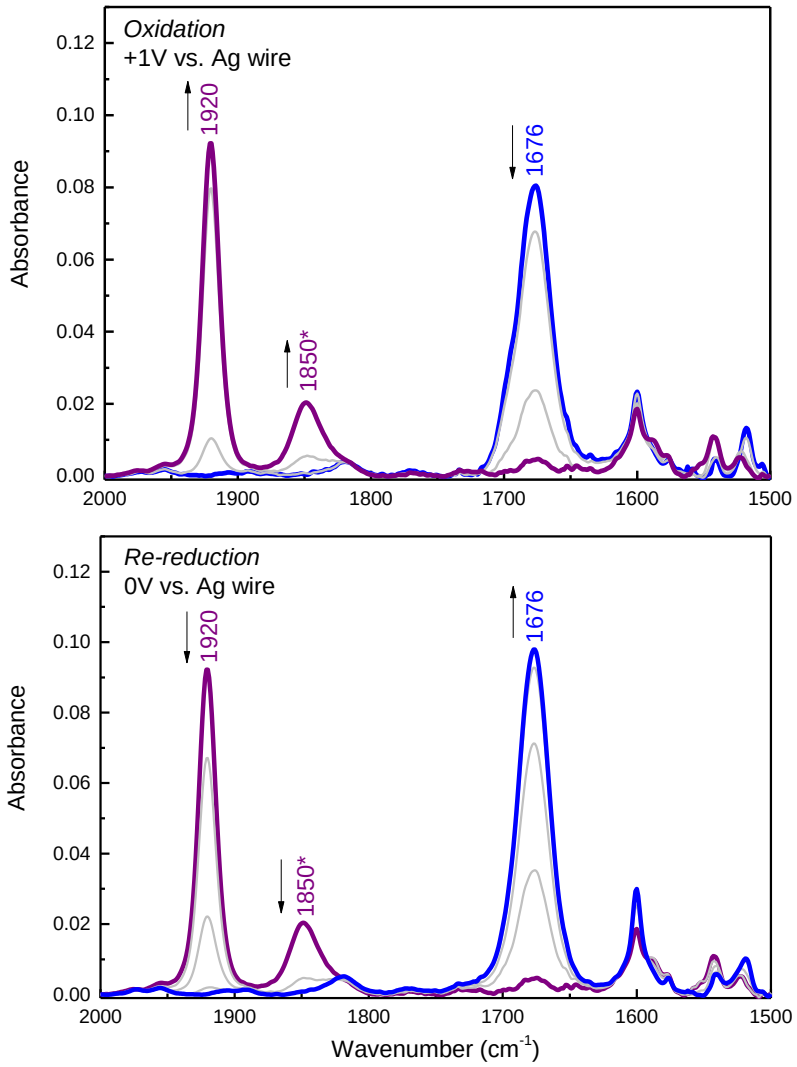

Figure 4.22. Top: IR spectra for the SEC oxidation of [Fe(TPP)(NO)] in the presence of ~1 equiv. MI (blue to purple), measured in a 0.10 M tetrabutylammonium hexafluorophosphate solution in dry CH_2Cl_2 at room temperature. Bottom: Re-reduction of the oxidation product (green to blue) shows that the oxidation is reversible. The working and counter electrodes were both a Pt mesh. The * denotes a small amount of the five-coordinate complex $[Fe(TPP)(NO)]^+$.

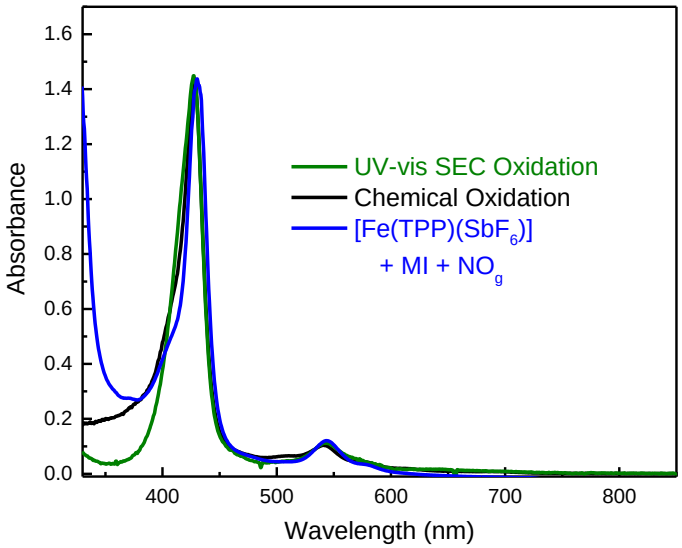

Figure 4.23. Comparison of the UV-vis spectra of $[Fe(TPP)(NO)(MI)]^+$ generated via different methods in dichloromethane: UV-vis SEC (green), chemical oxidation (black), and addition of NO gas to [Fe(TPP)(SbF6)] with ~1 equiv. MI (blue).

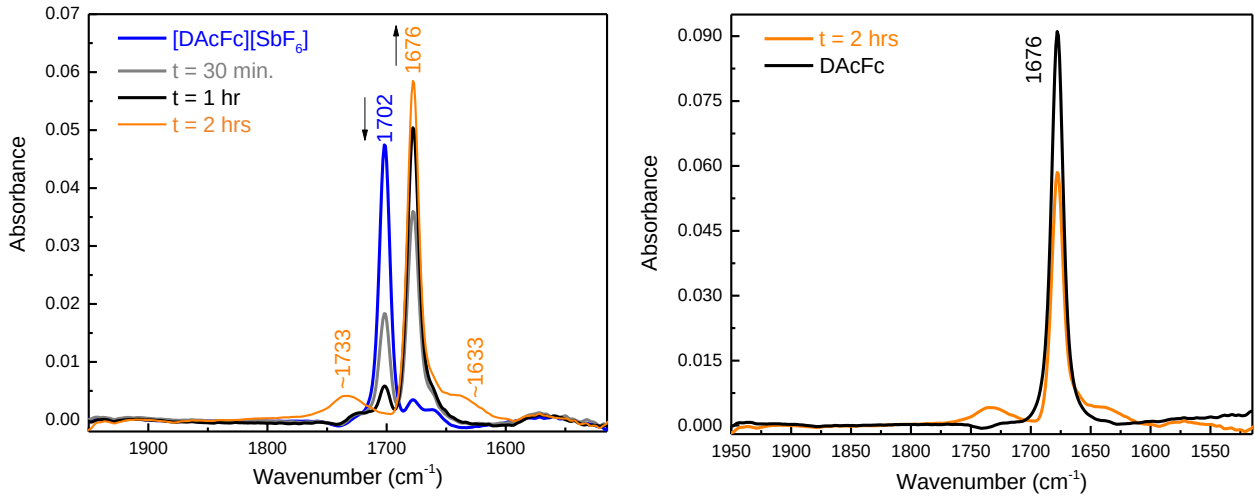

Figure 4.24. Left: Solution IR spectra of a 1.5 mM solution of $[DAcFc][SbF_6]$ (blue) in dimethoxyethane and of aliquots taken from a stirring solution of $[DAcFc][SbF_6]$ over time at room temperature. The C-O stretching frequency at 1702 cm^{-1} slowly decreases in intensity as a large new band at 1678 cm^{-1} appears (orange). Right: Solution IR spectra of the decomposed solution of $[DAcFc][SbF_6]$ (orange) and of a 1.5 mM solution of DAcFc in dimethoxyethane (black), showing that the band at 1672 cm^{-1} is the C-O stretching frequency of DAcFc.

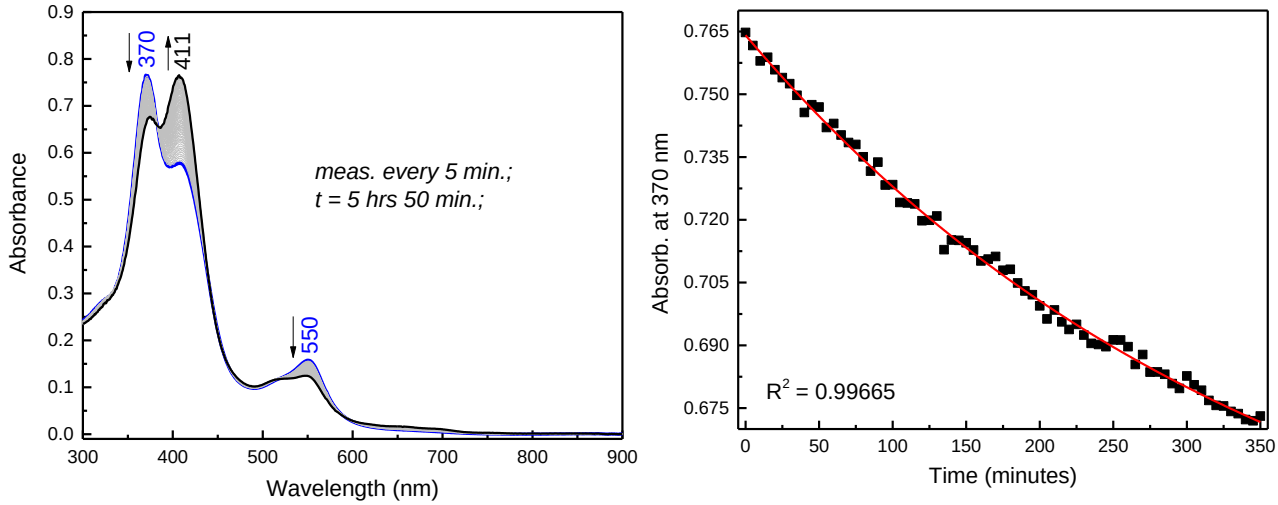

Figure 4.25. Left: *In situ* UV-vis monitoring of the decomposition of $[Fe(TPP)(NO)]^+$ (blue to black). $[Fe(TPP)(NO)]^+$ was generated via chemical oxidation of a solution of ~10 μM [Fe(TPP)(NO)] with 1.14 equiv. of [DAcFc][SbF_6] (the oxidant was dissolved in DME). Right: Fit of the UV-vis band at 370 nm over time. The data are fit to a single exponential function with k_{obs} = 4.7*10^{-5} s^{-1}.

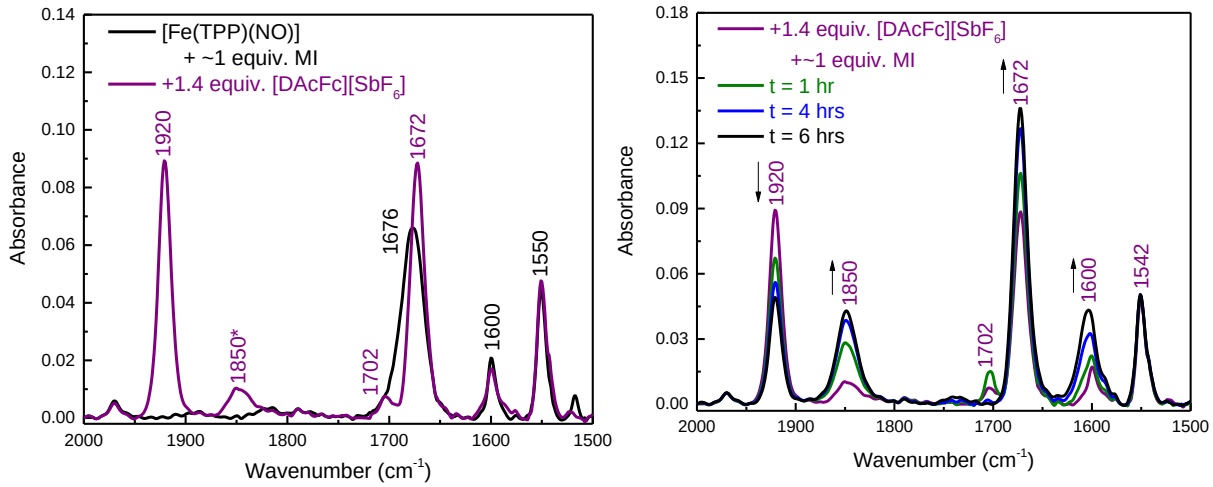

Figure 4.26. Solution IR spectra of a 1.8 mM solution of [Fe(TPP)(NO)] (black) in the presence of ~1 equiv. MI in CH_2Cl_2 and of the reaction product (in purple) after the addition of ~1.40 equiv. [DAcFc][SbF_6] to the solution. The N-O stretch at 1676 cm^{-1} shifts to 1920 cm^{-1} upon oxidation. The band at 1850 cm^{-1}(*) corresponds to a small amount of five-coordinate $[Fe(TPP)(NO)]^+$. The bands at 1702 and 1672 cm^{-1} are the C-O stretching frequencies of the respective $DAcFc^{0/+}$ reagents. Right: Continued monitoring of the $\{FeNO\}^6$ complex over a 6 hour time period shows slow NO loss and at the same time an increase in the 1850 cm^{-1} band of the 5C $\{FeNO\}^6$ complex. For these experiments, aliquots were taken from a stirring solution and transferred into a solution IR cell.

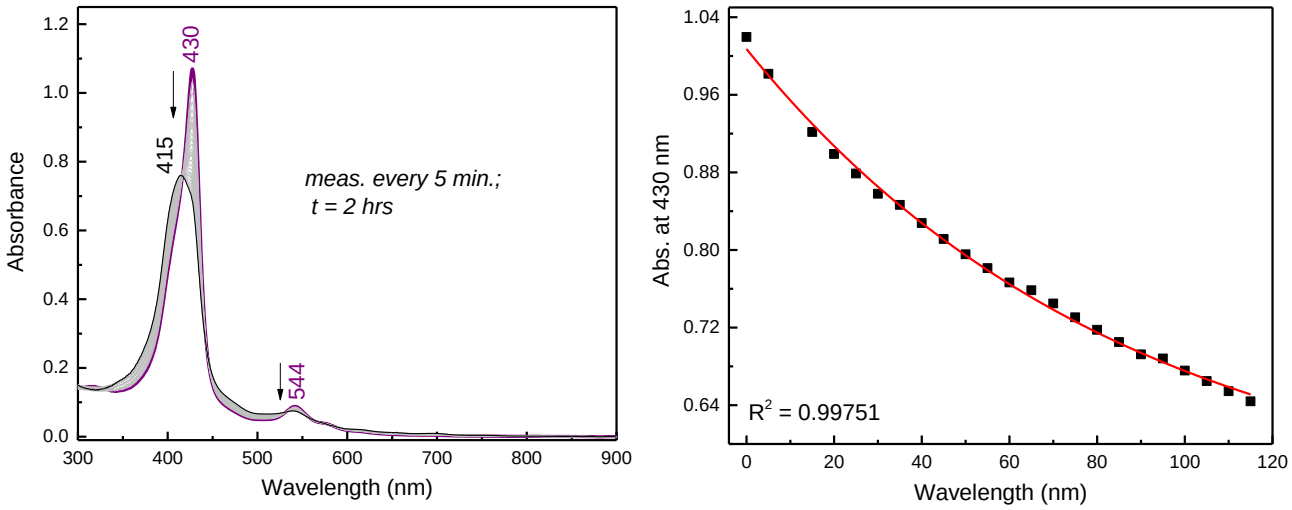

Figure 4.27. Left: *In situ* UV-vis monitoring of the decomposition of $[Fe(TPP)(NO)(MI)]^+$ (purple to black). $[Fe(TPP)(NO)(MI)]^+$ was generated via chemical oxidation of a solution of ~5 μM [Fe(TPP)(NO)] with ~1.3 equiv. of $[DAcFc][SbF_6]$ (the oxidant was dissolved in DME) in the presence of ~1 equiv. of MI. Right: Fit of the UV-vis band at 430 nm over time. The data are fit to a single exponential function with k_{obs} = 1.9*10^{-4} s^{-1}.

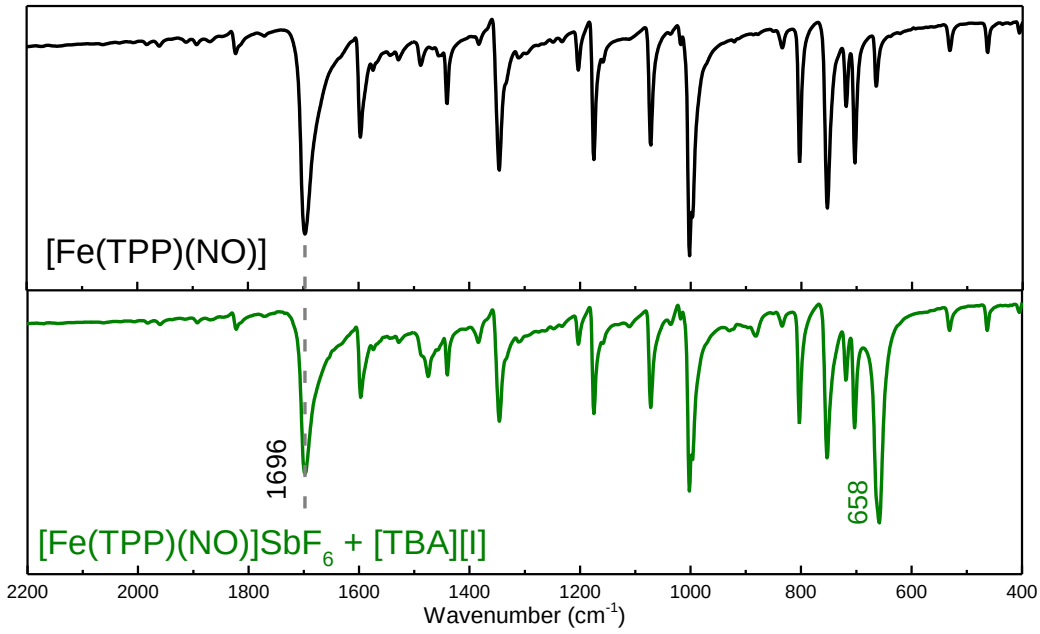

Figure 4.28. Top: IR spectrum of [Fe(TPP)(NO)] (black). Bottom: IR spectrum of the reaction product of $[Fe(TPP)(NO)]SbF_6$ with [TBA][I] under an NO atmosphere, which results in the iron NO complex, [Fe(TPP)(NO)], I_2, and $[TBA][SbF_6]$ (green). All spectra were taken in KBr pellets.

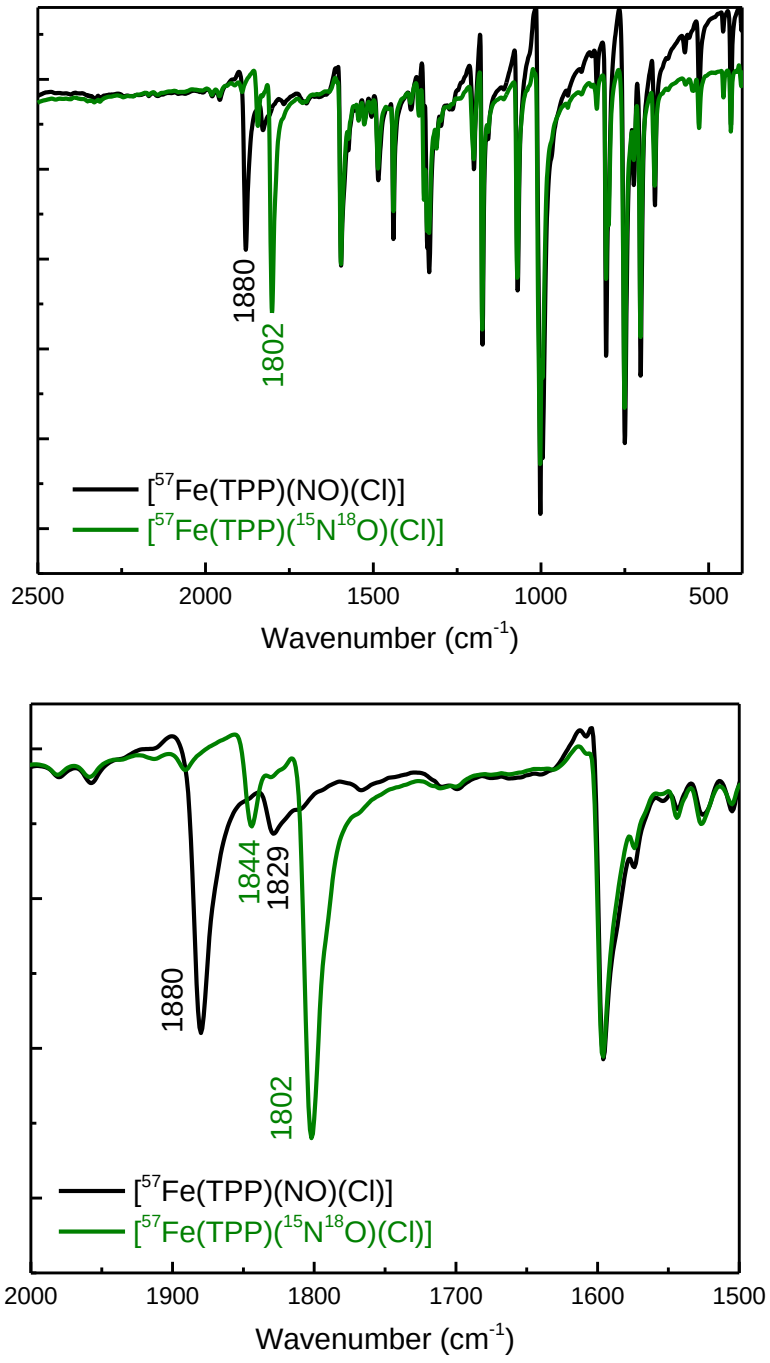

Figure 4.29. Top: Overlay of the IR spectra (measured in KBr pellets) of [^{57}Fe(TPP)(NO)(Cl)] (black) and the ^{15}N^{18}O labeled complex (green). Bottom: Zoomed in comparison of [^{57}Fe(TPP)(NO)(Cl)] (black) and the ^{15}N^{18}O labeled complex (green).

Synthesis

All reactions were performed under insert conditions using Schlenk techniques. The preparation and handling of air sensitive materials was carried out under a dinitrogen atmosphere in an MBraun glovebox equipped with a circulating purifier (O_2, H_2O < 0.1 ppm). Nitric oxide (Cryogenic Gases Inc., 99.5%) was purified by passage through an ascarite II column (NaOH on silica) followed by a cold trap at -80°C to remove higher order nitrogen oxide impurities. $^{15}N^{18}O$-Nitric oxide (Sigma Aldrich) was used without further purification. All solvents (including deuterated solvents) and 1-methylimidazole (MI) were distilled from CaH_2 under dinitrogen, then degassed via five freeze-pump-thaw cycles. Tetrabutylammonium hexafluorophosphate was recrystallized from ethanol. The purified solvents were stored over appropriately sized activated molecular sieves in the glovebox until used. 1,1'-diacetylferrocene was purchased from Fisher Scientific and used without any further purification. [Fe(TPP)(Cl)][64], [Fe(TPP)(X)][65] where X = PF_6^- or SbF_6^-, and [thianthrene][X][66] where X = BF_4^- or SbF_6^- were synthesized as previously reported. ^{57}Fe complexes were synthesized in the same way as the natural abundance isotope complexes, using $^{57}FeCl_2$ dimethanol salt as the iron source.

Root Mean Square Deviation Determination. The RMSD is calculated by the following equation:[7]

$$RMSD = \sqrt{\frac{1}{N}\sum(dist)^2}$$

where *N* corresponds to the number of atoms that constitute the mean heme plane and *dist* is the distance (in Å) of a specific atom to the mean heme plane. The RMSD can be calculated from the 25-atom core displacement or the 4-atom *meso* carbon displacement.

Synthesis of [Fe(η^5-$C_5H_4COMe)_2$][BF_4]: In the glovebox, 115 mg (0.426 mmol) 1,1'-diacetylferrocene and 129 mg (0.426 mmol) [thianthrene][BF_4] were dissolved in 7 mL dichloromethane, which caused a light blue solid to precipitate from the reaction mixture. The reaction was allowed to stir for ~30 minutes and at this point was vacuum filtered through a frit to give a teal blue powder. This powder was washed with dichloromethane and hexanes, and then stored in the glovebox freezer. Yield: 93 mg (0.261 mmol, 61%) UV-vis (CH_2Cl_2): 655 nm. Anal. Calcd. for $C_{14}H_{14}BF_4FeO_2$: C, 47.11; H, 3.95; N, 0.00. Found: C, 46.69; H, 3.58; N, 0.00. No peaks from the oxidant are observed in the ^{1}H-NMR spectrum. $^{19}F\{^1H\}$ NMR (CD_2Cl_2, 377 MHz): –168.341 (s). IR (KBr): ν(CO) = 1693 cm^{-1}, $\nu(BF_4)$ = 1054 cm^{-1}.

Synthesis of [Fe(TPP)(NO)]: A 219 mg (0.242 mmol) portion of [Fe(TPP)(SbF_6)] was dissolved in 8 mL dichloromethane and 1 mL methanol. Then, the solution was exposed to NO gas, which caused the solution to turn bright red in color. The solution was brought carefully into the glovebox and allowed to stir overnight. The following day, 30 mL methanol was added to the solution, which was then stored at -33°C in the glovebox freezer. After 2 days, the reaction mixture was vacuum filtered in the glovebox through a frit and the resulting dark purple powder was washed with hexanes. Yield: 145 mg (0.208 mmol, 86%) UV-vis (CH_2Cl_2): 404, 476, 538, 612 nm. ^{1}H-NMR (CD_2Cl_2, 400 MHz): $\delta = \sim 6.0$ (br, β pyrrole H); 7.46 (s, *para*-H); 7.80 (br, *ortho*-H); 8.26 (s, *meta*-H). Peaks were assigned based on a previous literature report.[29] Anal. Calcd. for $C_{44}H_{28}FeN_5O$: C, 75.65; H, 4.04; N, 10.03. Found: C, 73.99; H, 4.17; N, 9.78. IR (KBr): ν(NO) = 1696 cm^{-1}.

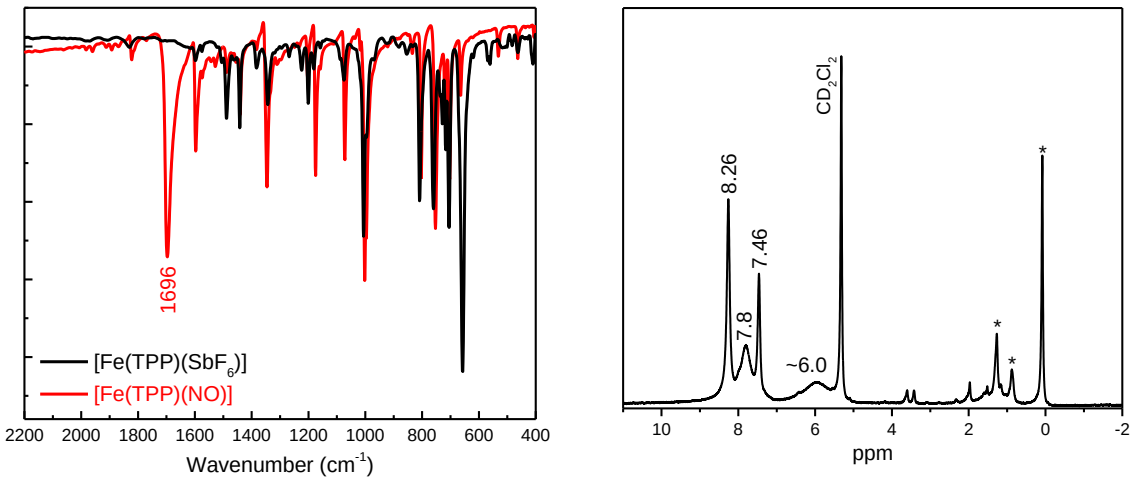

Figure 4.30. Left: Overlay of the IR spectra of the precursor, [Fe(TPP)(SbF_6)] (black), and of the iron NO complex, [Fe(TPP)(NO)] (red), measured in KBr pellets. Right: ^{1}H-NMR spectrum of [Fe(TPP)(NO)] recorded in CD_2Cl_2, with the line width set to 1 Hz. The *denotes residual hexanes and grease in the NMR sample.

Synthesis of [Fe(TPP)(NO)]SbF_6: A 65 mg (0.0720 mmol) portion of [Fe(TPP)(SbF_6)] was dissolved in 4 mL dichloromethane. Then, the solution was exposed to NO gas, which caused the solution to turn bright red in color. The solution was brought carefully into the glovebox and was layered with 20 mL hexanes and stored at -33°C in the glovebox freezer overnight. The next day, a purple solid was filtered off in the glovebox through a frit. The complex was stored in the glovebox freezer. Yield: 59 mg (0.0631 mmol, 88%) UV-vis (CH_2Cl_2): 370, 411, 550 nm. ^{1}H-NMR (CD_2Cl_2, 500 MHz): $\delta = 7.70 - 7.876$ (m). IR (KBr): ν(NO) = 1850 cm^{-1} and $\nu(SbF_6)$ = 656 cm^{-1}. $^{19}F\{^1H\}$ NMR (471 MHz): –126.99 (br, m).

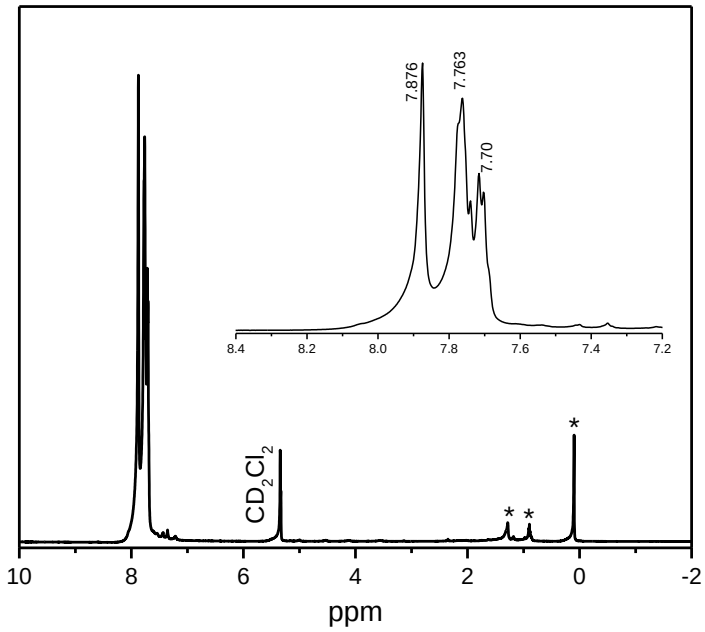

Figure 4.31. ^{1}H-NMR spectrum of [Fe(TPP)(NO)]SbF_6 recorded in CD_2Cl_2, with the line width set to 1 Hz. The *denotes residual hexanes and grease in the NMR sample. The $\{FeNO\}^6$ complex was prepared by reaction of [Fe(TPP)(SbF_6)] with excess NO gas.

Synthesis of [Fe(TPP)(NO)(MI)]SbF_6: A 63 mg (0.0697 mmol) portion of [Fe(TPP)(SbF_6)] with 5.6 μL 1-methylimidazole (0.0662 mmol) added was dissolved in 3 mL dichloromethane. Then, the solution was exposed to NO gas, which caused the solution to turn bright red in color. The solution was brought carefully into the glovebox and was layered with 16 mL hexanes and stored at -33°C in the glovebox freezer overnight. The next day, a purple solid was filtered off in the glovebox through a frit. The complex was stored in the glovebox freezer. Yield: 45 mg (0.0442 mmol, 64%). UV-vis (CH_2Cl_2): 430, 544, 580 nm. IR (KBr): ν(NO) = 1918 cm^{-1} and ν(SbF_6) = 658 cm^{-1}.

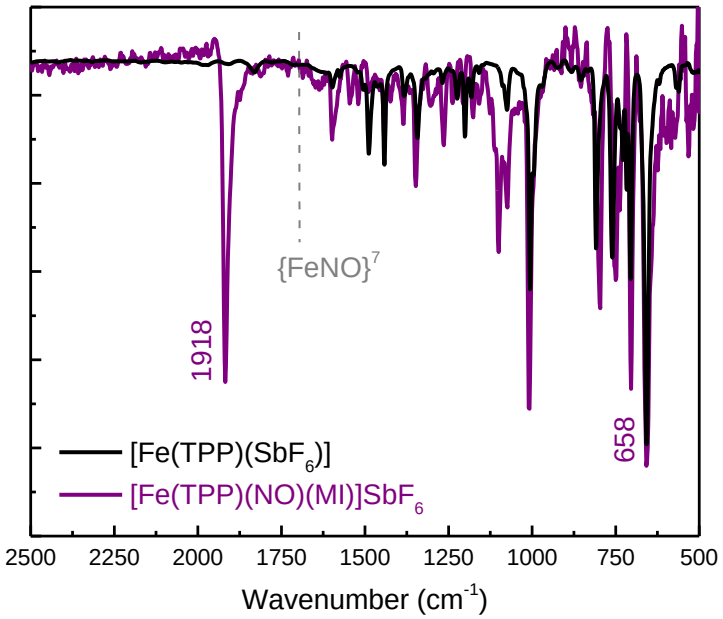

Figure 4.32. Overlay of the IR spectra of the precursor, [Fe(TPP)(SbF_6)] (black), and of the isolated ferric NO product, [Fe(TPP)(NO)(MI)]SbF_6 (purple), measured in KBr pellets. The $\{FeNO\}^6$ complex was prepared from the reaction of [Fe(TPP)(SbF_6)] with ~1 equiv. MI and excess NO gas.

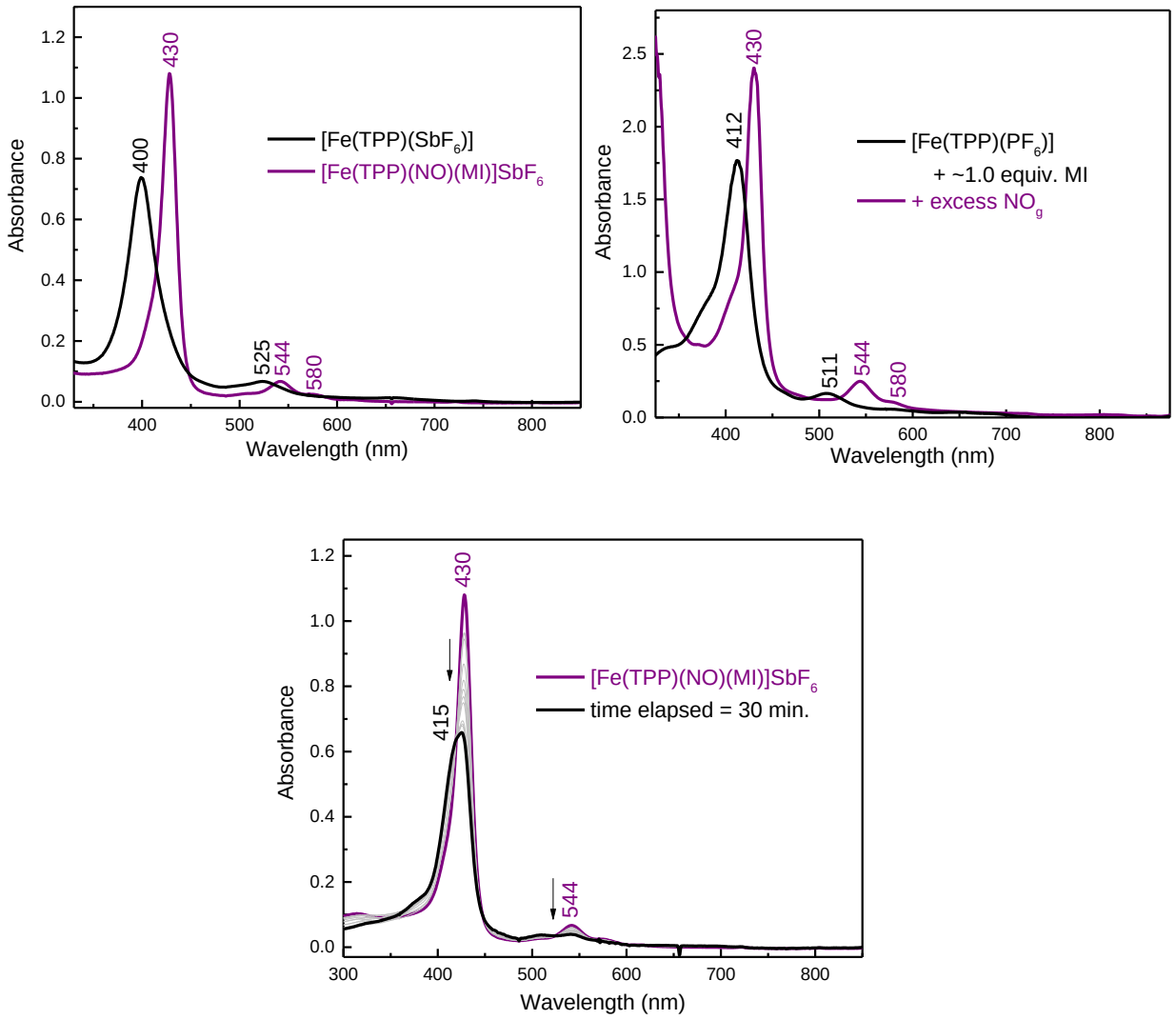

Figure 4.33. Top Left: UV-vis spectra of the ferric precursor, [Fe(TPP)(SbF_6)] (black), and the isolated ferric NO product, [Fe(TPP)(MI)(NO)]SbF_6 (purple), dissolved in CH_2Cl_2. Note: the $\{FeNO\}^6$ complex was prepared from the reaction of [Fe(TPP)(SbF_6)] with ~1 equiv. MI and excess NO gas. Top Right: UV-vis spectra of the ferric precursor, [Fe(TPP)(PF_6)], in the presence of ~1 equiv. MI (black), and after reaction of the solution with excess NO gas, resulting in the formation of [Fe(TPP)(MI)(NO)]PF_6 (purple) in CH_2Cl_2. Bottom: UV-vis monitoring of the dissolution of the bulk material, [Fe(TPP)(NO)(MI)]SbF_6 (purple), prepared via the method described above in dichloromethane in the absence of NO gas. Over a time period of 30 minutes, the $\{FeNO\}^6$ complex loses NO to form the ferric bis imidazole complex, [Fe(TPP)$(MI)_2$]SbF_6, and the ferric complex [Fe(TPP)(SbF_6)], shown in black. All spectra were recorded at room temperature.

Synthesis of [Fe(TPP)(NO)(Cl)]: A 104 mg (0.148 mmol) portion of [Fe(TPP)(Cl)] was dissolved in 11 mL dichloromethane. Then, the solution was exposed to NO gas, which caused the solution to turn brown-red in color. The solution was brought carefully into the glovebox and was layered with 30 mL hexanes and stored at -33°C in the glovebox freezer overnight. The next day, the resulting solid was filtered off in the glovebox through a frit. The complex was stored in the glovebox freezer. Yield: 40 mg (0.0545 mmol, 37%) UV-vis (CH_2Cl_2): 430, 544, 582 nm. IR (KBr): ν(NO) = 1880 cm^{-1}.

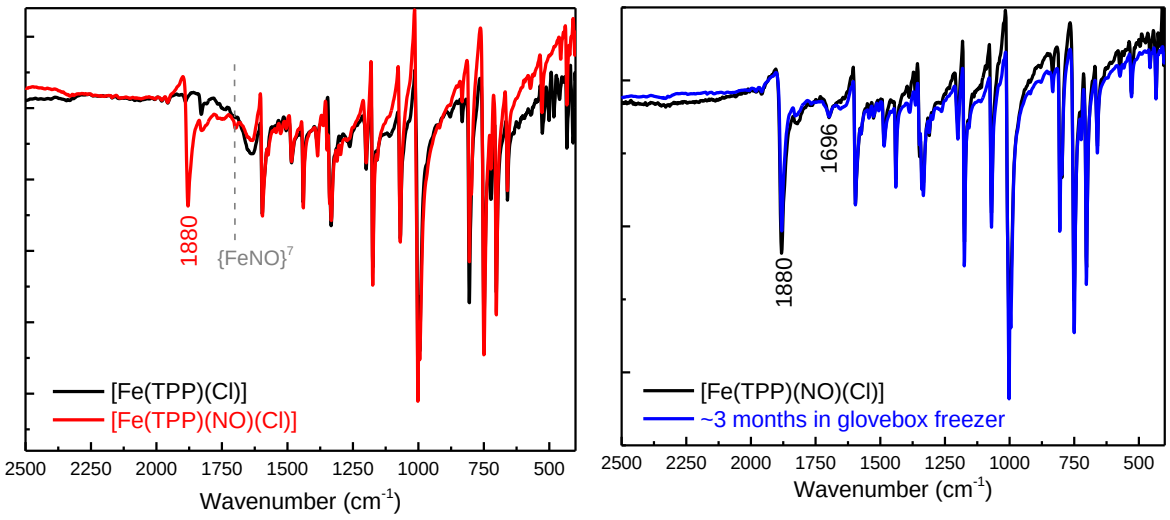

Figure 4.34. Left: Overlay of the IR spectra of the precursor, [Fe(TPP)(Cl)] (black), and of the iron NO complex, [Fe(TPP)(NO)(Cl)] (red), measured in KBr pellets. Right: Overlay of the IR spectra of the ferric NO complex, [Fe(TPP)(NO)(Cl)] (black), and of the same solid after ~3 months in the glovebox freezer (blue), indicating very small NO loss over time. The feature at 1696 cm^{-1} is the iron(II)-NO complex, [Fe(TPP)(NO)], which results from autoreduction of the ferric NO complex.

Synthesis of [Fe(TPP)(NO)(X)] using [TBA][X] (X = Cl^-, Br^-, I^-): 61.3 mg [Fe(TPP)(SbF_6)] (0.068 mmol) was dissolved in 4 mL dichloromethane, and then

exposed to NO gas causing the solution to turn bright red in color. Then, the solution was carefully brought into the glovebox and 22 mg tetrabutylammonium bromide (0.0682 mmol), dissolved in 0.3 mL dichloromethane, was injected into the solution, which was then allowed to stir for ~30 minutes. Over time the solution turned more brown-red in color, and at that point the solution was layered with 15 mL hexanes and left in the glovebox freezer. Several hours later the solution was vacuum filtered to give a purple solid coated in a white patina (the white patina is [TBA][SbF_6]). IR (KBr): ν(NO) = 1870 cm^{-1}. The procedure with tetrabutylammonium chloride (ν(NO) = 1880 cm^{-1}) and tetrabutylammonium iodine was carried out in a similar manner. However, with [TBA][I], the ferric NO complex is reduced by one-electron forming [Fe(TPP)(NO)] (ν(NO) = 1696 cm^{-1}), I_2, and [TBA][SbF_6].

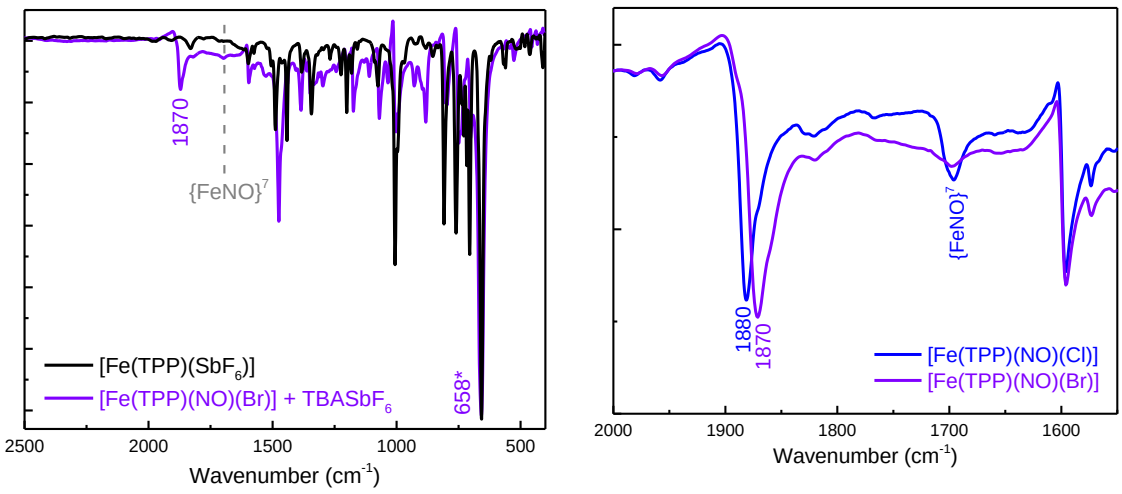

Figure 4.35. Left: Overlay of the IR spectra (taken in KBr pellets) of the precursor, [Fe(TPP)(SbF_6)] (black), which, upon reaction with NO gas and [TBA][Br], yields the iron NO complex, [Fe(TPP)(NO)(Br)], and [TBA][SbF_6] (purple). Right: Overlay of the IR spectra of the two iron NO complexes with halide coordination, [Fe(TPP)(NO)(Cl)] (blue) and [Fe(TPP)(NO)(Br)] (purple), measured in KBr pellets. The *denotes the Sb-F stretching frequency from [TBA][SbF_6].

Chemical Oxidation of [Fe(TPP)(NO)]: Under an inert atmosphere, 6.6 mg [Fe(TPP)(NO)] (0.0094 mmol) was dissolved in 3 mL dichloromethane. The solution was added to 5.7 mg of solid $[Fe(\eta^5\text{-}C_5H_4COMe)_2][SbF_6]$ (0.0113 mmol) and agitated until all of the solid had dissolved, forming $[Fe(TPP)(NO)]SbF_6$. The solution changed color from brown-red to bright red. EPR and solution IR data were recorded on the same sample to ensure full conversion and complete nitrosylation of the iron complex. UV-vis (CH_2Cl_2): 370, 411, 550 nm. ^{1}H-NMR (CD_2Cl_2, 400 MHz): $\delta = 7.25$ (s); 7.46 (s); 7.72 (s); 7.88 (s). ^{19}F{^{1}H} NMR (471 MHz): –125.83 (br, m). IR (CH_2Cl_2): ν(NO) = 1850 cm^{-1}.

Addition of MI: Under an inert atmosphere, 6.6 mg [Fe(TPP)(NO)] (0.0094 mmol) was dissolved with ~0.75 μL 1-methylimidazole (MI) in 3 mL dichloromethane. The solution was added to 5.7 mg of solid $[Fe(\eta^5\text{-}C_5H_4COMe)_2][SbF_6]$ (0.0113 mmol) and agitated until all of the solid had dissolved, forming $[Fe(TPP)(NO)(MI)]SbF_6$. The solution changed color from brown-red to bright red. EPR and solution IR data were recorded on the same sample to ensure full conversion and complete nitrosylation of the iron complex. Note: Samples of $[Fe(TPP)(NO)(MI)]^+$ generally contain a small amount of $[Fe(TPP)(NO)]SbF_6$, evident from a small solution IR band at 1850 cm^{-1}. UV-vis (CH_2Cl_2): 430, 544, 580 nm. ^{1}H-NMR (CD_2Cl_2, 400 MHz): $\delta = 2.06$ (s); 3.90 (s); 4.68 (s); 7.26 (s); 7.49 (s); 7.49 (s); 7.83 (s); 8.14 (s); 9.16 (s). IR (CH_2Cl_2): ν(NO) = 1920 cm^{-1}.

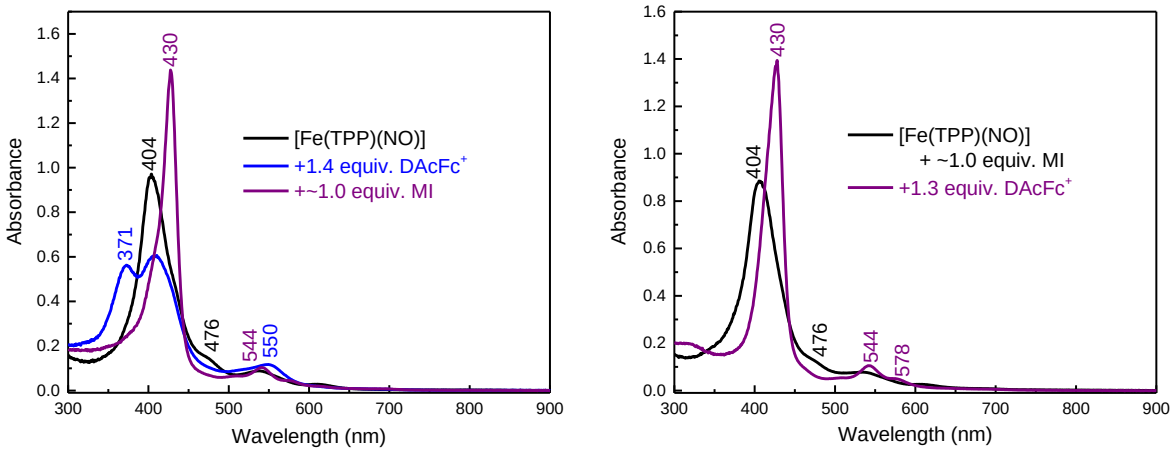

Figure 4.36. Left: UV-vis spectra of [Fe(TPP)(NO)] (black) with the chemical oxidant (dissolved in dimethoxyethane) [DAcFc][SbF_6], in dichloromethane, to form the ferric NO complex, $[Fe(TPP)(NO)]^+$ (blue). Then, ~1 equiv. MI was added to the solution of $[Fe(TPP)(NO)]^+$ to form the corresponding $[Fe(TPP)(NO)(MI)]^+$ complex (purple). Right: UV-vis spectra of [Fe(TPP)(NO)] (black) with ~1 equiv. MI added to the solution in dichloromethane. To this solution, ~1.3 equiv. [DAcFc][SbF_6] (dissolved in dimethoxyethane) was added to form the complex $[Fe(TPP)(NO)(MI)]^+$ (purple). All spectra were taken at room temperature. The UV-vis spectra of $[Fe(TPP)(NO)(MI)]^+$ are identical, independent of the method of preparation.

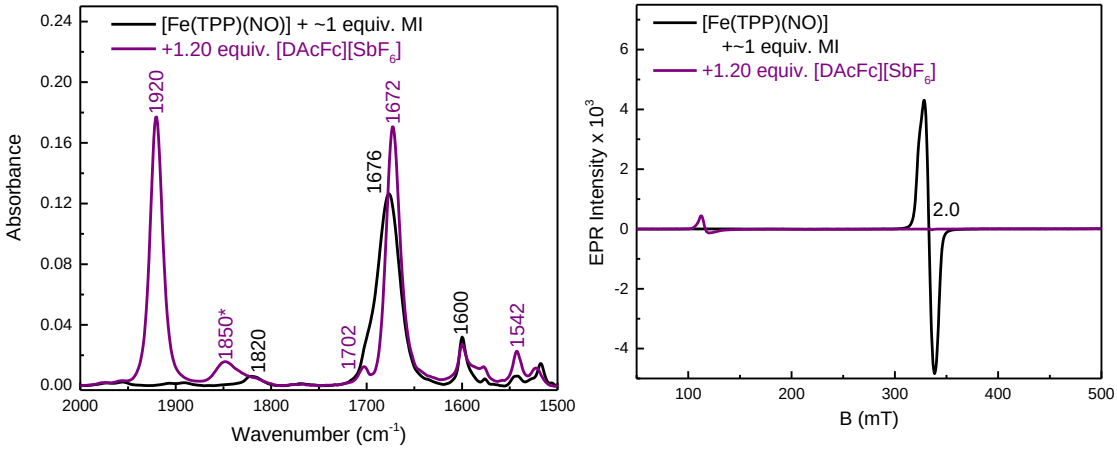

Figure 4.37. Left: Solution IR spectra of a 3.2 mM solution of [Fe(TPP)(NO)] (black) in the presence of ~1 equiv. MI in CH_2Cl_2 and of the reaction product (in purple) after the addition of ~1.20 equiv. [DAcFc][SbF_6] to the solution. The N-O stretch at 1676 cm^{-1} shifts to 1920 cm^{-1} upon oxidation. The band at 1850 cm^{-1}(*) corresponds to a small amount of five-coordinate $[Fe(TPP)(NO)]^+$. The bands at 1702 and 1672 cm^{-1} are the C-O stretching frequencies of the respective $DAcFc^{0/+}$ reagents. Right: EPR spectra of the same solution used in the solution IR experiments (on the left) at 4K. The black spectrum represents the $\{FeNO\}^7$ complex with a broad, isotropic S = 1/2 signal at g = 2.0, and the purple spectrum represents the corresponding oxidized species, $[Fe(TPP)(NO)]^+$, which is EPR silent and contains a minor g = 6 signal that spin integrates to ~5% of a ferric species. The sample was spin integrated against [Fe(TPP)(Cl)] using SpinCount.

Crystallization of [Fe(TPP)(NO)(MI)]PO_2F_2: 10 mg [Fe(TPP)(NO)(MI)]PF_6 (see discussion below regarding the counterion) was dissolved in 0.2 mL NO-saturated dichloromethane and placed in a 5 mm diameter glass tube and sealed with a septa. The solution was then carefully layered with 2 mL NO saturated hexanes and placed in a -33°C glovebox freezer. After 3 days, black needles suitable for X-ray analysis were collected.

It should be noted that in the crystal structure of this complex, the counterion is not the PF_6^- anion and was determined to be $PO_2F_2^-$ through a series of ^{31}P- and ^{19}F-NMR experiments. The $PO_2F_2^-$ counterion is formed during the methathesis reaction of the ferric chloride complex, [Fe(TPP)(Cl)], with $AgPF_6$ to form the ferric PF_6^- complex and AgCl. Interestingly, the PF_6^- anion further undergoes an iron-catalyzed hydrolysis (in the presence of trace amounts of water), resulting in a mixture of PF_6^- and $PO_2F_2^-$ counterions. This silver salt hydrolysis has been noted in previous reports.[67,68] Initially, we did not observe the $PO_2F_2^-$ counterion in the bulk material of [Fe(TPP)(PF_6)] because it is bound to the iron center, and the paramagnetism of the iron center masks the signals in the NMR spectra. To counteract this problem, excess (>2 equiv.) MI was added to the solution of the iron(III)-PF_6 complex to remove the $PO_2F_2^-$ ligand from the iron center (via formation of $[Fe(TPP)(MI)_2]^+$ and free $PO_2F_2^-$ and PF_6^-), which allowed us to observe the signals from both the PF_6^- and $PO_2F_2^-$ counterions in the ^{19}F- and ^{31}P-NMR spectra.

Crystallization of [Fe(TPP)(NO)(Cl)]: 55.6 mg [Fe(TPP)(Cl)] was dissolved in 6 mL dichloromethane. Then, the solution was exposed to NO gas and brought carefully into the glovebox. Next, ~0.2 mL solution was transferred to a 5 mm diameter glass tube and layered with 2 mL dimethoxyethane (DME) and placed in a -33°C glovebox freezer. After 4 days, brown prisms suitable for X-ray analysis were collected. Excess NO gas was not required.

Crystallization of [Fe(TPP)(NO)]BF_4: A portion of [Fe(TPP)(NO)] (15.5 mg, 22.2 mmol) was dissolved in 3.5 mL dichloromethane. To this solution, 9.9 mg of solid [DAcFc][BF_4] (27.7 mmol) was added, and the solution was agitated until the oxidant was completely dissolved. In a 5 mm diameter glass tube, 0.2 mL of the oxidized solution was carefully layered with 2 mL hexanes and placed in a -33°C glovebox freezer. After 3 days, brown block-like crystals suitable for X-ray analysis were collected.

Physical Methods

Infrared spectra were obtained from KBr disks on Perkin-Elmer BX and GX spectrometers at room temperature. Measurements in solution were performed in a cell equipped with two CaF_2 windows on the same instruments. Electronic absorption spectra were measured using an Analytical Jena Specord S600 instrument at room temperature. Electron paramagnetic resonance spectra were recorded on a Bruker X-band EMX spectrometer equipped with Oxford Instruments

liquid nitrogen and helium cryostats. EPR spectra were typically obtained on frozen solutions using 20 mW microwave power and 100 kHz field modulation with the amplitude set to 1 G. Sample concentrations were ~1 – 3 mM. Proton and fluorine NMR spectra were recorded on a Varian MR 400 MHz instrument or a Varian NMRS 500 MHz spectrometer at room temperature. Cyclic voltammograms were obtained using a CH instruments CHI600E electrochemical workstation with a three component electrochemical cell consisting of a glassy carbon working electrode, platinum counter electrode, and silver wire pseudo-reference electrode. All potentials were corrected to Fc/Fc^{+}. UV-vis and IR spectroelecrochemical measurements were performed using custom-built thin layer electrochemical cells as previously described.[28] All electrochemical and spectroelectrochemical measurements were carried out in the presence of 0.1 – 0.3 M tetrabutylammonium hexafluorophosphate. Nuclear Resonance Vibrational Spectroscopy (NRVS) was carried out as previously described[69] at beamline 3-ID-XOR at the Advanced Photon Source (APS) at Argonne National Laboratory. This beamline provides about 2.5×10^{9} photons/sec in ~1 meV bandwidth (8 cm^{-1}) at 14.4125 keV in a 0.5 mm (vertical) x 0.5 mm (horizontal) spot. Samples were loaded into 4 x 7 x 1 mm copper cells. The final spectra represent averages of 4 scans. The program Phoenix was used to convert the NRVS raw data to the Vibrational Density of States (VDOS).[70,71] All of the $\{^{57}FeNO\}^{6}$/$\{^{57}Fe^{15}N^{18}O\}^{6}$ complexes were pure based on IR spectroscopy. The resonance Raman measurements were performed using the 413.13 nm excitation line from a Kr^{+} ion

laser (Spectra Physics Beam Lok 2060-RS). Raman spectra were recorded at 77 K using an Acton two-stage TriVista 555 monochromator connected to a liquid nitrogen cooled CCD camera (Princeton instruments Spec-10:400B/LN). The total exposure time of the samples to the laser radiation was 3 minutes using 1-2 accumulations, and typical laser powers were in the 20 – 30 mW range.

Crystal structure determination. All crystals were measured on a Rigaku AFC10K Saturn 944+ CCD-based X-ray diffractometer equipped with a low temperature device and a Micromax-007HF Cu-target micro-focus rotating anode (λ = 1.54187 Å) operated at 1.2 kW power (40 kV, 30 mA). The X-ray intensities were measured at 85 K with the detector placed at a distance 42.00 mm from the crystals.

[Fe(TPP)(NO)(MI)]PO_2F_2: A black needle of [Fe(TPP)(NO)(MI)]PO_2F_2 of dimensions 0.22 x 0.05 x 0.02 mm was mounted on the diffractometer. A total of 4053 images were collected with an oscillation width of 1.0° in ω. The exposure time was 5 sec. for the low angle images, 30 sec. for high angle. The integration of the data yielded a total of 71715 reflections to a maximum 2θ value of 136.44° of which 9081 were independent and 6991 were greater than 2σ(I). The final cell constants were based on the xyz centroids of 18806 reflections above 10σ(I). Analysis of the data showed negligible decay during data collection. The data were processed with CrystalClear 2.0 and corrected for absorption.[72] The structure was

solved and refined with the Bruker SHELXTL (version 2008/4) software package,[73] using the space group P1bar with Z = 2 for the formula $FeC_{48}H_{34}N_7O$, $PO_2F_2^-$, CH_2Cl_2, and H_2O. All non-hydrogen atoms were refined anisotropically with the hydrogen atoms placed in idealized positions. Full matrix least-squares refinement based on F^2 converged at R1 = 0.1099 and wR2 = 0.2727 [based on I > 2□(I)], R1 = 0.1244 and wR2 = 0.2791 for all data.

[Fe(TPP)(NO)]BF_4: A brown block-like crystal of [Fe(TPP)(NO)]BF_4 of dimensions 0.22 x 0.12 x 0.12 mm was mounted on the diffractometer. A total of 2028 images were collected with an oscillation width of 1.0° in ω. The exposure times were 5 sec. for the low angle images, 30 sec. for high angle. Rigaku d*trek images were exported to CrysAlisPro for processing and corrected for absorption.[72,74] The integration of the data yielded a total of 64490 reflections to a maximum 2θ value of 139.14° of which 15452 were independent and 14777 were greater than $2\sigma(I)$. The final cell constants were based on the xyz centroids of 30783 reflections above $10\sigma(I)$. Analysis of the data showed negligible decay during data collection. The structure was solved and refined with the Bruker SHELXTL (version 2014/6) software package,[73] using the space group P1bar with Z = 4 for the formula $FeC_{44}H_{28}N_5O$, BF_4^-, and 2.25(CH_2Cl_2). All non-hydrogen atoms were refined anisotropically with the hydrogen atoms placed in idealized positions. Full matrix least-squares refinement based on F^2 converged at R1 = 0.0714 and wR2 = 0.1969 [based on I > $2\sigma(I)$], R1 = 0.0732 and wR2 = 0.1995 for all data.

[Fe(TPP)(NO)(Cl)]: A brown prism of [Fe(TPP)(NO)(Cl)] of dimensions 0.16 x 0.10 x 0.10 mm was mounted on the diffractometer. A total of 2028 images were collected with an oscillation width of 1.0° in ω. The exposure times were 1 sec. for the low angle images, 4 sec. for high angle. Rigaku d*trek images were exported to CrysAlisPro for processing and corrected for absorption.[72,74] The integration of the data yielded a total of 13642 reflections to a maximum 2θ value of 137.91° of which 870 were independent and 867 were greater than $2\sigma(I)$. The final cell constants were based on the xyz centroids of 6524 reflections above $10\sigma(I)$. Analysis of the data showed negligible decay during data collection. The structure was solved and refined with the Bruker SHELXTL (version 2014/6) software package,[73] using the space group I4/m with Z = 2 for the formula $FeC_{44}H_{28}N_5OCl$. All non-hydrogen atoms were refined anisotropically with the hydrogen atoms placed in idealized positions. The chloro and nitrosyl ligands are disordered 50/50 on both faces of the porphyrin. Full matrix least-squares refinement based on F^2 converged at R1 = 0.0492 and wR2 = 0.1506 [based on $I > 2\sigma(I)$], R1 = 0.0492 and wR2 = 0.1506 for all data.

4.7 References

1. Moncada, S.; Palmer, R. M.; Higgs, E. A. *Pharmacol. Rev.* 1991, *43*, 109.
2. Bredt, D. S.; Snyder, S. H. *Annu. Rev. Biochem* 1994, *63*, 175-195.
3. Snyder, S. H. *Science* 1992, *257*, 494.
4. Stuehr, D. J. *Annu. Rev. Pharmacool. Toxicol.* 1997, *37*, 339-359.
5. Li, H.; Poulos, T. L. *J. Inorg. Biochem.* 2005, *99*, 293-305.
6. Ignarro, L. J. *Biochem. Soc. Trans.* 1992, *20*, 465.
7. Walker, F. A. *J. Inorg. Biochem.* 2005, *99*, 216-236.
8. Enemark, J. H.; Feltham, R. D. *Coord. Chem. Rev.* 1974, *13*, 339-406.
9. Ferguson, S. J. *Curr. Opin. Chem. Biol.* 1998, *2*, 182-193.
10. Richardson, D. J.; Watmough, N. J. *Curr. Opin. Chem. Biol.* 1999, *3*, 207-219.
11. McQuarters, A. B.; Wirgau, N. E.; Lehnert, N. *Curr. Opin. Chem. Biol.* 2014, *19*, 82-89.
12. Lehnert, N.; Berto, T. C.; Galinato, M. G. I.; Goodrich, L. E. In *The Handbook of Porphyrin Science*; Kadish, K. M., Smith, K. M., Guilard, R., Eds.; World Scientific: New Jersey, 2011; Vol. 14, p 1-247.
13. Cooper, C. E. *Biochim. Biophys. Acta* 1999, *1411*, 290-309.
14. Hoshino, M.; Ozawa, K.; Seki, H.; Ford, P. C. *J. Am. Chem. Soc.* 1993, *115*, 9568-9575.
15. Lehnert, N.; Scheidt, W. R.; Wolf, M. W. In *Nitrosyl Complexes in Inorganic Chemistry, Biochemistry and Medicine II*; Mingos, D. M. P., Ed.; Springer Berlin Heidelberg: Berlin, Heidelberg, 2014, p 155-223.
16. Praneeth, V. K. K.; Paulat, F.; Berto, T. C.; Debeer George, S.; Nather, C.; Sulok, C. D.; Lehnert, N. *J. Am. Chem. Soc.* 2008, *130*, 15288-15303.
17. Ellison, M. K.; Scheidt, W. R. *J. Am. Chem. Soc.* 1999, *121*, 5210-5219.
18. Ellison, M. K.; Schulz, C. E.; Scheidt, W. R. *Inorg. Chem.* 2000, *39*, 5102-5110.
19. Scheidt, W. R.; Lee, Y. J.; Hatano, K. *J. Am. Chem. Soc.* 1984, *106*, 3191-3198.
20. Yi, G.-B.; Khan, M. A.; Richter-Addo, G. B. *Inorg. Chem.* 1997, *36*, 3876-3885.
21. Addison, A. W.; Stephanos, J. J. *Biochemistry* 1986, *25*, 4104-4113.
22. Hoshino, M.; Maeda, M.; Konishi, R.; Seki, H.; Ford, P. C. *J. Am. Chem. Soc.* 1996, *118*, 5702-5707.
23. Roncaroli, F.; Videla, M.; Slep, L. D.; Olabe, J. A. *Coord. Chem. Rev.* 2007, *251*, 1903-1930.
24. Li, J.; Peng, Q.; Oliver, A. G.; Alp, E. E.; Hu, M. Y.; Zhao, J.; Sage, J. T.; Scheidt, W. R. *J. Am. Chem. Soc.* 2014, *136*, 18100-18110.
25. Ellison, M. K.; Schulz, C. E.; Scheidt, W. R. *Inorg. Chem.* 1999, *38*, 100-108.
26. Xu, N.; Goodrich, L. E.; Lehnert, N.; Powell, D. R.; Richter-Addo, G. B. *Angew. Chem. Int. Ed.* 2013, *52*, 3896-3900.

27. Das, P. K.; Samanta, S.; McQuarters, A. B.; Lehnert, N.; Dey, A. *Proceedings of the National Academy of Sciences* 2016, *113*, 6611-6616.

28. Goodrich, L. E.; Roy, S.; Alp, E. E.; Zhao, J.; Hu, M. Y.; Lehnert, N. *Inorg. Chem.* 2013, *52*, 7766-7780.

29. Praneeth, V. K. K.; Näther, C.; Peters, G.; Lehnert, N. *Inorg. Chem.* 2006, *45*, 2795-2811.

30. Berto, T. C.; Praneeth, V. K. K.; Goodrich, L. E.; Lehnert, N. *J. Am. Chem. Soc.* 2009, *131*, 17116-17126.

31. Samanta, S.; Das, P. K.; Chatterjee, S.; Sengupta, K.; Mondal, B.; Dey, A. *Inorg. Chem.* 2013, *52*, 12963-12971.

32. Chatterjee, S.; Sengupta, K.; Samanta, S.; Das, P. K.; Dey, A. *Inorg. Chem.* 2013, *52*, 9897-9907.

33. Das, P. K.; Chatterjee, S.; Samanta, S.; Dey, A. *Inorg. Chem.* 2012, *51*, 10704-10714.

34. Chatterjee, S.; Sengupta, K.; Hematian, S.; Karlin, K. D.; Dey, A. *J. Am. Chem. Soc.* 2015, *137*, 12897-12905.

35. Collman, J. P.; Devaraj, N. K.; Decréau, R. A.; Yang, Y.; Yan, Y.-L.; Ebina, W.; Eberspacher, T. A.; Chidsey, C. E. D. *Science (New York, N.Y.)* 2007, *315*, 1565-1568.

36. Boulatov, R.; Collman, J. P.; Shiryaeva, I. M.; Sunderland, C. J. *J. Am. Chem. Soc.* 2002, *124*, 11923-11935.

37. Collman, J. P.; Fu, L.; Herrmann, P. C.; Zhang, X. *Science* 1997, *275*, 949.

38. Garcia-Bosch, I.; Adam, S. M.; Schaefer, A. W.; Sharma, S. K.; Peterson, R. L.; Solomon, E. I.; Karlin, K. D. *J. Am. Chem. Soc.* 2015, *137*, 1032-1035.

39. Wayland, B. B.; Olson, L. W. *J. Am. Chem. Soc.* 1974, *96*, 6037-6041.

40. Mu, X. H.; Kadish, K. M. *Inorg. Chem.* 1988, *27*, 4720-4725.

41. Connelly, N. G.; Geiger, W. E. *Chem. Rev.* 1996, *96*, 877-910.

42. Quinn, R.; Nappa, M.; Valentine, J. S. *J. Am. Chem. Soc.* 1982, *104*, 2588-2595.

43. Laverman, L. E.; Ford, P. C. *J. Am. Chem. Soc.* 2001, *123*, 11614-11622.

44. Franke, A.; Stochel, G.; Noriyuki, S.; Higuchi, T.; Okuzono, K.; Eldik, R. V. *J. Am. Chem. Soc.* 2005, *127*, 5360-5375.

45. Safo, M. K.; Walker, F. A.; Raitsimring, A. M.; Walters, W. P.; Dolata, D. P.; Debrunner, P. G.; Scheidt, W. R. *J. Am. Chem. Soc.* 1994, *116*, 7760-7770.

46. Grande, L. M.; Noll, B. C.; Oliver, A. G.; Scheidt, W. R. *Inorg. Chem.* 2010, *49*, 6552-6557.

47. Praneeth, V. K. K.; Neese, F.; Lehnert, N. *Inorg. Chem.* 2005, *44*, 2570-2572.

48. Vogel, K. M.; Kozlowski, P. M.; Zgierski, M. Z.; Spiro, T. G. *J. Am. Chem. Soc.* 1999, *121*, 9915-9921.

49. Soldatova, A. V.; Ibrahim, M.; Olson, J. S.; Czernuszewicz, R. S.; Spiro, T. G. *J. Am. Chem. Soc.* 2010, *132*, 4614-4625.

50. Linder, D. P.; Rodgers, K. R.; Banister, J.; Wyllie, G. R. A.; Ellison, M. K.; Scheidt, W. R. *J. Am. Chem. Soc.* 2004, *126*, 14136-14148.

51. Benko, B.; Yu, N. T. *Proceedings of the National Academy of Sciences* 1983, *80*, 7042-7046.

52. Maes, E. M.; Walker, F. A.; Montfort, W. R.; Czernuszewicz, R. S. *J. Am. Chem. Soc.* 2001, *123*, 11664-11672.

53. Goodrich, L. E.; Paulat, F.; Praneeth, V. K. K.; Lehnert, N. *Inorg. Chem.* 2010, *49*, 6293-6316.

54. Xu, N.; Powell, D. R.; Cheng, L.; Richter-Addo, G. B. *Chem. Commun.* 2006, 2030-2032.

55. Hu, S.; Kincaid, J. R. *J. Am. Chem. Soc.* 1991, *113*, 2843-2850.

56. Obayashi, E.; Tsukamoto, K.; Adachi, S.-i.; Takahashi, S.; Nomura, M.; Iizuka, T.; Shoun, H.; Shiro, Y. *J. Am. Chem. Soc.* 1997, *119*, 7807-7816.

57. Hu, S.; Kincaid, J. R. *J. Am. Chem. Soc.* 1991, *113*, 9760-9766.

58. Hu, S.; Kincaid, J. R. *J. Biol. Chem.* 1993, *268*, 6189-6193.

59. Miller, L. M.; Pedraza, A. J.; Chance, M. R. *Biochemistry* 1997, *1997*, 12199-12207.

60. Tomita, T.; Haruta, N.; Aki, M.; Kitagawa, T.; Ikeda-Saito, M. *J. Am. Chem. Soc.* 2001, *123*, 2666-2667.

61. Wang, Y.; Averill, B. A. *J. Am. Chem. Soc.* 1996, *118*, 3972-3973.

62. Sampath, V.; Zhao, X.; Caughey, W. S. *Biochem. Biophys. Res. Commun.* 1994, *198*, 281-287.

63. Ding, X. D.; Weichsel, A.; Andersen, J. F.; Shokhireva, T. K.; Balfour, C.; Pierik, A. J.; Averill, B. A.; Montfort, W. R.; Walker, F. A. *J. Am. Chem. Soc.* 1999, *121*, 128-138.

64. Adler, A. D.; Longo, F. R.; Kampas, F.; Kim, J. *J. Inorg. Nucl. Chem.* 1970, *32*, 2443-2445.

65. McQuarters, A. B.; Goodrich, L. E.; Goodrich, C. M.; Lehnert, N. *Z. Anorg. Allg. Chem.* 2013, *639*, 1520-1526.

66. Boduszek, B.; Shine, H. J. *The Journal of Organic Chemistry* 1988, *53*, 5142-5143.

67. Fernandez-Galan, R.; Manzano, B. R.; Otero, A.; Lanfranchi, M.; Pellinghelli, M. A. *Inorg. Chem.* 1994, *33*, 2309-2312.

68. White, C.; Thompson, S. J.; Maitlis, P. M. *J. Organomet. Chem.* 1977, *134*, 319-325.

69. Paulat, F.; Berto, T. C.; DeBeer George, S.; Goodrich, L.; Praneeth, V. K. K.; Sulok, C. D.; Lehnert, N. *Inorg. Chem.* 2008, *47*, 11449-11451.

70. Sage, J. T.; Paxson, C.; Wyllie, G. R. A.; Sturhahn, W.; Durbin, S. M.; Champion, P. M.; Alp, E. E.; Scheidt, W. R. *J. Phys.: Condens. Matter* 2001, *13*, 7707.

71. Sturhahn, W. *Hyperfine Interact.* 2000, *125*, 149-172.

72. In *CrystalClear Expert 2.0 r12*; Rigaku Americas and Rigaku Corporation: 9009, TX, USA 77381-5209, 2011.

73. Sheldrick, G. M. In *SHELXTL*; v. 2008/4 ed.; Bruker Analytical X-ray: Madison, WI, 2008.

74. In *CrysAlisPro 1.171.38.41* Rigaku Oxford Diffraction: 2015.

Chapter 5

Conclusions

In denitrification, nitrate is reduced in a step-wise manner to dinitrogen (bacteria), or N_2O (fungi). The two-electron reduction of nitric oxide (NO) to nitrous oxide (N_2O) is carried out by a class of enzymes called Nitric Oxide Reductases (NORs). Cytochrome P450 nitric oxide reductase (P450nor) carries out this important reaction for anaerobic respiration. The active site of this enzyme contains a heme thiolate, which is structurally similar to Cyt. P450 monooxygenase type enzymes.[1-4] This dissertation focuses on small molecule models of reactive intermediates in the mechanism of P450nor.

The key question in the catalytic cycle of P450nor has been the protonation state of Intermediate *I*. Previous work from enzyme studies imply that Intermediate *I* is the double protonated, iron(IV)-$NHOH^-$/iron(III)-NHOH(radical) species, rather than a singly protonated iron(II)-NHO complex.[5] Based on QM/MM studies,[6] it is believed that electronic structure of this species is best described as an iron(III)-NHOH(radical) type complex. Chapter 2 is focused on modeling the doubly protonated intermediate responsible for N-N bond formation in P450nor. Here, a new iron(III)-NHOMe complex using a bis-picket fence porphyrin is prepared. The one-electron oxidation of this complex to the corresponding formally ferryl species, $[Fe(3,5\text{-Me-BAFP})(NHOMe)]^+$, as a chemical model for Intermediate *I*. In-depth

spectroscopic characterization showed that the electronic structure of the model is an iron(III)-NHOMe(radical) type complex, rather than an iron(IV)-$NHOMe^-$ species. The oxidized species reacts with NO gas to form a ferric complex like P450nor, however we did not detect any N_2O. The N-containing products will be further analyzed via isotope labeling studies for future studies. There are important differences between this model complex and P450nor that could influence the mechanism of N-N bond formation. In P450nor, Intermediate *I* is six-coordinate with a proximal thiolate ligand bound to the iron center, whereas, in our model, the complex is five-coordinate (ie. no ligand trans to the $NHOMe^-$ ligand). The role of the thiolate ligand is proposed to modulate the electron density of the iron center, which makes the bound HNO unit more basic to form the doubly protonated intermediate.[7] Additionally, the thiolate ligand influences the spin state of the protein. The spin state of our oxidized species, $[Fe(3,5\text{-Me-BAFP})(NHOMe)]^+$, is high-spin, whereas P450nor is low-spin. The spin state likely plays a *crucial* role in N-N bond formation, since the properties of high- and low-spin iron complexes are inherently different. With this, future studies should focus on generation of a six-coordinate Intermediate *I* model that is low-spin. One could envision doing this by the addition of MI (MI = 1-methylimidazole) to the oxidized species, $[Fe(3,5\text{-Me-BAFP})(NHOMe)]^+$, at low temperature to form the six-coordinate complex $[Fe(3,5\text{-Me-BAFP})(NO)(MI)]^+$. We have preliminary evidence that this species is formed by UV-vis spectroscopy. Further spectroscopic confirmation of the ground state of this complex is necessary (by rRaman and

Mössbauer spectroscopy). The low-spin adduct could be key to N-N bond formation like that of P450nor.

Chapter 3 describes the synthesis and spectroscopic characterization of ferrous porphyrin RNO complexes. These complexes are isoelectronic to $\{FeNHO\}^8$ complexes, however they do not suffer from the same stability problems discussed in Chapter 1. We synthesized ferrous RNO complexes where the R group was an isopropyl or phenyl group using the TPP^{2-} and 3,5-Me-$BAFP^{2-}$ porphyrin ligands. From this, we examined the vibrational spectroscopy of [Fe(TPP)(iPrNO)] in detail. This is a major step forward in understanding the Fe-NO vibrations for $\{FeNHO\}^8$/$\{FeRNO\}^8$ species in proteins that were previously ambiguous. We also learned that $\{FeRNO\}^8$ complexes are unreactive toward NO and do not form N-N bonds (even with a ligand such as MI bound to the iron center) In P450nor, the proximal thiolate ligand plays a rule in tuning the electronics of the iron complex to form Intermediate *I*.[7] In this way, one could imagine that a proximal thiolate ligand could influence the electronics of an $FeNHO\}^8$/$\{FeRNO\}^8$ species, resulting in reactivity with NO for N-N bond formation. We showed that ferrous RNO complexes have no *trans* effect. For future studies, one could synthesize a $\{FeRNO\}^8$ complex with a neutral thiol donor ligand. It would be synthetically challenging to prepare a $\{FeRNO\}^8$ with a strong anionic donor, such a thiolate ligand. However, it may be possible to prepare this kind of complex with a weaker thiolate donor, such as the two hydrogen bond stabilized thiolate ligand, $SR\text{-}H_2^-$ (this ligand is discussed in Chapter 1). Lastly, we showed that the reaction of $\{FeiPrNO\}^8$ complexes with excess trifluoroacetic acid (TFA) results in a ferric

complex (at room temperature). We envisioned that TFA could protonate the iPrNO moiety to yield an iron(III)-NOHR(radical) species based on our work in Chapter 2. This species is an analogue to Intermediate *I* in P450nor. However, our initial attempts at the detection of the reaction products revealed that this intermediate was not formed, instead the reactivity is driven by the carboxylic acid. This finding needs further proof by carrying out the reaction with a different strong acid such as HCl.

Chapter 4 reports the synthesis of a new series of ferric heme-nitrosyl complexes. Our new route to synthesize {FeNO}^{6} complexes in the absence of excess NO gas makes future reactivity studies feasible with reagents that would typically react with free NO gas in solution. We spectroscopically and structurally characterized the 5C complex, [Fe(TPP)(NO)]$^+$ and the 6C complexes [Fe(TPP)(NO)(MI)]$^+$ and [Fe(TPP)(NO)(Cl)] with axial imidazole and halide coordination. The latter complex is a key intermediate in reductive nitrosylation that has never been characterized. Finally, we determined the k_{off} rates for NO loss from the different complexes prepared here, which emphasized the ability of halides to denitrosylate {FeNO}^{6} complexes. This new method has opened a new synthetic avenue to synthesize oxygen- and thiolate-ligated {FeNO}^{6} complexes, which decompose in the presence of excess NO gas. A thiolate bound {FeNO}^{6} complex would serve as a direct model for P450nor. In addition, to model the hydride transfer reaction in P450nor futures studies will focus on the reaction of six-coordinate {FeNO}^{6} complexes with hydrides. We tried this reaction with {FeNO}^{6} using the bis-picket fence porphyrin (3,5-Me-BAFP^{2-}) and have

preliminary evidence that this reaction yields a ferrous NHO complex (by UV-vis spectroscopy). Further spectroscopy is necessary to characterize this reaction product for future studies. The formation of stable ferrous NHO adducts would provide a platform to look at reactivity of these complexes with NO and determine if the trans ligand influences N-N bond formation. Lastly, another important difference between our model for Intermediate *I* generated in Chapter 2, is that our complex has an NHOMe(radical) ligand rather than NHOH(radical) ligand (P450nor). In our chemical model, the oxygen atom of the ligand is substituted with a methyl group to impart stability on the hydroxylamine and prevent disproportionation of the ligand. An alternative way to access this NHOH(radical) type species would be by reaction of a ferrous NHO complex with a strong acid. In summary, all of the future studies presented here would provide key insight into the factors that are important in the design of a model complex for Intermediate *I* and ways to learn more about the protonation state of this intermediate.

References

1. Ferguson, S. J. *Curr. Opin. Chem. Biol.* 1998, *2*, 182-193.
2. Zumft, W. G. *Microbiol. Mol. Biol. Rev.* 1997, *61*, 533-616.
3. Lehnert, N.; Berto, T. C.; Galinato, M. G. I.; Goodrich, L. E. In *The Handbook of Porphyrin Science*; Kadish, K. M., Smith, K. M., Guilard, R., Eds.; World Scientific: New Jersey, 2011; Vol. 14, p 1-247.
4. McQuarters, A. B.; Wirgau, N. E.; Lehnert, N. *Curr. Opin. Chem. Biol.* 2014, *19*, 82-89.
5. Riplinger, C.; Bill, E.; Daiber, A.; Ullrich, V.; Shoun, H.; Neese, F. *Chemistry – A European Journal* 2014, *20*, 1602-1614.
6. Riplinger, C.; Neese, F. *ChemPhysChem* 2011, *12*, 3192-3203.
7. Lehnert, N.; Praneeth, V. K. K.; Paulat, F. *J. Comput. Chem.* 2006, *27*, 1338-1351.